Technische Universität München
TUM School of Natural Sciences

Solid polymer electrolytes from poly(vinylphospho-nates) and polymer application as interlayers in hybrid polymer-oxide solid state batteries

Philipp Simon Pfändner

Vollständiger Abdruck der von der TUM School of Natural Sciences der Technischen Universität München zur Erlangung eines

Doktors der Naturwissenschaften (Dr. rer. nat.)

genehmigten Dissertation.

Vorsitz: Prof. Dr. Thomas Fässler

Prüfende der Dissertation:

1. Prof. Dr. Dr. h.c. Bernhard Rieger
2. Prof. Dr. Tom Nilges

Die Dissertation wurde am 16.06.2025 bei der Technischen Universität München eingereicht und durch die TUM School of Natural Sciences am 15.07.2025 angenommen.

“The most important step a man can take. It's not the first one, is it?
It's the next one. Always the next step, Dalinar.”

- Brandon Sanderson, Oathbringer

Die vorliegende Arbeit wurde in der Zeit von November 2020 bis Mai 2025 am WACKER-Lehrstuhl für Makromolekulare Chemie, Technische Universität München, unter Betreuung von Herrn *Prof. Dr. Dr. h.c. Bernhard Rieger* angefertigt

Danksagung

Als erstes möchte ich meinem Doktorvater **Prof. Dr. Dr. h.c. Bernhard Rieger** danken für die Möglichkeit, nach meiner Masterarbeit auch meine Promotion am WACKER-Lehrstuhl für Makromolekulare Chemie anfertigen zu dürfen. Ihre Leidenschaft für die Chemie war inspirierend und ich bin sehr dankbar, dass Sie nicht nur in Ihrer Spezialität den Polymeren unterwegs sind, sondern auch stets offen für andere Forschungsgebiete waren. Sie haben mir so den Zugang zur Batteriechemie ermöglicht, die meine Leidenschaft für die Naturwissenschaften nach bereits 5 Jahren des Studierens nochmal auf eine ganz neue Weise entfachen konnte. Auch wenn ich nicht immer mit allen Ergebnissen zufrieden war, haben Sie trotzdem immer die Erkenntnisse aus den Fehlschlägen hervorgehoben und mich auf ein Neues motivieren können. Vielen Dank dafür!

Des Weiteren möchte ich dem Urgestein unseres Lehrstuhls **Dr. Carsten Troll** danken. Du warst für uns immer ein Fels in der Brandung, wenn es mal zu heiß im Labor wurde oder auch nur mal am Grill. Es war immer wieder faszinierend, egal mit welchen verrückten Ideen ich um die Ecke gekommen bin, du hattest immer das richtige Werkzeug parat.

Ein großes Danke geht auch an meinen Mentor **Dr. Wolfgang Büchele** für die vielen Ratschläge, um meinen Weg in der Chemie zu finden.

Ich hatte das überaus große Glück, dass ich nicht nur durch den Lehrstuhl versorgt wurde, sondern auch noch überragende Unterstützung durch die TUMint Energy Research GmbH hatte, deren Administrative allen voran **Fabian Schatz, Jonas Lindner, Robert Schmid, Christoph Winkler, Vera von Rechenberg** und **Katarina Zeilinger**, die ein wahres Vorbild waren, wenn es darum ging, uns übermütige Batterie-PhDs bei Laune zu halten – mit überragenden Ausflügen, Projekttreffen und natürlich Bürodekoration. Und wenn es in absoluten Ausnahmefällen mal bei der TUMint nicht weiterging, konnte ich dann auch zurück ins Makro-Sekretariat springen und **Frau Bauer** um Hilfe bitten. Vielen Dank Euch allen!

Wie schon erwähnt, hatte ich das Vergnügen, gleich Teil von zwei Gruppen an exzellenten PhD-Studierenden zu sein. Vor den **Makros** habe ich über die Jahre sehr viel Hochachtung über deren Synthesekompetenz, handwerkliches Geschick bei der Reparatur von unserem Laborequipment und Gestankresistenz bekommen. Vielen Dank euch allen für unsere gemeinsame Zeit am Lehrstuhl und den wunderbaren Eispausen auf wackeligen Balkonen.

Zu meinen hartgesottenen Batteriekollegen der **TUMint** muss ich sagen: Hut ab! Auch wenn wir häufig über unsere Forschung und Ergebnisse lachen, habt ihr doch beeindruckende Arbeit über die Jahre geleistet, sowohl fachlich als auch bei unseren zahlreichen Ausflügen, Projekttreffen und gemeinsamen Konferenzen. Mit euch waren diese Momente wie die genialen Klassenfahrten von früher. Besonders erwähnen will ich hier **Gioele Conforto** und **Moritz Bohn**, die sich über die Jahre so viel Zeit genommen haben, um mir alle meine elektrochemischen Fragen zu beantworten. Ohne euch hätte ich kaum die Hälfte meiner Experimente richtig verstanden. Ein sehr großes Danke an euch!

Besonders muss ich hier meinem Projektpartner **Steffen Weinmann** danken, dass wir uns zusammen das Hybrid-Battery-Projekt angeschaut haben und ich mir dadurch sicher geworden bin, die perfekte Chemierichtung für mich gefunden zu haben.

Meinen Laboralltag durfte ich aber nicht nur mit meinen Kollegen teilen, sondern noch mit einer kleinen Armee an eifrigen Helfern, denen ich hoffentlich etwas meines Wissens und meiner Leidenschaft für Batterien und Polymere mit auf den Weg geben durfte. An alle meine Bacheloranden und Forschungspraktikanten **Julian Zuber, Ida Kalleder, Jan Plaumann, Ekrem Suylu, Benedikt Kirchner, Vivian Koplin Tubone, Friederike Ganster, Elisabeth Wimmer, Adrianos Klitz, Tilman Durst** und meinen Masteranden **Stefan Frei**: Die Zeiten, die ich in meiner Forschung am meisten genossen habe, war ganz klar, während wir zusammen getüftelt haben. Das Wissen, dass wir zusammen exzellente Chemie fabrizieren, hat mich immer etwas fröhlicher nach Garching düsen lassen. Vielen Dank, dass Ihr einen so großen Teil zu meiner Promotion beigetragen habt!

Hier muss ich mir noch die Zeit nehmen, einigen Menschen besonders zu danken, die meinen Weg nicht nur in der Chemie, sondern auch auf so vielen anderen Ebenen jeden Tag aufs Neue bereichert haben und das Leben erst richtig lebenswert gemacht haben.

Allen voran möchte ich meinem Masterarbeitsbetreuer **Tom** danken. Du hast mich in den härtesten Zeiten wieder aufgebaut und wahre Größe gezeigt. Ohne dich wäre ich nicht an diesem Punkt in meinem Leben angekommen. Meinen tiefsten Dank dafür!

Und natürlich hat keine meinen Laboralltag vier Jahre lang so intensiv begleitet, wie die beste PPP - PolymerPowerPartnerin - **Marina**! Auch wenn du gleich in unseren ersten gemeinsamen Monaten eiskalt mein Gesangstalent zunichte gemacht hast, bin ich ungeheuerlich froh, dass

du neben mir im Labor und bei den Polymerelektrolyten gelandet bist. Dein wunderbar trockener Humor und fürsorgliche Art sind mir extrem ans Herz gewachsen.

Als ich dann aber mehr und mehr ein Experte der Elektrochemie wurde und mich immer öfter in das TUMint Büro verkrochen habe, hatte ich das enorme Glück, eine neue Gang in meinem Leben begrüßen zu dürfen. **Samu**, **Anna K**, **Jule** und **Pati -** es ist immer wieder eine Wonne, Menschen zu finden, die genauso verrückt sind, wie man selbst und bei denen man seine ganze Dummheit in ihrer ganzen Pracht ausleben kann. Und hier nochmal ein besonderer Dank an Samu, dass du mich auf diesem letzten zermürbenden PhD Jahr begleitet und all den Frust mit mir geteilt hast! Und als im letzten Jahr die Gang durch ein fortschreitendes Leben örtlich zerrissen wurde, habe ich mit dir **Lea** das beste Upgrade überhaupt für alltäglichen Gossip und persönliche Weiterentwicklung bekommen. Vielen Dank, dass ihr mein Leben so sehr bereichert habt!

Mit der größten Dank überhaupt gehört der Person, mit der ich mit Abstand am meisten Zeit in der Uni, niemals sinnlos, vergeudet habe. **Yogi**, dass wir zusammen in der Ersti-Woche vor der Milchbar gelandet sind, war eine der besten Abzweigungen, die mein Leben hätte nehmen können. Es gibt nur sehr wenige Menschen, die man in jeder Lebenssituation anrufen würde. Schön, dass es dich gibt!

Und im gleichen Atemzug muss ich dir **Roberta** Danke sagen. Es gibt kaum eine Person in meinem Leben, auf die ich mich so sehr verlassen kann wie dich. Sei es einfach nur ein entspannter Abend oder das tiefgründigste Gespräch, du bist eine Freundin der Extraklasse!

Tobi, Jonas, Michi, Consti, Benni und **Philipp -** wir kennen uns mittlerweile seit gut 20 Jahren oder sogar noch mehr. Unsere Jahre der Freundschaft lassen sich durch nichts auf dieser Welt ersetzen. Auch wenn wir uns mittlerweile nicht mehr so häufig sehen können wie in unserer Jugend, verbindet uns doch so viel mehr auf einer tieferen Ebene, sodass ich mir sicher bin, euch bis an mein Lebensende an meiner Seite zu haben.

Da ich hier auch noch irgendwann zum wissenschaftlichen Teil kommen muss, habe ich leider nur noch Platz, um meinen ganzen **Freunden** zusammen zu danken. Es grämt mich, hier nicht jeden einzeln nennen zu können, aber unsere Geschichten könnten sehr viel mehr als eine Doktorarbeit füllen. Ihr wisst, ihr seid einer der zentralen Bestandteile meines Lebens. Danke,

dass ihr mich bis hierhin begleitet habt und auf viele weitere Jahre, bis wir grau und buckelig sind!

Als Letztes hier noch ein riesiges Danke an meine **Familie**, die mich über allen Maßen unterstützt hat. Zu wissen, dass immer jemand von euch hinter mir steht und egal in welchen Lebenssituationen unter die Arme greift, hat mir enorm viel Kraft gegeben. Mutti und Vati und der Rest der Bande, ich bin so unglaublich froh, euch zu haben

Abstract

The ongoing electrification of sectors such as transportation, portable electronics, and stationary energy storage imposes increasing demands on next-generation battery technologies. In particular, the need to simultaneously improve energy density, safety, and cycle life drives the search for innovative solid-state energy storage concepts. All-solid-state batteries (ASSBs) are considered a promising solution, offering higher energy densities, enhanced thermal stability, and reduced risk of leakage or fire compared to conventional lithium-ion batteries with liquid electrolytes. Among various electrolyte candidates for ASSBs, solid polymer electrolytes (SPEs) are especially attractive due to their cost-efficient production, excellent processability, mechanical flexibility, and compatibility with established polymer processing techniques. However, SPEs still face significant challenges, particularly lower ionic conductivity and limited electrochemical and thermal stability compared to their inorganic counterparts.

To address these limitations, the first part of this thesis investigates the tailored synthesis of novel polymer electrolytes via rare earth metal-mediated group transfer polymerization (REM-GTP), a technique that enables precise control over polymer architecture. Poly(vinyl phosphonates) with ethylene oxide side chains were synthesized by polymerizing monomers containing either one (P1-VP) or two (P2-VP) ethylene oxide units per side chain. The resulting polymers were processed into free-standing SPE films with various lithium salts and comprehensively characterized in terms of thermal, mechanical, and electrochemical properties. The polymers remained fully amorphous upon salt addition and exhibited high thermal stability, although the onset of thermal degradation was slightly lowered in the presence of salts. The ionic conductivities reached $1.8 \cdot 10^{-5}$ and $8.2 \cdot 10^{-5}$ S cm^{-1} for P1-VP and P2-VP at 60 °C, respectively. However, the oxidative stability was limited by the ethylene oxide side chains, and the high ratio of phosphonate units was hypothesized to restrict the lithium transference number and critical current density, ultimately affecting their performance in half-cell tests.

The second part of this work focuses on a hybrid polymer-oxide battery configuration, aiming to combine the advantages of different electrolyte systems to overcome the limitations of individual materials. Although inorganic electrolytes such as $Li_7La_3Zr_2O_{12}$ (LLZO) offer high ionic conductivity, they require elevated pressures to ensure sufficient electrode contact. To improve the interface between LLZO and $LiFePO_4$ (LFP) cathodes, polyethylene oxide (PEO) interlayers were introduced, which also served as the catholyte. These interlayers significantly

reduced interfacial resistance. It was found that SPEs outperformed composite polymer electrolytes (CPEs), likely due to their softer nature, which allowed for improved contact with the rigid LLZO surface. Furthermore, a minimum interlayer thickness was required to ensure complete coverage of the LLZO surface, as PEO tended to contract at elevated temperatures due to poor wetting of the ceramic surface.

Zusammenfassung

Die zunehmende Elektrifizierung in Bereichen wie Mobilität, tragbare Elektronik und stationäre Energiespeicherung stellt hohe Anforderungen an zukünftige Batterietechnologien. Insbesondere die Notwendigkeit, Energiedichte, Sicherheit und Lebensdauer gleichzeitig zu verbessern, treibt die Suche nach innovativen Speichertechnologien voran. Festkörperelektrolytbatterien (ASSBs) gelten in diesem Zusammenhang als vielversprechende Lösung, da sie im Vergleich zu konventionellen Lithium-Ionen-Batterien mit flüssigen Elektrolyten potenziell höhere Energiedichten, eine verbesserte thermische Stabilität sowie ein geringeres Risiko für Auslaufen oder Bränden bieten. Unter den verschiedenen Elektrolytkandidaten für ASSBs gelten polymere Festkörperelektrolyte (SPEs) als besonders vielversprechend. Sie vereinen Vorteile wie kostengünstige Herstellung, gute Verarbeitbarkeit, mechanische Flexibilität und die Möglichkeit zur Skalierung in etablierten Polymerverarbeitungstechnologien. Dennoch stellen die im Vergleich zu anorganischen Festkörperelektrolyten niedrigere Ionenleitfähigkeit sowie eine begrenzte elektrochemische und thermische Stabilität nach wie vor zentrale Herausforderungen dar.

Zur Verbesserung dieser Eigenschaften wurde im ersten Teil dieser Arbeit die gezielte Synthese neuartiger Polymerelektrolyte mithilfe der seltenen Erden katalysierten Gruppenübertragungspolymerisation (REM-GTP) untersucht, einer Methode, die eine präzise Kontrolle über die Polymerarchitektur ermöglicht. Hierzu wurden Polyvinylphosphonate mit Ethylenoxidseitenketten synthetisiert. Es gelang die Darstellung und Polymerisation von Monomeren mit einer (P1-VP) beziehungsweise zwei (P2-VP) Ethylenoxid-Einheiten in den Seitenketten. Die resultierenden Polymere wurden anschließend mit verschiedenen Lithiumsalzen zu selbsttragenden SPE-Folien verarbeitet und hinsichtlich ihrer thermischen, mechanischen und elektrochemischen Eigenschaften umfassend charakterisiert. Die Polymere zeigten auch nach Zugabe verschiedener Lithiumsalze eine vollständig amorphe Struktur sowie eine hohe thermische Stabilität; allerdings wurde der Beginn der thermischen Zersetzung durch die Salze leicht abgesenkt. Die Ionenleitfähigkeit erreichte bei 60 °C Werte von $1{,}8 \cdot 10^{-5}$ S cm^{-1} für P1-VP und $8{,}2 \cdot 10^{-5}$ S cm^{-1} für P2-VP. Die elektrochemische Stabilität wurde durch die Ethylenoxid-Seitenketten limitiert. Zudem wird vermutet, dass der hohe Anteil an Phosphonat-Gruppen die Lithium-Transferenzzahl und die kritische Stromdichte reduziert, was sich in einer verringerten Kapazität in Halbzelltests niederschlug.

Im zweiten Teil der Arbeit wird eine hybride Polymer-Oxid-Batteriekonfiguration untersucht. Ziel ist es, durch Kombination der Vorteile verschiedener Elektrolytsysteme die Einschränkungen einzelner Klassen zu überwinden. Oxidische Elektrolyte bieten zwar eine hohe Ionenleitfähigkeit, erfordern jedoch hohe Drücke, um einen guten Kontakt zu den Elektroden sicherzustellen. Zur Verbesserung der Grenzfläche zwischen LLZO-Elektrolyten und LFP-Kathoden wurden daher Polyethylenoxid (PEO) Zwischenschichten eingesetzt, die gleichzeitig als Katholyt dienen. Die Einführung dieser PEO-Zwischenschichten führte zu einer signifikanten Reduktion des Grenzflächenwiderstands. Die Ergebnisse zeigten, dass SPEs eine bessere Leistung als Elektrolyte mit anorganischen Additiven aufweisen, was auf den weicheren Charakter zurückgeführt wird. Es wurde zudem festgestellt, dass eine Mindestdicke der Zwischenschicht erforderlich ist, um eine vollständige Bedeckung der LLZO-Oberfläche sicherzustellen, da sich PEO bei erhöhten Temperaturen aufgrund schlechter Benetzbarkeit des LLZOs zusammenzieht.

List of Acronyms

Abbreviation	Description
1-VP	bis(2-methoxyethyl) vinylphosphonate
2-VP	bis(2-(2-methoxyethoxy)ethyl) vinylphosphonate
3-VP	bis(2-(2-(2-methoxyethoxy)ethoxy)ethyl) vinylphosphonate
AIBN	azobisisobutyronitrile
ASSB	all-solid-state battery
BESS	battery energy storage systems
C65	conductive carbon black
CC	current collector
Cp	cyclopentadienyl
CPE	composite polymer electrolytes
CV	cyclic voltammetry
DBPO	dibenzoyl peroxide
DCM	dichloromethane
DEVP	diethyl vinylphosphonate
DMF	*N,N*-dimethylformamide
DRT	distribution of relaxation time
DSC	differential scanning calorimetry
EDX	energy-dispersive X-ray spectroscopy
EIS	electrochemical impedance spectroscopy
EO	ethylene oxide
EV	electric vehicle
ESW	electrochemical stability window
EV	electric vehicle
GEIS	galvanostatic electrochemical impedance spectroscopy
GPE	gel polymer electrolytes
GPC	gel permeation chromatography
*I**	initiator efficiency
LCO	lithium cobalt oxide
LFP	lithium iron phosphate
LIB	lithium-ion battery
LiM	Lithium metal

LiTFSI	lithium bis(trifluoromethane)sulfonimide
LLZO	$Li_7La_3Zr_2O_{12}$
LTO	Lithium titanate oxide
LSV	linear sweep voltammetry
t_{Li^+}	Li^+ transference number
MeCN	acetonitrile
MS	molecular sieve
M_n	molecular weight
M_w	mass average molar mass
NCA	nickel cobalt aluminum oxide
NMC	nickel manganese cobalt oxide
NMR	nuclear magnetic resonance spectroscopy
Đ	dispersity
PEIS	potentiostatic electrochemical impedance spectroscopy
PEG	polyethylene glycol
PEO	polyethylene oxide
REM-GTP	rare-earth mediated group transfer polymerization
r.t.	room temperature
SEI	solid electrolyte interface
SEM	scanning electron microscopy
SN	succinonitrile
SPE	solid polymer electrolyte
T_g	glass transition temperature
T_m	melting temperature
TGA	thermogravimetric analysis
TLM	transmission line model
THF	tetrahydrofuran
TMP	trimethyl phosphate
TMS	trimethylsilyl
TOF	turnover frequency
TSC	total solid content
XRD	X-ray diffraction

Table of Contents

1 Introduction

In today's world, lithium-ion batteries have become a cornerstone of energy storage solutions, driving the growth of renewable energy sources and powering a wide range of applications from portable electronics to electric vehicles (EVs) and grid storage. Their high energy density, excellent cycle life, and low self-discharge rates have positioned them as the leading technology for these purposes.[1,2] As more aspects of our daily lives shift towards electrification, coupled with a global move towards renewable energy, the demand for energy storage is continuously rising. Renewable energy sources like solar and wind face a significant challenge due to their irregular nature, as they are only available under suitable conditions rather than on demand. This variability leads to fluctuations in energy production, with significant changes between day and night, cloudy and sunny weather, or calm and windy periods.[3] To ensure consistent electricity supply throughout the year, stabilize the electrical grid, and facilitate our mobility transition, large-scale battery energy storage systems (BESS) are essential. Among the existing technologies, lithium-ion battery (LIB) systems have emerged as the leading solution.[4,5] The drastic growth of BESS worldwide is depicted in **Figure 1-1**, illustrating an exponential increase in capacity from approximately 40 GWh in 2020 to over 350 GWh by 2024.[6]

To satisfy the continuous growing demand for batteries, the planning and construction of gigafactories with immense production capacities have become a global phenomenon over the last decade. As of August 2023, Asia led with a battery production capacity of 2.691 GWh,[7] while North America followed with 1.539 GWh as of August 2024.[8] Europe's journey towards battery independence, however, has been accompanied with challenges. Despite initial optimism, Europe's projected battery production capacity declined significantly from 1.897 GWh in December 2023 to 1.424 GWh in December 2024.[9] This decline highlights the significant challenges associated with producing high-quality batteries on a large scale, exemplified by the struggles faced by Northvolt.

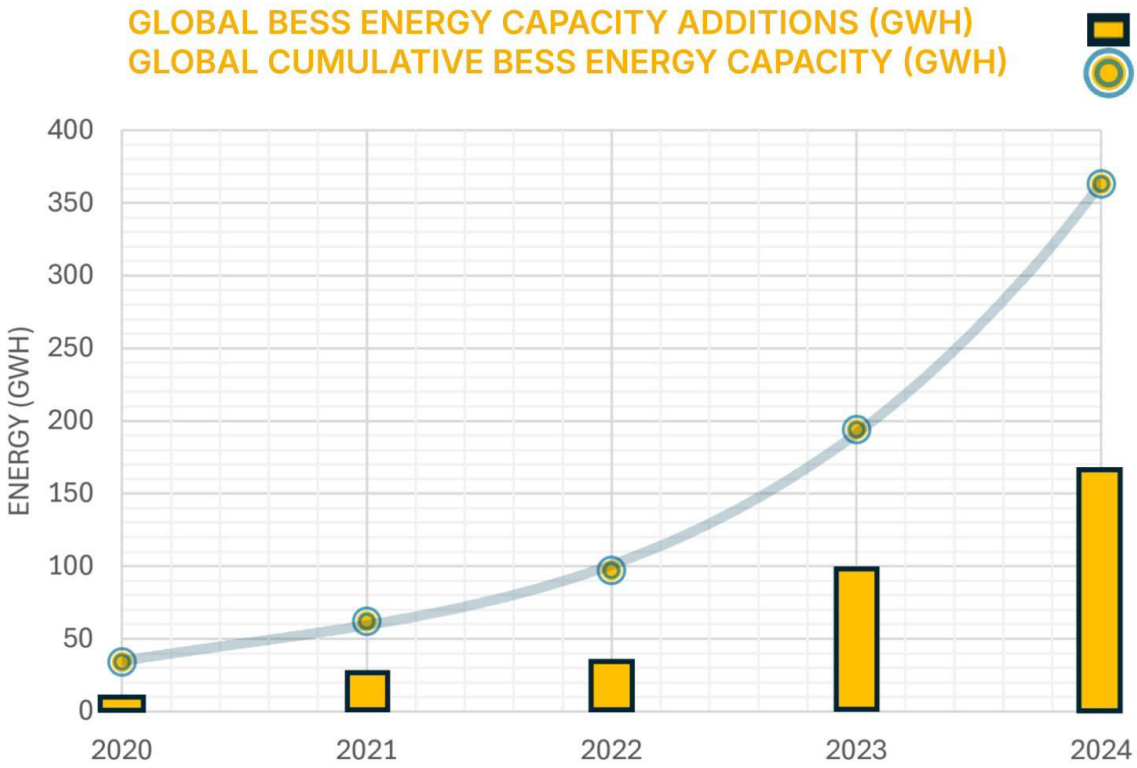

Figure 1-1: Global BESS capacity and yearly growth. Reprinted from Ref [6].

Once hailed as Europe's answer to dominant Asian producers such as Contemporary Amperex Technology (CATL) and BYD, Northvolt set ambitious sustainability targets, planning operations powered by 98% fossil-free energy and utilizing 50% recycled materials in its Li-ion cells.[10] These goals initially attracted substantial investment, including €500 million from Volkswagen in 2021[11] and €943 million from the European Investment Bank in 2024.[12] However, production issues, such as high scrap rates, led to mounting debts, and a fight for the company's survival by 2025. Despite these setbacks, there is still hope as Northvolt continues the construction of its third gigafactory in Heide, Germany, as of May 2025.[13,14]

Despite these struggles and China's continued leadership in battery innovations, the geopolitical landscape of 2025 further emphasizes Europe's need for battery independence and innovative spirit. While vehicle innovation was historically dominated by German manufacturers such as Volkswagen, Daimler, and BMW, recent years have witnessed remarkable advancements from China in EV technology.[15] Notably, BYD unveiled its "Super e-Platform" in March 2025, featuring flash-charging batteries with a rate of 10C, capable of charging 400 km of range in just five minutes, thus rivalling the convenience of refuelling

conventional combustion engines. [16] Additionally, CATL's "Naxtra Battery" achieved an energy density of 175 Wh kg^{-1}, currently the highest recorded for sodium-ion batteries as of April 2025 and thereby pathing the way for another competitive technology.[17]

With rising global tensions and potential trade conflicts with the newly elected government in the US, Europe's reliance on external battery resources from China and the US presents significant strategic risks. To secure its industrial future and facilitate a robust energy transition, the EU must decisively support its battery sector. Essential strategies include the development of a comprehensive economic security doctrine, diversifying supply chains, investing in domestic production, and fostering innovation in next-generation battery technologies.[18,19] These measures would significantly reduce dependencies, enhance competitiveness, and ensure a sustainable and resilient battery supply.[19] Europe's urgent need for domestic battery production is further underlined by the projected growth in global EV sales over the coming decades, as shown in **Figure 1-2**, translating into approximately 0.7-1.5 TWh of required battery capacity or the equivalent of 45–95 gigafactories by 2040.[20]

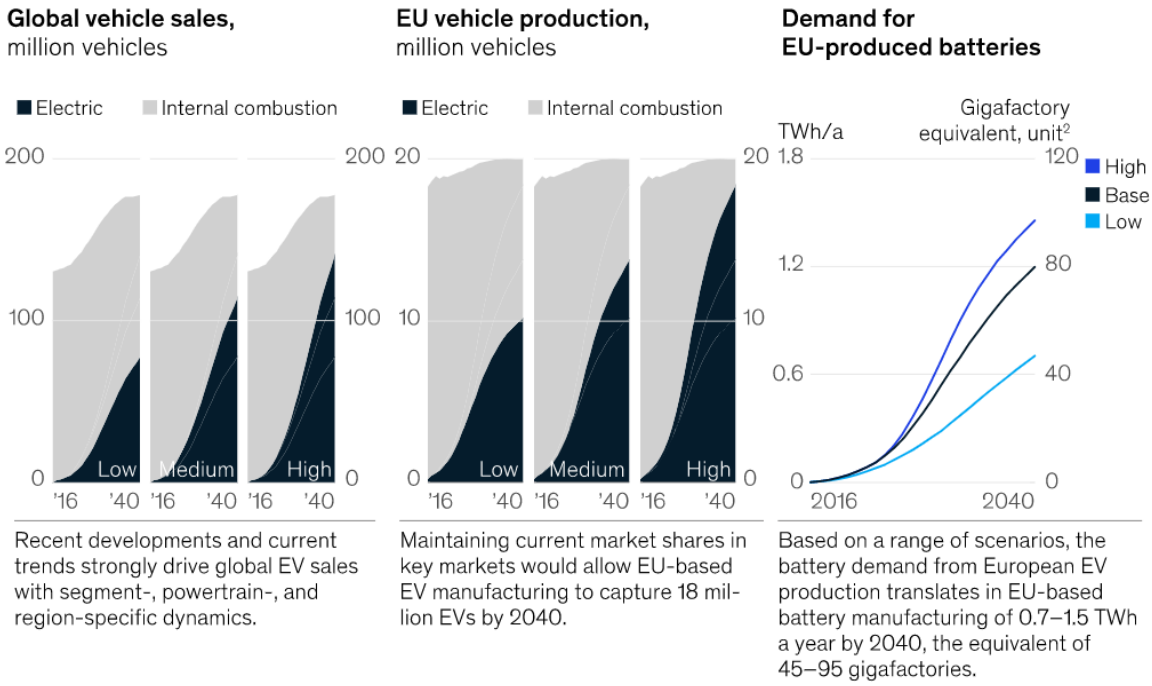

Figure 1-2: Low, medium and high projections for the development of global EV sales, vehicle production in the EU and corresponding demand for EU produced batteries. Reprinted from Ref [20].

One key technology for increasing battery energy density is the development of all-solid-state batteries, which replace liquid electrolytes in conventional lithium-ion batteries with polymer or inorganic solid electrolytes enabling new cell architectures and electrode

materials.[21–23] Nevertheless, similar to the challenges experienced in large-scale battery manufacturing, developing new technologies such as ASSBs to market maturity is profoundly challenging. While numerous manufacturers publicly announce their commitment to developing this promising technology, actual implementation in production vehicles remains to be seen. BYD, for instance, demonstrated pilot-line ASSB cells with capacities of 20 and 60 Ah but projects large-scale production no sooner than 2030.[24] CATL also invests significantly in ASSB technology, expanding its R&D team to over 1000 members and already develops 20 Ah cells reaching 500 Wh kg^{-1}.[25] Additionally, Japan's Maxwell announced that it will discontinue its production of prismatic lithium-ion batteries by May 2025 in favour of focussing on ASSB technology.[26,27] A comprehensive overview by BloombergNEF (**Figure 1-3**) shows targeted energy densities for different battery technologies over the coming years.[28] Clearly, ASSB technology will significantly shape global battery evolution in the near future, emphasizing the strategic importance for Europe to actively participate in its development to secure independent production capabilities.

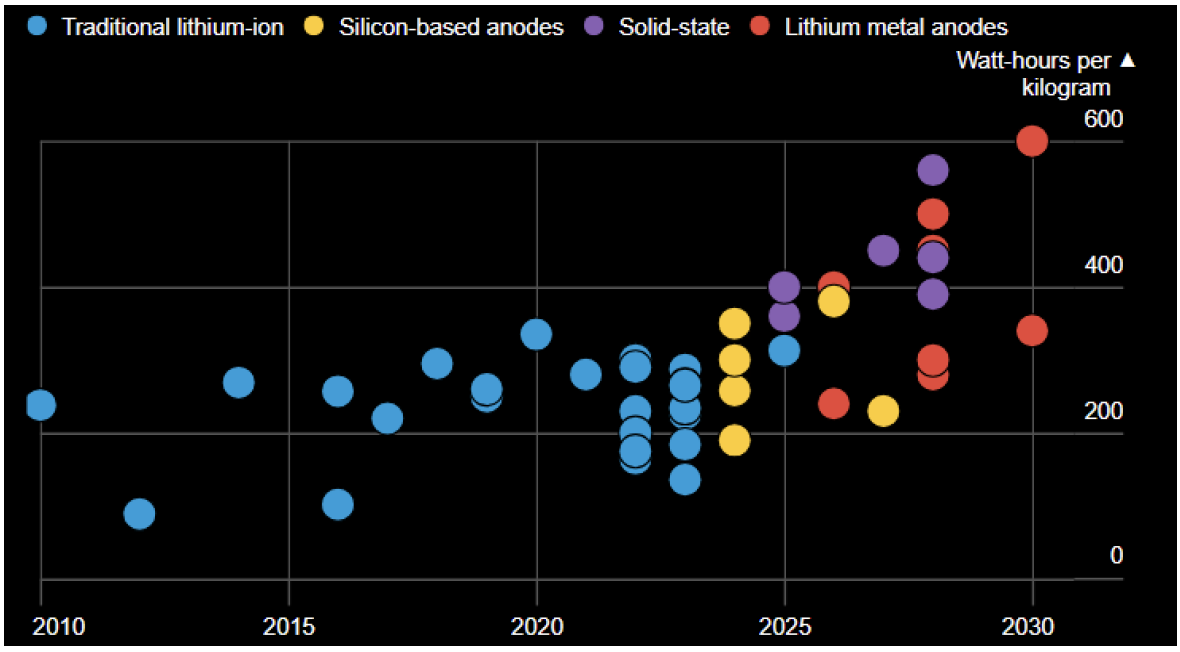

Figure 1-3: New lithium battery technologies to boost energy density. Selected cell energy density targets, 2010-2030 by BloombergNEF, company statements. Note: Silicon based anodes are typically paired with lithium nickel manganese cobalt oxide (NMC) cathodes. Solid-state batteries are typically paired with silicon-based anodes or Li metal anodes and nickel-based cathodes. Dates correspond to target commercialization dates. Reprinted from Ref [28].

2 Theoretical Background

2.1 Battery Fundamentals

The basic working principle of a battery is to convert chemical energy into electrical energy. Batteries can be categorized in two basic categories. Primary batteries are single use, as their active material cannot be regenerated. Secondary batteries, on the other hand, are rechargeable, as their electrochemical reactions are reversible, making them more economical and exclusively used in electromobility and energy storage.[29] This thesis will focus exclusively on secondary batteries.

The basic structure of a battery includes two electrodes (cathode and anode), an electrolyte, and a separator to prevent short circuits. During discharge, a redox reaction takes place where the cathode is reduced, and the anode is oxidized. Electrons flow through an external circuit to provide usable current, balanced by ionic movement through the electrolyte. While charging, these processes are reversed.[29,30] Despite the technical inaccuracy, the electrode with lower/negative potential is generally referred to as anode and the electrode with the higher/positive potential as cathode in battery research, regardless of the charging or discharging process.[31] Early rechargeable batteries, like the lead-acid (1880s)[32] and nickel-cadmium (1901) systems, used aqueous electrolytes and provided energy densities below 100 Wh kg^{-1}.[33] However, the toxicity of these systems and memory effect of cadmium prompted the development of nickel-metal hydride batteries.[34] In the search for higher energy densities, lithium was introduced as an electrode material as it provides the lowest reduction potential (−3.04 V vs. SHE) of all elements.[35] This greatly enhances the energy storage capacity of a battery, as the difference between the chemical potential of the anode (μ_a) and cathode (μ_c) results in the working voltage (U_{cell}) of the cell according to equation 1:

$$U_{cell} = \mu_C - \mu_A \qquad 1$$

which is directly proportional to the stored energy ($E_{battery}$) of a battery according to equation 2 with the transported electrical charge (Q):[36]

$$E_{battery} = Q \cdot U \qquad 2$$

With these considerations in mind Sony Corporation commercialized the first rechargeable lithium-ion battery in 1991, which laid the foundation for the most used battery today.[37] The initial LIBs introduced by Sony featured a comparatively low gravimetric energy density of 80 Wh kg^{-1} at cell level. Contemporary LIBs have significantly improved, achieving volumetric and gravimetric energy densities up to 770 Wh L^{-1} and 300 Wh kg^{-1}, respectively.[38,39] These advancements are largely attributed to the optimization of electrode materials. The most commonly used anode is a graphitic carbon (C_6), which allows for the reversible intercalation of lithium ions. On the cathode side, various layered transition metal oxides are employed, with lithium cobalt oxide ($LiCoO_2$, LCO) being particularly prevalent. $LiCoO_2$ possesses a stoichiometric octahedral lattice structure with alternating layers of Li^+ and Co^{3+} ions. During charging, lithium ions deintercalate from the cathode's layered structure to a certain extent (denoted as x), releasing an electron and oxidizing Co^{3+} to Co^{4+}. Simultaneously, at the anode, a lithium ion is reduced by an electron and is intercalated into the graphite layers in its atomic state.[40] During discharge, these processes are reversed. The individual reactions at the cathode and anode, as well as the overall cell reaction, are depicted in equations 3 to 5:[41,42]

Cathode: $Li_{1-x}CoO_2 + x\,Li^+ + x\,e^- \underset{\text{charge}}{\overset{\text{discharge}}{\rightleftharpoons}} LiCoO_2$ (3)

Anode: $Li_xC_n \underset{\text{charge}}{\overset{\text{discharge}}{\rightleftharpoons}} C_6 + x\,Li^+ + x\,e^-$ (4)

Full cell reaction: $Li_{1-x}CoO_2 + Li_xC_n \underset{\text{charge}}{\overset{\text{discharge}}{\rightleftharpoons}} LiCoO_2 + C_6$ (5)

To ensure the mechanical integrity of the porous electrode materials and serve as electric conductive pathway to the external electrical circuit, metal current collectors are used. Copper foil is used on the anode side due to its high electronic conductivity and resistance against alloy formation with lithium. On the cathode side, aluminum foil is employed. While most metals are unstable at the high potentials (~4.3 V vs. Li^+/Li) at which lithium cathodes operate, the native Al_2O_3 layer on aluminum foil transforms into AlF_3 in the presence of fluoride electrolyte salts, forming a chemically stable layer that resists oxidation and corrosion at elevated potentials.[43,44] A porous polymer membrane serves as the separator, preventing direct contact between electrodes and thereby avoiding short circuits. Typically, these separators are semi-crystalline polyolefins, such as polyethylene (PE) and polypropylene (PP), processed to create microporous structures, with a thickness of about 25 µm

or even less.[38,45] The separator's pores, along with those in the porous electrodes, are filled with a liquid electrolyte containing a lithium salt. This electrolyte facilitates ionic transport within the cell, while its insulating properties ensure that electrons must travel through an external electrical circuit. The separation of ionic and electronic transport is fundamental to harnessing electrical energy from the battery. Since lithium ions shuttle between the electrodes during charge and discharge cycles, this configuration is often referred to as a "rocking chair battery." **Figure 2-1** illustrates the working mechanism of a lithium-ion battery.[46,47]

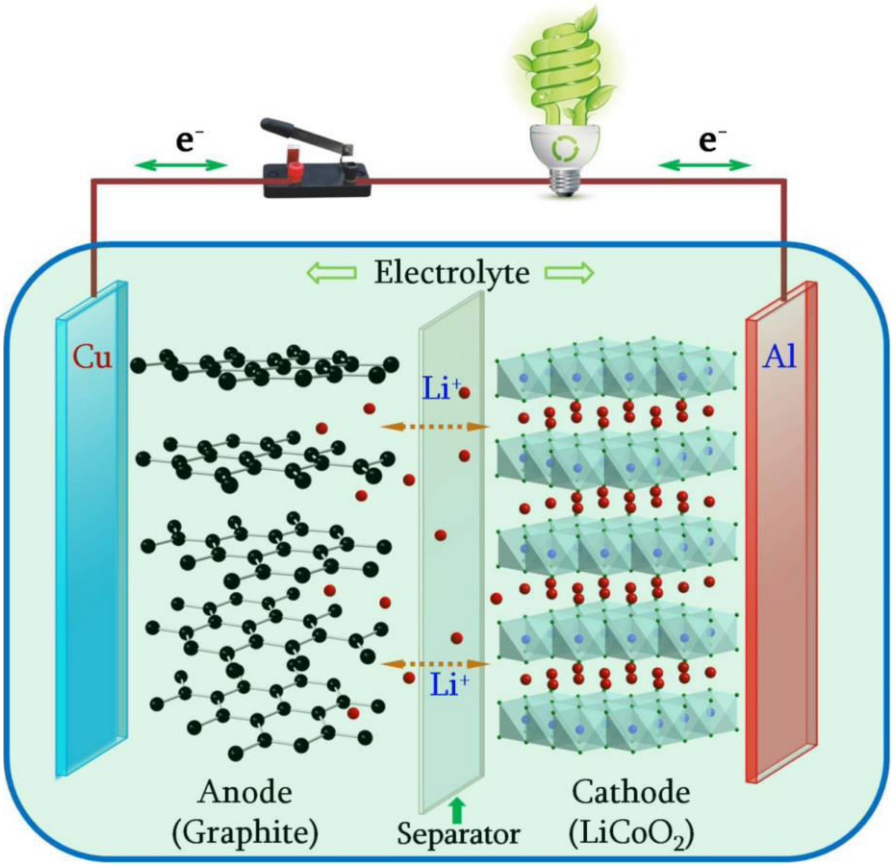

Figure 2-1: Schematic illustration of the main components and the working principle of lithium-ion batteries, using the example of an $LiCoO_2$/graphite full-cell during discharge. Reprinted with permission from Ref [36].

Most commercially available batteries utilize a mixture of cyclic and linear carbonates containing a dissolved lithium salt, which is typically $LiPF_6$ in a concentration of 1 M. The choice of electrolyte significantly affects cell capacity, operating temperature range, cycle life, and overall safety. Cyclic carbonates, such as ethylene carbonate (EC), have high dielectric constants that facilitate lithium salt dissolution, while linear carbonates, including dimethyl carbonate (DMC), ethyl methyl carbonate (EMC), and diethyl carbonate (DEC), reduce

solvent viscosity to enhance ionic conductivity (reaching 10^{-2} S cm^{-1}).[48] EC also plays a crucial role in forming a stable solid electrolyte interface (SEI) on the graphite anode during the initial charging cycle. The SEI is a nanometer-thick passivation layer composed of inorganic and organic electrolyte reduction products, such as lithium fluoride, lithium carbonate, and lithium ethylene dicarbonate.[49] This layer is electronically insulating but permeable to lithium ions, preventing further electrolyte decomposition while enabling reversible lithium intercalation and deintercalation.[50,51] To improve cycle stability, small quantities of electrolyte additives are incorporated into the liquid electrolyte. These additives undergo reduction on the graphite electrode during the first charge cycle, contributing to a more stable and protective SEI.[52] In commercial cells, commonly used additives include vinylene carbonate (VC) and prop-1-ene-1,3-sultone (PES), which enhance SEI durability and overall battery performance.[53] However, the exact electrolyte composition is often not disclosed by the manufactures, as these play a significant role in the overall cell performance. Despite their advantages, these organic liquid electrolytes present significant safety concerns. They are highly flammable and volatile, with low flash points ranging from approximately 15 °C to 33 °C. During charge and discharge cycles, the electrodes undergo volume changes due to lithium-ion intercalation, leading to pressure build-up within the cell. This can result in electrolyte leakage, fire, or even explosion if the battery is damaged.[47,54] Moreover, lithium tends to deposit unevenly on the anode, forming dendrites, which are branched structures that can penetrate the separator and cause internal short circuits, further increasing the risk of thermal runaway. To address these safety issues and to potentially increase energy density, there has been great efforts going into replacing liquid electrolytes with solid electrolytes to develop all-solid-state batteries.

2.2 All Solid-State Batteries

Even though state-of-the-art and upcoming lithium-ion batteries attempt to overcome the previously mentioned concerns, the all-solid-state battery concept may provide possible improvements, especially in terms of energy density and safety, owing to the use of non-flammable solid electrolytes.[55,56] ASSBs also potentially enable the use of lithium metal anodes, which have higher theoretical capacities compared to traditional graphite anodes.[57] Additionally, solid electrolytes simplify battery design by combining ion conduction and electrical isolation functions, typically handled separately in liquid electrolyte systems.[58] The slower degradation of solid materials is also expected to increase the cycle lifetime of these batteries, as demonstrated by a micro-battery developed by Dudney et al. already in 2015, which achieved over 10.000 cycles.[59] However, the scalability of this technology remains a challenge especially in terms of cost and production.[60,61] Replacing liquid or gel electrolytes and separators with an intrinsically non-flammable, non-volatile solid electrolyte holds great promise and is perhaps the ultimate solution for safer, high-energy-density all-solid-state lithium metal batteries. To achieve high energy density with solid electrolytes, it is necessary to use lithium metal (or other high-energy-density anodes) in an all-solid-state lithium metal battery configuration. This setup can increase volumetric and gravimetric energy density by up to 70% and 40%, respectively, compared to a 10% decrease in gravimetric energy density if traditional graphite anodes were used (**Figure 2-2**).[62] This decrease is due to the higher density of solid electrolytes compared to liquid electrolytes, resulting in a higher weight when maintaining the same thickness and volume.

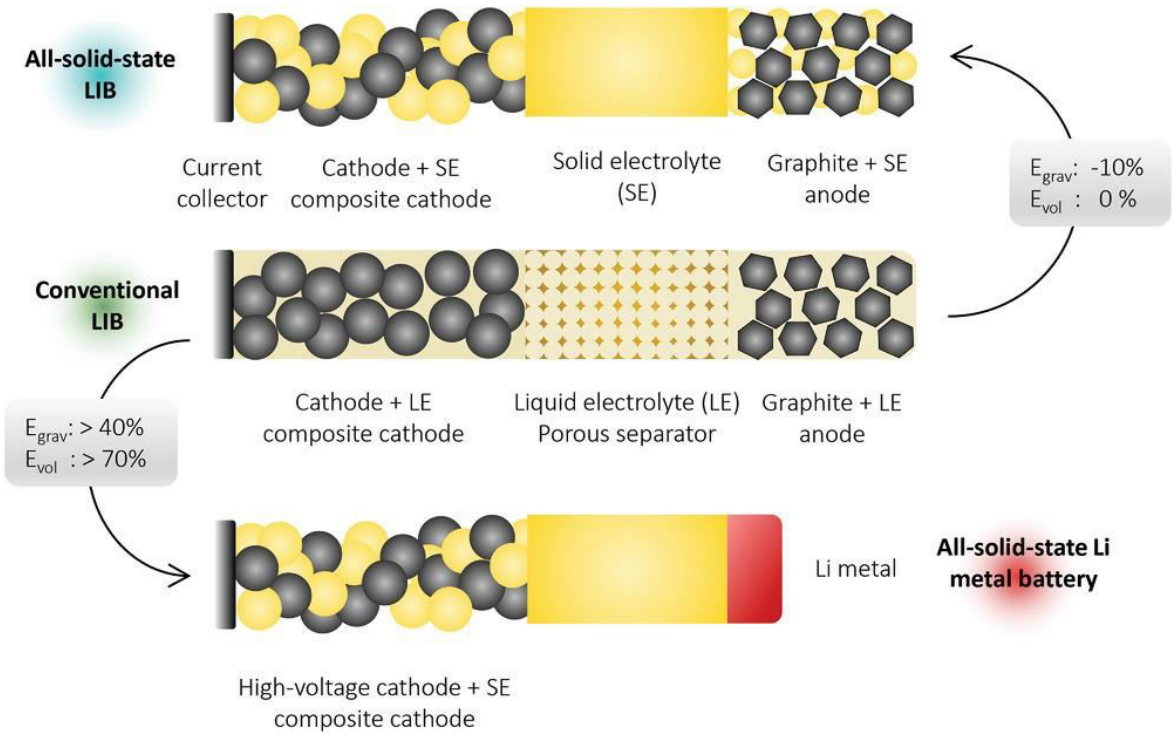

Figure 2-2: Change in energy density upon replacing liquid electrolyte in conventional LIB with solid electrolyte (all-solid-state LIB) and Li metal anode (all-solid-state Li metal batteries). The volumetric and gravimetric energy densities are represented by E_{vol} and E_{grav}, respectively.[62] Copyright 2020 John Wiley and Sons.

On the cathode side, the wider electrochemical stability of solid electrolytes can support an increase in cell voltage up to 5 V with the adoption of high-voltage cathodes. This can be achieved without significant electrolyte decomposition, potentially leading to an energy density increase of more than 20%.[39] Solid electrolytes can be broadly categorized into three groups: inorganic (ceramic) electrolytes, solid polymer electrolytes, and solid composite electrolytes (SCEs).[63–65] Inorganic ceramic electrolytes include sulfides,[66–70] oxides,[71–74] and halides,[75–77] each with its own set of advantages and disadvantages.

Sulfides exhibit very high ionic conductivity, with materials like $Li_{10}GeP_2S_{12}$ demonstrating an ionic conductivity greater than 10^{-2} S cm^{-1} at room temperature.[78] However, sulfides suffer from poor stability against lithium, leading to decomposition and the formation of a non-passivating layer that results in continuous interface growth and eventual cell failure. Oxides offer improved stability against lithium and better thermal and high-voltage stability compared to sulfides, with only minor losses in conductivity. For example, one of the most studied oxides $Li_7La_3Zr_2O_{12}$ (LLZO) exhibits a promising ionic conductivity of above 10^{-4} S cm^{-1} at room temperature.[72] Nevertheless, oxides face challenges in interfacial resistance, mechanical properties, and processability. Additionally, their limited compatibility

with current cathode chemistry due to the high temperatures required in co-sintering processes poses a significant drawback.[79] Solid polymer electrolytes offer low flammability and better tolerance to shock, vibration, and mechanical deformation compared to liquid electrolytes. They are formed by dissolving a lithium salt in a polar polymer matrix and provide excellent compatibility and electrode interfacial contact due to their flexibility.[63,80] SPEs are particularly advantageous in terms of production costs and scalability, making them a promising candidate for large-scale manufacturing. However, they must meet stringent requirements, including high ionic conductivity, a high lithium-ion transference number, low interfacial resistance, and thermal and electrochemical stability.[7,8] Solid composite electrolytes (SCEs) combine the benefits of inorganic solid electrolytes and solid polymer electrolytes. These hybrid materials maintain the high ionic conductivities and stability of inorganic materials while improving processability and mechanical properties through the addition of a polymer. This combination makes SCEs a highly promising class of materials for future energy storage systems.[65,81]

2.3 Fundamental Properties of Electrolytes

Before going into detail about some of the individual classes of solid electrolytes, first some general requirements of solid electrolytes are discussed. Their properties significantly impact the performance, safety, and longevity of ASSBs. First of all, mechanical stability is essential for maintaining structural integrity, keeping the electrodes separated, and suppressing lithium dendrite formation, thereby preventing short circuits. Solid electrolytes should exhibit a high shear modulus and fracture toughness to withstand stress and volume changes during battery operation.[72,82] Thermal stability is another critical factor, ensuring that the electrolyte retains its properties across the battery's operational temperature range. While LIBs typically operate from −20 °C to 60 °C,[83] or in special applications, such as military use, from −50 °C to 80 °C,[84] ASSBs can usually operate at temperatures exceeding 100 °C, depending on the electrolyte type.[85] A thermally stable electrolyte resists decomposition and maintains functionality under varying thermal conditions, whether in daily use or extreme situations like thermal runaway, which can occur if a battery is damaged, for example, during a car crash. This resistance to degradation is vital for minimizing hazardous potential and ensuring high safety standards.[22,86]

From an electrochemical perspective, one of the most critical and widely discussed properties is high ionic conductivity, which is essential for efficient lithium-ion transport.[87] At room temperature, a conductivity of at least 10^{-4} S cm^{-1} is often cited as desirable to match the performance of liquid electrolytes.[88] Many high-performing solid electrolytes achieve ionic conductivities between 10^{-4} and 10^{-3} S cm^{-1} at room temperature. However, this range is still 10 to 100 times lower than that of state-of-the-art liquid electrolytes, which typically exhibit room temperature ionic conductivities around 10^{-2} S cm^{-1}.[89] High ionic conductivity facilitates the movement of ions through the electrolyte, reducing the battery's internal resistance. This reduction in resistance leads to less energy loss as heat and more efficient charging and discharging processes. Additionally, it enables higher charging rates and extends the battery's lifetime by promoting a more uniform current distribution.

In addition, electrolytes need to exhibit negligible electronic conductivity to prevent self-discharge and enhances overall battery performance.[90] Ionic conductivity is typically determined using electrochemical impedance spectroscopy (EIS). This method measures the bulk resistance of the electrolyte and by considering its geometric dimensions can be used

to calculate the conductivity. To ensure the longevity and safety of a battery, the solid electrolyte must also possess a sufficient electrochemical stability window (ESW). The ESW refers to the range between the oxidation and reduction potentials of the electrolyte, indicating its resistance to degradation from electrochemical reactions. A wider gap between the highest occupied molecular orbital (HOMO) and the lowest unoccupied molecular orbital (LUMO) of the electrolyte correlates with a broader ESW.[91]

If the electrochemical potential of the anode exceeds the electrolyte's reduction potential, the electrolyte may be reduced if not kinetically inhibited, leading to degradation.[92,93] Conversely, if the cathode's electrochemical potential is lower than the electrolyte's oxidation potential, oxidation of the electrolyte can occur unless a passivation layer inhibits electron transfer.[94] A wide stability window, typically between 0 and 5 V vs. Li^+/Li, is essential to accommodate the operating potentials of various electrode materials without degradation. Therefore, designing electrolytes with sufficient stability window for the respective potentials of the used electrodes is crucial for maintaining the stability and performance of solid-state batteries. It should be noted that most electrolytes decompose at least partially when in contact with the electrodes at very high and low potentials, forming a passivating SEI layer. This passivation layer must be ionically conductive yet electronically insulating to ensure functionality and prevent continuous electrolyte decomposition, making it a critical factor for stable long-term cycling.[95,96]

Lastly, the Li^+ transference number (t_{Li^+}) must be considered, especially for polymer electrolytes. This number (between 0 and 1) represents the fraction of the total ionic conductivity contributed by lithium-ions. Most inorganic ceramic solids act as exclusive lithium-ion conductors, achieving a Li^+ transference number close to unity. In contrast, polymer electrolytes allow both lithium-ions and their counter anions to move through the electrolyte. Typically, Li^+ cations in solid polymer electrolytes exhibit lower mobility than their anionic counterparts due to interactions with the polymer matrix. This interaction can create a concentration gradient, particularly at high current densities, which opposes the desired movement of the ions.[97,98]

These mechanical, thermal, and electrochemical properties form the foundation for designing promising solid electrolytes and influence other critical parameters, such as the critical current density. These factors are often compared using radar chart as exemplary displayed in **Figure 2-3**. However, it is important to note that this point-based rating system

for individual electrolyte classes is subjective and depends on the authors' objectives and criteria. Therefore, ratings may vary across different sources.[82,94,99–101]

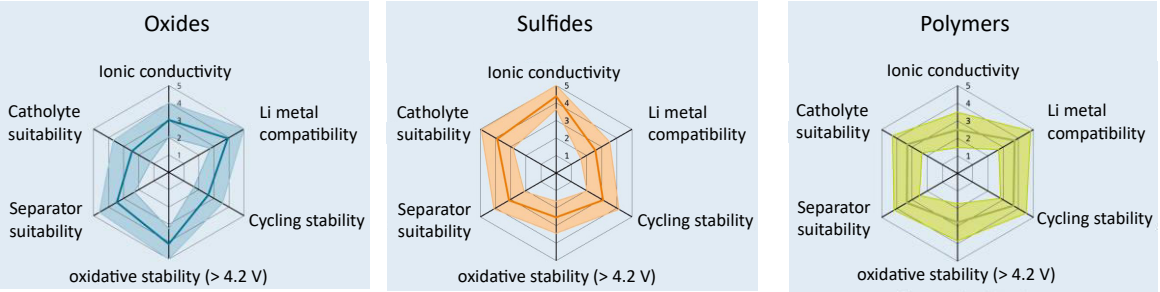

Figure 2-3: Radar charts of relevant properties for oxide, sulfide and polymer electrolytes. Adapted from Schmaltz et al.[102]

2.4 Inorganic Solid Electrolytes - Oxides

Inorganic solid electrolytes mainly consist of two prominent material classes characterized by their chemical composition: oxides and sulfides. In the following chapter oxides will be briefly discussed. Besides these two prominent examples there are also newer materials classes namely halides and phosphides. Since the main focus of this thesis is on polymer electrolytes, for a more detailed information on inorganic solid electrolyte properties the reader is referred to the numerous reviews devoted to these material classes.[68,75,77,103] In general, ionic conduction in inorganic solid electrolytes is primarily facilitated by the movement of ions through defects within the crystal structure. This process involves ions navigating energy barriers, known as migration energy (E_m), as they transition between crystallographic sites (**Figure 2-4A**). The presence of interstitials, vacancies, and partial occupancies in the lattice, influenced by the defect formation energy, plays a crucial role in determining ionic conductivity. These defects, such as Frenkel and Schottky defects, enable ion transport through vacancy and interstitial mechanisms (**Figure 2-4B**). In vacancy mechanisms, ions hop to adjacent vacant sites, minimizing lattice strain and reducing activation energy barriers. This mechanism relies on the availability of vacancies within the lattice, which significantly impacts the pathways and energy barriers for ion migration. Conversely, interstitial mechanisms involve the direct or indirect movement of ions through interstitial sites. Direct interstitial diffusion occurs when an ion moves to a neighbouring interstitial site, often leading to significant lattice strain due to the size disparity between interstitial and matrix atoms. Indirect interstitial diffusion, or the knock-off mechanism, involves an

interstitial ion displacing a matrix atom, which then migrates to another interstitial site (**Figure 2-4C-F**).[104–106]

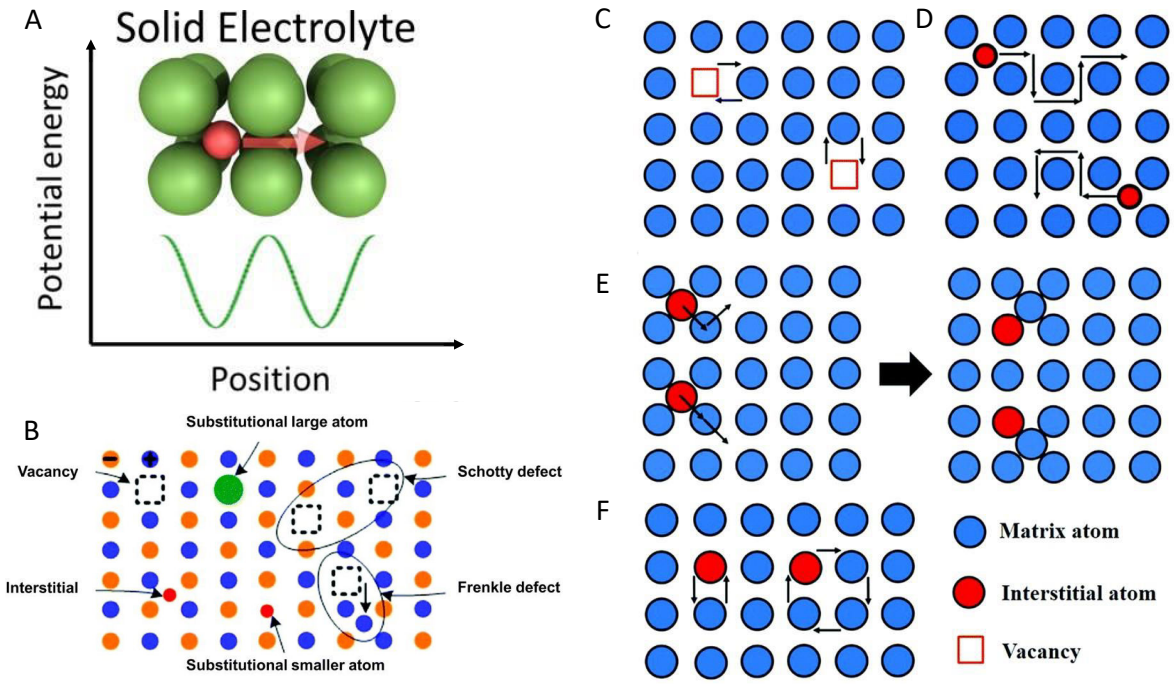

Figure 2-4: Potential energy of migration in solid electrolytes of an interstitial, charged mobile ion in a crystalline solid (top right A).[106] Copyright 2016 American Chemical Society. Some typical point defects in the inorganic solid electrolyte (bottom left B). Different mechanisms for lithium-ion transport in the active inorganic region, Vacancy diffusion mechanism (C), direct interstitial mechanism (D), interstitial knock-off mechanism (E), and direct exchange and ring mechanism (F).[104] Copyright 2022 Royal Society of Chemistry.

Oxide solid electrolytes represent a class of materials with high thermal and chemical stability, high mechanical strength, and competitive ionic conductivity. Their development for solid-state batteries is motivated by superior safety compared to liquid electrolytes, and by their stability against lithium metal, water, air, and elevated temperatures. The most prominent oxide solid electrolytes include garnet-type (e.g., $Li_7La_3Zr_2O_{12}$, LLZO), perovskite-type (e.g., $Li_3xLa_{2/3-x}TiO_3$, LLTO), NASICON-type ($LiM_2(PO_4)_3$ with M being Ti, Ge, Zr, and other elements e.g., $Li_{1+x}Al_xTi_{2-x}(PO_4)_3$, LATP), and LISICON-type (general formula $Li_{16-2x}M_x(TO_4)_4$ with M a divalent and T a tetravalent cation e.g. $Li_{14}Zn(GeO_4)_4$).[72,104] Among these, LLZO was studied intensively over the last decade due to its high ionic conductivity (up to $1.4 \cdot 10^{-3}$ S cm^{-1} at room temperature) and excellent electrochemical stability with lithium as well as its wide electrochemical stability window of up to 6 V vs Li^+/Li. The high oxidation resistance leads to its compatibility with high-voltage cathode materials, while its low

electronic conductivity, combined with mechanical strength, is expected to suppress dendrite formation.[73] Despite these advantages, LLZO and other oxide electrolytes pose several challenges. They are inherently hard and brittle, leading to mechanical issues during cycling and limiting uniform contact at interfaces. Achieving intimate interfacial contact often requires high pressure with interfacial resistance remaining a major bottleneck for practical implementation. The high elastic modulus is beneficial for dendrite suppression, yet it contributes to poor electrode/electrolyte interface contact. A key issue in LLZO is stabilizing the highly conductive cubic phase. The tetragonal phase is thermodynamically more stable at room temperature but exhibits much lower ionic conductivity. To stabilize the cubic structure, doping with elements such as Al, Ta, or Nb is required. Ta-doping is particularly effective in promoting the cubic phase and enhancing lithium-ion conductivity.[74] Additionally, LLZO is known to absorb moisture and CO_2 from air, forming surface layers (e.g., Li_2CO_3) which acts like an insulating layer and therefore needs to be removed for better performance.[107] Synthesis and sintering of oxide solid electrolytes typically require high temperatures (>1100 °C), which limits scalability and increases manufacturing costs.[62]

In conclusion, thermally, oxide electrolytes are highly stable, with no risk of combustion or decomposition under abuse conditions, while they also pose preferable electrochemical properties. Their high hardness and melting points make them withstand extreme situations, a key safety advantage over polymers and sulfides. However, their relatively high mass density and brittleness are drawbacks for achieving high energy density and mechanical flexibility. Strategies such as reducing the manufacturing temperature and electrolyte thickness or forming composites with polymers are key research areas to increase the viability of solid oxide electrolytes.

2.5 Solid Polymer Electrolytes

Solid polymer electrolytes have emerged as critical components for advanced battery systems due to their significant advantages over traditional liquid and inorganic solid electrolytes. As previously discussed, SPEs provide enhanced safety attributes such as reduced flammability and superior mechanical resilience, including tolerance to shocks, vibrations, and deformation. Compared to inorganic solid electrolytes, polymer-based electrolytes offer distinct benefits in terms of mechanical flexibility and ease of processing. Unlike inorganic electrolytes, which are typically brittle and challenging to fabricate, including high synthesis and processing costs, SPEs can readily be processed into various shapes and integrated into diverse battery architectures using established manufacturing techniques such as extrusion or casting. The inherent flexibility of polymer electrolytes facilitates good interfacial contact with electrode surfaces, significantly reducing interfacial resistance and consequently enhancing overall battery performance.[94,108–112]

Similar to conventional liquid electrolytes, fundamental SPEs are composed of alkali metal salts dissolved within a polymer matrix. However, numerous strategies have been employed to modify their physical and (electro)chemical properties, resulting in three primary classes of polymer electrolytes. These include dry solid polymer electrolytes (SPEs)[110,113,114], gel polymer electrolytes (GPEs)[54,115,116], and composite polymer electrolytes (CPEs)[117–119] as displayed in **Figure 2-5**. Each category exhibits unique characteristics that can be strategically tailored to meet specific requirements in battery design, performance, and application scenarios. Firstly, dry solid polymer electrolytes are formed by dissolving a lithium salt within a polar polymer matrix, resulting in a solid, flexible material that facilitates ion transport. This configuration is often referred to as a dual-ion conducting polymer electrolyte (DICPE), where both mobile cations and anions migrate through the polymer matrix. To mitigate polarization caused by charge separation due to the movement of these ions, anions can be chemically linked to the polymer backbone, preventing their migration and eliminating the electrostatic forces that counteract cation movement. This approach, known as a single-ion conducting polymer electrolyte (SICPE), effectively immobilizes the anions.

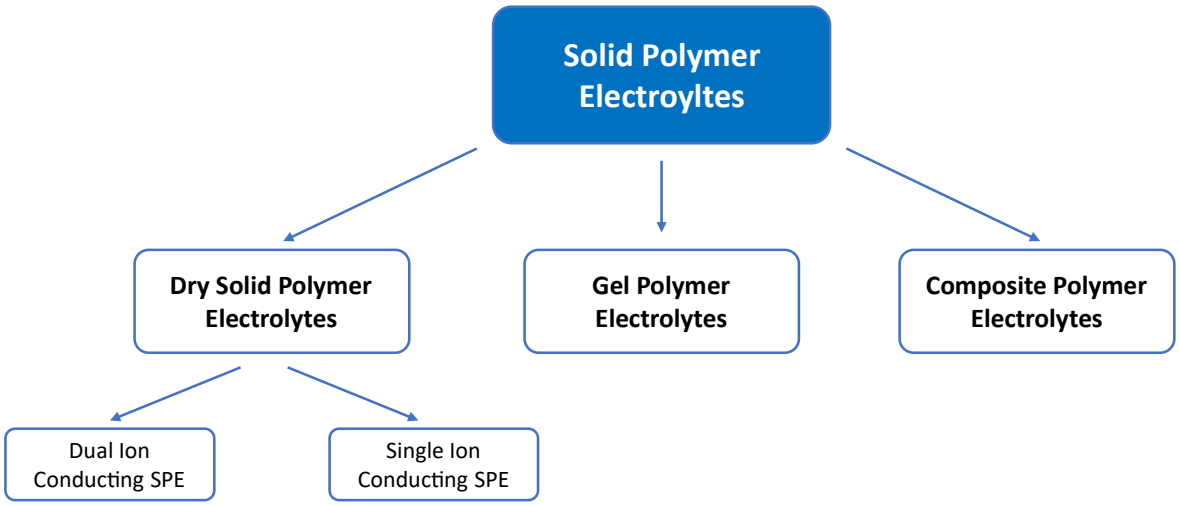

Figure 2-5: Main classification of solid polymer electrolytes.

One general disadvantage of SPEs is their relatively low ionic conductivity (10^{-6} - 10^{-4} S cm^{-1})[109,117] at room temperature compared to common liquid (10^{-3} -10^{-2} S cm^{-1})[105,109] and inorganic electrolytes (10^{-4} -10^{-2} S cm^{-1})[22,90,120]. To enhance ionic conductivity, a liquid component can be incorporated within the polymer matrix without dissolving it, forming a gel polymer electrolyte. Alternatively, inorganic particles, known as fillers, can be added to the polymer matrix, creating a composite polymer electrolyte. This approach not only enhances ionic conductivity but also improves mechanical strength and other beneficial properties.

The ion conduction mechanism in solid polymer electrolytes fundamentally differs from that in inorganic solid electrolytes, where ions migrate via vacancies in crystalline lattices. Ionic transport in SPEs, however, is a more complex phenomenon influenced by numerous factors such as the dielectric constant of the polymer host, degree of ion pairing, ion size, and polymer morphology. In general, solid polymer electrolytes contain heteroatoms like oxygen or nitrogen capable of solvating embedded lithium ions. **Scheme 2-1** displays some examples for commonly studied polymers and special creations for the application as solid electrolytes:

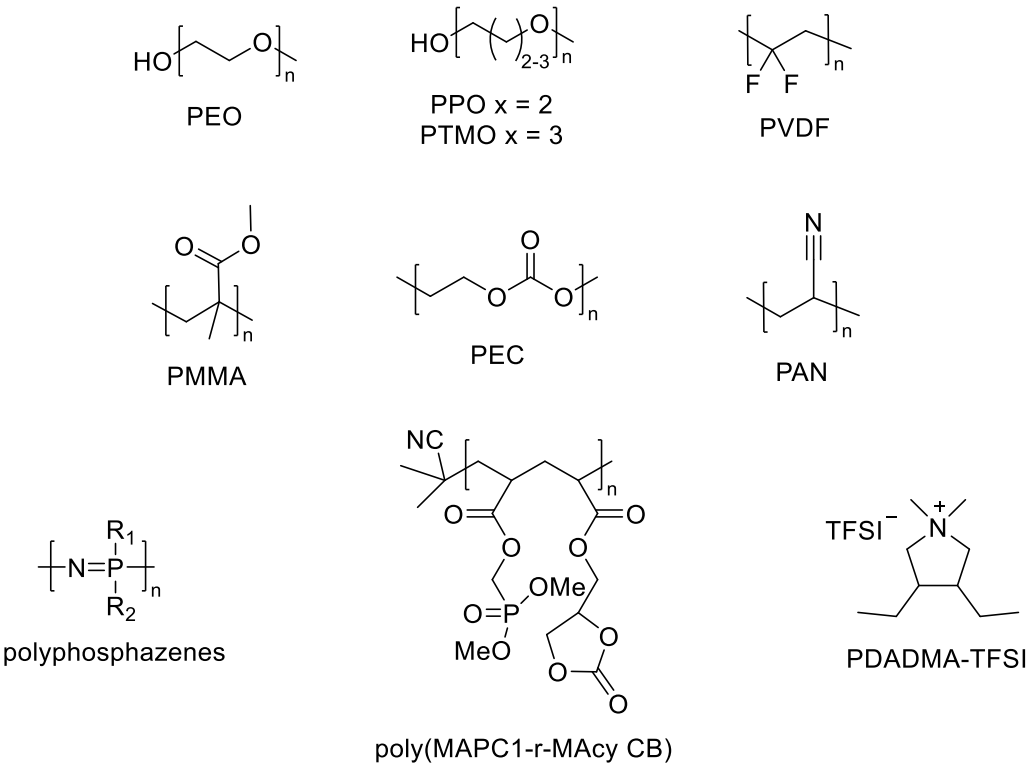

Scheme 2-1: Chemical structures of exemplary polymers which have been studied as solid electrolytes. PEO = polyethylene oxide; PPO = polypropylene oxide; PTMO = polytetramethylene oxide; PVDF = polyvinyl-idene difluoride; PMMA = polymethyl methacrylate; PEC = polyethylene carbonate; PAN = polyacryl nitrile; polyphosphazenes $R_{1,2}$ = various side chains[121,122]; poly(MAPC1-r-Macy CB)[123]; PDAMDMA-TFSI[124].

While ionic conductivity in ceramics generally follows Arrhenius behaviour, expressed by equation 6:[125]

$$\sigma = A \exp\left(\frac{-E_a}{RT}\right) \qquad 6$$

with E_a being the activation energy, T the absolute temperature, A the pre-exponential factor and R the Boltzmann constant, polymer electrolytes like PEO show Vogel-Tamman-Fulcher (VTF) behaviour (equation 7),[125] where the segmental motion of the polymers play a critical role. In SPEs, lithium-ion conduction primarily occurs within the amorphous regions through segmental movements of polymer chains, facilitated by local free-volume domains.[65]

$$\sigma = AT^{-1/2} \exp\left(\frac{-B}{T - T_0}\right) \qquad 7$$

Hereby, B is the pseudo-activation energy for conductivity (expressed in unit of E_a/k), and T_0 is the reference temperature, which normally falls 10 to 50 K below the experimental (kinetic) glass transition temperature (T_g). The VTF equation was devised for describing the diffusion process in glassy and disordered materials, mainly used for describing the ionic conduction in SPEs and GPEs above T_g of polymer hosts.[125]

Ionic conductivity in solid polymer electrolytes is strongly influenced by the proportion of amorphous content, as ion transport relies on the flexibility of polymer segments. This flexibility is governed by the glass transition temperature. Polymers with lower T_g typically have a higher amorphous fraction and thus exhibit improved ionic conductivity. Segmental motion of the polymer backbone is a key factor enabling ion mobility, as it allows for inter- and intra-chain hopping between coordination sites. These dynamic sites are not fixed and vary with temperature and time. As a result, ionic conduction in SPEs is generally described as a combination of two processes, namely ion motion along a single chain and ion hopping between chains, which can be described as intra- and inter-chain ion hopping between coordination sites. Among these, inter-chain hopping is considered the dominant mechanism for ion transport through the polymer matrix and is illustrated in **Figure 2-6**.[110,113,126]

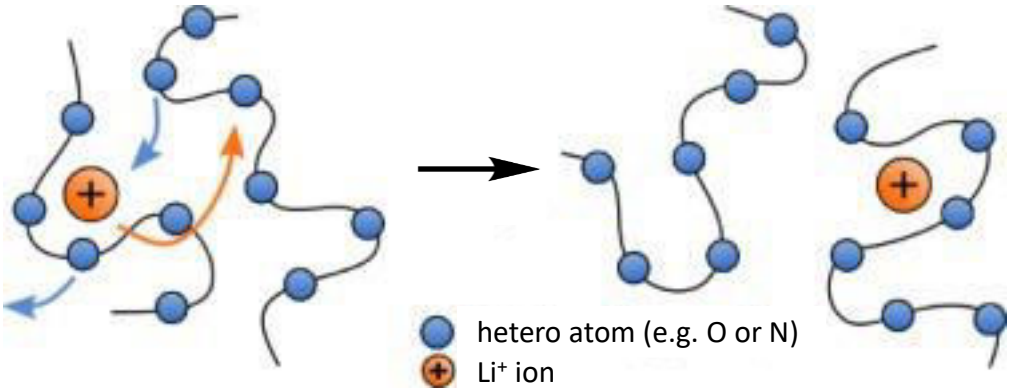

Figure 2-6: Most commonly accepted ion conduction mechanism in SPEs via inter-chain hopping of Li^+ ions coordinated by heteroatoms of the polymer host matrix. Adapted from Ref [127]. Copyright 2021, Elsevier.

As segmental motion, by definition, cannot occur in crystalline complexes, such crystalline ion–polymer complexes are believed to be insulators. Even though there is some controversy if ion conduction can take place via different mechanisms in the crystalline regions.[63,128] SPEs often consist of both amorphous and crystalline phases, with the latter contributing to mechanical stability but limiting ion mobility. Above T_g, polymers transition from a glassy to a rubbery state, characterized by increased chain mobility and enhanced

ion conduction (**Figure 2-7**). This transition is exclusive to the amorphous regions as crystalline domains instead undergo melting transitions.[127]

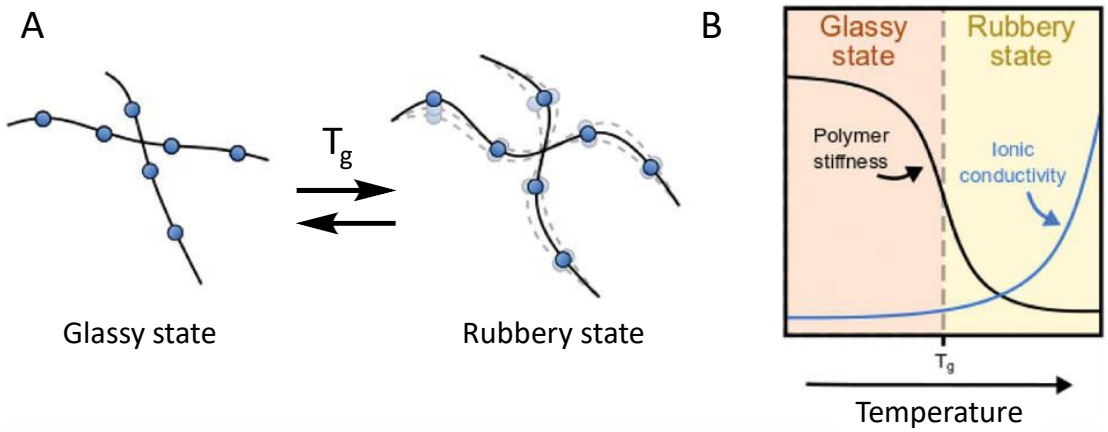

Figure 2-7: **A** Schematic illustration of polymer segment behaviour above and below the glass transition temperature. Above Tg, increased polymer chain flexibility facilitates ion conduction. **B** Relationship between polymer stiffness and ionic conductivity as a function of temperature.[127] Copyright 2021, Elsevier.

However, lowering the T_g often compromises mechanical integrity, making careful selection of polymer molecular weight essential to achieve optimal mechanical stability alongside sufficient ionic conductivity. As stated above, in classical polymer electrolyte systems, such as PEO-based electrolytes, lithium ions coordinate directly with ether oxygens (-C-O-C-) through electron lone pairs, enabling ion transport via continuous coupling and decoupling events driven by segmental polymer chain motions. The efficiency of the ion conduction further depends significantly on the polymer's structural properties and chemistry. For instance, polymers possessing higher densities of active polar groups, such as polyoxymethylene (POM), provide more lithium-ion solvation sites compared to structurally similar but less active analogues like poly(trimethylene oxide) (PTMO). Polymer structural arrangements also strongly influence solvation capacity. For example, poly(propylene oxide) (PPO) accommodates more lithium ions than PTMO despite identical carbon-to-oxygen ratios.[129]

Generally, three main strategies can be applied to enhance ionic conductivity. First, the addition of more lithium salt increases the concentration of mobile ions. As the ion conduction is driven by chemical and electrochemical potential gradients, an increase in the ion concentration is direct proportional to the conductivity. This relation is described by the Kohlrausch equation (8):[126]

$$\sigma = \sum_i \mu_i q_i n_i \qquad 8$$

With μ_i being the mobility, q_i the charge and n_i the concentration of the ions. Furthermore, the Nernst-Einstein relation (9) connects the ionic conductivity with the diffusion coefficient D:

$$\sigma = \frac{n_i q^2}{k_B T} D \qquad 9$$

With k_B being the Bolzmanns's constant and T the absolute temperature. Although equations 8 and 9 fail to hold quantitatively in concentrated electrolytes, they still give important indications of how to understand and thereby optimize the ionic conduction. One would like to increase both the concentration of the dissociated ions and the diffusion coefficient of the mobile ions. Second, reducing the T_g improves polymer segment mobility, thereby facilitating ionic transport. Third, it is possible to decouple ionic conduction from polymer segment relaxation entirely by designing structures where ions can diffuse independently, establishing fixed conduction pathways that do not rely on polymer chain dynamics (as utilized in GPEs and CPEs). Some approaches for achieving highly conductive solid polymer electrolytes are summarized in **Figure 2-8**.[126]

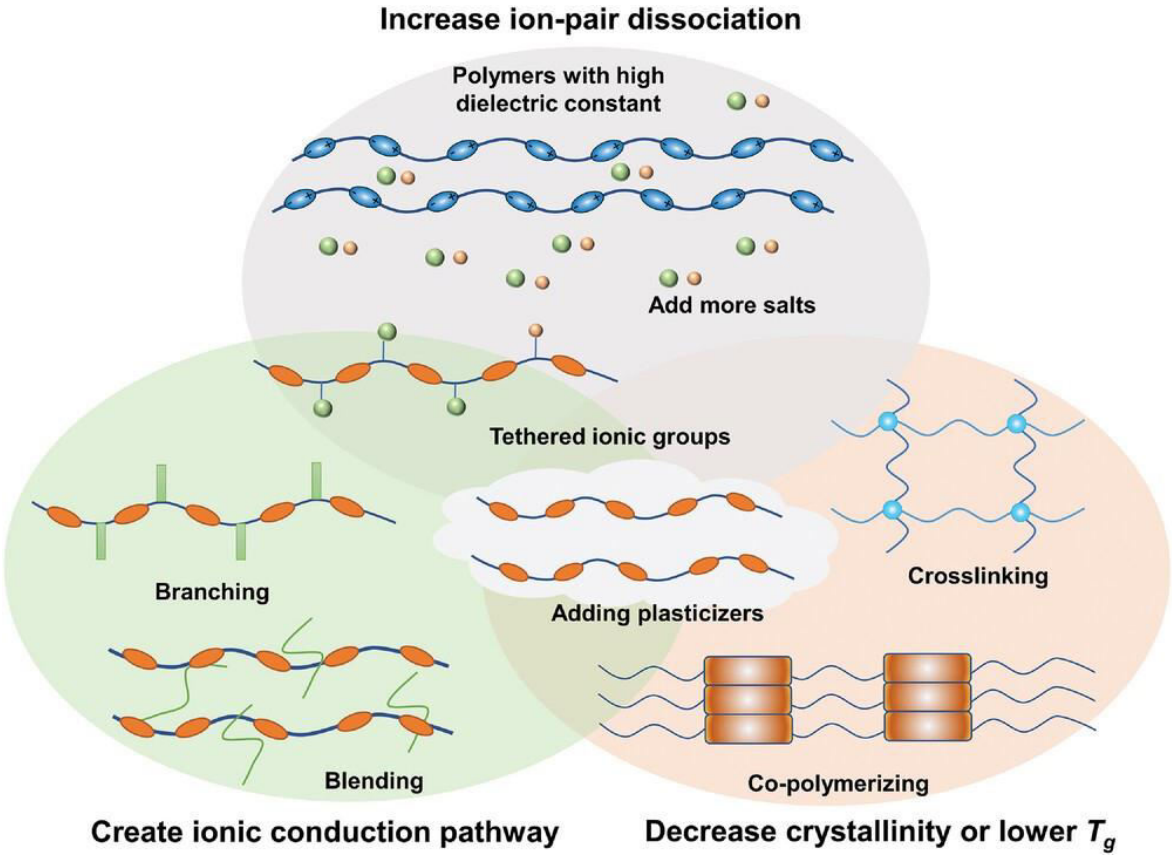

Figure 2-8: Different strategies to improve the ionic conductivity in SPEs.[126] Copyright 2023 John Wiley and Sons.

2.5.1 PEO based Solid Polymer Electrolytes

Polyethylene oxide is a crystalline, thermoplastic, water-soluble polymer with the chemical structure (−CH_2−CH_2−O−). The name PEO is usually used, when the molecular weight of the polymer exceeds 20.000 g mol^{-1}. Polymers with lower molecular weights are referred to as polyethylene glycols (PEG). Due to its readily availability and excellent solvation capability for lithium salts, PEO is the most extensively studied polymer electrolyte of the last decades. In SPE systems, the ethylene oxide (EO) units exhibit a high dielectric constant, effectively coordinating lithium ions and enabling good polymer chain flexibility, both essential for fast lithium-ion transport.

In general, PEO is synthesized via catalytic ring-opening polymerization of ethylene oxide. At room temperature, PEO is semi-crystalline, exhibiting crystallinity levels between 70–84%.[130] The crystalline regions exhibit a melting temperature (T_m) of ~65 °C, while the amorphous regions show a relatively low glass transition temperature of approximately −64 °C.[131] Ion conduction in PEO-based SPEs predominantly occurs within the amorphous

phase via the previously described intra- and inter-chain ion hopping mechanisms, involving the continuous formation and cleavage of Li–O bonds. The segmental rearrangement of EO ligands promotes the long-range migration of lithium ions, allowing rapid ion transport.[54] While the polymer host maintains solid-like mechanical characteristics due to chain entanglement, lithium ions exhibit liquid-like local environments on the microscopic scale, enabling effective conduction through polymer segmental motions.[132] However, at room temperature, ion conduction is severely restricted by the high crystallinity of PEO, which limits its practical applicability in typical lithium-ion battery cycling conditions. Upon heating above the melting temperature of its crystalline domains, PEO transitions into a predominantly amorphous and molten state, significantly reducing its mechanical properties. Under these conditions, lithium dendrite formation becomes more pronounced, raising critical battery safety concerns. In contrast, as temperature decreases, ionic conductivity diminishes sharply due to an increased crystalline fraction and reduced segmental motion. Additionally, PEO faces electrochemical stability limitations at high voltages, as oxidation of its terminal hydroxyl groups occurs around 4 V vs. Li^+/Li (**Figure 2-9**).[133,134] This restricts compatibility with high-voltage cathode materials.

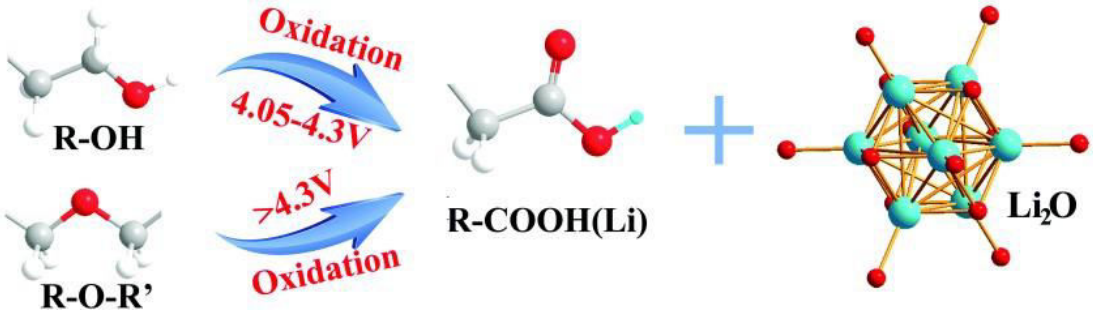

Figure 2-9: Possible oxidation mechanism for alcohol and ether groups in polymers at high voltages.[133] Copyright 2020, Royal Society of Chemistry.

To improve the ionic conductivity of PEO-based SPEs at ambient conditions, previous research has explored approaches to increase amorphous fractions, including plasticizing, blending, electrospinning, copolymerization, cross-linking, and adding inorganic fillers.[135–139] These modifications help reduce crystallinity, enhance electrochemical stability, and partially inhibit lithium dendrite growth. Among these strategies, composite polymer electrolytes that combine the advantageous properties of both polymer matrices and inorganic fillers represent one of the most promising paths toward future improvements of PEO-based SPE systems.

2.5.2 Phosphorus Containing Polymer Electrolytes

As discussed in chapter 2.1, the electrolyte in classical lithium-ion batteries typically consists of highly flammable organic liquids, significantly increasing the risk of ignition and combustion. Enhancing battery safety consequently strongly depends on reducing electrolyte flammability, which represents a major safety advantage of solid electrolytes. However, organic polymer electrolytes remain intrinsically flammable, thus requiring further modifications to improve their safety. Hydrogen radicals are known to initiate combustion processes and thus, suppressing their formation or propagation is a critical approach. One strategy involves the addition of flame-retardant compounds, such as trimethyl phosphate (TMP), commonly utilized in the plastics industry.[140] Although phosphate-based flame retardants effectively decrease electrolyte flammability by capturing hydrogen radicals, their use is often accompanied by adverse reactions with battery anodes, negatively impacting the overall stability and lifetime of the battery cell.[141] Consequently, phosphonates, capable of effectively scavenging hydrogen radicals without significantly impairing electrochemical performance, represent a promising alternative as flame retardants in battery electrolytes.

To eliminate issues related to phosphate-based small molecules, one promising approach involves incorporating phosphorus atoms directly into the polymer electrolyte structure, typically in oxidation states of +III or +V.[142] These phosphorus-containing polymer electrolytes are considered promising candidates for next-generation energy storage applications. Various copolymers have been developed by combining building blocks containing flame-retardant phosphonate units, ion-conducting groups, and lithium salts. At room temperature, these copolymers exhibit ionic conductivities around 10^{-5} S cm^{-1}, thus comparable to conventional SPEs based on ethylene oxide. Compared to homopolymer blends of similar composition, the copolymer-based SPEs demonstrate improved stability within a broader electrochemical window (0.5–4.5 V vs. Li^+/Li) and at elevated temperatures exceeding 120 °C.[141] This improvement in electrochemical and thermal stability is attributed to the superior lithium salt solubility provided by the copolymer structure.

Several low-molecular-weight alkyl phosphates and phosphonates, including TMP, triethyl phosphate (TEP), diethyl ethylphosphonate (DEEP), 2-(triphenylphosphoranylidene)

succinic anhydride, and ethyl phosphate–polyethylene glycol-based copolymers, have been developed and tested as additives in liquid electrolytes.[140]

In contrast to these small molecules, polymeric flame retardants provide additional advantages such as higher melting points, superior thermal and electrochemical stability, and negligible volatility or leakage. These characteristics significantly improve interfacial stability and are particularly beneficial for pure SPE systems. Furthermore, phosphorus-containing polymer electrolytes offer enhanced acidity, corrosion resistance, improved adhesion to electrode materials, and increased ion-exchange capacities. These properties continue to drive interest in phosphorus-based solid polymer electrolytes.[142] Polyphosphoesters represent a structurally versatile polymer class, as phosphorus units can be incorporated either in the polymer backbone or in side chains, providing multiple functionalization sites beyond those forming the backbone.[143] Such structural flexibility allows for further optimization through tailored side-chain functionalization. In addition to poly(MAPC1-r-Macy CB), shown in Scheme 2-1, further examples of phosphorus-containing polymer electrolytes are presented in **Scheme 2-2**.

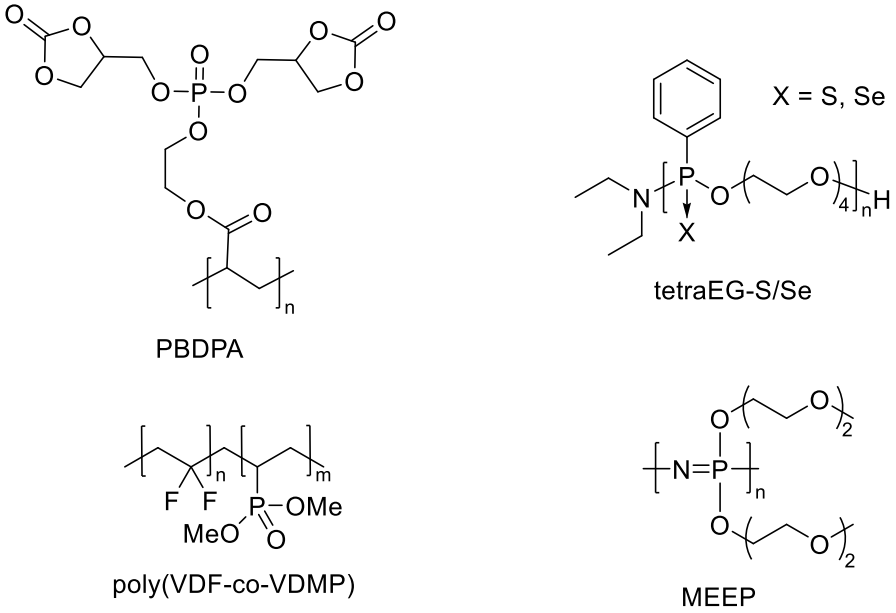

Scheme 2-2: Chemical structures of various phosphorous containing SPEs studied in literature: PBDPA[144]; tetraEG-S/Se[145]; poly(VDF-co-VDMP)[146]; poly[bis(2-(2-methoxyethoxy) ethoxy) phosphazene] (MEEP)[147].

Furthermore, polyphosphoesters exhibit biodegradability through hydrolytic and enzymatic pathways, expanding their potential applications across various fields beyond battery technologies.[148] One interesting class of polymers in this regard are poly(vinyl

phosphonates). These have been extensively studied by the group of Rieger et al., uncovering their promising properties in terms of biodegradability,[149] flame retardancy,[150] tuneable polymerization behaviour via catalytic methods,[151–153] and a highly amorphous character,[154] which would benefit ion transport through the polymer. In addition to these features, poly(vinylphosphonates) offer considerable structural flexibility through side chain functionalization. The phosphonate group provides a versatile center for introducing various functional moieties, allowing fine-tuning of physicochemical properties such as ion coordination strength, polarity, and segmental mobility. This design flexibility is similar to that of poly(phosphazenes), which also possess two side groups per repeat unit and are known for their broad functionalization possibilities.[130] Furthermore, poly(vinyl phosphonates) have demonstrated good thermal and oxidative stability, making them suitable candidates for applications under demanding conditions, including high-voltage or elevated-temperature operation.[154]

2.5.3 Composite Polymer Electrolytes

The most studied approach to enhance the mechanical and electrochemical properties of polymer electrolytes is by adding inorganic particles, so-called fillers, into the polymer matrix, thereby creating a composite polymer electrolyte (**Figure 2-10**). These materials combine the flexibility and processability of conventional SPEs while simultaneously enhancing the ionic conductivity and mechanical strength due to the presence of inorganic particles.[155] Depending on the type of filler used, they can be either inert or ion-conducting, while parts of their beneficial effects are commonly explained by Lewis acid–base interactions between filler surfaces and either the polymer chains or lithium salts.[156]

Furthermore, fillers can reduce the crystallinity of the polymer host, promote lithium salt dissociation, and create additional ion-conduction pathways. A key factor influencing the performance of CPEs is the structure and chemistry of the filler–polymer interface, with the effectiveness of the composite system strongly depending on features like particle size, concentration, and dispersion. In some cases, fillers have also been shown to form Li^+-conducting interfacial layers in situ at the electrode–electrolyte interface, which may contribute to lower interfacial impedance and improved overall performance.[112]

As mentioned above, fillers can be divided into two main categories. Inert fillers typically include ceramic oxides such as Al_2O_3, TiO_2, and SiO_2. These materials do not conduct Li^+ ions themselves but can influence the polymer matrix in several beneficial ways. When dispersed within the polymer, they can act as physical or chemical crosslinking centers, suppressing the recrystallization of polymer chains and thereby reducing the overall crystallinity and improving segmental motion. Additionally, Lewis acid–base interactions between the surface groups of the inert fillers and the ions from the lithium salt can enhance salt dissociation and immobilize the anions, which further improves lithium-ion transport and increases the number of mobile lithium ions.[155]

Active fillers, on the other hand, are lithium-ion-conducting inorganic materials that not only provide the same benefits as inert fillers but also contribute directly to ion transport by forming additional conduction pathways. These pathways can be established through a percolating network of interconnected filler particles or at the filler–polymer interface, both of which enhance overall ionic conductivity.[80]

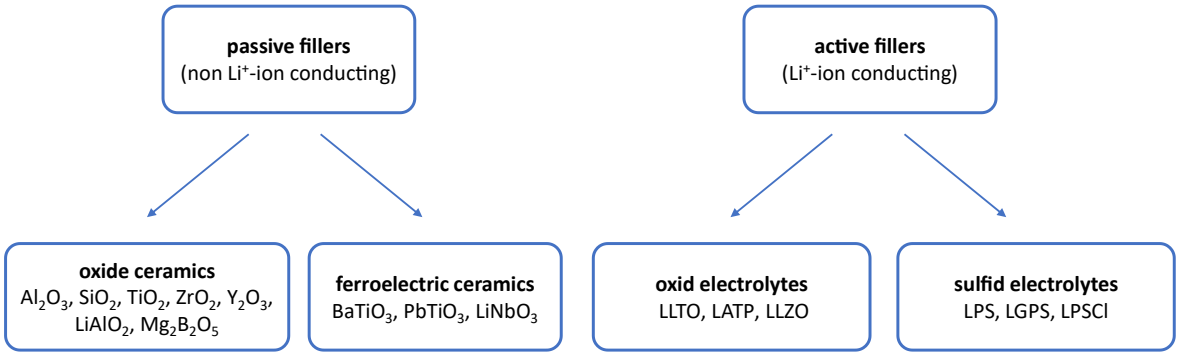

Figure 2-10: Classification of different filler materials with exemplary compounds for each class.

However, there is ongoing debate as to whether, at low filler content, the enhanced conductivity at the interface or within the particle itself can significantly impact the total ionic conductivity of the CPE. The surrounding polymer matrix often acts as a bottleneck, with conductivity values typically one or more orders of magnitude lower than those of the fillers. To ensure a continuous network of the highly conductive phase, increasingly complex 0–3D structures have been developed to maximize the benefit of incorporating active fillers into CPEs (**Figure 2-11**).[157–160] Common active fillers include oxide-based perovskites, NASICON-type materials, garnet-structured oxides, and sulfides. For example, Zhu et al. reported a significant improvement in conductivity by incorporating 15 wt% LLTO nanowires

into a PEO-LiTFSI matrix, achieving a conductivity of $2.4 \cdot 10^{-4}$ S cm^{-1} at room temperature which is nearly one order of magnitude higher than that of the unfilled PEO-LiTFSI system.[161]

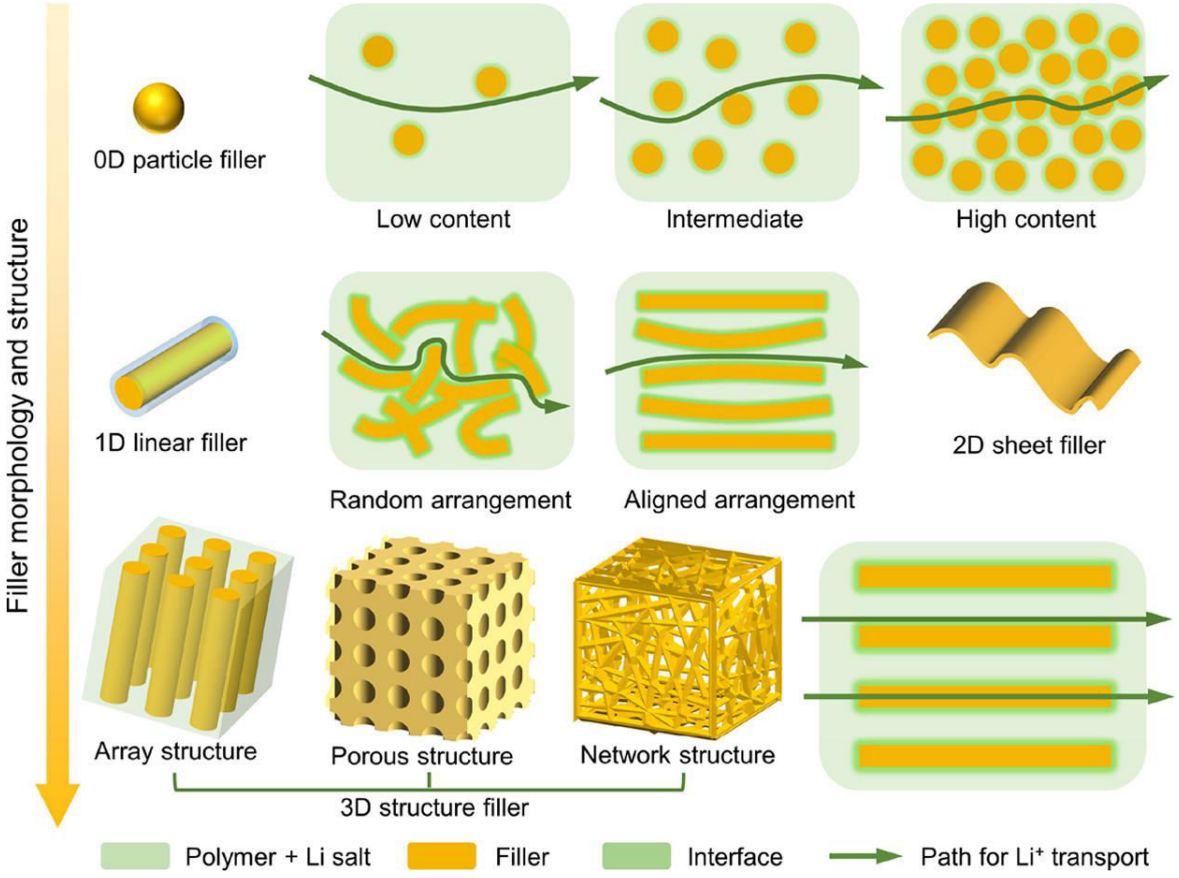

Figure 2-11: Schematic diagram of the different transportation pathways of Li^+ ions in CPEs according to different filler morphologies.[156] Copyright 2021, American Chemical Society.

None of the existing solid electrolytes fully addresses all challenges associated with all-solid-state batteries, as each class has its own strengths and limitations, the most promising strategy for next-generation batteries lies in combining the advantages of both inorganic and polymer-based electrolytes through hybrid and composite approaches.

2.6 Cathode Materials

Cathode materials host lithium ions in the fully discharged state, acting as the primary lithium source and thereby largely determining the overall capacity of the full-cell. To optimize cycle life and energy density, cathode active materials should exhibit high reversible capacity and operating potential. Because cathode materials constitute approximately 40–50% of the total cell cost, advancements in this field can significantly influence the economics of battery production, with a small improvement having a large impact on the grand scale.[162] Various cathode materials have been studied and employed based on specific performance criteria, such as high energy density, extended cycling stability, or improved safety. **Table 2-1** summarizes several commonly used cathode materials.

Table 2-1: List of common cathode materials and respective typical applications due to their properties.

Exemplary material	Specific capacity [mAh g^{-1}]	Applications	Ref
$LiCoO_2$ (LCO)	140-170	Mainly smaller portable electronics	[163]
$LiMn_2O_4$ (LMO)	110	Low cost, eco friendly applications	[164]
$LiNi_{0.8}Co_{0.15}Al_{0.05}O_2$ (NCA)	~180	High power automotives	[165–167]
$LiNi_xMn_yCo_zO_2$ (NMC)	160-215[a]	Portable and high power applications including power tools and EVs	[168–171]
$LiFePO_4$ (LFP)	155-170	High safety – stationary batteries and EVs	[163,172]

[a] increasing with the ratio of nickel in NMC (highest for NMC 811).

This section provides an overview of some cathode materials, specifically lithium cobalt oxide, lithium manganese oxide, lithium nickel manganese cobalt oxide, and lithium iron phosphate.

2.6.1 Lithium Cobalt Oxide (LCO)

In 1981, John B. Goodenough reported lithium cobalt oxide ($LiCoO_2$) as a cathode active material for batteries, demonstrating the reversible deintercalation and reintercalation of lithium ions. This groundbreaking discovery paved the way for LCO to become a prominent

intercalation cathode material for lithium-ion batteries.[173] The commercialization of LIBs featuring LCO cathodes was pioneered by SONY in 1991.[174]

Since then, LCO has been extensively studied in academic research and widely applied in industrial fields. With advancements in electrolyte technology and other supporting innovations, it has become a staple in portable consumer electronics and various other products. The rapid development of electronic devices has fuelled a sharp increase in demand for higher energy density, a requirement which LCO can meet with its high theoretical capacity and electrode density. Despite its high theoretical capacity of 270 mAh g^{-1}, the practical discharge capacity of $LiCoO_2$ typically ranges from 140 to 170 mAh g^{-1} at voltages between 4.2 and 4.45 V vs. Li^+/Li, depending on the cut-off voltage and material modifications, like coating and doping strategies.[164,165] Moreover, the majority of the world's cobalt reserves are located in the Democratic Republic of Congo and China, raising concerns about potential global supply shortages. Additionally, significant ethical and environmental issues are associated with the exploitation of child labour and the toxicity of cobalt.

These concerns have driven the search for alternatives to $LiCoO_2$.[175] Compared to other lithium-rich cathode materials, high-voltage $LiCoO_2$ cathodes still offer a significant advantage in volumetric energy density. This makes them crucial for powering portable devices, where LCO-based LIBs continue to dominate the market. However, the high charging cut-off voltages can also lead to negative effects, particularly the rapid decay of cycle capacity. This degradation is primarily caused by the destruction of the crystal structure and the aggravation of interface side reactions.[164]

2.6.2 Lithium Manganese Oxide (LMO)

The spinel oxide lithium manganese oxide was first introduced by Thackeray and Goodenough in 1983.[176] In this structure, manganese ions (Mn^{3+} and Mn^{4+}) occupy octahedral sites, whereas lithium ions reside in tetrahedral sites within the spinel framework. The three-dimensional diffusion channels through adjacent octahedral voids enable higher lithium-ion conductivity and better rate capability compared to layered materials, which exhibit two-dimensional diffusion pathways.[177]

Lithium manganese oxide has a theoretical capacity of approximately 148 mAh g^{-1}. However, in practical applications this is typically reduced to around 110 mAh g^{-1}.[178] Operating

at an average potential of about 4.0 V vs. Li^+/Li, LMO achieves a comparatively low energy density of about 440 Wh kg^{-1} at the material level. Additionally, LMO suffers from poor performance at elevated temperatures due to its instability toward proton-containing electrolytes, causing manganese dissolution from the cathode. Specifically, Mn^{3+} undergoes disproportionation into Mn^{2+} and Mn^{4+}, after which Mn^{2+} dissolves into the electrolyte and subsequently deposits onto the anode surface.[179] This deposition accelerates the degradation of the solid electrolyte interphase and contributes to capacity fading in the full cell.

Consequently, LMO is not used as the exclusive CAM in lithium-ion batteries but rather, it is frequently incorporated into composite cathodes, where it provides high power density during acceleration, complemented by other cathode active materials such as NMC, to provide higher energy density for extended driving ranges. One approach to improve this material is with the partial substitution of manganese with nickel, resulting in the formation of the high-voltage lithium nickel manganese oxide (LMNO), which operates at comparatively high average potential of approximately 4.7 V vs. Li^+/Li.[180] With a reversible capacity of about 135 mAh g^{-1}, LMNO reaches an energy density of up to 635 Wh kg^{-1}, and therefore around 1.4 times more than lithium manganese oxide. Within this high-voltage spinel structure, manganese ions remain in a stable Mn^{4+} oxidation state, while nickel ions participate in the redox transition between Ni^{2+} and Ni^{4+} during cycling.[181] However, LMNO operates above the oxidative stability of most electrolytes, its application is limited to specific systems. Because of this bottleneck its commercial availability is only anticipated for the late 2020s.[182]

2.6.3 Lithium Nickel Manganese Cobalt Oxide (NMC)

As raw materials account for over 50% of the total cost of cathode active materials, even partial substitution of cobalt with more affordable alternatives presents significant economic advantages.[183] Consequently, research into cobalt substitution lead to the development of layered oxide cathodes composed of cobalt combined either with nickel and manganese or with nickel and aluminum. These advancements resulted in the establishment of nickel manganese cobalt oxide (NMC) and nickel cobalt aluminum oxide (NCA) cathode classes.[184]

The initial commercialized variant, nickel manganese cobalt oxide with equal atomic proportions ($Li[Ni_{0.33}Co_{0.33}Mn_{0.33}]O_2$ - NMC111), was notably utilized in the first-generation

BMW i3.[185] The ratio of nickel to cobalt to manganese is usually written behind the acronym with the general formula being $LiNi_xMn_yCo_zO_2$ (with x + y + z = 1). This first developed NMC variant delivered a reversible capacity of up to 160 mAh g^{-1} at an upper cut-off voltage of 4.3 V vs. Li^+/Li.[186] While still far away from its theoretical capacity of around 275 mAh g^{-1} (and therefore similar to LCO),[187] this first NMC materials already reaches the specific capacity of LCO. Further increasing the nickel content enhances the accessible specific capacity at a given cut-off voltage. For example, NMC622 and NMC 811 offer capacities of approximately 198 mAh g^{-1} and 215 mAh g^{-1}, respectively, both measured at a 4.2 V cut-off. Hence, by increasing the nickel ratio an increase in specific capacity of about 30% can be achieved from NMC111 to NMC811.[171] With this an energy density of 800 Wh kg^{-1} on material level can be achieved which is substantially higher than LCO (570 Wh kg^{-1}) and LMO (440 Wh kg^{-1}).[169]

Nickel, as the primary redox-active element, contributes to high capacity but compromises cycling and thermal stability. In contrast, cobalt stabilizes the crystal structure and enhances reaction kinetics, while manganese, remaining electrochemically inactive, primarily acts as a structural stabilizer, improving both cycle life and safety.[186] However, elevating nickel content introduces several critical challenges, particularly impacting cycle life and thermal stability. Higher nickel levels (NMC811) correlate with diminished thermal stability due to an increased presence of thermodynamically unstable Ni^{4+} ions. At elevated temperatures, these Ni^{4+} ions readily reduce to Ni^{2+}, releasing oxygen and causing structural degradation.[187] Moreover, all layered oxide cathodes experience anisotropic volume contractions upon lithium extraction. Although this contraction is a general phenomenon dependent primarily on lithium utilization, it is significantly more pronounced in nickel-rich compositions, which are typically cycled to higher degrees of delithiation. For instance, volume contraction is around 2.4% for NMC111 versus approximately 8.0% for NMC811 at the same voltage cut-off of 4.3 V vs. Li^+/Li.[184,188,189] Repeated volume changes during cycling can induce particle cracking, leading to various implications. While moderate cracking may benefit the short-term charge kinetics by exposing fresh surface area, excessive cracking can compromise electrical contact between crystallites and accelerate surface degradation processes.[169,188,190] Especially in solid-state batteries, particle cracking poses a severe issue, as cracks cannot be readily filled by liquid electrolytes, resulting in the loss of electronic and ionic connectivity (**Figure 2-12**).[191]

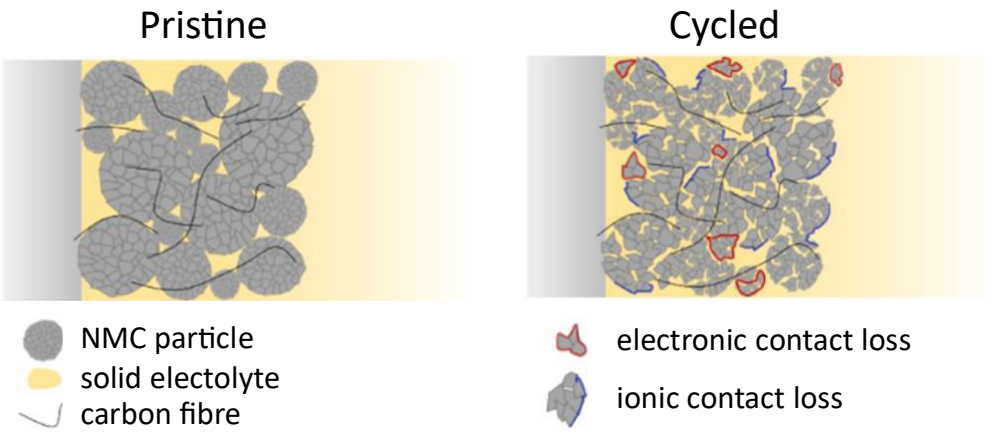

Figure 2-12: Schematic illustration of a pristine and cycled cathode in an ASSB with polycrystalline NCM, conductive carbon and solid electrolyte. After cycling, cracking and contact loss occurs, leaving NCM particles disconnected from the electronic network (red lines) and/or the ionic network (blue lines). Adapted from Ref [191].

This contact loss resulting from particle cracking, extends lithium-ion diffusion pathways, causing capacity loss by diffusion limitation. To address these chemo-mechanical degradation, morphological and microstructural optimization is investigated. Single-crystalline NMC materials, for example, demonstrate significantly reduced susceptibility to particle cracking and mechanical degradation compared to their polycrystalline counterparts, thus delivering superior performance retention in solid-state battery configurations.[192] Consequently, NMC materials offer high energy density and with the potential application in ASSBs make them a promising candidate for reaching the targeted energy density for EVs.[193]

2.6.4 Lithium Iron Phosphate (LFP)

Lithium iron phosphate ($LiFePO_4$) was first introduced as a cathode active material in 1997 by Padhi and Goodenough.[194] Its attractive properties like low material cost, environmental friendliness, good thermal and chemical stability, and long cycle life have made it a prominent candidate for lithium-ion batteries, especially in applications where safety and cost outweigh gravimetric energy density.

LFP belongs to the family of phospho-olivines and crystallizes in an orthorhombic olivine structure. This olivine structure is characterized by a hexagonally close-packed oxygen array in which FeO_6 octahedra share edges and faces. Hereby, lithium ions occupy one-dimensional channels. This restricted transport pathway causes a strong anisotropy in lithium

diffusion and makes ionic conductivity particularly sensitive to crystallographic defects and impurities. The narrow channels are prone to blockage, which significantly affects rate performance and overall cell kinetics (**Figure 2-13**) Upon delithiation, $FePO_4$ forms as a separate phase without significant distortion of the olivine framework.[195–197]

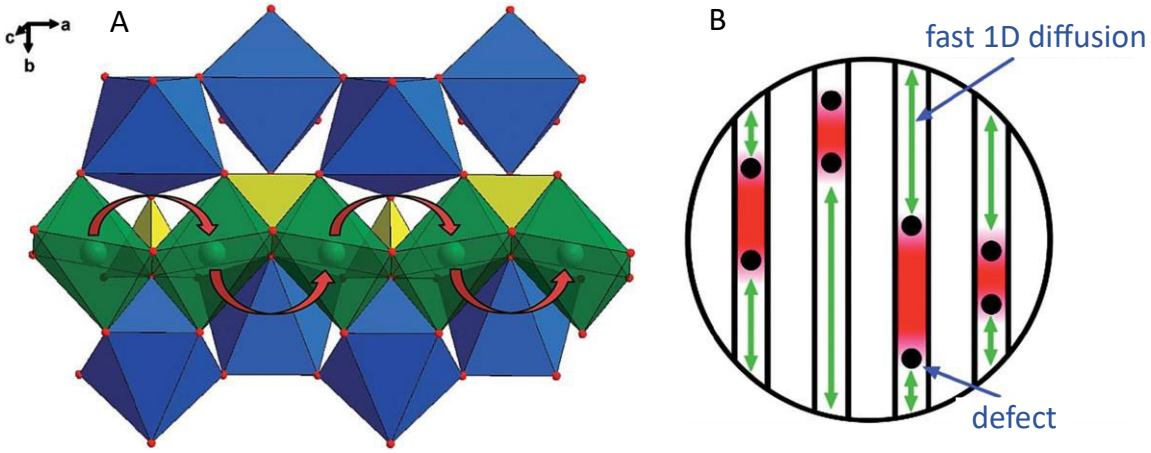

Figure 2-13: **A** Structure of $LiFePO_4$ depicting the curved trajectory of Li-ion transport along the b-axis, shown with red arrows. The FeO6 octahedra are shown in blue, the PO_4 tetrahedral in yellow, and the LiO_6 in green. **B** Schematic illustration of lithium ions diffusion impeded by immobile point defects in 1D channels.[196] Copyright 2024, Elsevier.

Other intrinsic drawbacks of LFP include low electronic conductivity (~10^{-7} to 10^{-10} S cm^{-1})[197,198] and poor lithium-ion diffusivity (~10^{-13} to 10^{-15} cm^2 s^{-1} depending on the SOC).[199] Some reported diffusion coefficients are even lower, with sources citing values up to 10^{-18} cm^2 s^{-1}.[200–202] This is several orders of magnitude lower than the diffusion coefficients in typical carbon anodes (10^{-12} to 10^{-7} cm^2 s^{-1}) or in electrolyte media (e.g., 4.1 · 10^{-5} cm^2 s^{-1} in 1 M $LiPF_6$ in EC/DEC = 1/1).[203] Therefore, controlling lithium transport within the LFP structure and individual particles is essential for ensuring their economic viability. To overcome related limitations, several strategies have been developed.

Nanoscale LFP particles (100–500 nm) coated with conductive carbon layers can significantly enhance both electronic conductivity and lithium-ion mobility. Such modifications enable practical capacities of approximately 160 mAh g^{-1}, close to its theoretical value of 170 mAh g^{-1}.[204–206] Further improvements have been pursued via cation doping (e.g. substitution of Li^+ with supervalent cations) and synthesis optimization to obtain homogeneous polycrystalline LFP.[207] From an electrochemical standpoint, LFP operates at a relatively low voltage plateau of approximately 3.4 V vs. Li^+/Li, which limits its theoretical

gravimetric energy density to 540 Wh kg^{-1}.[206] This value is lower compared to previously described CAMs such as LCO or NMC, which offer higher energy densities in part due to their higher oxidation potential.

Due to this fact, LFP only gained broad commercial traction around 2020.[208] Its resurgence was driven by several factors, including cost stability, raw material availability, and advances in materials engineering. One key development was the improvement of energy density at the pack level through innovations in battery pack design, particularly BYD's blade pack concept, which was the first to implement a cell-to-pack architecture. This increased volumetric efficiency without modifying the intrinsic cell chemistry.[209] Additionally, LFP contains no cobalt or nickel, two critical elements associated with high cost and supply chain risks, which makes it a sustainable and environmentally favourable cathode option.[195,210] The long-term sustainability of LFP battery systems depends also on the development of efficient recycling strategies. In particular, pretreatment and direct regeneration methods are being explored to improve material recovery and reduce the environmental impact of end-of-life LFP cells. These approaches aim to close the material loop and support the broader circular economy for lithium-ion batteries.[195,196]

A competition between LFP and NMC/NCA as cathode materials is currently ongoing. Regional differences are apparent. In China, manufacturers such as CATL primarily focus on LFP, while in Europe and the USA the emphasis has so far been on high-energy materials such as NMC and NCA. (**Figure 2-14**). It is, however, unlikely that one chemistry will fully replace the other. Instead, both are expected to remain relevant, each serving different applications depending on specific requirements in terms of cost, safety, energy density, and raw material availability.[211]

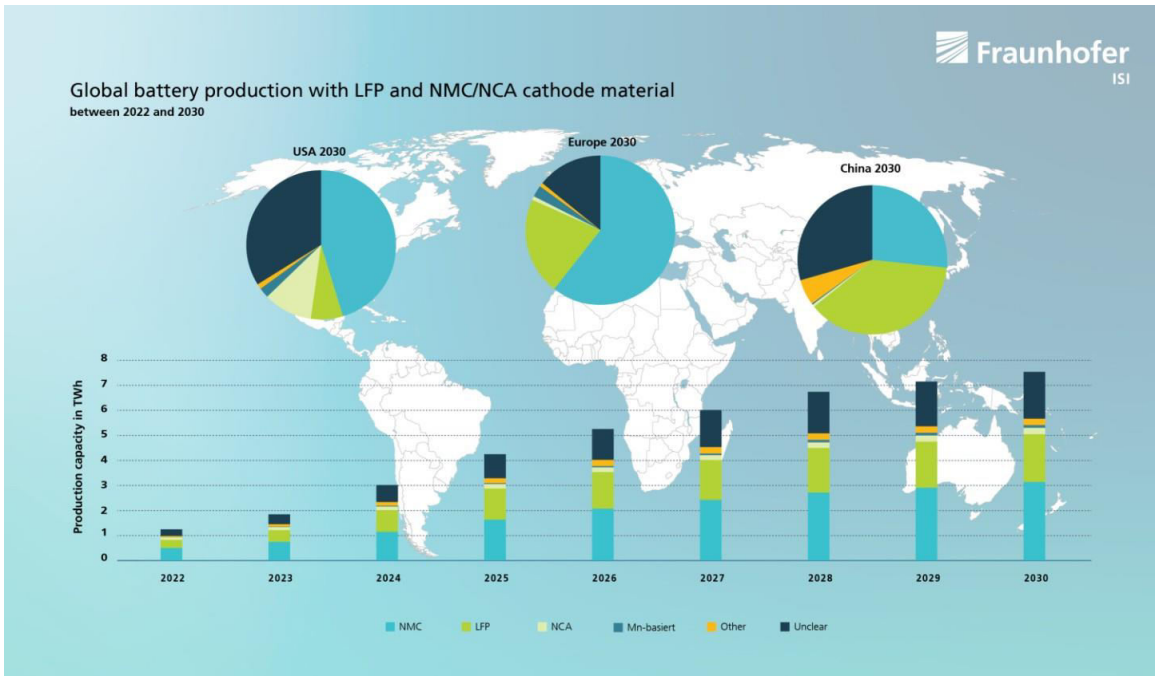

Figure 2-14: Global battery production with LFP and NMC/NCA cathode material between 2022 and 2030.[211]

2.7 Anode Materials

Unlike the previously discussed cathodes, anodes serve as host materials for lithium ions in the fully charged state. Similar to cathode materials, anodes can also be classified based on their working mechanisms, as outlined in **Table 2-2**.

Table 2-2: Theoretical capacities of anode materials which are representatives of the different working mechanisms.

Working mechanism	Exemplary material	Theoretical capacity [mAh g^{-1}]	Ref
Lithium intercalation	Graphite	372 (LiC_6)	[212]
	Lithium titanate oxide	175 – 293[a]	[213]
Alloy formation with lithium	Silicon	3590 ($Li_{15}Si_4$)	[214]
		4200 ($Li_{22}Si_5$)	[215]
Conversion reaction	Fe_2O_3	1007	[216]
Metals	Lithium	3860	[217]

[a] 175 mAh g^{-1} at 1.55 V vs. Li^+/Li and 293 mAh g^{-1} if all Ti^{3+} convert into Ti^{4+} below 1.0 V.

2.7.1 Intercalation Materials

Intercalating anodes are a cornerstone of LIB technology, with graphite being the most widely used material, accounting for approximately 98% of the market.[218] Graphite has been the state-of-the-art anode material since the commercialization of the first LIB due to its highly reversible lithium-ion intercalation and stable structural properties. Structurally, it consists of ordered, stacked carbon sheets with a honeycomb-like arrangement, allowing lithium-ion intercalation without significant disruption to the host structure. This process occurs at a low potential of 0.1-0.2 V vs. Li^+/Li, enabling a high nominal cell voltage. However, the low operating potential also increases the risk of lithium plating, where excess lithium ions are reduced on the graphite surface during overcharging or when the cell potential drops below 0 V. Lithium plating can lead to the formation of metallic lithium, posing severe safety risks, such as short circuits due to separator penetration, and negatively impacts battery performance.[29,218,219] Despite this limitation, graphite remains the preferred intercalating anode material due to its unmatched cycle stability and minimal volumetric expansion, which is only 13.2% when fully lithiated.[220]

Lithium titanate oxide (LTO) is another intercalating anode material, occupying a niche market with approximately 2% of LIB applications.[218] LTO offers excellent reversibility in lithium-ion intercalation and extraction, along with its "zero-strain" property, which minimizes volumetric changes during cycling.[37] This characteristic ensures superior structural stability and contributes to its exceptional cycle life, making LTO especially suitable for applications where durability and safety are critical.

Additionally, LTO exhibits outstanding thermal stability at elevated temperatures, outperforming graphite in high-temperature environments. Electrochemically, LTO displays a spinel structure which supports the reversible insertion and extraction of lithium ions. During lithiation, three lithium ions intercalate into the structure, transforming $Li_4Ti_5O_{12}$ into $Li_7Ti_5O_{12}$. LTO exhibits a theoretical capacity of 170-175 mAh g^{-1} at 1.55 V vs. Li^+/Li, a potential higher than the reduction potential of most organic electrolytes (~0.8 V). This elevated potential prevents the formation of a SEI layer, helping to maintain low cell impedance. However, LTO's practical application is limited by its low electrical conductivity, along with challenges such as SEI formation and capacity loss at potentials below 0.7 V. Additionally, its lower energy density compared to graphite restricts its broader adoption.

While graphite remains the dominant intercalating anode due to its superior energy density, stability, and scalability, LTO fulfils a specialized role in applications requiring enhanced safety, thermal resilience, and exceptional cycle life. These characteristics make LTO particularly suitable for large cells in stationary applications[29,213]

2.7.2 Alloy/Silicon based Electrodes

As shown in **Table 2-2**, silicon possesses an exceptionally high theoretical capacity due to its ability to form alloys with lithium during lithiation. The fully lithiated phase at room temperature, $Li_{22}Si_5$, illustrates this, as five silicon atoms can alloy with 22 lithium ions, explaining the remarkable capacity. However, this advantage comes with significant challenges, primarily the volumetric expansion of up to 300–400% during lithiation.[212] Such extreme volume changes induce mechanical stress, leading to issues like disconnection from the current collector, loss of active material due to particle separation, and continuous SEI layer breakage and reformation.[221] These factors contribute to poor cycle life and substantial irreversible capacity loss in consecutive cycles.[215,222]

Moreover, silicon's inherent low electrical conductivity (~10^{-5} S cm^{-1}) and slow ion diffusion (~10-14 cm^2 s^{-1}) further hinder its large-scale application.[212] On a microscopic level, silicon particles are prone to pulverization, resulting in electrically isolated regions and further loss of active material. To mitigate these challenges, understanding and optimizing the working mechanism of silicon is essential. During the first lithiation of crystalline silicon (*c*-Si), an amorphous alloy (*a*-Li_xSi) is formed below 170 mV vs. Li^+/Li. By employing a lower cut-off potential of 170 mV, the amorphous alloy can undergo reversible lithiation without additional amorphization.[223,224] Additionally, partial lithiation to one-third of the theoretical capacity (~1200 mAh g^{-1}) reduces volume expansion to approximately 100%, minimizing SEI breakage and improving cycle life.[225]

Despite these challenges, silicon is one of the most promising candidates for next-generation anode materials. Its high theoretical capacity, combined with strategies to mitigate its drawbacks, positions it as a strong contender to replace graphite. Furthermore, its natural abundance as the second most abundant element in the Earth's crust supports its scalability and economic feasibility. With continued advancements in material design and optimization, silicon has the potential to become the new state-of-the-art anode material in lithium-ion batteries.[212]

2.7.3 Conversion Electrodes

Conversion reactions represent a distinct working mechanism for anode materials, differing from lithium intercalation by involving actual chemical reactions rather than the insertion of Li^+ ions into a host material's lattice. These reactions typically follow the general form (equation 10):

$$M_aX_b + (b \times c)Li^- + (b \times c)e^- \rightleftarrows aM + bLi_cX \qquad 10$$

where M denotes a transition metal and X an anionic species such as oxides or sulfides. Conversion electrodes offer high theoretical capacities, generally ranging from 500 to 1500 mAh g^{-1}, and their chemical stability contributes to enhanced battery safety by reducing the risks of thermal runaway and decreasing overall battery mass.[163] A prominent example of a conversion electrode is iron oxide, which exhibits a theoretical capacity three times higher than graphite (1007 mAh g^{-1} for Fe_2O_3 and 924 mAh g^{-1} for Fe_3O_4). However, several drawbacks limit its practical application. Iron oxide undergoes significant

volumetric changes of approximately 100% during lithiation, leading to mechanical stress, pressure buildup, and potential safety risks in the closed system of a battery. Additionally, the material suffers from poor rate capability and low initial coulombic efficiency. Another challenge is the large difference between charge and discharge voltages, which results in inefficient round-trip energy efficiency.[216]

2.7.4 Lithium Metal

Lithium metal (LiM) anodes are widely regarded as the "Holy Grail" of anode materials for next-generation batteries due to their exceptional properties. With a theoretical specific capacity of 3860 mAh g^{-1}, approximately 10 times higher than that of graphite (372 mAh g^{-1}), and a low density of 0.534 g cm^{-3}, LiM offers unparalleled potential for enhancing both gravimetric and volumetric energy densities while reducing the total cell mass and volume. Its low reduction potential (−3.04 V vs. SHE) further enables high cell voltages, making it ideal for achieving high-energy-density batteries.[226]

Lithium metal's potential was first demonstrated in the 1970s with lithium-metal batteries using TiS_2 cathodes, which achieved high energy density and fast charging rates.[227] However, the application of LiM in practical batteries has been hindered by significant challenges. A critical issue with lithium metal anodes is their low melting point of 180 °C, which raises safety concerns during stress conditions. More significantly, lithium metal is prone to dendrite formation during cycling, resulting from uneven lithium deposition. This uneven deposition not only promotes dendrite growth, which can penetrate the separator and cause short circuits, but also contributes to the generation of electrically isolated "dead" lithium (**Figure 2-15**).[35,228,229]

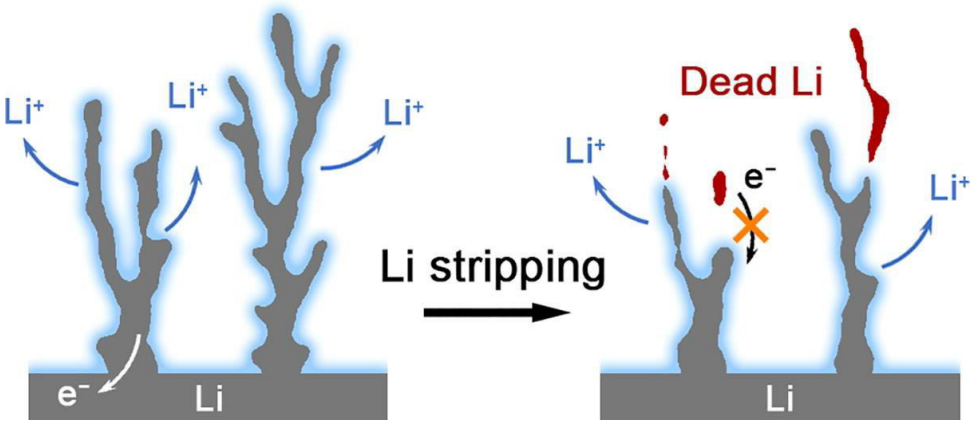

Figure 2-15: The formation of dead Li during the lithium stripping process.[228] Copyright 2025 Elsevier.

The high reactivity of LiM intensifies these problems by triggering side reactions with organic electrolytes, leading to SEI formation. This process consumes both fresh lithium and electrolyte, reducing active material availability and resulting in poor coulombic efficiency, often falling below 90% in unoptimized systems.[168,226] Additionally, the repeated plating and stripping of lithium induce volume changes that compromise the SEI's mechanical integrity, causing its breakdown and reformation, further accelerating capacity loss and the accumulation of dead lithium.[227] Efforts to overcome these challenges have focused on optimizing electrolyte compositions and interface stabilization. Fluorinated additives such as 3,3,3-fluoroethylmethyl carbonate (FEMC),[230] bisfluoroacetamide (BFA),[231] and tris(pentafluorophenyl)borane (TPFPB)[232] have been shown to form LiF-rich SEI layers that enhance stability, suppress dendrite growth, and reduce side reactions.[35]

As previously stated, ASSBs with lithium metal anodes offer another promising approach by the increased electrochemical stability of the solid electrolytes and higher mechanical integrity, which can hinder lithium dendrite growth. The ultimate goal, however, is to eliminate the need for excess lithium by enabling uniform lithium plating directly onto the current collector during charging (anode-free lithium metal batteries), thereby maximizing energy density.[217] Despite these challenges, rapid progress in material design, modification strategies, and electrolyte engineering underscores the transformative potential of LiM anodes. By addressing issues such as dendrite formation, SEI instability, and volume changes, lithium metal anodes could unlock the next generation of high-energy-density batteries, making them a cornerstone of future high energy dense batteries.[227] A summary of the presented electrode materials with their respective electrochemical potentials and specific capacities is given in **Figure 2-16**.

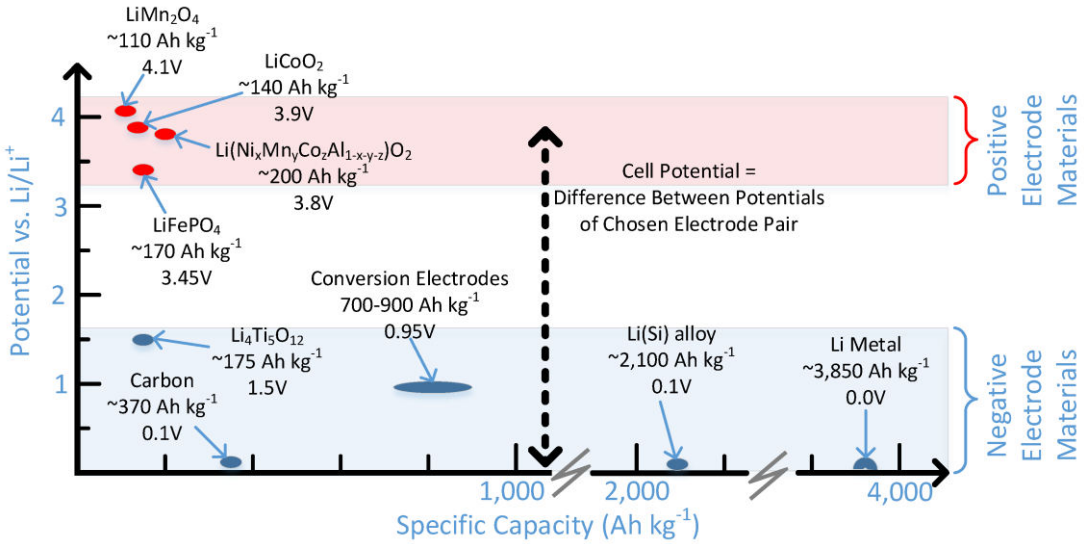

Figure 2-16: Summary of the presented electrode material options. The displayed capacity of the silicon alloy is 50% of the theoretical capacity of the material due to the limitation for application when fully lithiated. Reprinted with permission from Ref [163].

2.8 Impedance Spectroscopy

Electrochemical impedance spectroscopy is a highly versatile and powerful analytical technique for investigating electrochemical systems. It involves applying sinusoidal potential or current perturbations to a system at different frequencies and recording its corresponding response.". The technique can be performed in two modes: galvanostatic electrochemical impedance spectroscopy (GEIS), where a controlled current perturbation is applied, and potentiostatic electrochemical impedance spectroscopy (PEIS), where the perturbation is in the form of a controlled voltage. GEIS is particularly suited for systems with low impedance, such as commercial batteries, as it avoids signal overflow during measurements. Despite differences in the input signals, both techniques operate on the same fundamental principles.[233]

Of the two methods, PEIS is more commonly used, as it fulfils the requirements for most systems and provides valuable insights into the characteristic frequencies of various electrochemical processes. For example, ion migration typically dominates at high frequencies, while diffusion processes are more prominent at lower frequencies.[234] The impedance Z is defined as the complex ratio of the applied potential dE to the resulting current dI and is expressed in equation 11:[235]

$$Z = \frac{dE}{dI} \qquad 11$$

Analogous to resistance, impedance is a frequency-dependent, complex quantity. It follows the same mathematical rules as described in Kirchhoffs law for series (additive) and parallel (reciprocal addition) connections. By altering the excitation frequency, an impedance spectrum is obtained, providing a detailed understanding of the electrochemical processes occurring in the system. These processes, such as charge carrier transfer, diffusion of active species, and the formation of the electrochemical double layer, occur at different time scales and can be distinguished with the distribution of relaxation times (DRT) technique.[88]

To ensure the system remains in a steady state, the amplitude of the applied signal has to be small enough to maintain linearity between the voltage $E(t)$ and the current $I(t)$. A sinusoidal voltage signal is given by equation 12:

$$E(t) = |\Delta E| sin(\omega t) \qquad 12$$

where $|\Delta E|$ is the voltage amplitude, and ω is the angular frequency. The current response $I(t)$ shares the same angular frequency but includes a phase shift φ (equation 13), depending on the system's characteristics:

$$I(t) = |\Delta I| sin(\omega t + \varphi) \quad 13$$

Combining these equations with the help of Euler's formula, the impedance can be expressed as displayed in equation 14:[236]

$$Z = |Z|(cos\varphi + i \cdot sin\varphi) \quad 14$$

For its validity steady-state conditions need to be fulfilled. This equation reveals that impedance has both real $Z^{'}$ and imaginary $Z^{''}$ components. These components can be visualized in a Nyquist plot, where $Z^{'}$ is plotted on the x-axis and $-Z^{''}$ on the y-axis. Another common representation is the Bode plot, where the impedance magnitude $|Z|$ and phase angle φ are plotted against frequency.

One of the most widely used methods for interpreting impedance data is equivalent circuit analysis. This approach models electrochemical processes using an equivalent electrical circuit composed of basic elements such as resistors, capacitors, inductors, and their combinations, as well as more complex components designed to simulate specific electrochemical phenomena. A commonly employed model is the Randles circuit (**Figure 2-17**), which includes the internal resistance (R_{int}), double layer capacitance (C_{dl}), charge transfer resistance (R_{ct}), and a Warburg element (Z_w). The Warburg element accounts for diffusion processes based on semi-infinite linear diffusion and exhibits an impedance inversely proportional to the square root of frequency in a 45° line in the Nyquist plot. The Randles circuit is particularly prevalent in battery studies, as it effectively represents impedance spectra under a wide range of typical operating conditions.[237] This equivalent circuit depicted in **Figure 2-17** is particularly common in battery studies and provides an effective representation of impedance spectra for simple conditions, when for example studying just one electrode.[234]

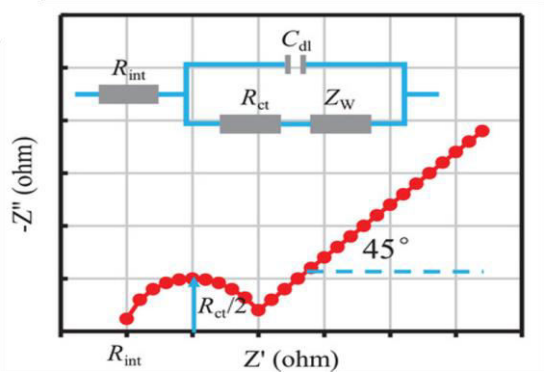

Figure 2-17: Schematic representation of a Nyquist plot (red) and the corresponding equivalent circuit (blue).[237] Copyright 2025 John Wiley and Sons.

However, the analysis becomes increasingly complex for full battery cells, where overlapping semicircles in Nyquist plots can obscure individual processes. **Figure 2-18** illustrates a Nyquist plot for a $LiFePO_4$ | Li cell, where no distinct semicircles are observed, complicating the fitting process.[238]

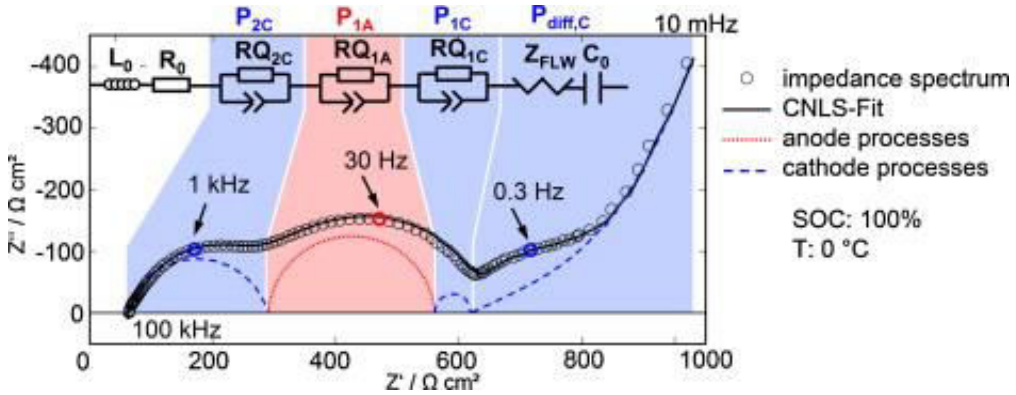

Figure 2-18: Equivalent circuit model for a $LiFePO_4$ | Li cell derived from combined analysis of impedance spectra.[238] Copyright Elsevier 2025.

To address these challenges, the afore mentioned DRT method can be employed. This approach separates loss processes based on their characteristic frequencies, providing a clearer picture of individual contributions. Processes occurring on different time scales appear at different frequencies, as shown in **Figure 2-19**, which depicts the observed frequency ranges of loss processes in $LiFePO_4$ | Li cells.[238]

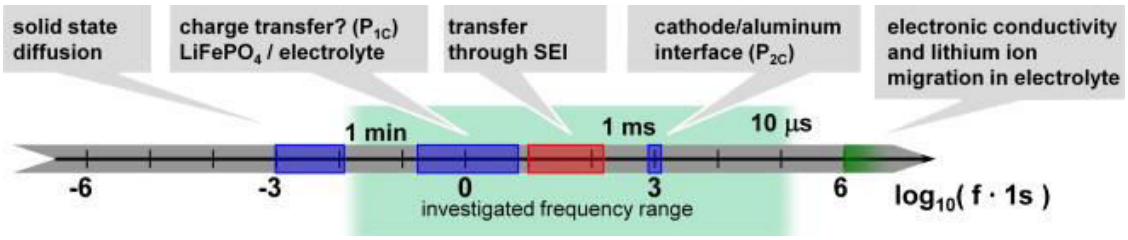

Figure 2-19: Observed frequency ranges of the identified loss processes in $LiFePO_4$ | Li cells.[238] Copyright Elsevier 2025.

Despite its versatility, impedance spectroscopy is not without limitations. Accurate data interpretation requires a physically consistent equivalent circuit model that aligns with the specific characteristics of the system. Ambiguity can arise when multiple equivalent circuit models fit the same experimental data equally well, underscoring the importance of combining impedance spectroscopy with complementary techniques for a reasonable analysis.[235,239,240]

Beyond modelling diffusion processes in electrodes using Warburg elements, a more sophisticated approach involves the use of transmission line models (TLMs). TLMs provide a physical framework to address the impedance characteristics of porous electrodes. For a simple electrode/electrolyte interface, the electrochemical behaviour is typically represented by a series-connected RC element and the resistance of the solution **Figure 2-20a**).

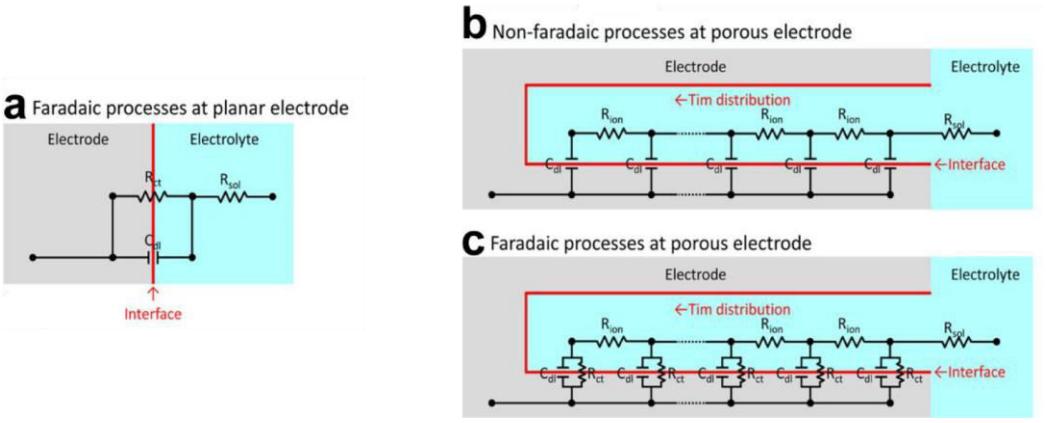

Figure 2-20: Schematic representations of electrode structures and their equivalent circuit models used in the TLM approach. Adapted from ref [241]. Copyright 2015 American Chemical Society.

However, this simplified model assumes that the interface is a uniform and continuous plane, which is a condition that is rarely true for LIBs and becomes even less applicable for solid-state batteries, where contact issues between CAM particles and the catholyte further complicate the interface.[242] TLMs treat the entire interface of a porous electrode as

a continuum of infinitesimally small interfaces. Each small interface accounts for three key physicochemical processes, namely electron conduction in the electrode, ion conduction in the electrolyte, and interfacial reactions. **Figure 2-20b** and **c** illustrate TLMs for different interfacial reaction scenarios. In the non-faradaic process (**b**, also referred to as the electron-blocking condition and comparable to a Warburg open circuit), no charge transfer occurs. In contrast, the faradaic process (**c**, comparable to a Warburg short circuit) involves electron transfer leading to oxidation or reduction reactions (non-electron-blocking conditions). Electron-blocking conditions are typically observed during impedance spectroscopy when a battery cell is fully charged or discharged, as these states correspond to the cathode being fully delithiated or fully lithiated.[233,241]

Each RC element in the TLM represents an electrochemical reaction occurring on the nanometer scale of the total pore surface. These RC elements have distinct time constants, reflecting the varying time-scale characteristics of processes on the pore surface. This enables TLMs to estimate the depth of electrochemical accessibility and the electrochemically active surface area of the porous electrode. TLMs offer significant advantages in assessing ionic diffusion resistance (R_{ion}) in porous electrodes and extracting parameters related to ionic conductivity. Consequently, they are powerful tools for investigating structural degradation during battery aging, such as changes in pore volume and tortuosity within the electrode. For instance, Nara et al. demonstrated that TLMs provided better fitting accuracy compared to conventional Randles circuits when modelling LIB impedance spectra.[243] Furthermore, TLMs allow direct extraction of the pore resistance from the impedance spectrum of a porous electrode, offering rapid insights into electrode quality as demonstrated by Landesfeind et al. (**Figure 2-21**).[244]

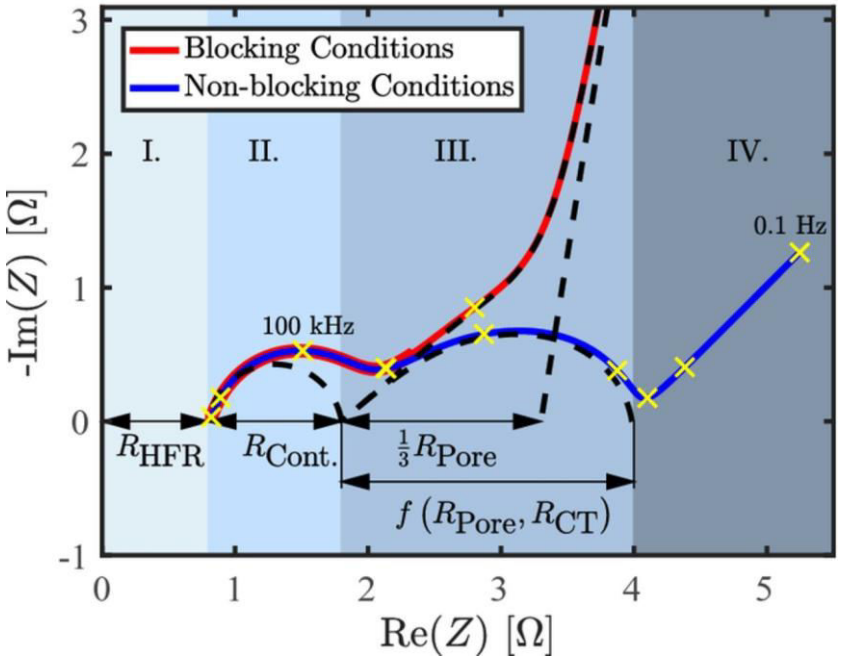

Figure 2-21: Simulated impedance response of a porous cathode electrode either under blocking conditions (red line) or under non-blocking conditions (blue line). The different processes and corresponding frequency regions are differentiated in the regions I-IV. Reprinted from ref [244].

3 Aim of this Thesis

The demand for high-energy-density storage is driven by the electrification of transportation and the integration of renewable energy sources. All-solid-state batteries are key to meeting these demands, replacing flammable liquid electrolytes with solid counterparts to enhance safety and reduce the risk of thermal runaway, which is crucial for electric vehicle batteries. Solid-state electrolytes also improve cell design and energy density by enabling thinner separator layers and the use of high-capacity lithium metal anodes. This simplifies manufacturing and reduces material costs. However, transitioning to solid electrolytes introduces challenges like limited interfacial contact, and consequently lithium dendrite formation due to current density hotspots. Inorganic electrolytes, while highly conductive, are brittle and require impractical stack pressures to achieve sufficient interfacial contact. In contrast, polymer-based electrolytes offer a more flexible solution and are able to accommodate volume changes during cycling for maintaining interface contact. Although polymers like PEO have limited ionic conductivity at room temperature due to their semi-crystalline nature, recent efforts aim to reduce crystallinity and enhance mobility show great potential.

To overcome the limitations of current polymer electrolytes, the first part of this work investigates the potential of polyvinylphosphonates functionalized with ethylene oxide side chains (**Scheme 3-1**) to form PX-VP polymers with X being the number of repetition units in the side chains. As detailed in chapter 2.5.2, vinylphosphonates offer several advantageous properties for solid-state electrolytes, including inherent flame retardancy, biodegradability, and a high degree of amorphous character, which enhances lithium-ion mobility. Their polymerization can be precisely controlled using catalytic techniques, specifically REM-GTP. This allows for the creation of tailored polymer structures with high molecular weights and narrow dispersities, as well as the possibility for copolymerization and end-group functionalization. Additionally, the phosphonate functionality provides a versatile

platform for side chain modification, enabling systematic adjustment of properties such as coordination strength, segmental mobility, and overall polarity.

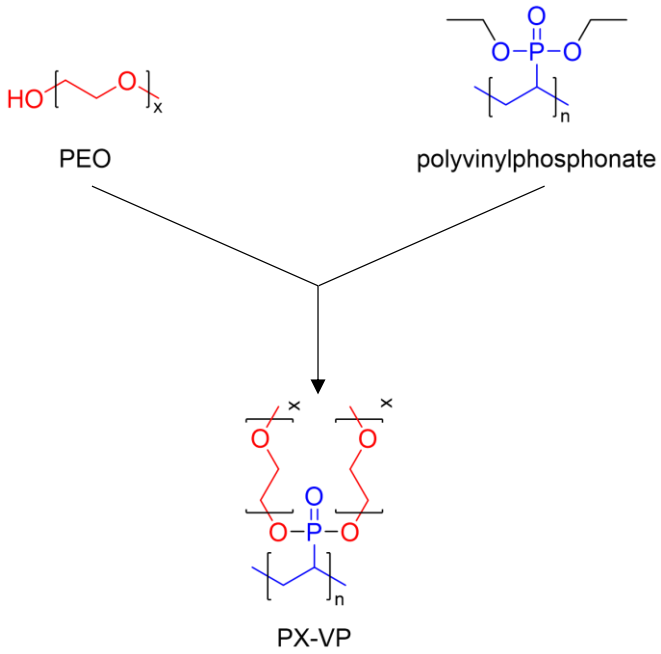

Scheme 3-1: Concept of combining the beneficial properties of PEO and polyvinylphosphonates to form a highly amorphous polymer with intrinsic flame retardancy of the phosphonate and ability to dissolve Li^+ ions via the ether side chains.

To evaluate the generated polymers for their suitability as polymer electrolytes, their mechanical and thermal properties will be assessed. Furthermore, their electrochemical properties are investigated, including ionic conductivity, electrochemical stability, and lithium-ion transference number. Half-cells with lithium metal anodes will be built and tested with LFP cathodes to determine practical performance.

As previously mentioned, cathode and anode materials experience volume changes during charging and discharging, which is a primary cause of contact loss between the electrodes and the electrolyte in ASSBs, leading to capacity fading and dendrite formation due to increased current densities at hot spots. These changes result from lithium plating and stripping, as well as the expansion of active materials, such as a 6.77% expansion for LFP.[245] In NMC, the volume change is more complex, with primary particles shrinking during lithiation while secondary particles expand, leading to particle cracking and further contact loss.[246] Building on the challenges posed by volume changes in electrodes, polymer electrolytes offer a promising solution due to their inherent softness, which allows them to maintain better interfacial contact during the breathing of electrodes. To investigate this cushioning

effect, the second part of this thesis will focus on studying the breathing behaviour of ASSBs during cycling. This will be accomplished by monitoring thickness and pressure changes using a specialized measuring cell provided by Sphere Energy.

Building on the strategy of enhancing interfacial contact with soft polymers, to address the poor contact between hard oxide electrolytes and electrode materials. This issue is particularly pronounced when oxide electrolytes are used as a catholyte, such as with LCO, and sintered together to form a cathode.[81] To investigate interfacial resistances and the impact of polymers in hybrid oxide-polymer solid-state batteries, the first step will involve creating and analysing a composite cathode with PEO as the catholyte (**Figure 3-1**). In the second step, half-cells with a PEO-SPE interlayer will be constructed and analysed to determine if further improvements to the interface can be achieved.

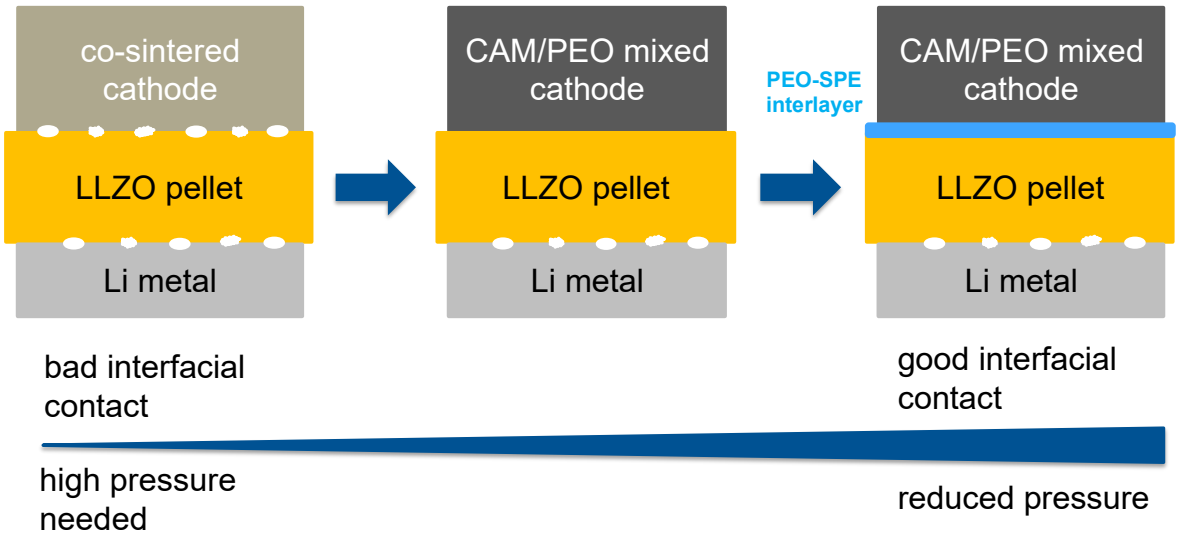

Figure 3-1: Overview of the strategy to improve interfacial contact and reduce interfacial impedance between a cathode, an LLZO electrolyte, and a lithium metal anode by incorporating a polymer electrolyte (PEO) into the cathode and as an interlayer between the LLZO pellet and the mixed cathode.

4 Results and Discussion

Parts of the following chapters were published in ACS Applied Polymer Materials: "Introducing a Catalytic Polymerization Approach for Bottlebrush-Vinylphosphonate Solid Polymer Electrolytes with Ethylene Oxide Side Chains"[247]

4.1 Polyvinylphosphonates as Solid Polymer Electrolyte

In the following chapters, vinylphosphonate monomers serve as the backbone structure for the attachment of ethylene oxide and carbonate-based side chains, enabling the synthesis of defined polymers. These are evaluated regarding their thermal and electrochemical properties, with a focus on their application as solid polymer electrolytes in ASSBs.

4.1.1 Synthesis of Vinylphosphonate Monomers Functionalized with Ethylene Oxide

As the first functionalization approach, ethylene oxide side chains of varying lengths were attached to the vinylphosphonate units. The synthesis of these novel monomers began with the chlorination of vinylphosphonic acid using oxalyl chloride, following a literature-reported procedure.[248] In this reaction, *N,N*-dimethylformamide (DMF) acts as a catalyst, facilitating the conversion of carboxylic acids into acyl chlorides via the reversible formation of an imidoyl chloride intermediate, which subsequently reacts with the acid while regenerating DMF. In the next step, the chlorine atoms in vinylphosphonic dichloride were substituted with oligo(ethylene oxide) units of different chain lengths. For this purpose, hydroxy-terminated oligo(ethylene oxides) were first deprotonated with triethylamine and then introduced via a nucleophilic substitution reaction at the phosphorus atom. The resulting $HCl{\cdot}NEt_3$ precipitate was removed from the reaction equilibrium, ensuring the completion of the substitution process. The general reaction is displayed in **Scheme 4-1**. The resulting monomers were labelled according to the number of ethylene oxide repetition units in the side chains.

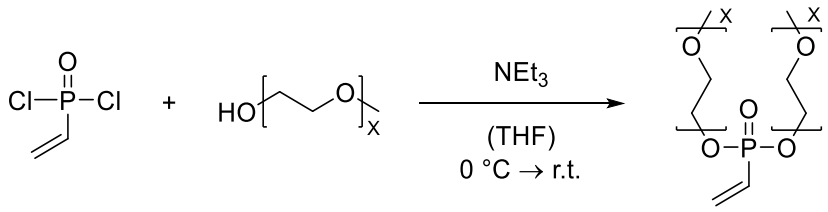

Scheme 4-1: General reaction scheme for the synthesis of vinylphosphonate monomers functionalized with ethylene oxide side chains with different number of repetition units. Monomers were synthesized with X = 1, 2, 3 and 7 repetition units.

For the synthesis of bis(2-methoxyethyl) vinylphosphonate (1-VP), methoxyethanol was used as the reactant. Similarly, diethylene glycol monomethyl ether led to bis(2-(2-methoxyethoxy)ethyl) vinylphosphonate (2-VP), triethylene glycol monomethyl ether yielded 3-VP, and a commercial poly(ethylene glycol) monomethyl ether (average molecular weight 350 g mol^{-1}) was used for the synthesis of 7-VP. In all cases, the desired monomers with various ethylene oxide side chains were successfully obtained in high yields (>70 %) and the structures of all monomers were confirmed by ^{1}H and ^{31}P-NMR spectroscopy. However, it was evident that longer side chains required extended reaction times for full conversion, which is expected due to the slower diffusion of the larger side chains. The primary challenge, however, lays in the purification process, which became increasingly demanding as the side chain length increased.

The purification and drying of the synthesized monomers were essential to ensure their suitability for further polymerization. The drying process was performed prior to purification when the monomers were subsequently distilled, and after purification when column chromatography was applied. Residual moisture removal was crucial, as water can interfere with polymerization. The most effective drying method involved passing the monomers through an activated Al_2O_3 column (using dry DCM as an eluent) followed by storage over activated molecular sieve 4 Å (MS 4 Å). The residual moisture content was measured using Karl-Fischer titration. Although a Karl-Fischer oven was tested—where the sample is heated and only the released gases are analysed—it was found to be ineffective due to the small sample volume (<500 µL) and low water content, which fell below the detection threshold. Instead, direct injection of 200 µL of monomer into a Karl-Fischer titrator provided accurate water content measurements, consistently yielding values below 20 ppm with the Al_2O_3 and molecular sieve drying method. In contrast, drying with CaH_2 resulted

in higher water contents (>100 ppm) and, in some cases, led to oligomerization, as confirmed by ^{31}P-NMR spectroscopy. Interestingly, during Karl-Fischer analysis, samples with higher water content exhibited brown discoloration when heated in the Karl-Fischer oven, suggesting that H_2O accelerates degradation at elevated temperatures.

During purification, it was observed that the starting alcohol was not fully removed by extraction but was more effectively eliminated by distillation. As a result, extraction was largely omitted without negatively affecting the purity of the final monomers. However, solubility differences between the monomers influenced the purification strategy. Due to its higher polarity, 1-VP exhibited reduced solubility in DCM, making extraction ineffective before distillation. Both 1-VP and 2-VP were efficiently purified using standard distillation techniques with a rotary vane pump and a silicon oil bath. However, as the molecular mass increased, distillation became more challenging. For 3-VP, successful purification was achieved using a turbopump, which reached a vacuum of 10^{-5} to 10^{-6} mbar, along with a sand bath for heating to 230–250 °C. In the case of 7-VP, the boiling point could not be reached using these techniques, making distillation impractical. As an alternative, column chromatography was tested for the purification of both 3-VP and 7-VP. However, the results were generally inferior to those obtained through distillation.

4.1.2 Polymerization of Ethylene Oxide Functionalized Vinylphosphonates with REM-GTP Catalysts

Yttrium-based catalytic systems are widely used for the polymerization of various *Michael*-type monomers, particularly in REM-GTP of dialkyl vinylphosphonates (DAVPs). These catalysts exhibit high activity, as demonstrated in the polymerization of diethyl vinylphosphonate (DEVP), where YCp_3 achieves a turnover frequency (TOF) of 21.000 h^{-1}. Even higher TOF values have been reported with the introduction of pyridine-based initiators for the REM-GTP of DAVPs. Similar to other REM systems, the complex Cp_2LnCH_2TMS (Ln = Y or Lu) undergoes selective C–H bond activation with *sym*-collidine, leading to highly active catalytic species. Notably, Cp_2Y(*sym*-collidine) achieves a TOF of 59.400 h^{-1} in the polymerization of DEVP.[154,249] Consequently, this catalyst was also studied for the polymerization of the ethylene oxide functionalized vinylphosphonates. The corresponding polymerization reaction is illustrated in **Scheme 4-2**.

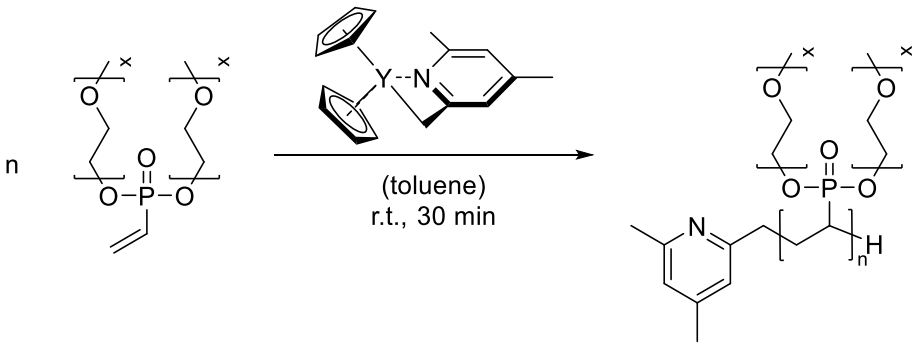

Scheme 4-2: REM-GTP of the synthesized vinyl phosphonates catalysed by Cp_2Y(*sym*-collidine) and the resulting polymers with the transferred *sym*-collidine group (X = 1, 2, 3, 7).

Kinetic studies revealed a TOF of at least 9407 h^{-1} for 1-VP and 5942 h^{-1} for 2-VP using the Cp_2Y(*sym*-collidine) catalyst (**Figure 4-1**), with full monomer conversion achieved in under 5 min. These results suggest that the increased steric demand of the functionalized monomers reduces catalytic activity. Despite this, the catalyst enabled the synthesis of high-molecular-weight polymers, yielding up to 380 kg mol^{-1} for P1-VP and 650 kg mol^{-1} for P2-VP, as confirmed by gel permeation chromatography (GPC) and NMR (Appendix **Figure 8-1** to **Figure 8-6**).

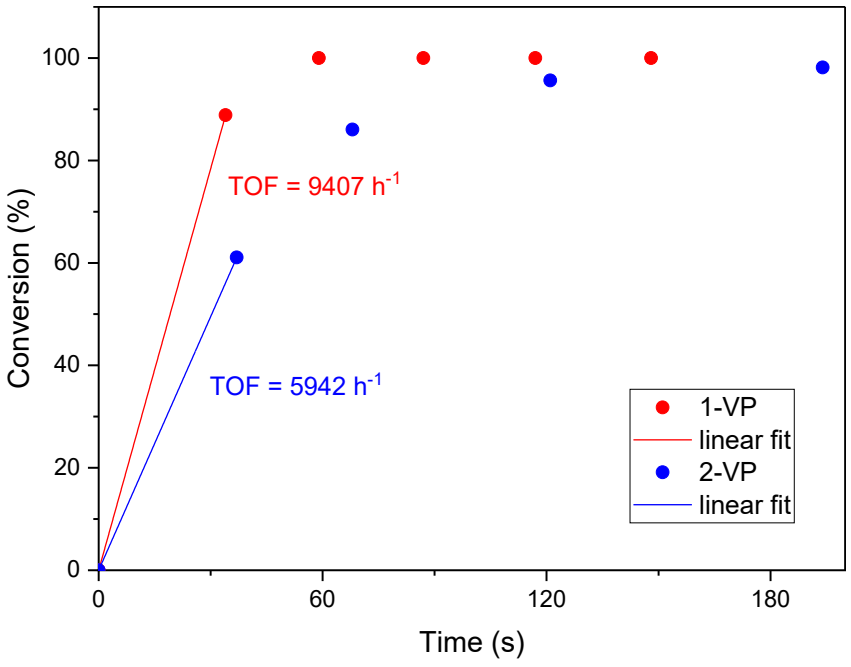

Figure 4-1: Determination of the catalytic activity of Cp_2Y(*sym*-collidine) for the polymerization of 1-VP and 2-VP ([Mon]/[Cat] = 200/1). The turnover frequency is determined from linear fit between the starting point and the first measurement step after 30 s.

For the polymerization of 3-VP and 7-VP, monomer purity proved to be a limiting factor, with maximum conversions of 90% for 3-VP and less than 20% for 7-VP. This highlights a

key drawback of the catalytic system, as it is highly sensitive to impurities and residual moisture. A general trend was observed for P1-VP and P2-VP where full conversion was achieved with a [Mon]/[Cat] ratio of 200/1 when the water content was below 50 ppm. At moisture levels below 20 ppm, a significantly higher monomer-to-catalyst ratio of 1000/1 was possible.

In addition to the Cp_2Y(*sym*-collidine) catalyst, the previously mentioned YCp_3·THF and the lutetium variants of both catalysts were also tested (**Figure 4-2**). Lutetium-based systems have demonstrated even higher activity in DEVP polymerization, with $LuCp_3$ reaching a TOF of 265,000 h^{-1}.[151,153,154] For YCp_3·THF, significantly lower TOF values of 262 h^{-1} for 1-VP and 176 h^{-1} for 2-VP were observed, resulting in reaction times exceeding 60 min before full conversion was achieved. Additionally, a short initiation period of approximately 10 s was noted after mixing the monomer with the catalyst (**Figure 8-7**). These factors led to lower molecular weights (<100 kg mol^{-1}) and broader dispersities (Đ > 2). In contrast, both lutetium catalysts produced polymers with very high molecular weights exceeding 1000 kg mol^{-1} and narrow dispersities (Đ < 1.3). Despite their superior performance in achieving high molecular weights, further investigation of these catalysts was not pursued due to the high cost of lutetium and the lack of a significant advantage for polymer electrolytes, where such high molecular weights are not necessarily beneficial.

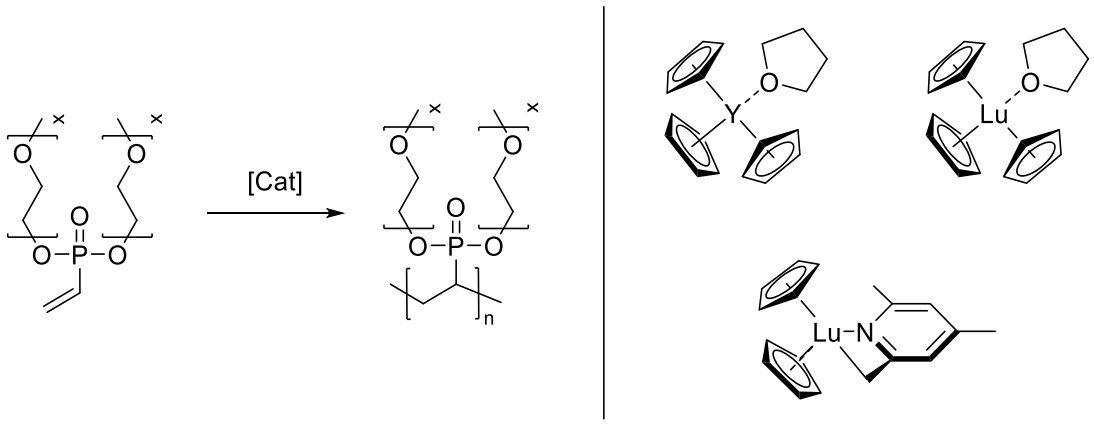

Figure 4-2: Other REM-GTP catalysts studied for the polymerization of functionalized vinylphosphonates.

To provide a complete assessment, radical polymerization was also tested using azobisisobutyronitrile (AIBN) and dibenzoyl peroxide (DBPO) as initiators. However, only low molar masses were obtained, which is consistent with literature reports and can be attributed to the resonance stabilization of the radical in the phosphonate.[250] The pronounced stability

of the formed radical species, combined with the frequent occurrence of chain transfer reactions either to the monomer or the growing polymer chain, resulted in low molecular masses and low conversions. With AIBN, a conversion of 43% was achieved after 6 h of reaction time, whereas no conversion was observed for DBPO (**Table 8-2**). In conclusion, for the synthesis of polymer electrolytes, Cp_2Y(*sym*-collidine) proves to be an effective catalytic system for the polymerization of oligo(ethylene oxide)-functionalized vinylphosphonates.

4.1.3 Introduction of Carbonate Units to the Side Chains

One advantage of the vinylphosphonate structural motif is the ability to introduce various functional groups into the side chains without significantly altering the polymerization behaviour. Carbonate functional groups are of particular interest, as they are widely used as organic solvents in liquid electrolytes. Additionally, studies by Schönhoff et al. on carbonate functionalities in solid polymer electrolytes demonstrated that carbonates coordinate lithium ions more weakly than ether units, such as those in PEO. This weaker coordination can enhance the lithium transference number but may also reduce ionic conductivity.[251] Furthermore, the interaction of lithium ions with cyclic carbonates was found to be stronger than with linear carbonates, with variations depending on the substituents.[252] Based on these findings, two types of carbonate side chains were investigated as substituents for vinylphosphonate monomers: a linear carbonate attached to an ethylene oxide unit and a cyclic carbonate.

The synthesis of 2-(2-hydroxyethoxy)ethyl methyl carbonate as carbonate-terminated ethylene oxide side chains was optimized by evaluating various catalysts, including K_2CO_3, $NaOCH_3$, NaOH, NEt_3, and CaH_2. The overall reaction is displayed in **Scheme 4-3**, while the studied reaction conditions are displayed in **Table 4-1**.

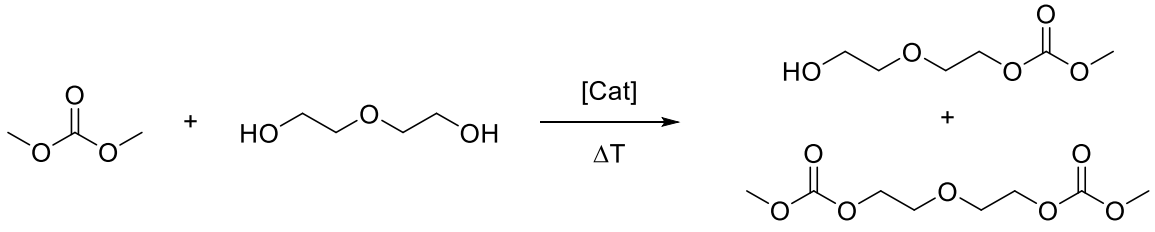

Scheme 4-3: Reaction scheme for the synthesis of a carbonate terminated ethylene oxide side chain, with the disubstituted side product.

Among these, CaH_2 proved to be the most effective catalyst, as confirmed by ^{1}H-NMR spectroscopy of the obtained reaction mixture. The reaction was best carried out without a solvent, as solvent addition led to lower yields. A reaction time of 5 hours was identified as optimal, ensuring a good conversion to the monosubstituted product while minimizing the formation of the disubstituted byproduct, which increased at longer reaction times. Various purification strategies were explored, including extraction, distillation, catalyst removal, neutralization, and chromatography. Extraction was performed using EtOAc and water, but phase separation was difficult to distinguish, raising concerns about product loss to the aqueous phase. Distillation was attempted under different conditions (with and without a Vigreux column at ~10 mbar and temperatures up to 170 °C) but proved ineffective, as no product was recovered.

Table 4-1: Studied reaction conditions for the synthesis of carbonate terminated ethylene oxide side chains

Catalyst	Reaction time	Conversion[a]	Purification method
K_2CO_3	20 h	<10%	none
$NaOCH_3$	20 h	<10%	none
NaOH	20 h	<10%	none
NEt_3	20 h	~30%	distillation
CaH_2	3 - 20 h	>90%	Extraction, distillation, filtration, neutralization with HCl and $NaHCO_3$, column chromatography

[a]determined via aliquot ^{1}H-NMR, tested solvents: DMSO, THF, reaction carried out in bulk.

The removal of CaH_2 by filtration was straightforward, effectively eliminating all solid catalyst, while NEt_3 was removed by evaporation. Neutralization with HCl resulted in a biphasic solution with milky-white upper components, whereas $NaHCO_3$ treatment led to a gel-like consistency, rendering both methods unsuitable. Column chromatography was tested using different solvent mixtures, including DCM/MeOH (98/2), pure DCM, pure EtOAc, pure pentane, and various ratios of pentane/EtOAc (3/1 to 1/5), but none provided sufficient separation. Due to the challenges in isolating the monosubstituted product, the most effective approach relied on a combination of catalyst removal and extraction, though complete purification remained problematic.

The resulting product was used to study the synthesis of a carbonate functionalized vinylphosphonate, as shown in **Scheme 4-4**. However, the final product could not be isolated, likely due to the insufficient purity of 2-(2-hydroxyethoxy)ethyl methyl carbonate. Unfortunately, none of the tested purification methods yielded a product with sufficient purity.

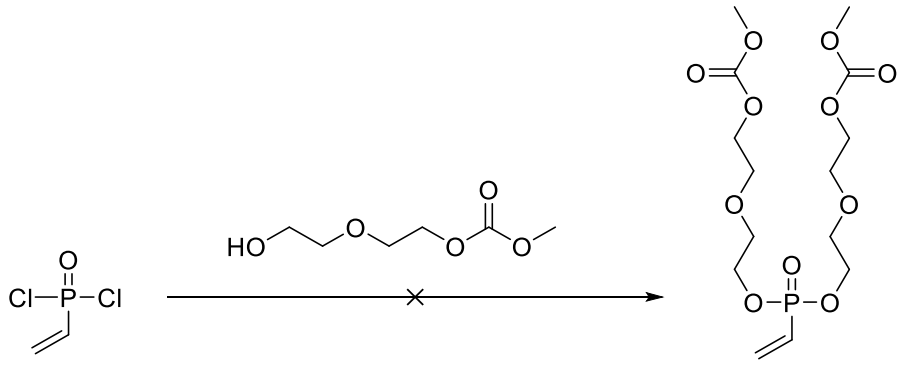

Scheme 4-4: Reaction scheme for the synthesis of a vinylphosphonate monomer functionalized with linear carbonates.

The second approach for functionalizing vinylphosphonates with carbonates involved incorporating cyclic propylene carbonate side chains, analogous to a phosphate monomer reported by Wang et al. However, the phosphate monomer featured an acrylate functionality, enabling polymerization via radical polymerization. Using AIBN for in-situ or ex-situ polymerization, they successfully synthesized a quasi-solid-state polymer electrolyte with an ionic conductivity of up to $5.65 \cdot 10^{-4}$ Scm^{-1}, demonstrating good flame retardancy and 72% capacity retention after 150 cycles (compared to 37% for ex-situ polymerization).[144] The primary structural difference between the phosphate monomer and the vinylphosphonate lies in the oxidation state of phosphorus (+V in phosphate vs. +III in phosphonate) and their respective backbone structures. Both monomers are shown in **Scheme 4-5**.

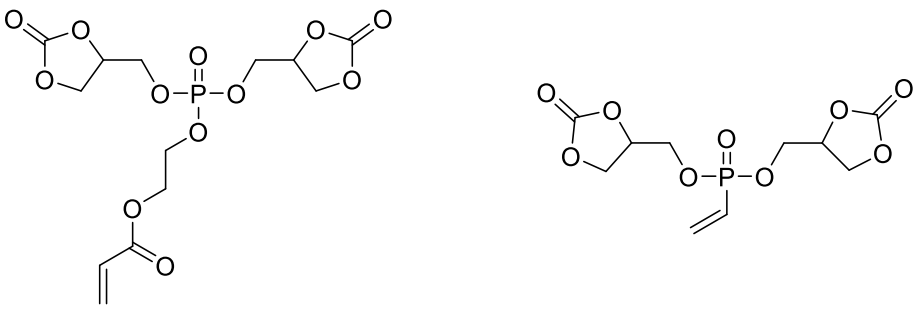

Scheme 4-5: Comparison of the phosphate monomer structure reported by Wang et al.[144] (left) and the target vinylphosphonate functionalized with the same cyclic carbonate groups (right).

For the synthesis of the vinylphosphonate, commercially available 4-(hydroxymethyl)-1,3-dioxolan-2-one was used in a reaction starting from vinylphosphonate dichloride, following the same reaction procedure as for the synthesis of ethylene oxide functionalized vinylphosphonates. After 48 hours of reaction time, a conversion of 63% was achieved, as confirmed by ^{31}P-NMR. However, purification remained a significant challenge, as neither distillation (up to 130 °C and 10^{-5} mbar), nor column chromatography on alumina or silica, nor extraction yielded a carbonate-functionalized monomer of sufficient purity for polymerization via REM-GTP.

It is worth noting that while the Michael system in the vinylphosphonate remains unchanged and should allow REM-GTP polymerization, the carbonate functionality in the side chain could potentially coordinate to the metal center of the catalyst. This coordination might compete with the P=O bond interaction required for propagation, potentially affecting the polymerization process. Ultimately, the primary challenge in introducing functionalized groups into the polymer electrolyte lies in the purification of the functionalized vinylphosphonates. Given that the focus of this study is on understanding the effect of the phosphonate group on the electrochemical properties, further investigation into this functionalization approach was not pursued in this work.

4.1.4 Preparation of PX-VP Solid Polymer Electrolyte Films

Solution casting was used for the main production method for poly(vinylphosphonate) SPE films, as free-standing films were required for the electrochemical analyses. Following the isolation and purification of the polymers, SPE films were prepared using various lithium conducting salts, including $LiBF_4$ and lithium bis(trifluoromethane)sulfonimide (LiTFSI). The amount of lithium salt added to the polymer was referenced to the number of ethylene oxide units in the side chains of the monomers, ensuring a consistent ratio of Li^+ ions to EO unit (two EO units for 1-VP, four for 2-VP, and six for 3-VP). The solvents tested for solution casting were DMF, THF, and MeCN, as all three effectively dissolved both the polymers and the salts. However, DMF evaporated very slowly, requiring several days, which significantly prolonged the drying process. Residual solvent can also influence the mechanical and electrochemical properties of SPEs, and since DMF is difficult to remove entirely, its use was considered impractical.[1–3] In contrast, THF and MeCN produced comparable results for the poly(vinylphosphonate) films. MeCN was ultimately chosen as the solvent for all film

production due to its superior ability to dissolve PEO, which was extensively used in hybrid polymer-oxide cells (chapter 4.2 and onwards). After dissolving both the polymer and conducting salt, the solution was stirred for 3 hours on a magnetic stirrer to ensure complete dissolution, as polymers with higher molecular weights required more time to fully dissolve. Once dissolution was achieved, the polymer solution was cast into Teflon trays and dried under vacuum after solvent evaporation. Initially, drying was performed in a vacuum oven at 45 °C, but it was observed that the films rapidly absorbed moisture from the atmosphere during transfer to a glovebox. To prevent this, all film production was conducted under an inert atmosphere, with final drying carried out in vacuo in the antechamber of a glovebox. The entire process is illustrated in **Figure 4-3.**

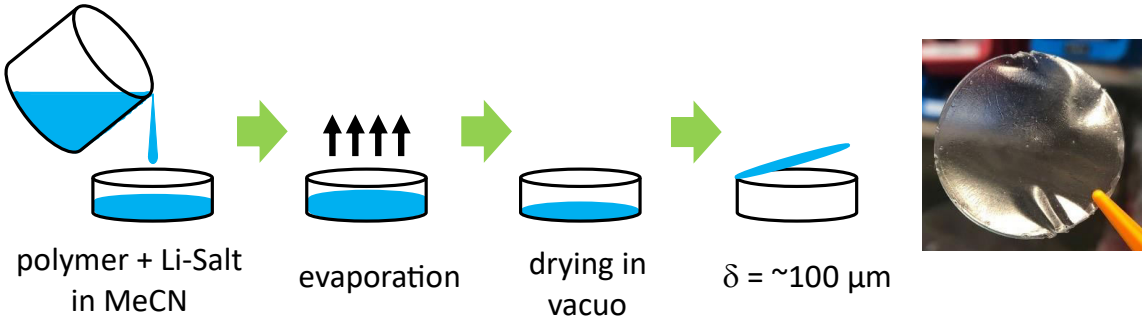

Figure 4-3: Production of SPE foils via solution casting from MeCN in Teflon trays (⌀ = 45 mm). Thickness measurements of the films were conducted with a dial gauge.

As a maximum a ratio of EO/Li^+ = 1/1 with various Li-salts was prepared. Hereby, no undissolved lithium salt was observed on the final films, which was confirmed by X-ray diffraction (XRD) measurement (see chapter 4.1.5). Glass trays were also tested, but the films did not detach from these after drying. A similar issue was encountered when Mylar foil was used to line the trays. Additionally, the final films exhibited a thickness variation, with the centre being up to 30 µm thinner than the edges, which was attributed to increased wetting at the dish boundaries.

To analyse the purity of the produced SPE films, scanning electron microscopy (SEM) images in combination with energy-dispersive X-ray spectroscopy (EDX) were taken (**Figure 4-4**). The images revealed multiple impurities on the film surfaces. The EDX spectrum indicated that these particles were likely a mixture of dust from the molecular sieve (spectrum 1 - increased Al, Si, and O content) and NaCl (spectrum 3). The EDX spectrum of the clean surface (spectrum 2) showed only elements present in the polymer and the

conducting salt LiTFSI. To eliminate these impurities, the solvent was filtered after drying, and a higher-purity conducting salt was used (99.95%). These measures effectively removed both types of impurities.

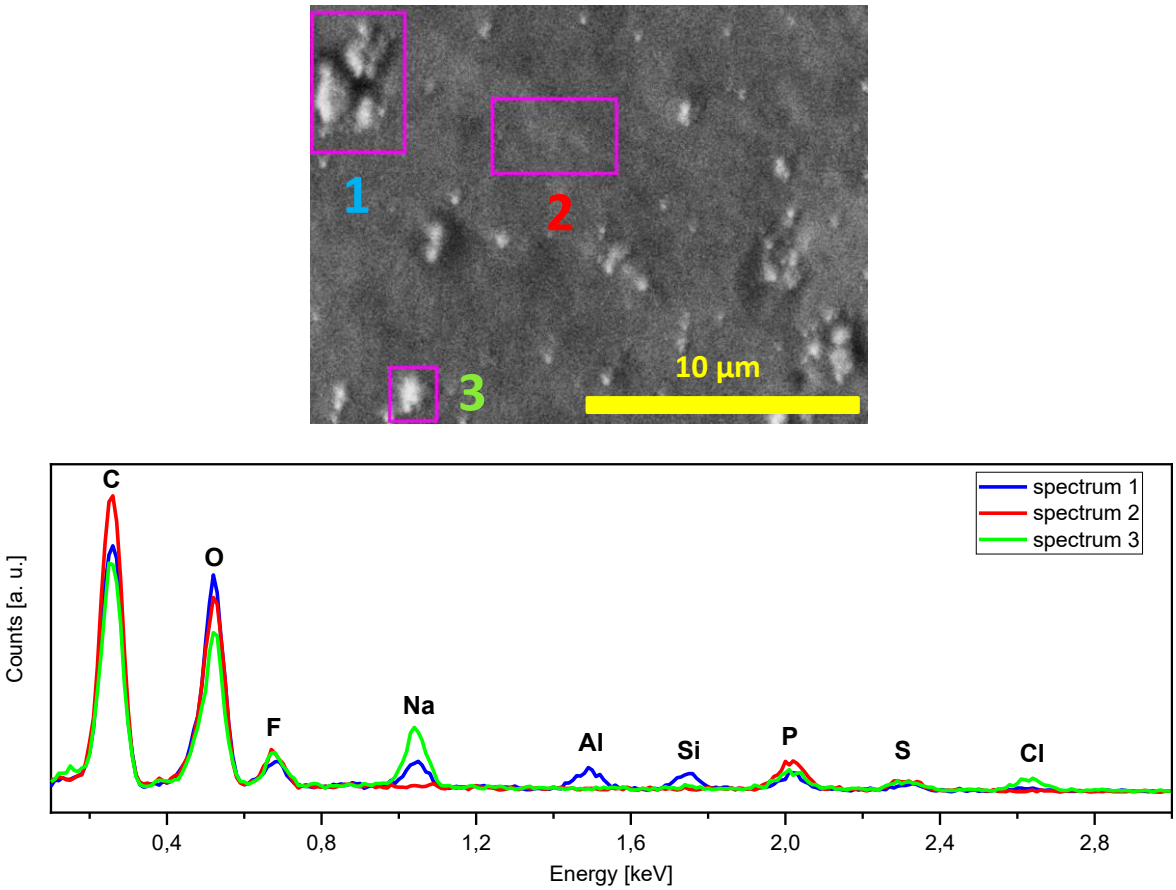

Figure 4-4: SEM image (top) and EDX spectrum (bottom) of a P2-VP SPE film (2) with LiTFSI and molecular sieve (1) and NaCl (3) impurities.

Additionally, mixing was tested using a speedmixer and a dispermat. For SPE films, no benefits were observed with these methods, and the process was unnecessarily complicated. However, for the production of CPE films with various fillers (e.g., Al_2O_3, TiO_2, LLZO), stronger shearing forces are necessary to homogeneously disperse the fillers in the polymer solution. The speedmixer proved superior in this regard, easily producing homogeneous solutions. In contrast, the dispermat required more volume for the blade to effectively reach the mixture, leading to higher consumption of polymer and lithium salt. Moreover, mixing was insufficient if the alignment of the blade and crucible was not ideal. Subsequent doctor blading of the homogeneous dispersions onto aluminum foil yielded films with an adjustable thickness of less than 10 µm after drying. The processes are displayed in **Figure**

4-5. Due to the polymer's stickiness, removing the films from the aluminum foil proved impossible, rendering this method unsuitable for producing freestanding films.

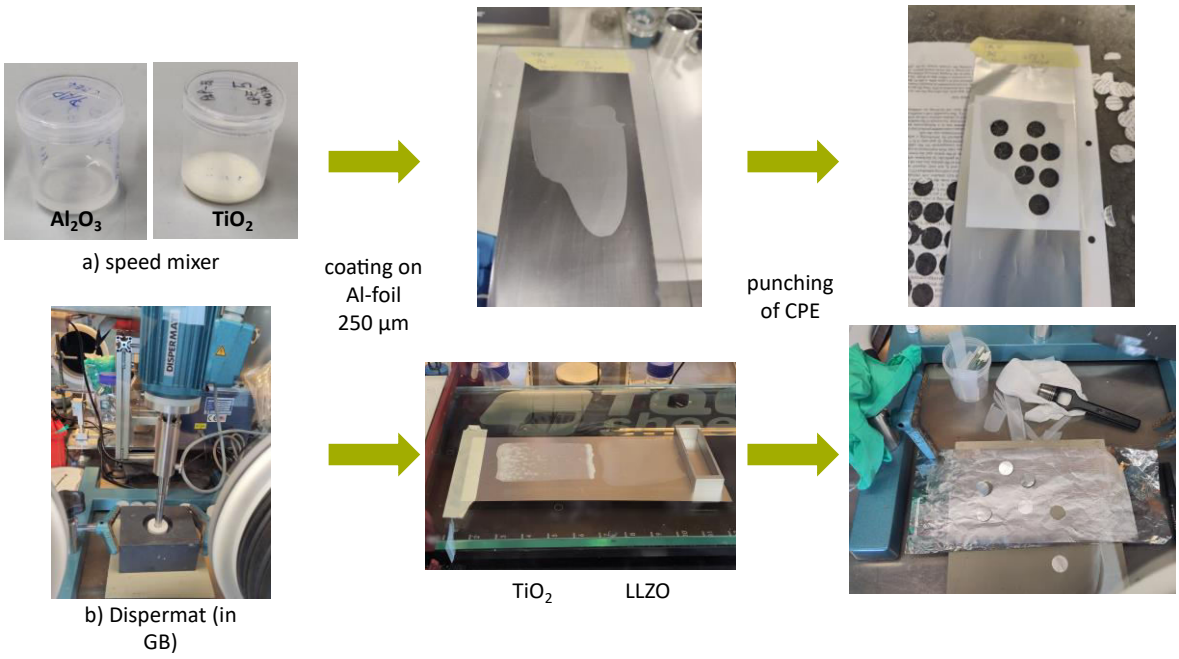

Figure 4-5: Production of SPE/CPE films by doctor blading onto Al-foil. Pictures on the top shop the mixing process in a speedmixer and consequent processing under air, while the bottom pictures show the mixing procedure in a dispermat in an Ar filled GB along with the processing under inert atmosphere.

4.1.5 Thermal and Mechanical Properties of the Functionalized Poly(vinylphosphonates)

The thermal stability of solid polymer electrolytes is a key component in the safety performance of lithium metal batteries, thermal gravimetric analysis (TGA) is used to evaluate the thermal stability of the herein synthesized polymers. **Figure 4-6** displays the TGA curves of P1-VP and P2-VP without Li-salt, as well as their respective SPE films with $LiBF_4$. Both SPE samples exhibit a weight loss of approximately 3% prior to reaching 100 °C, which is attributed to residual MeCN and moisture absorption during the transfer of samples into the TGA, as $LiBF_4$ is known for its hygroscopic properties. Moreover, P1-VP exhibited an initial degradation temperature (T_d) of approximately 260 °C, with a corresponding weight loss of 50%, attributed to the cleavage of the C–O bond between the phosphonate group and the ethylene oxide side chains, leading to the formation of polyvinylphosphonic acid.[154] An analogous initial degradation of 65% is visible for P2-VP, but with the onset occurring at 210 °C. A second degradation phase for both polymers started at around 420 °C, associated with the breakdown of the phosphonate structure. With the addition of $LiBF_4$, the initial

degradation is reduced to 225 °C for P1-VP and 160 °C for P2-VP. The reduced thermal stability of PEO-based solid polymer electrolytes with $LiBF_4$ is superimposable with literature data, showing the same decomposition onset of 160 °C.[253–255] Interestingly, the second degradation step is shifted to a higher temperature in both cases, suggesting that the interaction between polyvinylphosphonic acid and $LiBF_4$ might stabilize the material, as no separate decomposition of $LiBF_4$ was observed at its typical decomposition temperature of 400 °C.[256] Both effects, the earlier initial decomposition, and the delayed second decomposition, are enhanced with increasing amounts of $LiBF_4$ (**Figure 8-8** and **Figure 8-9**).

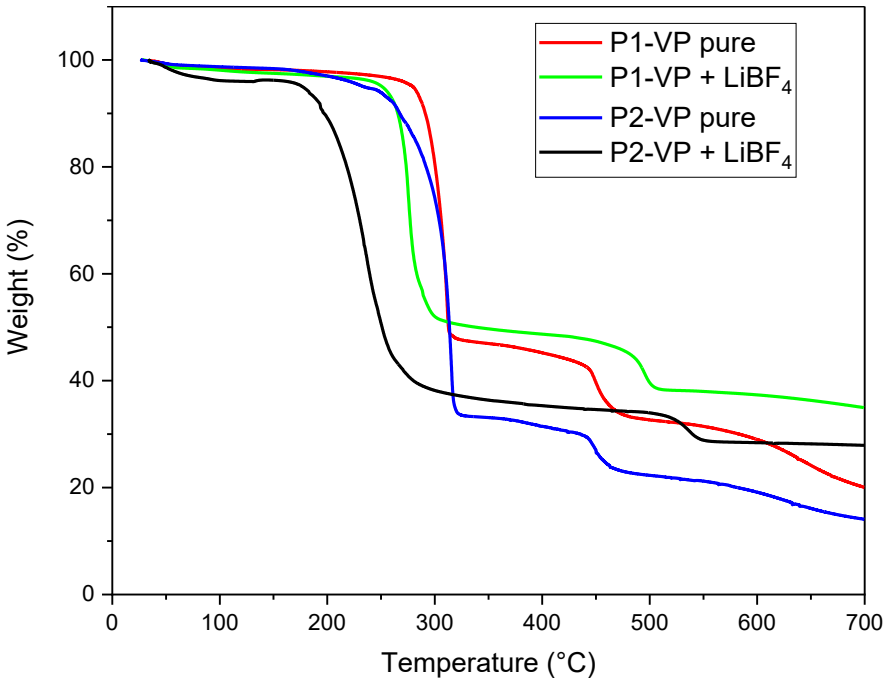

Figure 4-6: TGA curves of P1-VP and P2-VP under inert atmosphere, with and without $LiBF_4$ (EO/Li^+ = 10/1); Decreasing decomposition onset for both polymers with the addition of $LiBF_4$.

When LiTFSI is used as conducting salt, the onset of thermal decomposition shifts to ~270 °C for both polymers (**Figure 4-7**). In contrast to the two-step degradation observed for $LiBF_4$ containing samples, the decomposition with LiTFSI proceeds in a more linear manner and finishes at about 480 °C. This behaviour is consistent with literature, where LiTFSI generally exhibits higher thermal stability than other fluorine-containing Li salts and decomposes between 340 and 380 °C.[257] Consequently, the use of LiTFSI enhances the thermal stability of the SPEs compared to $LiBF_4$. However, the lower onset temperature of the SPE decomposition is unlikely to result solely from differences of the BF_4^- and $TFSI^-$ anion decomposition products. The data suggest that coordination of Li^+ ions to ether oxygen atoms weakens the C–O bond in the side chains, thereby reducing the thermal stability

independent of the anion. Further mechanistic studies are required to verify this hypothesis but are beyond the scope of this thesis. Overall, TGA analysis indicates that the investigated PX-VP polymers remain thermally stable under elevated temperature conditions relevant for lithium battery operation.

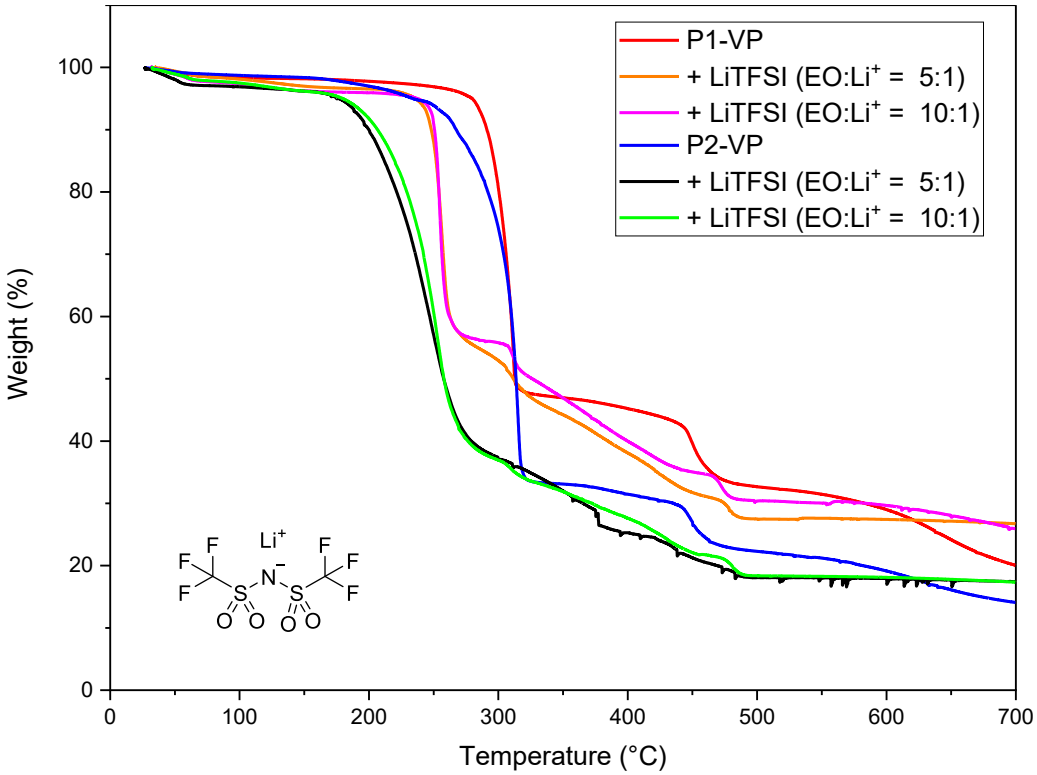

Figure 4-7: TGA curves of P1-VP and P2-VP pure polymers and their respective SPEs with various amounts of LiTFSI. The amount of LiTFSI is given as ratio of EO units in the monomer side chains to Li^+ ions.

To evaluate the fire resistance of the electrolytes, SPE films with $LiBF_4$ from both polymers were exposed to an open flame using a lighter (**Figure 4-8**).

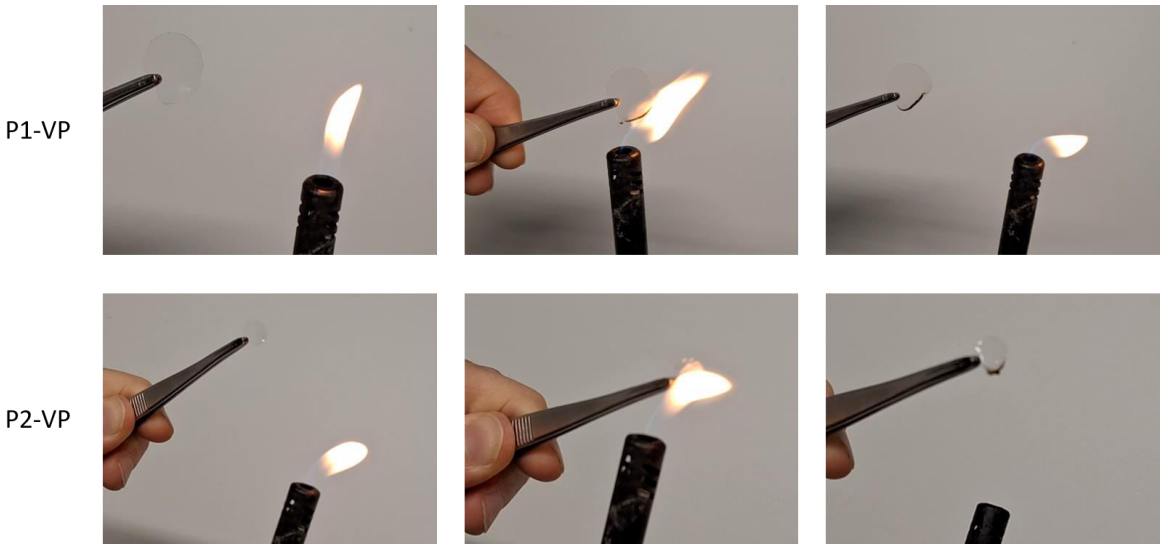

Figure 4-8: Flammability tests performed on the SPEs films from P1-VP and P2-VP with $LiBF_4$ (EO/Li^+ = 10/1).

In both cases, the flame self-extinguished within a few seconds, leaving a blackened, charred edge. Notably, the fire did not propagate or consume the entire electrolyte film. The P1-VP film exhibited less shrinkage compared to the P2-VP film, indicating that a higher molar ratio of phosphonate units in the side chains enhances flame retardancy, as expected.

To analyse the crystallinity of the polymer electrolytes, XRD measurements of the pure polymers and the respective SPE films with $LiBF_4$ are performed (**Figure 4-9**). No sharp reflexes are visible for all four samples, indicating the absence of crystalline regions and the purely amorphous character of the polymers and electrolyte films. Instead for both polymers and SPE films two broad amorphous halos appear. The first in the range from <5 to 10° and the second from 15 to 30°. While the maximum of the second halo appears to be identical for all for samples, the first halo is shifted to higher angles for the P1-VP samples. This shift is attributed to a higher density of the P1-VP due to the shorter side chains and therefore better chain alignment.[258]

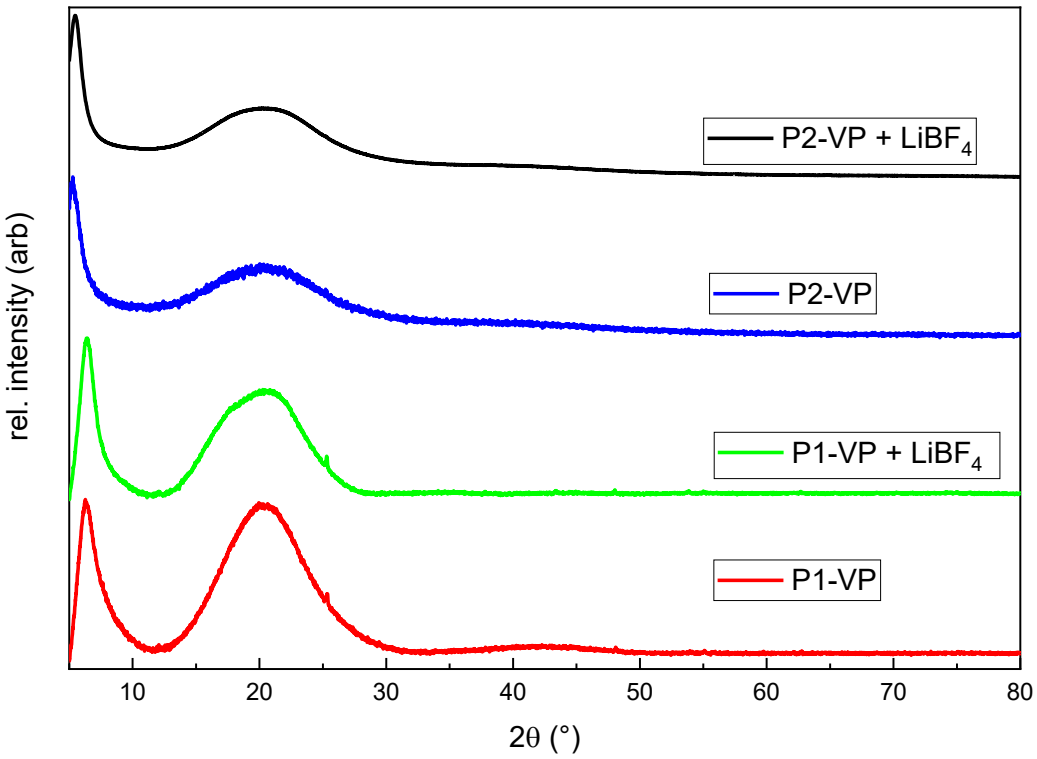

Figure 4-9: XRD patterns of P1-VP and P2-VP under inert atmosphere, with and without $LiBF_4$ (EO/Li^+ = 10/1)

To confirm the fully amorphous character and investigate the glass transition temperatures of the polymers, differential scanning calorimetry (DSC) measurements are performed. For P1-VP and P2-VP, glass transition temperatures of −48 °C and −67 °C, respectively, are observed with no detectable melting temperature, confirming the purely amorphous character of the polymers (**Figure 4-10**). The shift of the T_g to lower temperature observed in P2-VP can be explained by the longer side chains. These elongated side chains hinder the alignment of polymer chains, thereby diminishing the chemical interactions between them. This phenomenon is commonly observed in brush-type polymers.[63,110,259]

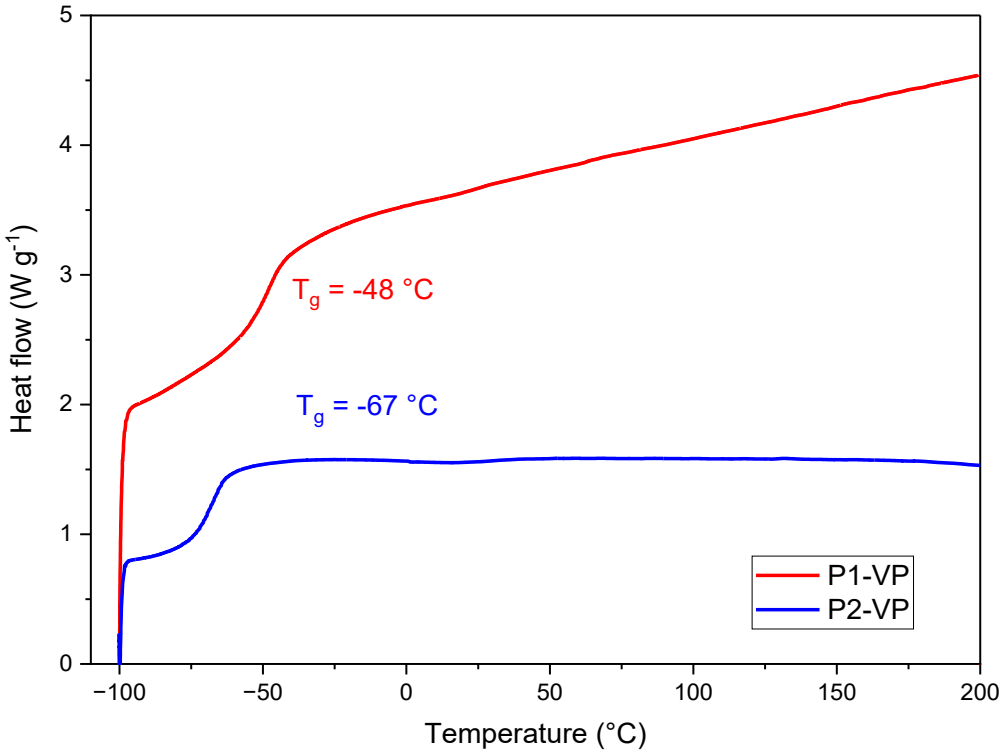

Figure 4-10: DSC curves of pure P1-VP and P2-VP polymers with visible glass transitions of the amorphous regions but no observable melting temperature. Depicted is here the second heating cycle of the measurement.

For pure PEO, a T_g of −64 to −50 °C is reported, increasing with molecular mass.[138,260–262] Consequently, the flexibility of the chains decreases with short EO side chains, while it increases as the chains lengthen and the alignment of the polymer chains is reduced. This effect was further investigated for pure P2-VP with molecular weights ranging from 150 to 400 kg mol^{-1}. Within this range, no significant change in T_g was observed (**Figure 8-10**). Nevertheless, an increase in T_g with increasing molecular weight is expected for PX-VP polymers, as this is a general trend observed in polymers, predominantly at low molecular weights, as described by the Flory-Fox equation.[263] Since lower molecular masses negatively affect the mechanical integrity of the SPE films, these molecular masses were not studied in detail.

To investigate the influence of Li-salt concentrations on the T_g, SPEs with varying quantities of $LiBF_4$ were also analysed via DSC. The results for the P2-VP electrolytes are displayed in **Figure 4-11**. It is evident that with increasing amounts of $LiBF_4$, the T_g increases from −54 °C (EO/Li^+ = 15/1) to −20 °C (EO/Li^+ = 5/1), as also observed in literature for PEO.[264,265] The same tendency is observed for P1-VP (**Figure 8-11**). The increase in T_g with higher $LiBF_4$

content correlates with enhanced mechanical rigidity of the SPE films, rendering them harder, less tacky, and more manageable during processing.

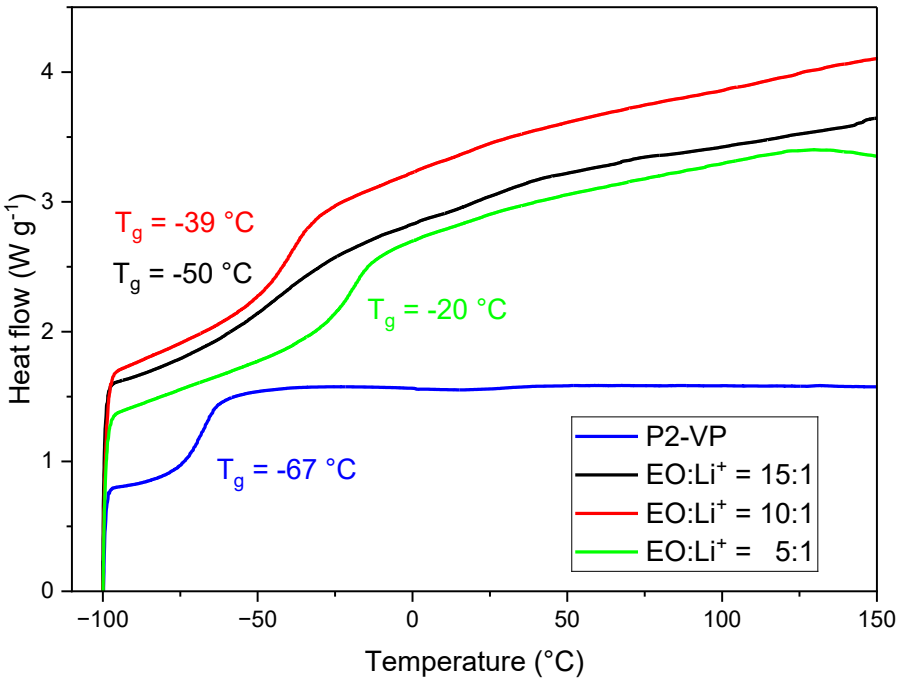

Figure 4-11: DSC curves of pure P2-VP and SPE films with various amounts of $LiBF_4$ (ratios are given as EO/Li^+).

Films with a higher EO/Li^+ ratio of 5/1 exhibited increased brittleness, making them prone to breaking, whereas films with a ratio of 15/1 were excessively soft, often resulting in cell short-circuiting (**Figure 4-12**). Although SPE films with high concentrations of Li-conducting salt exhibited increased brittleness, no sharp crystalline reflections were detected in the XRD, nor were any melting transitions observed in the DSC. These results indicate that the films remain fully amorphous despite their reduced mechanical flexibility. Due to the hygroscopic nature of the SPE films, their mechanical properties could not be evaluated, as exposure to air caused the films to become excessively soft and tacky within minutes. As a compromise between handleability and low T_g/high ionic conductivity a ratio of EO/Li^+ = 10/1 is chosen for subsequent electrochemical testing.

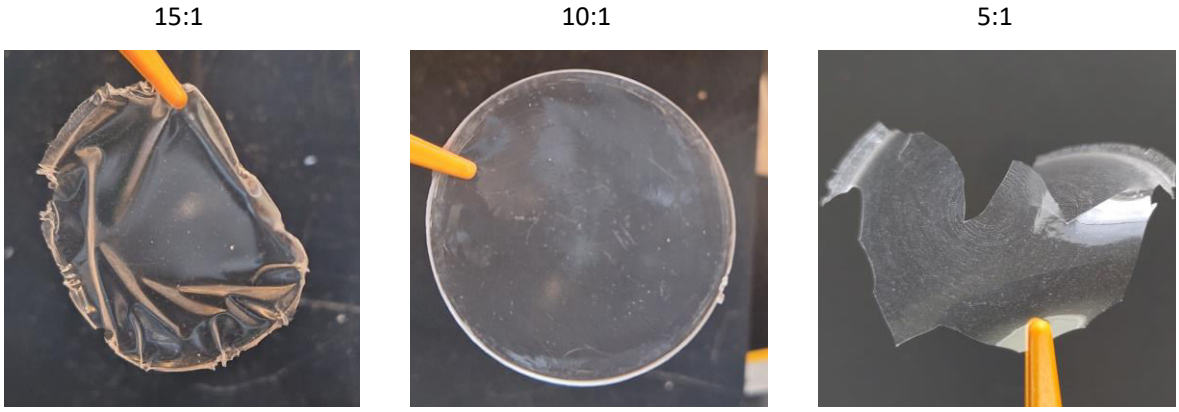

Figure 4-12: Visible mechanical integrity variations in P2-VP SPE films with various amounts of $LiBF_4$. Ratios are given in EO/Li^+.

4.1.6 Ionic Conductivity of PX-VP with Different Li-Conducting Salts

To determine which lithium conducting salt enables the highest ionic conductivity in PX-VP based solid polymer electrolytes, temperature-dependent conductivity measurements were performed on P2-VP films containing $LiBF_4$, $LiPF_6$, and LiTFSI (**Figure 8-12**). The SPE with $LiPF_6$ displays hereby the lowest overall ionic conductivity of $1.8 \cdot 10^{-6}$ S cm^{-1} at 25 °C, while a conductivity of $8.1 \cdot 10^{-6}$ S cm^{-1} and $3.1 \cdot 10^{-5}$ S cm^{-1} was achieved for LiTFSI and $LiBF_4$ respectively. The same trend is found at 85 °C. From the Arrhenius plot the activation energy for the ion hopping for Li^+ along the polymer chains was determined using equation 6. Consistent with the previous results the lowest activation energy was found for $LiBF_4$ with 0.47 eV while the SPE with $LiPF_6$ performed worst with an activation energy of 0.58 eV. All values for the ionic conductivity and activation energy are listed in **Table 4-2**. The low activation energy of lithium conduction in the SPE is the basis for the free movement of lithium ions.[266] Therefore, $LiBF_4$ is chosen as a conducting salt for all further electrochemical measurements.

Table 4-2: Ionic conductivities and activation energy for the ion hopping in P2-VP SPE foils.

Li-salt	$\sigma_{25\,°C}$ [S cm^{-1}]	$\sigma_{85\,°C}$ [S cm^{-1}]	E_A [eV]
$LiPF_6$	$1.8 \cdot 10^{-6}$	$1.4 \cdot 10^{-4}$	0.58
$LiBF_4$	$8.1 \cdot 10^{-5}$	$8.2 \cdot 10^{-4}$	0.47
LiTFSI	$3.1 \cdot 10^{-5}$	$5.0 \cdot 10^{-4}$	0.52

The results for the temperature dependent measurements of P2-VP are further compared to P1-VP SPE films with $LiBF_4$ (**Figure 4-13**). On average, at 20 °C a value of $1.5 \cdot 10^{-5}$ S cm^{-1}

is measured for P2-VP, while P1-VP reached $1.8 \cdot 10^{-6}$ S cm^{-1}. All measurements are conducted at least in triplicates.

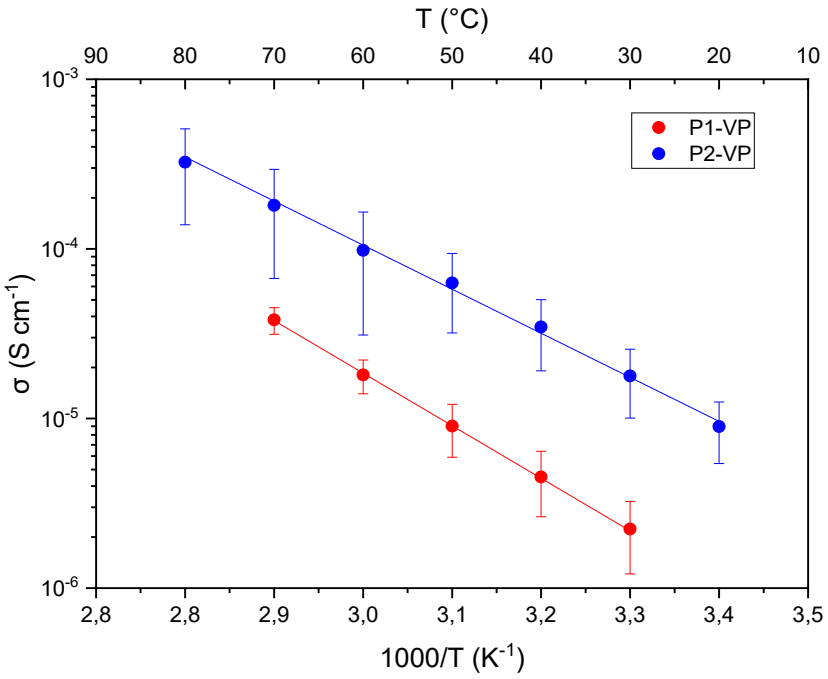

Figure 4-13: Temperature dependence of ionic conductivities of P1-VP and P2-VP with $LiBF_4$ (EO/Li^+ = 10/1).

The results correlate with the observed T_gs of the respective polymers, which indicate higher chain flexibility in P2-VP compared to P1-VP. The increased chain length of the ethylene oxide side chains consequently benefits the ion transport in the polymer.

The correlation between Tg and ionic conductivity is further evidenced by the observed decrease in ionic conductivity with increasing salt concentration, which, as shown in previous chapters, leads to a higher Tg. This increase in Tg reduces chain flexibility, thereby limiting ion mobility (**Figure 8-13**). The ionic conductivity is in good agreement proportional to the inverse of the absolute temperature and thus follows the Arrhenius model for polymers above the T_g.[111] Consequently, the activation energy of P1-VP and P2-VP is calculated to be 0.57 and 0.47 eV, respectively. This indicates a stronger coordination of the Li-ions to P1-VP, as it represents the basis for easy movement of Li-ions from one polymer chain to another.[266] The results for the ionic conductivities at 20 and 60 °C, as well as the activation energies, are summarized in **Table 4-3**.

Table 4-3. Mean ionic conductivities and activation energy for the ion hopping in P1-VP and P2-VP SPE foils. Literature values for solution casted PEO with $LiBF_4$ for comparison.

polymer	$\sigma_{20\,°C}$ [S cm^{-1}]	$\sigma_{60\,°C}$ [S cm^{-1}]	E_A [eV]
P1-VP	$1.8 \cdot 10^{-6}$	$1.8 \cdot 10^{-5}$	0.57
P2-VP	$1.5 \cdot 10^{-5}$	$8.2 \cdot 10^{-5}$	0.47
PEO[113,138,139]	10^{-7}-10^{-6}	$2 \cdot 10^{-6}$	0.78

4.1.7 Electrochemical Stability

For applications involving high-voltage cathodes, it is essential to evaluate the electrochemical stability window of the polymers, as it is directly linked to the safety of solid-state batteries.[267] Therefore, asymmetric Li cells with stainless steel (SS) current collectors (CC) are assembled (Li|SPE|SS) and the anodic stability of P1-VP and P2-VP is studied via linear sweep voltammetry (LSV) up to 6 V vs. Li^+/Li. As shown in **Figure 4-14**, both polymers show an onset for an oxidative current at 4.3 V vs. Li^+/Li. This is in accordance with the oxidation of the R-O-R units in the ether side chains, which in general limits the oxidative stability of PEO based solid polymer electrolytes.[133,268] As in this case, the ether units are present in the side chains of the polymers, oxidation of these units is hypothesized to not lead to the destruction of the polymer backbone, which in turn ensures the mechanical integrity of the polymer electrolyte. However, this hypothesis could not be proven as post-mortem analysis of the polymers was unsuccessful as the SPE foils could not be separated from the lithium foil after cell disassembly (**Figure 8-14**).

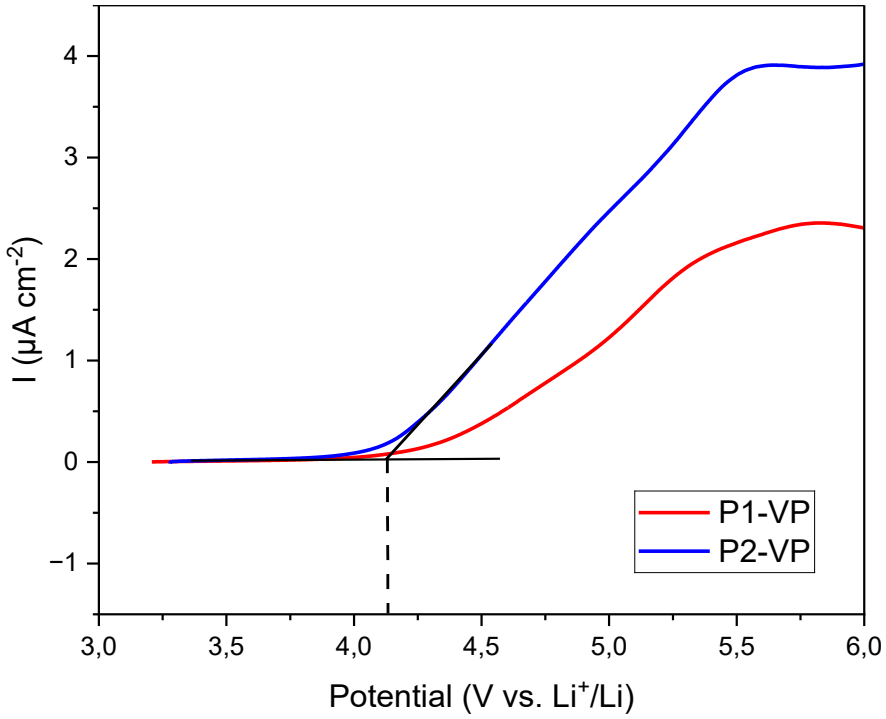

Figure 4-14. Linear sweep voltammetry measurements of P1-VP and P2-VP SPEs with $LiBF_4$ (EO/Li^+ = 10/1) in Li|SPE|SS coin cells at 60 °C from the OCV potential to 6 V vs. Li^+/Li with a scan rate of 0.5 mV s^{-1}.

In addition, the cathodic stability was investigated via cyclic voltammetry (CV) in the range of −1 to 3 V vs. Li^+/Li (**Figure 4-15**). For P2-VP, distinct currents associated with lithium plating and stripping are observed below and above 0 V vs. Li^+/Li, respectively. In contrast, P1-VP exhibits no distinct signals for lithium reduction or oxidation. This absence of redox activity may indicate that lithium-ion reduction at the working electrode is kinetically hindered by slow ion transport through the P1-VP matrix, resulting in a negligible cathodic current and insufficient lithium deposition for subsequent stripping. Notably, when the voltage is only scanned down to 0.2 V and thereby excluding lithium plating and stripping, additional current features appear in P2-VP, suggesting possible side reactions involving the ethylene oxide side chains around 1 V vs. Li^+/Li (**Figure 8-15**). However, due to the inherently slow kinetics in solid-state systems, a quantitative interpretation of the CV response remains challenging.

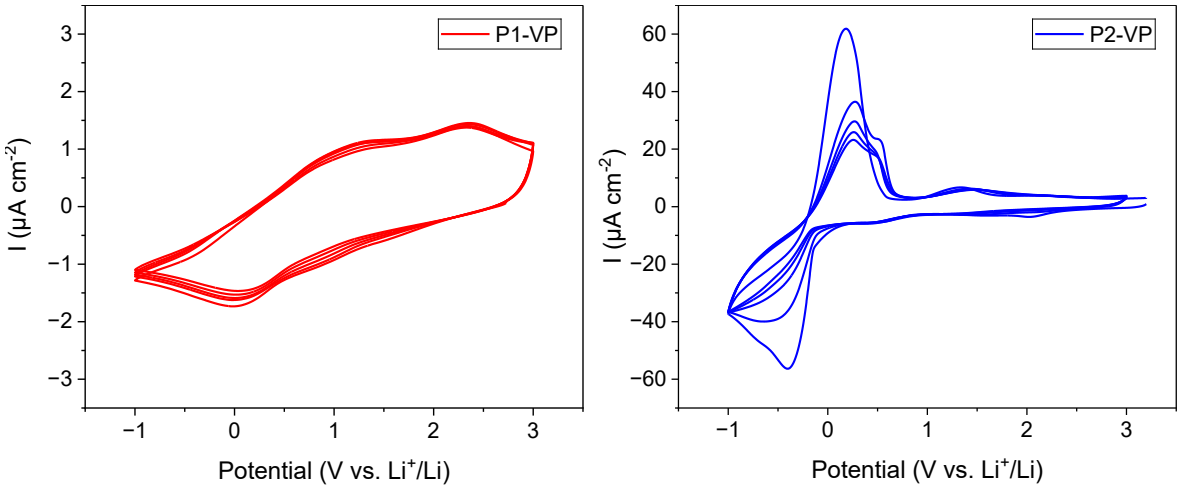

Figure 4-15: Cyclic voltammetry measurements of P1-VP and P2-VP SPEs with $LiBF_4$ (EO/Li^+ = 10/1) in Li|SPE|SS coin cells at 60 °C between −1 to 3 V vs. Li^+/Li with a scan rate of 0.5 mV s^{-1}.

4.1.8 Lithium Transference Number

The ion transport characteristics of the P1-VP and P2-VP electrolyte are further investigated by determining the Li^+ transference number (t_{Li^+}) via the Bruce-Vincent-Evans method in symmetric Li|SPE|Li cells.[269] **Figure 4-16A** and **B** display the chronoamperometry curves for a P1-VP and P2-VP SPE at 60 °C, respectively, while the insets show the Nyquist plots before and after the cell polarization. For P1-VP, t_{Li^+} only reaches 0.03 while t_{Li^+} for the P2-VP SPE is calculated to be 0.12. The exact values for the calculation are displayed in **Table 8-5**. The low t_{Li^+} for P1-VP is hypothesized to result from the strong coordination of Li-ions to the phosphonate units of the polymer, which may limit their mobility in the absence of other coordination sites. In P2-VP, the longer ethylene oxide side chains could provide additional coordination sites for Li-ions beyond the phosphonate groups, leading to an increased t_{Li^+}. The transference number in P2-VP is still lower compared to other phosphonate based polymer electrolytes (0.28[144], 0.37[270], 0.7[146]), which however feature a higher ratio of additional functional groups and therefore coordinating sites or add solvent to form a gel polymer electrolyte.

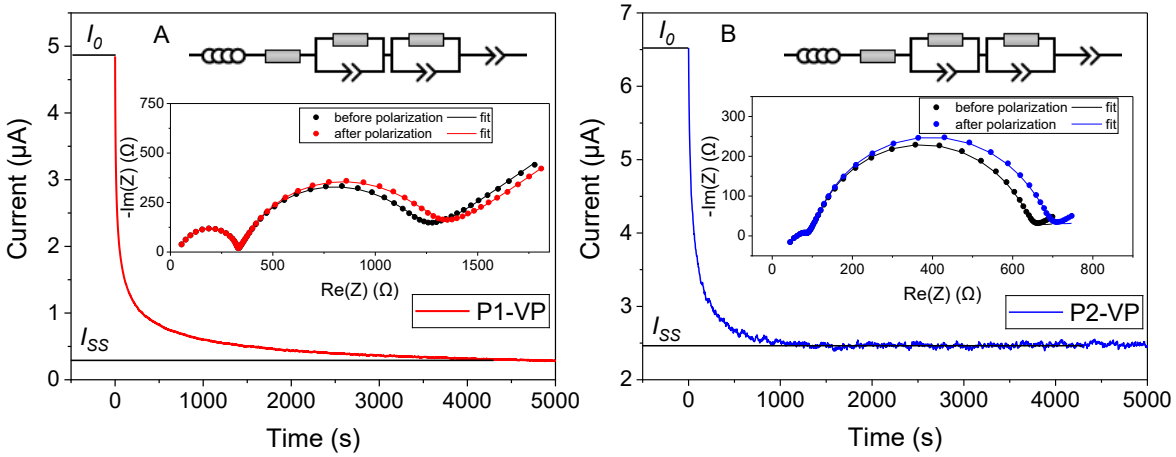

Figure 4-16. The chronoamperometry profile (ΔV = 10 mV) of symmetric Li|SPE|Li cells of **A** P1-VP and **B** P2-VP SPEs with $LiBF_4$ (EO/Li^+ = 10/1), and the impedance before and after the polarization in steady-state current conditions (insert). Equivalent circuits for fitting the impedance data are displayed above the Nyquist plots.

4.1.9 CCD and Li-shuttle Measurements

As the Li^+ transference number strongly influences the polarization of a battery cell during cycling, the critical current density was assessed for both electrolytes in symmetric Li|SPE|Li cells at 60 °C, with gradually increasing current densities from 1 to 50 µA cm^{-2}. As seen in **Figure 4-17A**, the potential profile for P1-VP starts to develop a potential polarization at a current density of 5 µA cm^{-2} and drastically increases to the cut-off potential of 4 V at a current density of 10 µA cm^{-2}. For P2-VP in **Figure 4-17B**, the increase in the overpotential appears when raising the current density above 10 µA cm^{-2}. Consequently, the CCD for these polymers is not reached by short-circuiting due to inhomogeneous lithium platting and stripping at high current densities, but due to the polarization buildup in the polymer electrolyte, which is a consequence from their low t_{Li^+}.

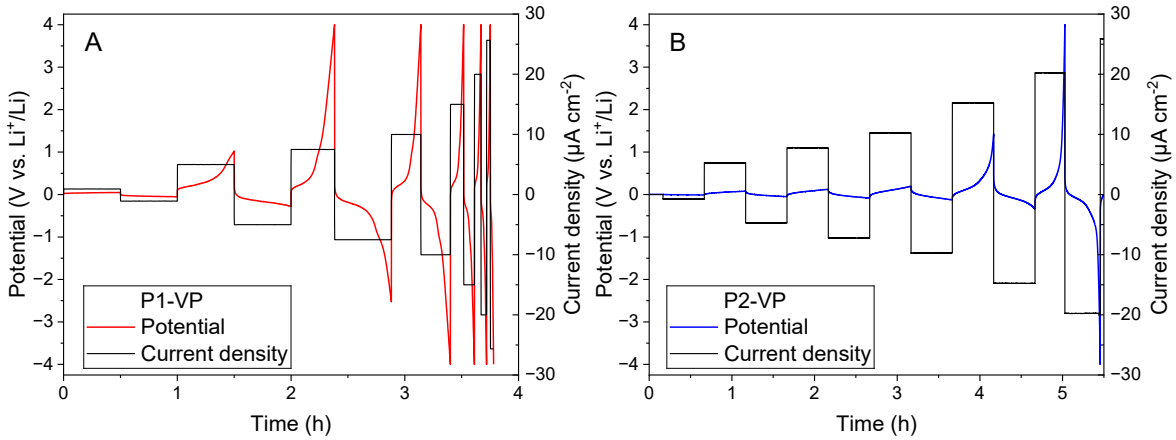

Figure 4-17. Electrochemical performances of Li plating/stripping test in Li|SPE|Li coin cell with a P1-VP (**A**) and P2-VP (**B**) + $LiBF_4$ SPE film (EO/Li^+ = 10/1). CCD tests with step-increasing current densities and resulting potential response at 60 °C.

Interface compatibility is another crucial factor influencing the performance of lithium metal batteries, significantly impacting both cycle life and rate capability.[63,271,272] To study the performance of the electrolyte/lithium interface, long term lithium plating/stripping experiments are conducted with current densities of 5 and 10 µA cm^{-2} for P1-VP and P2-VP, respectively. The galvanostatic cycling profiles of both SPEs in symmetrical Li|SPE|Li coin cells are displayed in **Figure 4-18**, with a positive potential marking lithium stripping and a negative potential marking lithium plating. For both polymers, the voltage profile is stable for over 250 h. While for P2-VP, the voltage profile flattens at an overpotential of around 80 mV, P1-VP displays a continuous rise in polarization up to 200 mV during the plating/striping process of 30 min. This again indicates an increased resistance caused by polarization as a consequence of the low t_{Li^+}. Commonly, a current density of >3 mA cm^{-2} is considered a prerequisite for the long-term cycling of solid-state batteries without shorting to ensure sufficient charging and discharging capability. However, this is rarely achieved in solid electrolytes and is highly dependent on factors such as cell chemistry, temperature, stack pressure, and plating capacity.[91,229,273]

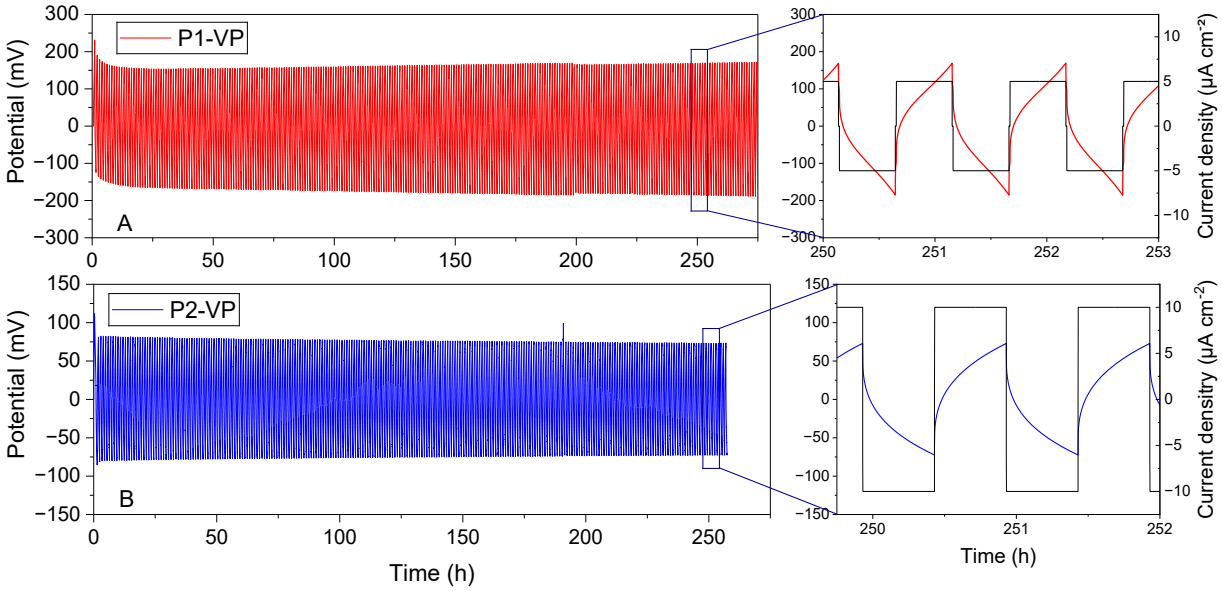

Figure 4-18. Galvanostatic cycling of Li|SPE|Li coin cells with **A** P1-VP and **B** P2-VP SPEs with $LiBF_4$ (EO/Li^+ = 10/1) at 60 °C (30 min per plating/stripping process, 5 and 10 µA cm^{-2}, respectively).

4.1.10 Cathode Preparation and Analysis

Cathodes for half cell testing were prepared via the doctor blade method. Optimization of cathode slurry composition was essential to achieve homogeneous films and good performance in half cell tests. Initially, a polymer electrolyte solution comprising PEO, PVDF, and LiTFSI was dissolved in 2 mL NMP at 60 °C under stirring for several hours. This preliminary dissolution step was critical since adequate polymer dissolution could not be attained in the planetary mixer alone. Following complete polymer dissolution, conductive carbon (C65) was added and dispersed for 5 min at 1500 rpm using a planetary centrifugal mixer. Insufficient mixing duration or lower rotational speeds led to inadequate dispersion of C65. Subsequently, the active material (NMC or LFP) was incorporated through an additional 10 min mixing step at 1500 rpm. The optimal total solid content (TSC) for achieving medium viscosity slurries suitable for casting at 33 mm s^{-1} was determined to be 25%, corresponding to 4 mL of NMP. Reduced solvent quantities resulted in higher viscosity slurries that could not be efficiently transferred from the mixing vial onto the aluminum foil substrate. For instance, increasing the TSC to 28.5% (3.5 mL NMP) already resulted in uneven slurry distribution, causing inhomogeneous cathode coatings. Besides solvent content, the ratio of PEO to PVDF significantly influenced slurry viscosity. Higher PEO content generally lowered viscosity, whereas increased PVDF content raised viscosity slurry, but also required

the use of NMP as a solvent. Attempts were initially made to exclusively use PEO with MeCN to avoid NMP due to its toxicity, high boiling point, and prolonged drying time. However, coatings produced using only MeCN exhibited increased porosity due to rapid solvent evaporation. High PEO content also compromised adhesion of the dried coating to the aluminum foil during the subsequent pressing step. The same problem arose when using P2-VP instead of PEO as the catholyte. Initial compression tests at 250 MPa with either predominantly PEO (M_w = 300 kg mol^{-1}) or PVDF (M_w = 275 kg mol^{-1}) resulted in adhesion to the stainless steel die, destroying the cathodes. Using a Teflon foil interlayer between cathode and die failed to solve this issue. To enhance the cohesion within the cathode film and improve adhesion to the aluminum substrate, a high molecular weight PVDF designed for battery applications (Solef® 5130, M_w = 1.000–1.100 kg mol^{-1}) was employed. Adjusting the PEO/PVDF ratio to 65/35 achieved a balance between ionic and electronic conductivity and mechanical stability. The different cathodes and their adhesion to the Al-foil are displayed in **Figure 4-19**.

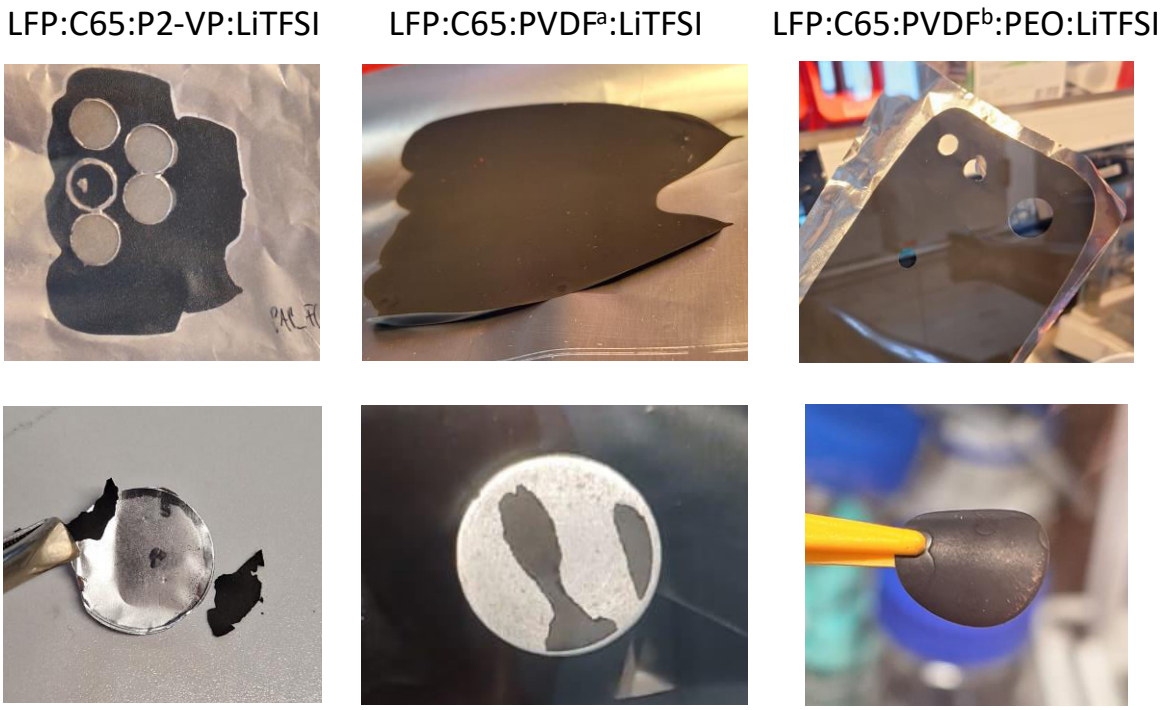

Figure 4-19: LFP cathodes with different catholytes and binders and the corresponding adhesion to the Al-foil. [a] PVDF (M_w = 275 kg mol^{-1}), [b] Solef® 5130 PVDF.

Following slurry preparation, cathodes were doctor bladed onto 20 µm thick aluminum foil at velocities of 33 mm s^{-1} using gaps ranging from 200 to 600 µm. Cathodes were subsequently dried in a glove box for several days, followed by vacuum drying in the GB

antechamber. SEM analysis of dried cathodes revealed crack formation (**Figure 4-20**), necessitating subsequent pressing to reduce porosity and enhance contacts between the particles and the matrix for improved electronic and ionic conductivity.

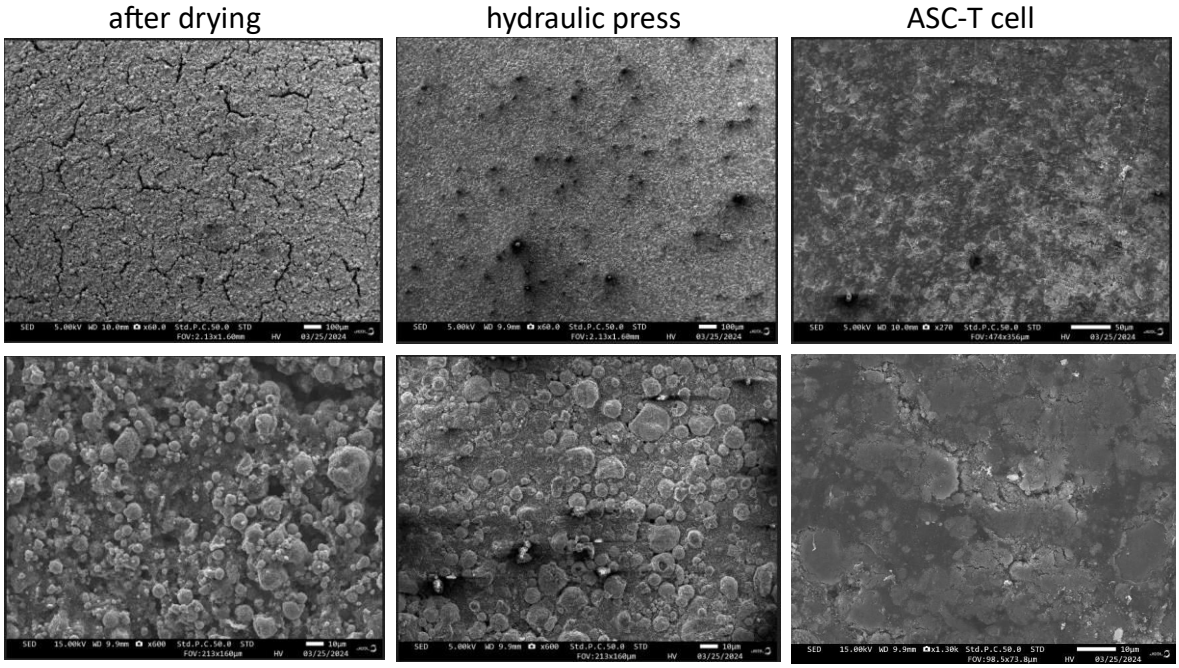

Figure 4-20: SEM images of LFP cathodes with visible cracks and increased porosity after solvent evaporation, with more homogeneous surface and decreased porosity after drying, and collapsed LFP particles after pressing at 250 MPa for 5 min. EDX images for the cathodes pressed in the ASC-T cell are displayed in **Figure 8-16**.

Various pressing conditions were evaluated using a hydraulic press and an ASC-T cell from Sphere Energy, with pressures ranging from 100 to 1000 MPa and durations from 1 to 5 min. Hydraulic pressing showed no further reduction in porosity above 250 MPa. In contrast, cathodes compressed using the ASC-T cell exhibited visibly shiny surfaces at pressures at 200 MPa. Comparative SEM imaging of LFP cathodes pressed in both setups indicated intact LFP particles after hydraulic pressing, whereas cathodes compressed in the ASC-T cell demonstrated significant particle collapse, presumably due to uneven pressure distribution from the cell pistons. Consequently, cathodes processed with the ASC-T cell were unsuitable for practical applications. Ultimately, a pressing protocol of 250 MPa for 2 min was adopted, resulting in LFP cathode films with final thicknesses ranging from 20 to 50 µm and area loadings between 1 and 10 mg cm^{-2} (equivalent to 0.15–1.5 mAh cm^{-2}, assuming a specific capacity of 150 mAh g^{-1} for LFP).

To further analyse the prepared cathodes, the porosity was calculated according to equation 16.[166] Utilizing bulk density values for the individual components (**Table 6-1**), the

calculated porosity ranged from 10 to 30%, with considerable variation observed within the same cathode sheet after punching and pressing. Generally, cathodes exhibiting lower porosity performed better in subsequent electrochemical tests.

For detailed assessment of the bulk morphology, cathode samples were cut in half and prepared for SEM via a cross-section polisher. **Figure 4-21** displays a cross-sectional SEM image showing the cathode layer on top of the Al-foil current collector. LFP particles exhibit a size distribution ranging approximately from 5 to 20 µm in diameter, with the largest particles closely matching the thickness of the cathode film. The particles are densely packed, typically separated by less than 1 µm, indicating good particle-to-particle connectivity. However, noticeable detachment of the cathode film from the Al-foil is observed at several locations, suggesting that the PDVF binder quantity employed might be insufficient. However, it is uncertain whether this detachment was caused by sample preparation during cutting and polishing. On the bottom of the Al-foil droplets are visible which are caused by melting of the Al current collector and Cu foil (used to attach the sample in the cross-section polisher).

A comparative SEM analysis of a half-cell sample featuring a lithium metal anode, which was prepared by cutting with a scalpel (**Figure 8-17**), did not show similar detachment. This sample could not be polished due to concerns about contamination from lithium evaporation. Additionally, a distinct bright line is visible between the cathode and Al current collector. EDX spectroscopy analysis shows the presence of Fe within this interface, indicating potential alloy formation between Fe (from LFP) and Al (**Figure 8-18**). Since LFP is known for its thermal stability and negligible reactivity with aluminum under standard conditions, this phenomenon might also be introduced by the polishing process. Similar observations of bright interfaces between LFP cathodes and aluminum current collectors have been reported in literature, particularly in aged electrode samples.[245]

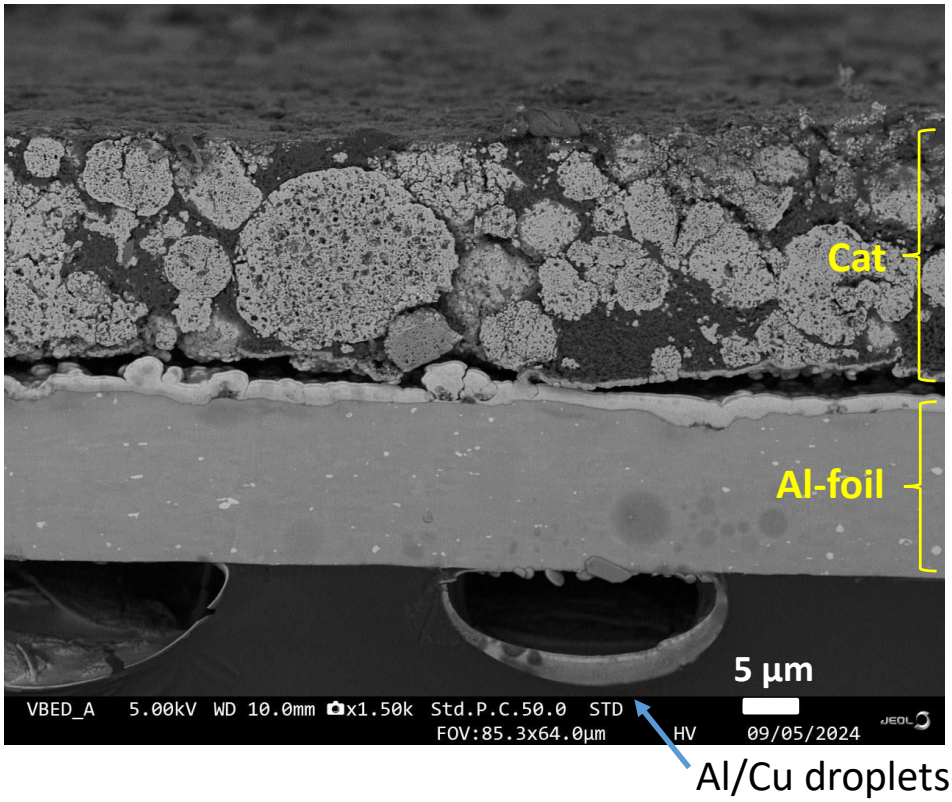

Figure 4-21: Cross-section SEM image of a polished LFP cathode.

While initially both LFP and NMC were used for the preparation of cathodes, due to time and resource restrictions only LFP cathodes were optimized. Preliminary comparisons suggested no significant performance differences between cathodes prepared from NMC and LFP using the optimized LFP protocol, apart from higher areal capacities for NMC due to its greater specific capacity (180 mAh g^{-1}).

To investigate the electrochemical properties of the produced cathodes, both electronic and ionic resistances were measured. The temperature and pressure-dependent electronic conductivity (σ_{el}) was assessed using chronoamperometry on a stacked configuration of two cathode disks (Al-Cat-Cat-Al) to eliminate interference from asymmetry. An exemplary measurement is displayed in **Figure 8-19**. The results are displayed in **Figure 4-22**. At 25 °C and an applied pressure of 5 MPa, the cathodes exhibited the lowest electronic conductivity of approximately 10 mS cm^{-1}. This value increased to 40 mS cm^{-1} with higher applied pressure, attributed to greater compression, reduced porosity, and enhanced particle contact, particularly of the carbon additive. Raising the temperature to 60 °C did not result in a significant change in electronic conductivity. Although most cathode materials are semiconductors, and their electronic conductivity typically increases with temperature, the

major contribution in this case comes from the conductive carbon additive. Hereby, the electronic conductivity remains largely unchanged or may slightly decrease with increasing temperature.[274,275]

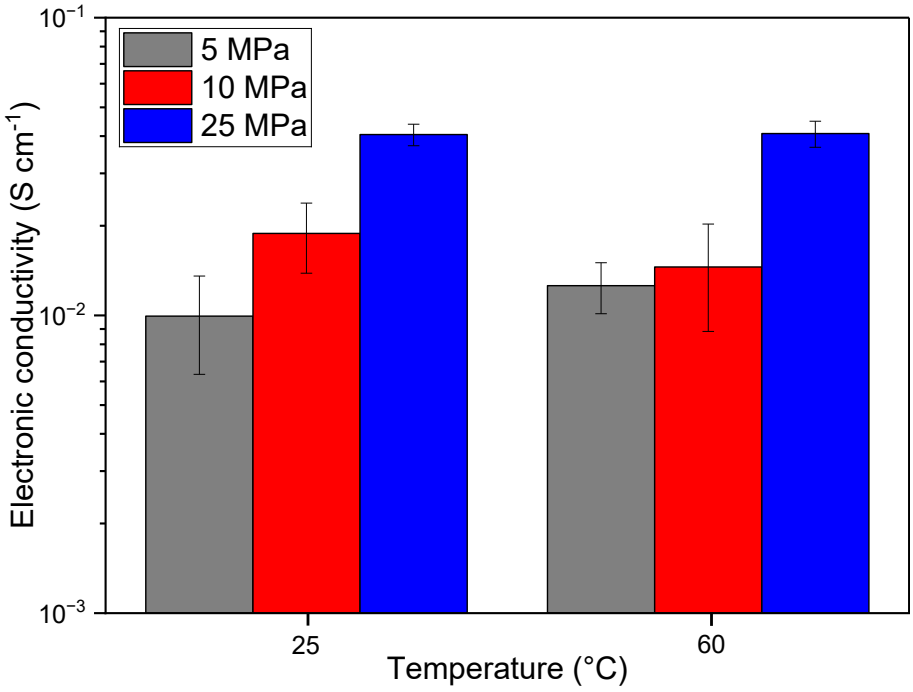

Figure 4-22: Pressure and temperature dependent electronic conductivity of LFP cathodes.

To measure the ionic resistance of the cathodes, two cathode discs were stacked in the ASC-T cell and separated by a PEO SPE film in an Al-Cat-SPE-Cat-Al configuration. The SPE film was essential to isolate the ionic transport contribution, as excluding it would result in short-circuiting due to the significantly higher electronic conductivity of the cathodes, as confirmed in previous measurements. Consequently, impedance spectroscopy was performed across various temperatures and pressures and the resulting spectra were fitted using a transmission line model, according to similar work by Landesfeind et al., allowing determination of the ionic resistance of the cathode.[244,276] Parameter values and ionic resistance data for two representative samples are listed in **Table 4-4**. As expected, ionic resistance decreased with increasing temperature and pressure. This behaviour is attributed to reduced porosity, improved mechanical contact, and enhanced ion mobility due to thermally activated charge transport.

Table 4-4: Cell parameters for the impedance measurements of cathodes in an LFP|PEO|LFP stack to determine the ionic resistance (R_{ion}) in the cathode. The initial thickness of the cathode and PEO SPE film before cell assembly is given.

Cathode sample	δ_0(Cat) [µm]	δ_0(SPE) [µm]	Temperature [°C]	Pressure [MPa]	R_{ion} [Ω]
1	22	44	25	5	1250
			60	5	156
			60	25	50.6
2	34	118	25	5	1938
			60	5	107.6
			60	50	14.24

Notably, at 5 MPa, the impedance spectra exhibit a characteristic straight line at low frequencies, indicative of ionic blocking conditions. However, this feature disappears when the applied pressure is increased to 25 MPa (**Figure 4-23**). In a subsequent experiment, the thickness of the PEO film was increased from 44 to 118 µm. Under these conditions, the blocking feature persisted until a pressure of 50 MPa (**Figure 8-20**).

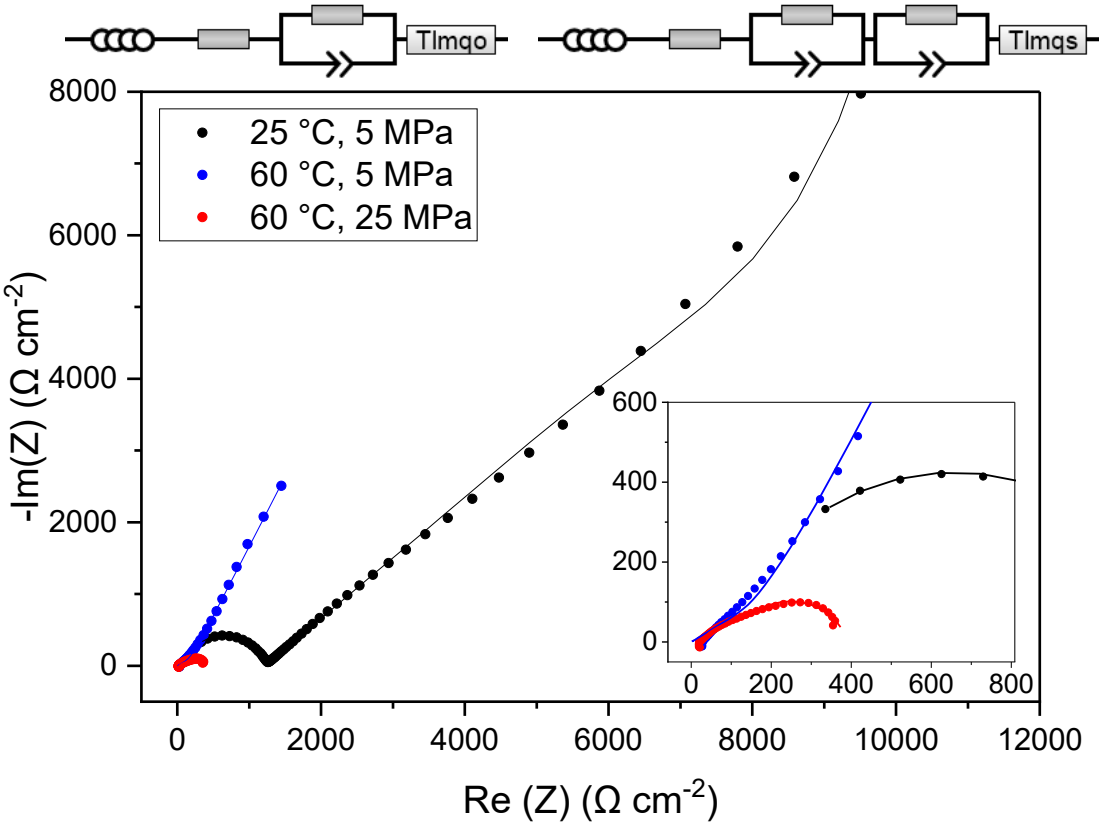

Figure 4-23: Impedance spectra of an LFP|PEO|LFP stack in the ASC-T cell at various temperatures and pressures with respective fits. The equivalent circuit for blocking features uses at 5 MPa use a TLMqo (top left) transmission line model in the Relaxis software (black and blue curve). The non-blocking feature in the red curve is fitted with a TLMqs (rop right).

Upon maintaining pressure for approximately one hour, short-circuit behaviour appeared in the impedance spectra. These observations suggest that at elevated temperatures and pressures, the mechanical integrity of the PEO film becomes insufficient to prevent contact between the cathode discs. This leads to the formation of unintended electronic pathways, thereby eliminating the ionic blocking conditions. Consequently, the transmission line model used for fitting the impedance data had to be adjusted to account for the loss of blocking behaviour in these cases.

4.1.11 Half Cells Testing

To further validate these findings, half-cells with LFP cathodes and lithium metal anodes were assembled. The electrochemical performance of the cathodes was first evaluated using a standard PEO-CPE at 60 °C and a CCCV protocol. The corresponding charge-discharge profiles are shown in **Figure 4-24**. At C/10, a discharge capacity of 137 mAh g^{-1} was measured, which is in good agreement with the specified value of 151 mAh g^{-1} provided by the supplier. At C/3, the capacity decreased slightly to 124 mAh g^{-1}. However, a pronounced capacity loss was observed at 1C, yielding only 83 mAh g^{-1}. This drop is attributed to an increasing internal resistance by polarization and mass transport limitations at higher current densities.[277]

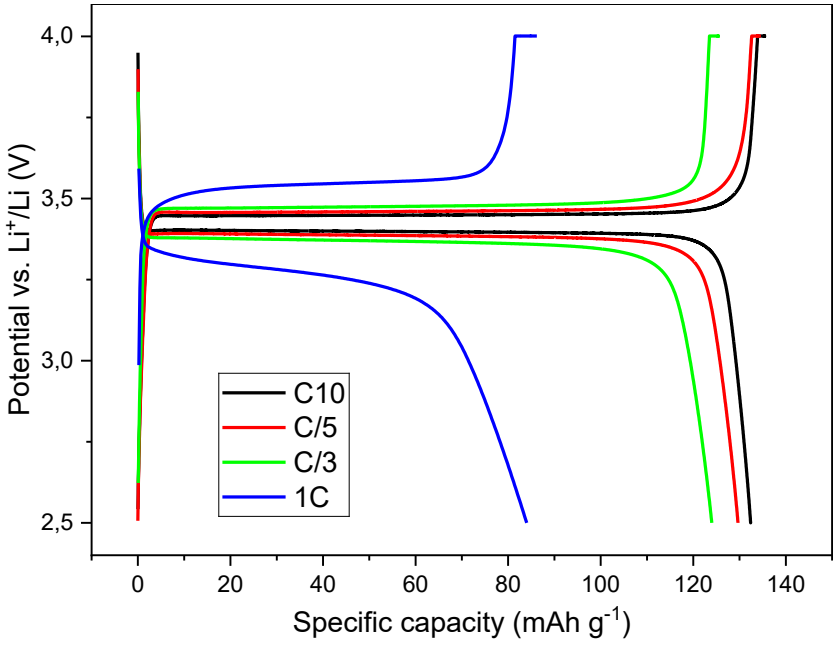

Figure 4-24: Charge-discharge profiles of LFP|PEO|Li half cell at various C-rates at 60 °C (PEO-CPE composition EO/SN/$LiBF_4$ = 36/8/1 with 10 wt% SiO_2).

These effects are also reflected in the decreasing coulombic efficiency during extended cycling (**Figure 4-25**). While the efficiency remained consistently above 95% at C/10, it progressively declined at higher C-rates, which can be attributed to increased SEI and CEI formation due to electrolyte decomposition.

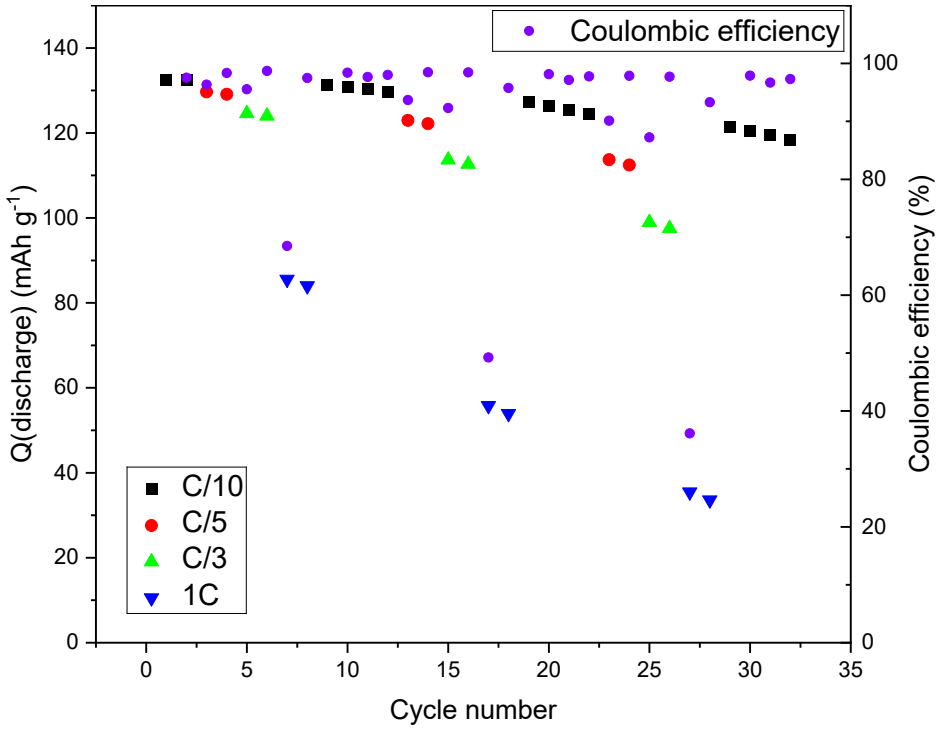

Figure 4-25: Cycling and rate performance of of LFP|PEO|Li half cells at 60 °C

The degradation of the electrolyte is further confirmed by impedance spectroscopy, showing an increase in total cell impedance from ~10 Ω cm^{-2} before cycling to ~50 Ω cm^{-2} after cycling (**Figure 8-21**). Despite these effects, the results demonstrate that the cathodes are well-suited for application in cell tests.

The half cells with PX-VP SPE separators were cycled with a constant current of 5 µA cm^{-2} and 10 µA cm^{-2} for P1-VP and P2-VP, respectively (**Figure 4-26**). The P1-VP cells exhibited a low specific capacity of approximately 2 mAh g^{-1}, whereas the P2-VP cells achieved up to 10 mAh g^{-1}. Notably, for P2-VP, most of the capacity increase during charging occurred during the constant voltage phase. For both electrolytes, the polarization overpotential caused by the low t_{Li^+} was evident, as reflected in the continuously increasing cell potential during charging. This behavior contrasts with the typical charging profile of LFP, which generally displays a plateau at approximately 3.4 V vs. Li$^+$/Li. The corresponding EIS measurements for both cells are displayed in **Figure 8-22** and **Figure 8-23**, respectively. An increase in SEI

and CEI interfacial resistance is observed, analogous to the behaviour in half-cells with PEO, indicating that both SPEs undergo degradation and form interphases with the electrodes under the applied cycling conditions. In contrast, the bulk resistance of the electrolyte remains unchanged. These results show that, the low t_{Li^+} of the polyvinylphosphonate electrolytes is detrimental to their performance as solid polymer electrolytes in ASSBs.

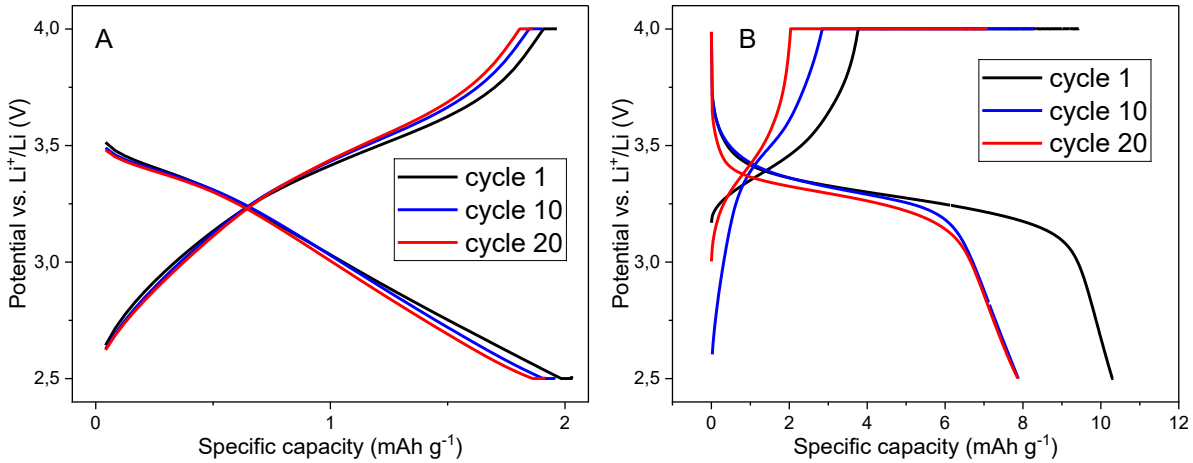

Figure 4-26: Charge-discharge profiles of half cells LFP|SPE|Li at 60 °C with **A** P1-VP and **B** P2-VP SPEs with $LiBF_4$ (EO/Li^+ = 10/1). A CCCV protocol was applied with a constant current of 5 and 10 µA cm^{-2}, respectively

4.2 Polymer-Oxide Hybrid Batteries

In the following chapters, the volume and pressure changes during cycling of solid-state batteries are investigated, with a focus on hybrid polymer-oxide systems. The aim is to understand the breathing behaviour of these batteries and evaluate whether the use of soft polymer electrolyte interlayers can mitigate mechanical stress caused by volume changes. Since the lithium transference number of the in the previous chapters investigated PX-VP SPEs was found to be insufficient for the application in battery cells, a more suitable polymer electrolyte system was needed. Therefore, PEO was chosen as the polymer electrolyte and LLZO was used as the ceramic component. This project was conducted in collaboration with Steffen Weinmann from the group of Prof. Jennifer Rupp, who synthesized the LLZO and prepared the oxide solid electrolyte pellets.

4.2.1 The ASC-T Measuring Cell Setup

One issue already encountered during the measurements with PX-VP SPEs is the uncertainty in determining the actual film thickness within the cell. Typically, the thickness can only be measured either prior to cell assembly or after disassembly. Both approaches are prone to error for subsequent calculations, as the polymer electrolyte film is compressed under applied pressure during assembly, while during disassembling coin cells require significant force to separate the cell components, which may further compress the film and result in inaccurate post-measurement thickness values.

To obtain accurate thickness measurements under operating conditions, an in-situ approach is required. This is enabled by the ASC-T test cell from Sphere Energy, which allows real-time thickness and pressure monitoring. The setup is shown in **Figure 4-27**, configured in the “constant pressure” mode, which allows vertical displacement of the upper piston in response to expansion or contraction of the cell stack. To enable pressure-sensitive measurements, the “spring cell top” can be replaced with a rigid spacer to fix the gap between the screw and the piston. In this configuration, any expansion of the cell stack results in a measurable force on the pressure sensor (beige platform in **Figure 4-27**) positioned beneath the cell in the pressure frame.

Figure 4-27: ASC-T cell in a constant pressure setup for monitoring thickness (and pressure) during electrochemical measurements. The thickness is measured by a sensor positioned on a platform, which is connected to a spacer between the top cell piston and the spring/screw to apply a specific pressure.

Initial testing revealed that the deformation sensor does not exclusively capture the compression of the sample inside the cell but also the elastic deformation of the cell housing itself under applied pressure. This complicates the accurate determination of the sample thickness during measurement. To quantify the inherent deformation of the empty cell, measurements were performed without any sample. The cell was incrementally compressed, and the resulting deformation plotted against the applied pressure (**Figure 4-28A**). The curves do not start at 0 µm, as a minimum preload is required to align the cell components. At low pressures, a steep increase in deformation is observed, which gradually flattens around 5 MPa. This behaviour is attributed to the initial compression of softer components, such as the PEI housing, followed by minor deformation of more rigid parts such as the stainless steel current collectors.

Repeated measurements of the empty cell showed slight variation in displacement at a given pressure, making it difficult to define a reproducible calibration baseline. This limitation becomes evident when comparing the deformation of the empty cell to that of a cell containing a PEO-based SPE (**Figure 4-28B**). Due to sensitivity to the initial alignment of the cell components, the absolute thickness of the sample stack cannot be reliably determined from these measurements. This is particularly problematic in the low-pressure regime

below 5 MPa, where small changes in pressure result in disproportionately large changes in deformation due to the flexibility of the cell housing.

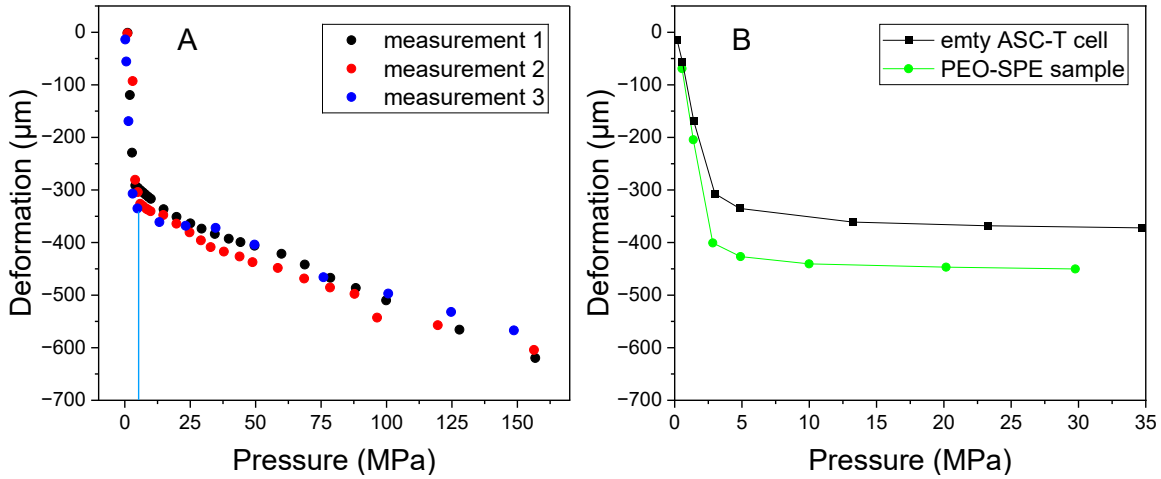

Figure 4-28: Deformation vs. applied pressure measurements of **A** the empty ASC-T cell in the constant gap setup and **B** comparison of the empty cell to PEO SPE samples.

At each applied pressure point an EIS measurement was performed with the PEO-SPE film. The resulting Nyquist plots are shown in **Figure 4-29**. It is visible that the diameter of the semicircle, corresponding to the bulk impedance of the film, decreases with increasing pressure, becoming nearly constant above 5 MPa. This behaviour is consistent with the observed flattening in the deformation measurements above 5 MPa. However, while the bulk resistance decreases by approximately one third, the measured deformation difference between the empty cell and the setup containing the PEO-SPE is between 80 and 100 µm and therefore exceeding the initial film thickness of 62 µm. This discrepancy shows that the in-situ thickness measurement does not reliably reflect the actual compression of soft membranes. The measured deformation is largely influenced by elastic deformation of the cell housing and alignment effects within the cell stack, making it unsuitable for accurate thickness determination of soft polymer electrolyte films.

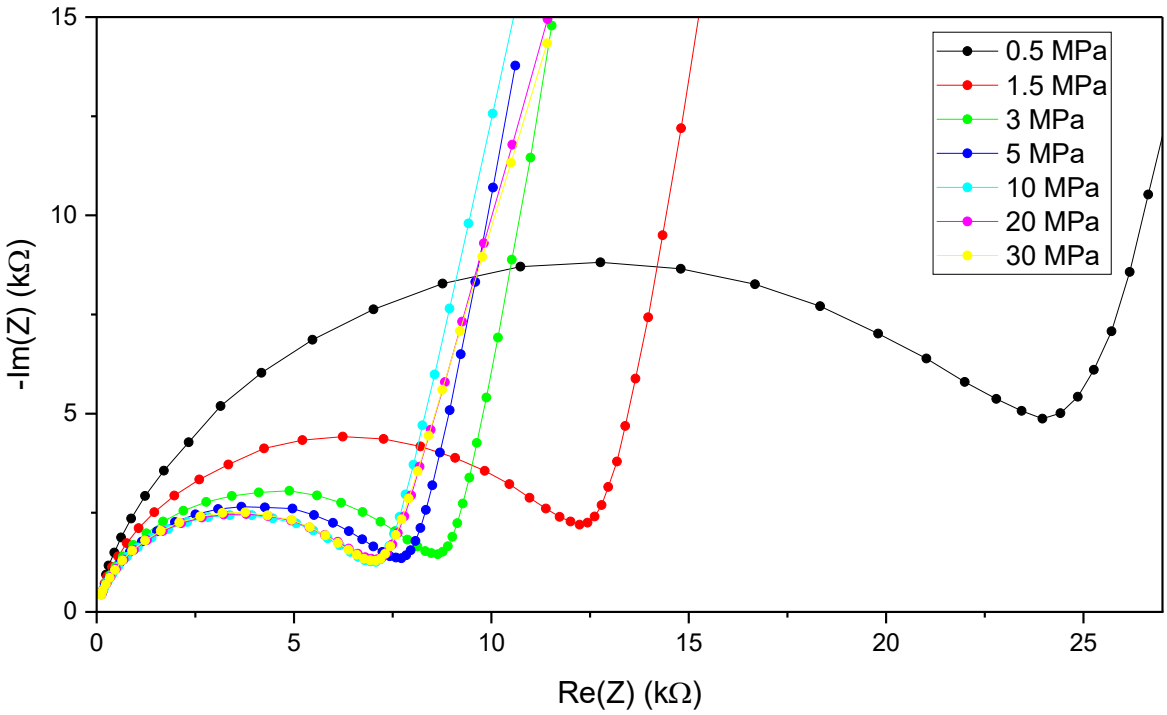

Figure 4-29: Impedance evolution of a PEO-SPE film with increasing applied pressure in the ASC-T cell setup.

After disassembly, the compressed PEO film exhibited a distinct indentation (**Figure 8-25**), suggesting that the applied pressure was not uniformly distributed across the membrane area. To assess the pressure distribution, pressure-sensitive foils (Fujifilm, Japan) were used with all three available CC pistons. The results are summarized in **Table 4-5**. In all cases, the pressure distribution was found to be highly inhomogeneous. Contact was limited to localized regions where the current collectors pressed directly against each other, with no uniform pressure applied over the entire CC area. Such non-uniform or irreproducible pressure distributions are also known issues in conventional coin cell setups.[278] In the present case, they cannot be fully avoided and may consequently introduce additional variability in the cell measurements. These results further indicate that the test cell is only partially suitable for accurate evaluation of soft SPE membranes.

Table 4-5: Results of the pressure tests with pressure foils at different pressures and current collector combinations.

CC combination	3 MPa	4 MPa	5 MPa	10 MPa
I + II				
I + III				
II + III	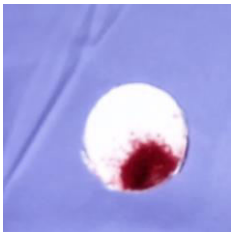	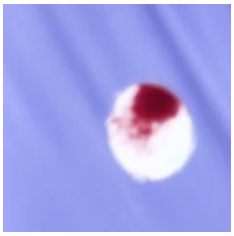		

While initial experiments demonstrated that the ASC-T cell is not ideally suited for the investigation of batteries employing soft SPEs, the potential of the setup for systems with hard SEs was further evaluated. For this purpose, a solid-state battery configuration previously studied at TUMint Energy Research GmbH was assembled, with a NMC cathode, a LPSCl electrolyte, and an indium-lithium alloy anode. Upon alloying with lithium, indium exhibits a volume expansion of up to 105%, which is lower than that of pure lithium metal.[279] However, the indium–lithium alloy is expected to be more stable in contact with sulfide-based SEs due to its higher electrochemical potential. The alloy exhibits a flat potential plateau at 0.62 V vs. Li^+/Li across a broad compositional range, which provides a stable and well-defined reference potential.

Prior to assembly, the cathode was pressed at 200 MPa for 5 min using a hydraulic press. The initial stack pressure was set to 100 MPa and decreased to approximately 90 MPa during a 2 h equilibration period in the constant gap configuration. The cell was cycled at C/10 for 16 cycles, followed by 12 cycles at C/3, and subsequently at 1C. During the initial C/10

cycling (constant current of 0.13 mA), a clear correlation between pressure and cell voltage was observed, as shown in **Figure 4-30**. During charging, lithium ions are alloyed with the indium anode, leading to volumetric expansion of the anode and thus an increase in pressure within the stack. Despite using the constant gap configuration, a small positive deformation was recorded, correlating with the increase in pressure and cell potential (**Figure 8-26**). At maximum, a thickness change of approximately 7 µm was measured between the charged and discharged states.

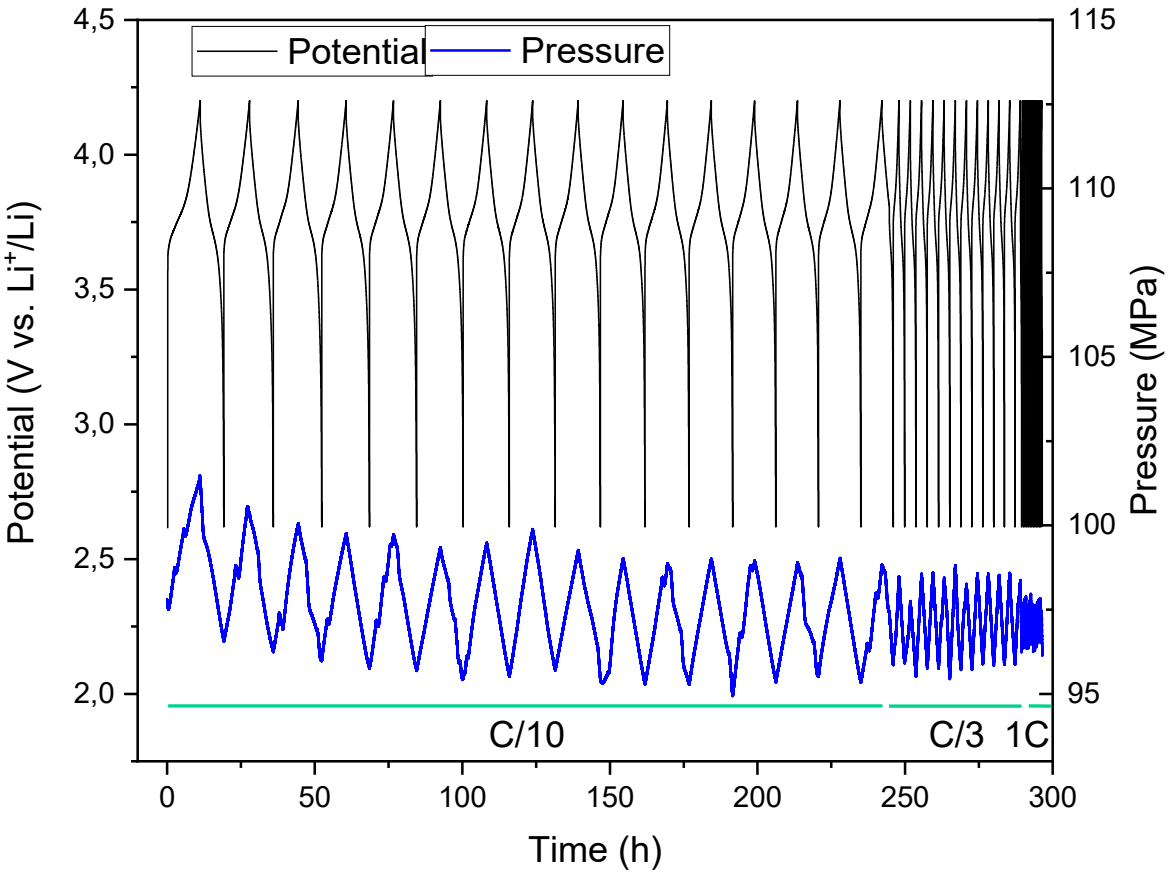

Figure 4-30: Cycling profile of an NMC|LPSCl|InLi test cell with corresponding pressure to validate the measurement in the ASC-T cell at elevated pressures. The cell was in the constant gap setup.

In the corresponding cycle, 1.05 mAh of lithium was inserted into the indium anode, corresponding to a composition of approximately $Li_{0.244}In$. Assuming constant volume for the cathode and solid electrolyte, and using the densities of pure indium (ρ_{In} = 7.31 g cm^{-3}) and the Li-In alloy (ρ_{InLi} = 5.11 g cm^{-3}),[280] the theoretical thickness increase of the indium layer (d = 8 mm, h = 50 µm) is calculated to be approximately 6.2 µm. The measured value aligns well with this estimation. It is further noted that both the pressure and displacement signals exhibit similar irregularities, which are unlikely to originate from electrochemical

effects. Rather, they are attributed to minor mechanical shifts within the ASC-T cell components during cycling.

The same correlation between cell pressure and cycling behaviour was observed at higher charge/discharge rates (**Figure 8-27**). However, the magnitude of the pressure change was reduced at higher C-rates, which aligns with a decrease in capacity and therefore coulombic efficiency. These results confirm that the ASC-T cell setup performs well for systems with hard SEs and high applied pressures but is limited in its ability to accurately measure pressure distribution and deformation in systems employing soft SEs at pressures below 10 MPa.

4.2.2 PEO Film Production

Firstly, due to the high crystallinity of PEO, modifications were required to achieve sufficient ionic conductivity. Therefore, succinonitrile (SN) was added as a plasticizer to reduce crystallinity and enhance chain mobility, as reported in literature.[281] In addition, to benefit from the improved mechanical and electrochemical properties of CPEs, different inorganic fillers were tested as additives. PEO-based SPE and CPE membranes were prepared either via solution casting, yielding films with a thickness of approximately 100 µm, or by doctor blading, producing films with a thickness below 50 µm. Thin SPE films were not feasible by solution casting as lowering the polymer concentration in the casting solution resulted in the PTFE dish being only partially covered after solvent evaporation. The PEO films tended to form small thick pools, rather than homogeneous films. On the other hand, reducing the solvent volume resulted in the PTFE dish not being fully covered from the beginning due to the poor wetting of the PTFE with MeCN.

Initial optimization focused on SPEs based on PEO, LiTFSI, and SN. Several mixing procedures and solvent systems were tested, as simple stirring of the components in MeCN frequently resulted in incomplete dissolution. The most effective method involved dry stirring of PEO and LiTFSI, followed by the gradual addition of MeCN containing dissolved SN. Other approaches, such as stirring at 60 °C or replacing MeCN with THF, DSMO or DMF resulted either in gelation, incomplete dissolution or slow evaporation. The obtained SPE membranes exhibited low mechanical stability and high surface stickiness, complicating handling and processing. To improve the mechanical integrity, ceramic fillers were

incorporated to prepare CPEs. LLZO was investigated as an active filler, while Al_2O_3 and SiO_2 were employed as passive fillers. The fillers were added to the polymer solution and dispersed using a planetary mixer to ensure homogeneity and deagglomeration. A mixing speed of 1500 rpm for two cycles of 2.5 min each yielded optimal results. Longer mixing durations led to pressure build-up due to solvent evaporation, and occasionally causing lid rupture, whereas shorter mixing times resulted in insufficient dispersion.

CPEs containing SiO_2 and Al_2O_3 exhibited improved film stability and reduced stickiness. In contrast, membranes with LLZO as filler turned brown during drying (**Figure 4-31A**), which may indicate side reactions involving MeCN. However, such reactions have not been reported in literature, where MeCN is commonly used for these systems. For the preparation of CPE dispersions, doctor blading was found to be advantageous due to faster solvent evaporation, which reduced sedimentation of the filler particles. However, this method required larger volumes of material per film, resulting in higher material consumption. Therefore, solution casting was used for initial composition screening, while doctor blading was applied for the preparation of thin, large-area films (**Figure 4-31C**).

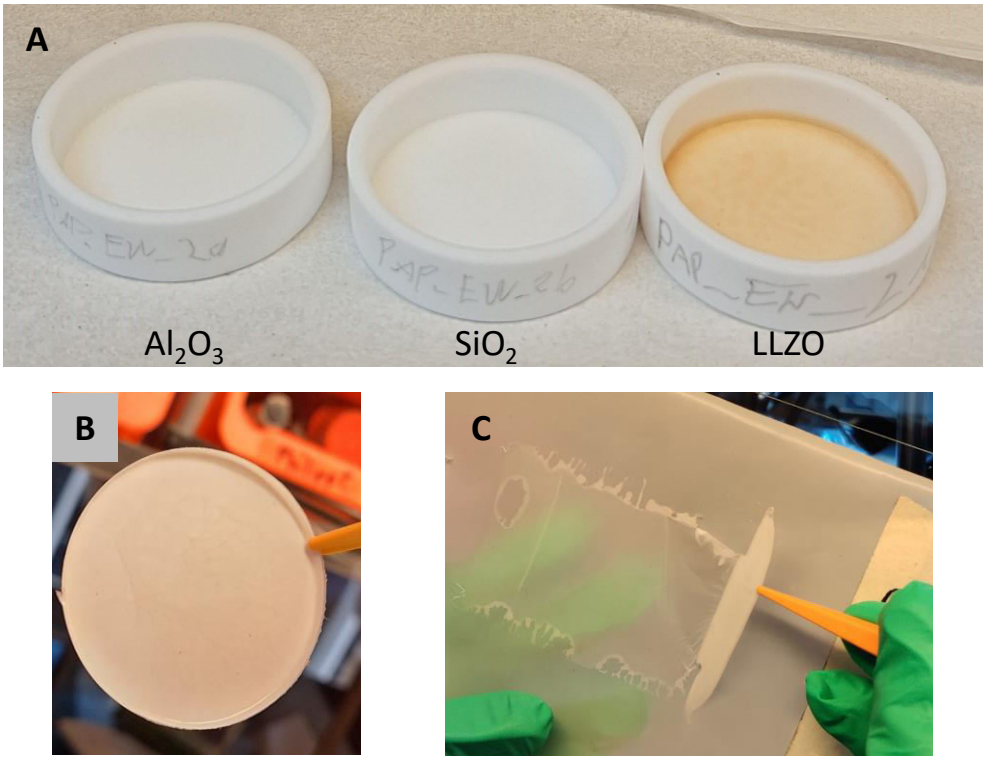

Figure 4-31: Composite polymer electrolyte membranes from PEO. **A** CPEs with Al_2O_3, SiO_2 and LLZO as fillers after evaporation of the MeCN solvent. LLZO shows clear discolouration. **B** free standing PEO-CPE (PEO/SN/LiTFSI = 36/8/1; 15 wt% SiO_2 – standard for most further measurements. **C** Thinner doctor bladed PEO-CPE membrane used as interlayers between LLZO and the cathode.

To evaluate morphological changes induced by the addition of fillers, XRD measurements were performed on the produced SPE and CPE films, as shown in **Figure 4-32**. For the SPE containing only SN as an additive, the main reflexes of crystalline PEO are clearly visible at 19° and 23°. Compared to literature data on pure PEO, the number and intensity of sharp reflexes are reduced, confirming the crystallinity-suppressing effect of SN.[282] Upon addition of SiO_2 and Al_2O_3, no significant morphological changes are detected. However, a slight reduction in intensity of minor reflexes at 15° and 27° suggests a further decrease in crystallinity. No additional reflections corresponding to the filler phases are visible, as both SiO_2 and Al_2O_3 were used in amorphous form. In contrast, for the CPE containing LLZO, additional reflexes corresponding to crystalline LLZO appear alongside the characteristic PEO reflexes. These results indicate that the incorporation of inorganic fillers slightly suppresses PEO crystallization, thereby increasing the proportion of the amorphous phase, which is beneficial for ionic conductivity.

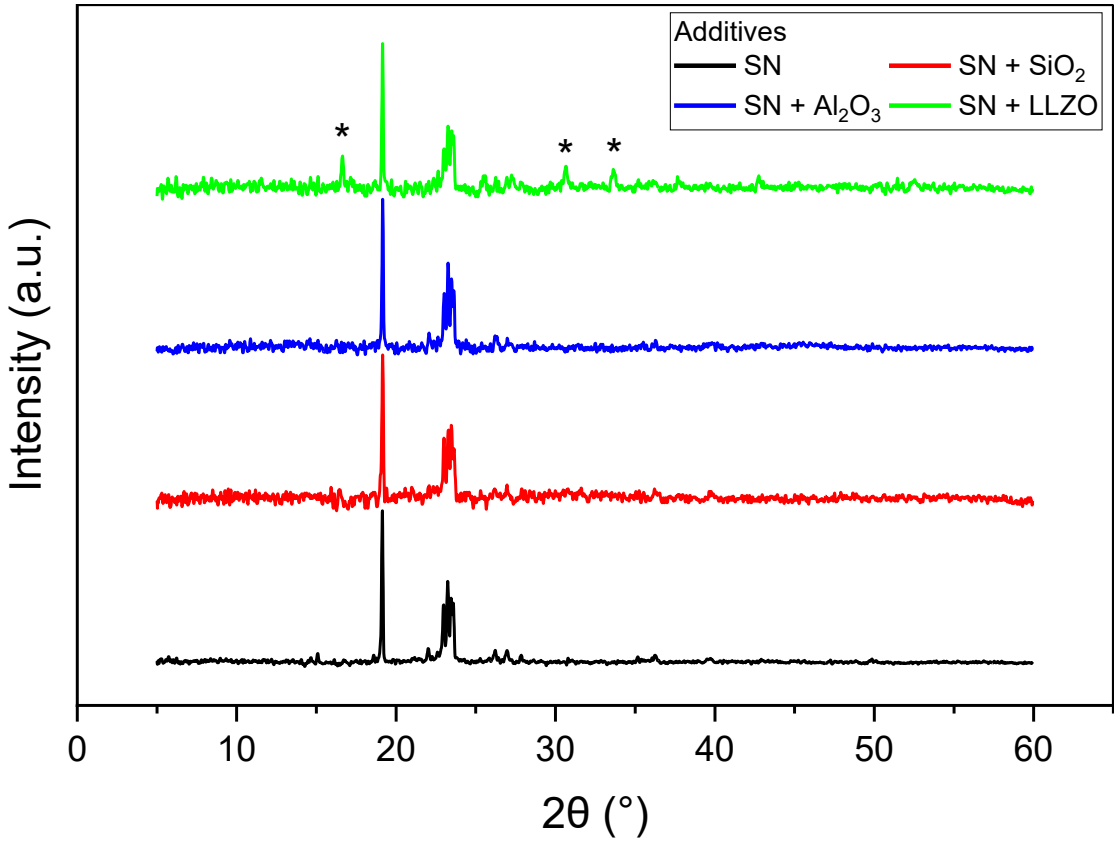

Figure 4-32: XRD patterns of PEO SPE/CPE films with various fillers (10 wt%). Basic composition of PEO/SN/LiTFSI = 36/8/1. Main LLZO reflexes are marked by *.

To evaluate the electrochemical performance of the prepared SPE and CPE membranes, ionic conductivities were determined by EIS measurements. Representative Nyquist plots

for CPEs containing 10 wt% SiO_2 and Al_2O_3 at different temperatures are shown in **Figure 4-33**. As expected from the Arrhenius behaviour, the impedance decreases with increasing temperature due to enhanced Li-ion mobility. The CPE containing SiO_2 exhibits a lower overall impedance compared to the Al_2O_3-containing sample. Fitting of the impedance spectra for the SiO_2-CPE at elevated temperatures was challenging, due to the absence of a distinct semicircle.

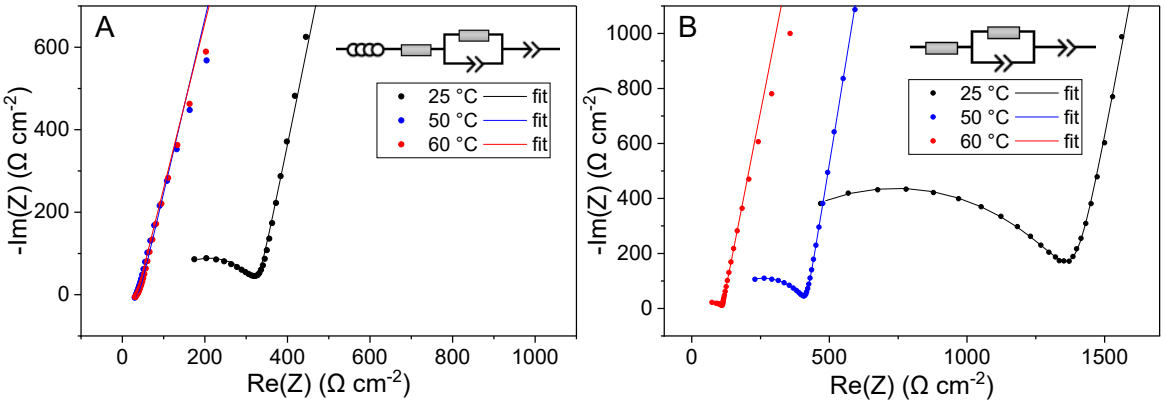

Figure 4-33: Nyquist plots for PEO CPEs with **A** 10 wt% SiO_2 and **B** 10 wt% Al_2O_3 at 25, 50 and 60 °C respectively. Due to the lower overall impedance in sample **A** with SiO_2 the equivalent circuit needed an additional inductor element to account for the cable induction especially visible at elevated temperatures.

The calculated ionic conductivities of the SPEs and CPEs with SN and different fillers are summarized in **Table 4-6**. CPEs with Al_2O_3 did show minorly improved conductivity compared to the filler-free SPEs. In contrast, CPEs with SiO_2 and LLZO exhibited higher conductivities, particularly at elevated temperatures. Consequently, the brown discoloration observed in LLZO-containing films did not negatively affect ionic conductivity, indicating that LLZO is a functional filler despite its less favourable handling properties due to increased stickiness. While SiO_2 and Al_2O_3 improved the mechanical integrity of the films, only SiO_2 resulted in a simultaneous increase in ionic conductivity. Considering both electrochemical and mechanical performance, SiO_2 was identified as the most suitable filler for the formulation of PEO-based CPEs.

Table 4-6: Ionic conductivities of SPE and CPE films at 25 and 60 °C. Thicknesses raged from 93 to 129 µm (before cell assembly).

Additives	σ [mS cm^{-1}] at 25 °C	σ [mS cm^{-1}] at 60 °C
SN	0.1	0.97
SN + 10 wt% SiO_2	0.2	2.11
SN + 20 wt% SiO_2	0.2	1.91
SN + 10 wt% Al_2O_3	0.04	1.49
SN + 20 wt% Al_2O_3	0.03	1.21
SN + 10 wt% LLZO	0.2	1.83

The functionality of the produced PEO films was previously confirmed in coin cells, as shown in chapter 4.11. To further evaluate the applicability of the ASC-T setup for LFP|PEO|(LLZO)|Li half-cells, the same PEO films were tested under similar conditions. Despite using the same configuration as in coin cells, the discharge capacity was significantly reduced to 100 mAh g^{-1} at C/10 (**Figure 4-34**). Moreover, the coulombic efficiency was notably lower, reaching only 83% at C/10 and decreasing further to 36% at 1C.

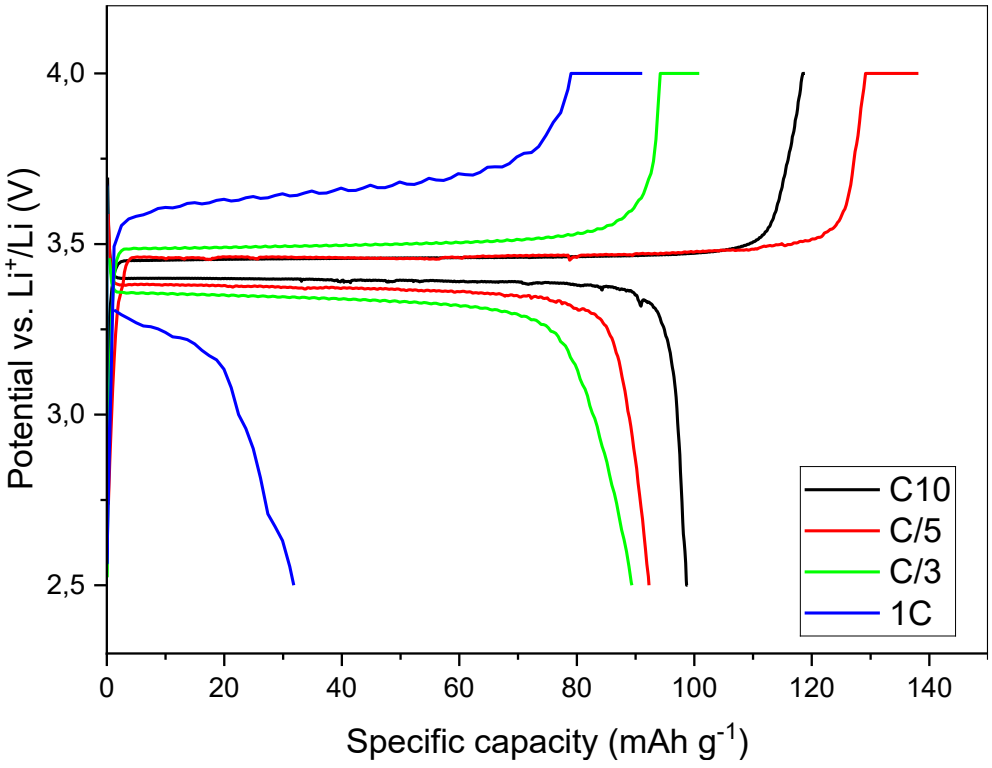

Figure 4-34: Charge-discharge curves of an LFP|PEO|Li half cell at various C-rates in the ASC-T cell setup at 2 MPa and 60 °C (PEO-CPE composition EO/SN/LiTFSI = 36/8/1 with 15 wt% SiO_2,).

This behaviour is likely attributed to an inhomogeneous pressure distribution in the ASC-T cell at the applied pressure of 2 MPa, resulting in hotspots with improved interfacial contact that promote non-uniform lithium-ion transport and faster kinetics for the underlying cell reactions. Attempts to increase the pressure led to a higher incidence of short-circuited cells, making this approach unsuitable for improving pressure uniformity and cell performance. Impedance spectroscopy further revealed that the total cell resistance in the ASC-T setup was approximately 5 to 10 times higher than in coin cells, although still within a range that permits reasonable electrochemical performance (**Figure 8-28**). As a consequence of these results the following measurements with LLZO were performed at increased pressures of 5 to 10 MPa. Post-mortem analysis of the cycled cells revealed a white discoloration along the edges of the lithium foils, suggesting that the setup may not have been fully airtight, thereby introducing a potential source of error. At the time, it was not possible to operate the setup within a glovebox environment.

4.2.3 LLZO Preparation and Interface Characterization

Due to the limited mechanical strength and low ionic conductivity of SPEs, LLZO was investigated as an oxidic solid electrolyte to address these shortcomings in a hybrid polymer–oxide solid-state battery. The LLZO was synthesized by collaboration partner Steffen Weinmann following a literature-known procedure.[283] The produced powder was pressed into pellets with a diameter of 10 mm. After sintering, the pellet diameter slightly exceeded the 8 mm inner diameter of the ASC-T cell. Therefore, the pellet edges were polished to fit into the PEI sleeve. This introduced a minor deviation from perfect circularity, which was considered negligible.

For initial characterization, a symmetrical Li|LLZO|Li cell was assembled to investigate the pressure dependence of the interfacial resistance between LLZO and lithium. In contrast to the PEO-based membranes, the bulk impedance of LLZO remained constant over the entire pressure range studied (**Figure 4-35**). However, the interfacial impedance between Li and LLZO showed a significant decrease with increasing pressure, reaching a plateau at approximately 27 MPa. This pressure threshold is considerably higher than the 5 MPa required for the stabilization of the bulk impedance in PEO-based systems (**Figure 4-29**). The corresponding impedance spectra at different applied pressures are shown in **Figure 8-29**.

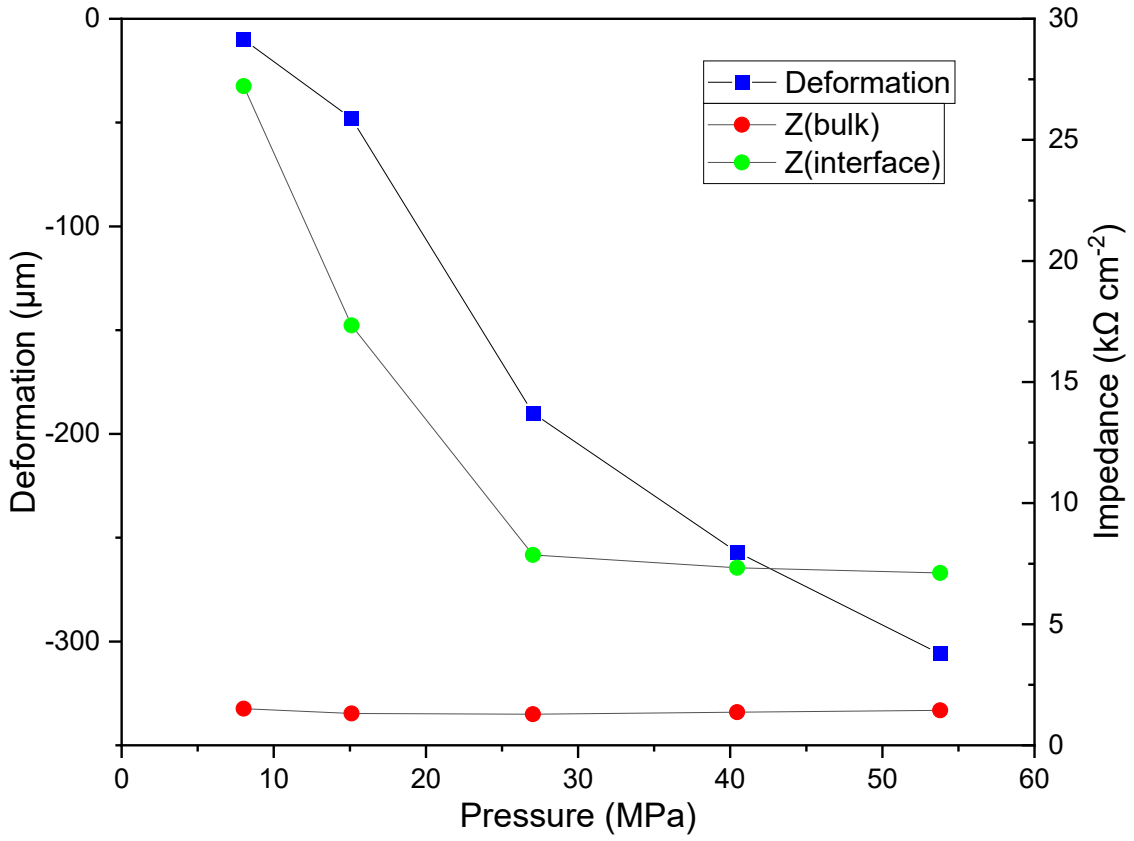

Figure 4-35: Pressure dependency of the bulk and interfacial impedance in a Li|LLZO|Li cell setup, with the corresponding deformation. Measurements were conducted in the ASC-T cell at 25 °C. The LLZO pellet was polished prior to use, with no additional surface modifications applied.

LLZO is known to suffer from interfacial instabilities with lithium metal, including void formation, which impairs contact and increases resistance. To mitigate these effects, the application of thin interfacial metal layers has been shown to enhance Li wettability and homogenize Li-ion flux.[284] Based on this, a thin gold layer (<50 nm) was sputtered onto the LLZO pellet surface to improve interfacial contact with lithium. As shown in **Figure 8-30**, this treatment resulted in a substantial reduction in interfacial resistance. From the impedance spectrum, the combined resistance of the grain boundaries (R_{gb}) and the interface (R_{int}) was determined to be below 500 Ω cm^{-2} at an applied pressure of 2 MPa. This demonstrates that interfacial metallization can significantly reduce interface resistance in LLZO-based systems and enables more precise investigation of other interface effects in hybrid cell architectures.

To further investigate the cathodic interface of LLZO, symmetrical LFP|LLZO|LFP cells were analysed by impedance spectroscopy (**Figure 4-36**). At 25 °C, the interfacial resistance, represented by the semicircle in the impedance spectra, exceeded 1000 kΩ cm^{-2}, even when

the applied pressure was increased to 50 MPa. Raising the temperature to 50 °C significantly reduced the interfacial resistance, likely due to softening of the PEO binder in the cathode. However, the resistance remained above 300 kΩ cm², which is too high for practical battery applications.

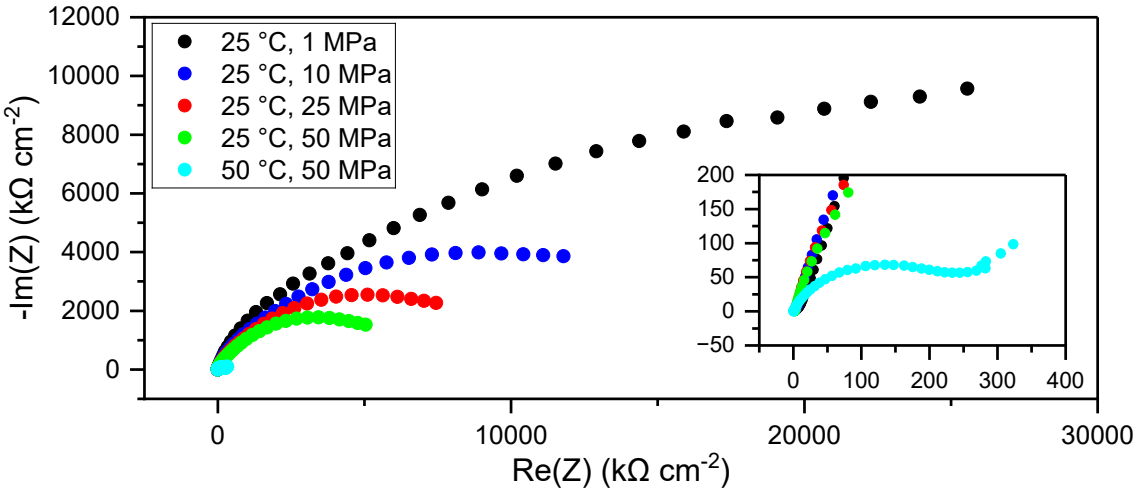

Figure 4-36: Impedance evolution with increasing applied pressure and temperature of an LFP|LLZO|LFP cell in the ASC-T cell in the constant pressure setup.

To evaluate whether a PEO interlayer can improve the interfacial contact, an LFP|PEO|LLZO|PEO|LFP configuration was assembled and analysed likewise. As shown in **Figure 4-37**, the interfacial resistance was considerably reduced, reaching approximately 70 kΩ cm^{-2} at 25 °C and 5 MPa. Further increasing the temperature and pressure improved the contact, reducing the resistance to below 20 kΩ cm^{-2} at 50 °C and 50 MPa. These results demonstrate that the introduction of a PEO interlayer between the LLZO pellet and the LFP cathode significantly enhances the interface. This confirms that the PEO content within the cathode composite alone is insufficient to establish a low-resistance contact with a rigid oxide electrolyte.

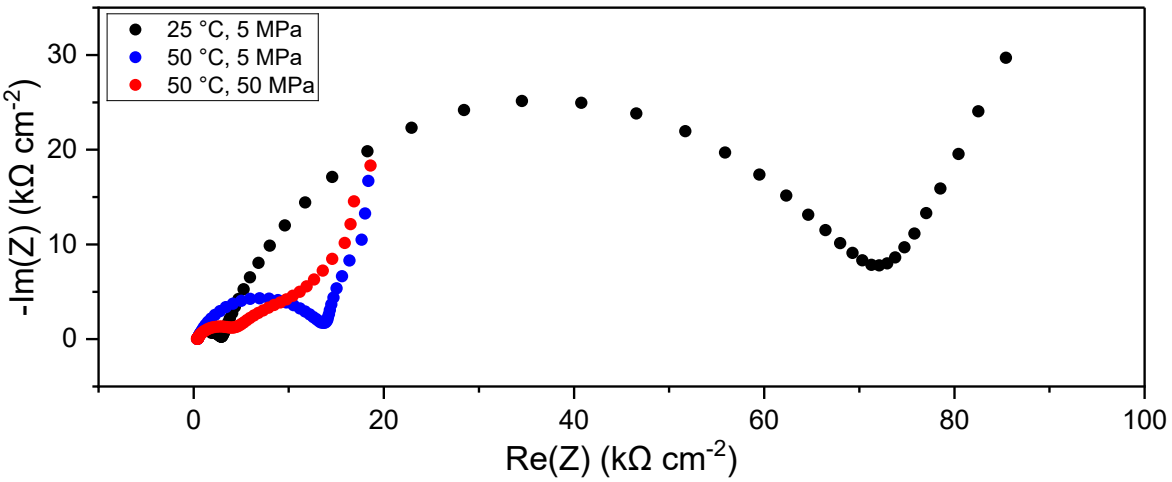

Figure 4-37: Impedance evolution with increasing applied pressure and temperature of an LFP|PEO|LLZO|PEO|LFP cell in the ASC-T cell in the constant pressure setup. PEO-CPE films with a thickness of 110 µm and 10 wt% SiO_2 were used.

Since PEO generally exhibits lower ionic conductivity than LLZO, the SPE interlayer represents a limiting factor for the overall conductivity of the hybrid polymer-oxide electrolyte. One strategy to address this issue is to minimize the interlayer thickness. As described in chapter 4.2.2, significantly thinner films can be produced by doctor blading a PEO-based precursor dispersion onto PTFE foil compared to the solution casting method. An alternative approach, drop-casting a PEO-SPE solution directly onto the LLZO pellet, was also evaluated. However, this method did not yield satisfactory results. Combined with observations of the discolouration behaviour of LLZO fillers in MeCN, this approach was not pursued further. In contrast, doctor-bladed films with a thickness of approximately 5 µm were successfully prepared and used as interlayers. LLZO pellets were sandwiched between two of these thin films and the interfacial properties were investigated by EIS. The results were compared to LLZO pellets sandwiched between solution-cast PEO-CPE films, each with a thickness of ~100 µm. Contrary to expectations, the thin-film configuration exhibited an interfacial resistance approximately seven times higher at 60 °C.

Post-mortem analysis revealed the cause of this increased resistance. Upon heating to 60 °C, the thin PEO films contracted, no longer fully covering the LLZO surface. This suggests poor wetting of the LLZO surface by the PEO matrix. In contrast, the thicker solution-cast films maintained full surface coverage during the measurement, ensuring consistent interfacial contact across the entire pellet area (**Figure 4-38**). These results indicate that a minimum film thickness is required to ensure complete surface coverage and stable interfacial

contact in hybrid polymer-oxide systems. Therefore, for subsequent studies, PEO films with a thickness of approximately 40-50 µm were used, as this thickness provided a suitable compromise between mechanical stability, full surface coverage, and minimized interfacial resistance. These films were produced by doctor blading using a 600 µm gap.

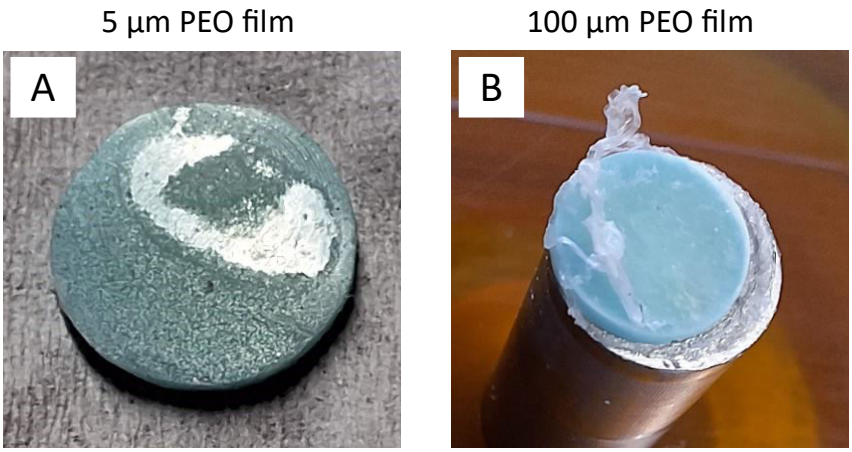

Figure 4-38: **A** LLZO pellet only partially covered by a thin PEO film after heating to 60 °C. **B** using a thicker PEO film the LLZO pellet is still fully covered after heating to 60 °C.

Throughout the experiments, it was observed that PEO-CPEs with higher filler content exhibited increased interfacial resistance compared to samples with lower filler ratio. To investigate whether the improved mechanical integrity of CPEs with a high filler content influences interfacial resistance, symmetrical PEO|LLZO|PEO cells were assembled using either filler-free SPEs or CPEs containing 15 wt% SiO_2. At 25 °C, both cell types showed high interfacial impedance, with the PEO-SPE exhibiting slightly higher resistance. However, upon heating to 60 °C, this trend reversed (**Figure 4-39**). The interfacial resistance of the SPE decreased substantially more and was approximately five times lower than that of the CPE. Interestingly, at 80 °C and therefore above the glass transition temperature of PEO, the CPEs again showed slightly improved performance compared to the SPEs. When cooling back down to 60 °C, however, the interfacial resistance of the CPE increased more substantially than that of the SPE. These observations suggest that while higher filler content improves the mechanical properties and overall electrochemical stability of the PEO matrix, it may negatively affect interfacial contact with LLZO.

One possible explanation is that the softer SPE may better adapt to the surface of the LLZO pellet, potentially penetrating surface pores and increasing the effective contact area. However, as the LLZO pellets exhibited a porosity of only ~5%, this alone is unlikely to fully

explain the improved interfacial contact. Moreover, the observed increase in interfacial resistance upon cooling from 80 °C to 60 °C suggests that a reversible reduction in effective contact area is improbable. Further investigation is required to understand the underlying mechanism, but this could not be completed within the scope of this work.

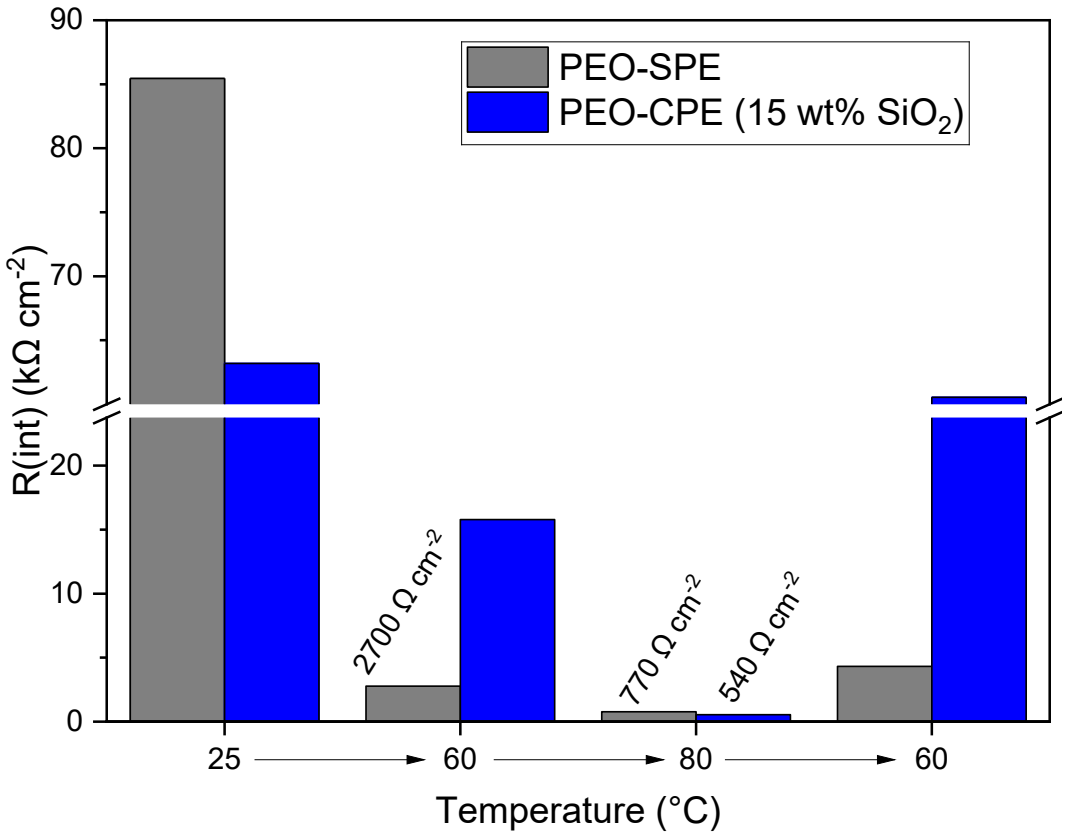

Figure 4-39: Interfacial resistances of PEO|LLZO|PEO cells with 1) PEO-SPEs on both sides and 2) PEO-CPEs with 15 wt% SiO_2. After the measurement at 80 °C the samples were cooled again to 60 °C for the final measurement.

Given the importance of sufficient mechanical integrity for separator function, CPEs with a reduced filler content of approximately 10 wt% SiO_2 were used for subsequent half-cell experiments. This allowed comparison to reference half-cells without LLZO while maintaining sufficient film stability.

4.2.4 Half Cells with LLZO

Following the characterization of individual interfaces in an ASSB with a hybrid PEO-LLZO electrolyte, half-cells using the prepared cathodes and lithium metal anodes were assembled and tested. As a baseline for evaluating interfacial improvements, an LFP|LLZO|Li cell was assembled and measured in the ASC-T setup at 60 °C under a comparatively high

applied pressure of 22 MPa (**Figure 8-31**). The purpose was to verify the insufficient contact between the LLZO pellet and the PEO-based cathode composite. Initial cycling attempts resulted in immediate polarization of the interfaces, with the cell potential reaching the cut-off limits without any observable charge being stored or extracted. This behaviour, together with the high interfacial resistance confirmed by EIS (**Figure 8-32**), clearly demonstrates that this configuration is not functional in its current form and requires interface modification to become feasible.

To improve the interfacial contact between the LLZO pellet and the LFP cathode, a doctor-bladed PEO-SPE film with a thickness of 40 µm was inserted as an interlayer. The film was prepared without any filler to reduce mechanical rigidity and enhance conformity with the LLZO surface. The assembled cell was cycled using a CCCV protocol at various C-rates (C/10, C/5, C/3). The resulting charge-discharge profiles are shown in **Figure 4-40**. At C/10 and C/5, the cell delivered a discharge capacity of 110 mAh g^{-1} with a coulombic efficiency of 95%. When the rate was increased to C/3, the discharge capacity dropped to 38 mAh g^{-1} and the efficiency declined to 70%.

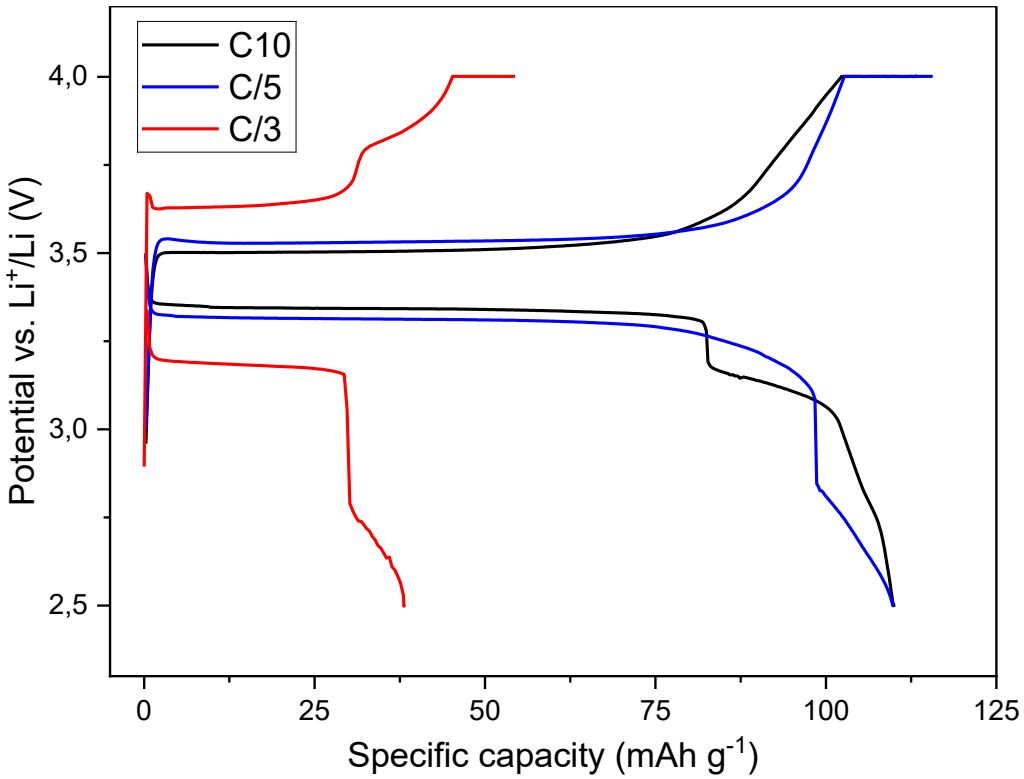

Figure 4-40: Charge-discharge profiles of an LFP|PEO|LLZO|Li half cell cycled at various C-rates in the ASC-T cell setup at 60 °C and 2 MPa (PEO-SPE composition EO/SN/LiTFSI = 36/8/1 without added fillers, δ = 40 µm).

At lower C-rates, the hybrid cell outperformed the reference setup without the LLZO pellet (**Figure 4-34**). The reduced performance at higher C-rates is attributed to the overall increased cell resistance, in particular due to the additional LLZO-PEO interface, which still poses the major contribution to the total resistance as evident from the impedance spectra (**Figure 4-41**). The measurement at 25 °C exhibits a loop in the low-frequency region (LFR), indicating insufficient equilibration. This suggests that the LLZO-PEO interface is not immediately fully formed but rather improves gradually as the PEO diffuses into surface voids or irregularities of the LLZO.

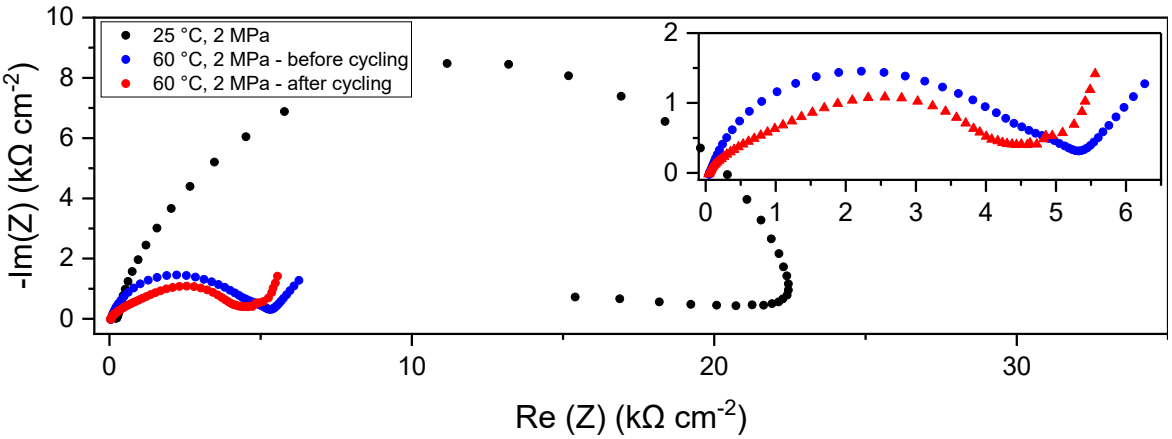

Figure 4-41: Impedance spectra of an LFP|PEO|LLZO|Li cell in the ASC-T setup at 60 °C and 2 MPa. Cell was not fully equilibrated at 25 °C resulting in the loop in the LFR area (~20 kΩ cm²).

In contrast to earlier measurements, a decrease in total cell impedance was observed after cycling. This behaviour is also attributed to the slow formation of the LLZO-PEO interface, which likely remained incomplete even after the initial 10 h equilibration at 60 °C. These results confirm that the use of a PEO interlayer significantly improves the cathodic interface in hybrid cells with hard LLZO electrolytes. However, when employing a relatively thick PEO interlayer that could function as a separator but lacks sufficient ionic conductivity due to the absence of fillers, the resulting high overall impedance limits performance at elevated C-rates.

As shown in the previous chapter, further reduction of the PEO interlayer thickness lead to incomplete coverage of the LLZO pellet due to pooling of the PEO on the LLZO surface at elevated temperatures. This behaviour was confirmed in a half-cell using a 5 µm PEO-CPE interlayer containing 20 wt% SiO_2 between the LLZO and the LFP cathode. The filler was added again to assess whether increased mechanical rigidity could mitigate the pooling

effect. Impedance spectra revealed that upon heating to 60 °C, the interfacial contact initially improved, reaching a lower interfacial resistance than that observed with the thicker PEO-SPE layer, with a starting value of ~1 kΩ cm² (**Figure 4-42**). However, over the 10 h equilibration period, the interfacial resistance increased to ~15 kΩ cm² and continued to rise during subsequent cycling at 60 °C. Although an initial discharge capacity of 80 mAh g^{-1} was achieved at C/10, this rapidly declined due to progressive degradation of the interfacial contact, attributed to contraction of the thin PEO layer at elevated temperatures (**Figure 8-33**).

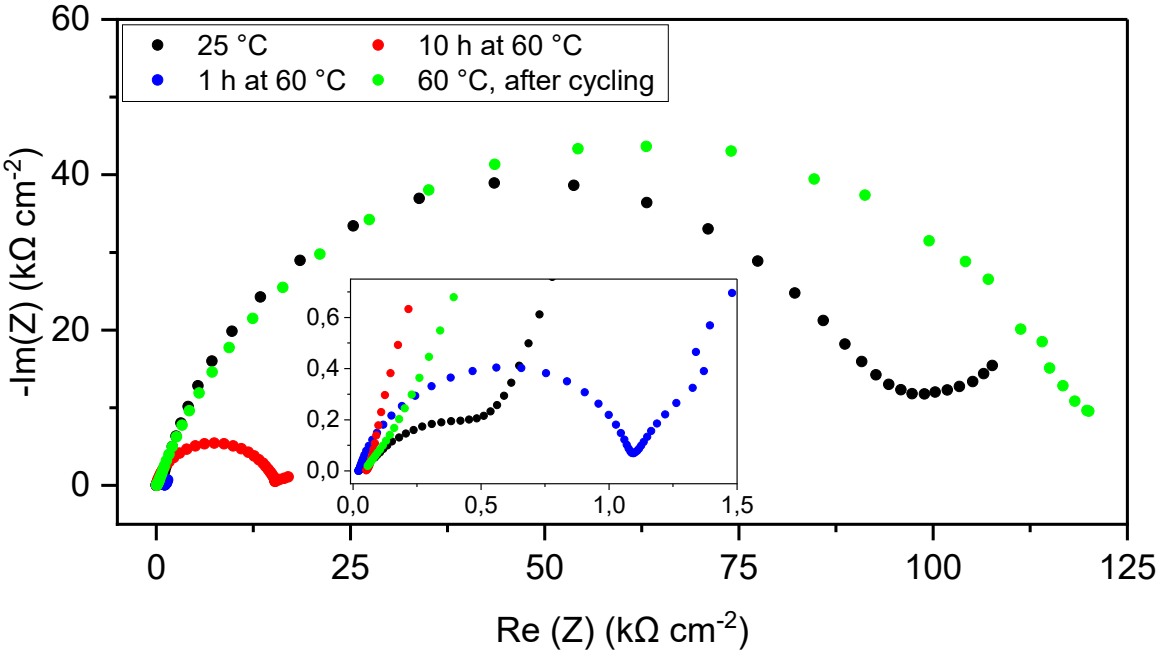

Figure 4-42: Impedance spectra of an LFP|PEO|LLZO|Li cell in the ASC-T setup at 60 °C and 5 MPa. PEO-CPE composition EO/SN/LiTFSI = 36/8/1 with 20wt% SiO_2, δ = 5 µm.

These experiments underline that the interface between LLZO and electrode materials remains a critical challenge in the development of hybrid polymer-oxide solid-state batteries. Without tailored interface engineering, high stack pressures are required to ensure sufficient contact, which limits practical applicability. The use of PEO as a polymer interlayer is insufficient on its own, as the poor wettability of LLZO by PEO significantly impairs interfacial contact and results in high interfacial resistance. This highlights the need for further studies into the surface interactions between LLZO and potential polymer interlayers.

5 Summary and Outlook

Throughout the first part of this thesis, functionalized vinylphosphonates with short ethylene oxide, or carbonate side chains were synthesized. While the polymerization of the monomers with one and two ethylene oxide units could be achieved via REM-GTP, for longer chains and the monomers with the carbonate functionalities impurities inhibited successful polymerization. P1-VP and P2-VP however were obtained with narrow dispersities ($Đ < 1.1$) and high molar masses exceeding 350 kg mol^{-1}. These polymers were then used to prepare free-standing SPE films by solution casting with various lithium conducting salts. TGA revealed that the polymers are thermally stable up to 260 °C (P1-VP) and 210 °C (P2-VP), with degradation onset reduced by salt addition. Differential scanning calorimetry and XRD measurements confirmed the amorphous character of the SPE films. Ionic conductivities of $1.8 \cdot 10^{-5}$ S cm^{-1} for P1-VP and $8.2 \cdot 10^{-5}$ S cm^{-1} for P2-VP at 60 °C were achieved with $LiBF_4$ as conducting salt. The higher ionic conductivity of P2-VP is attributed to longer ethylene oxide side chains, which improve segmental flexibility and thereby enabling more efficient ion transport. This was supported by lower activation energies for Li-ion hopping of 0.59 eV and 0.47 eV for P1-VP and P2-VP, respectively. Electrochemical characterization via LSV confirmed an anodic stability of up to 4.3 V vs. Li^+/Li for both materials. Low Li^+ transference numbers of 0.03 for P1-VP and 0.12 for P2-VP were measured, attributed to strong coordination between Li^+ and the phosphonate groups. This coordination limits the mobility of lithium ions and leads to strong polarization during lithium plating and stripping. P2-VP performed slightly better, supporting the hypothesis that longer side chains reduce the influence of the phosphonate anchor on ionic mobility. These limitations led to low critical current densities (5 µA cm^{-2} for P1-VP, 10 µA cm^{-2} for P2-VP) and significant overpotentials in Li-shuttle measurements. In half-cell tests with LFP cathodes, specific capacities remained well below theoretical values due to the high polarization resistance and insufficient lithium-ion transport.

Based on these findings, future work should focus on modifying the polymer structure to reduce the lithium coordination strength of the phosphonate units without compromising the thermal and mechanical stability of the material. This includes investigating the coordination environment of lithium ions in the polymer matrix through solid-state Li-NMR

spectroscopy to elucidate the binding mechanism and quantify the interaction strength. Furthermore, increasing the side chain length or introducing alternative functionalities could help to spatially separate the coordinating ether moieties from the phosphonate unit and thereby improve lithium mobility. It is also of interest to determine whether lower phosphonate contents or smaller molar ratios still impede lithium transport and to what extent these effects scale with side chain architecture.

In the second part of this work, a special testing cell (ASC-T cell, Sphere Energy) was evaluated as a tool to investigate thickness and volume changes in solid-state battery systems during cycling. The setup proved to be well-suited for an exemplary system operating at high pressures around 100 MPa, where a sulfidic electrolyte showed thickness changes consistent with theoretical values. However, at lower pressures below 5 MPa, which are relevant for polymer-based electrolytes, the mechanical deformation of the cell housing overshadowed the thickness variations of SPEs. As a result, precise in situ measurements of softer SPE systems could not be performed with this setup in its current configuration.

Despite these limitations, the ASC-T cell was successfully applied to study the interfaces in a hybrid polymer-oxide battery featuring a PEO interlayer between an LLZO solid electrolyte and an LFP cathode. A standard LFP cathode directly contacted to the LLZO pellet resulted in high interfacial resistances exceeding 300 kΩ cm², even under elevated pressure and temperatures of 50 MPa and 50 °C. The introduction of a PEO based SPE interlayer led to a significant reduction in interfacial resistance, confirming the necessity of suitable interlayers to ensure adequate contact. Systematic variation of the PEO film thickness revealed that layers below 40 µm exhibited pooling on the LLZO surface at elevated temperatures of 60 °C. Hereby, the thin films contracted and failed to maintain continuous coverage, resulting in a growing interfacial impedance. A thickness of 40 µm was found to be sufficient to maintain full surface coverage after thermal equilibration, minimizing the interfacial impedance. Attempts to enhance the electrochemical properties of the PEO film by incorporating inorganic fillers such as SiO_2, were found to worsen the contact with LLZO. This observation suggests that softer polymers, while mechanically weaker, are able to form a more intimate and continuous interface with the grain structure of LLZO. Electrochemical testing in half-cell configurations confirmed these findings. Among the tested interlayer thicknesses, the 40 µm PEO-SPE film resulted in the best performance. Thinner

layers suffered from incomplete coverage, while thicker films introduced additional resistance due to increased ionic path length.

Future investigations should address how the wetting behaviour of LLZO with various polymers can be systematically improved. This includes both surface modifications of the LLZO and the design of polymers with specific functional groups that enable targeted interactions with the ceramic surface. The potential of end-group functionalization introduced through REM-GTP polymerization is of particular interest in this context, as it may allow for tailored interfacial chemistry without compromising the bulk properties of the polymer.[285,286] Literature reports show that improved interfacial resistance between LLZO and surrounding media is possible by specific surface modifications.[287,288] In addition, modifying the ASC-T cell setup for higher sensitivity at low pressures would allow in situ measurement of polymer volume changes under realistic operating conditions. This is especially relevant in the ongoing effort to reduce the thickness of the ceramic separator, where the substitution of pellets with fragile LLZO tapes requires soft interlayers to maintain structural integrity. In this context, the use of adjusted polymers for improved wettability of the LLZO surface with lower molecular weight may be advantageous, as their increased softness could further improve interfacial contact. On the anode side, improving the LLZO-Li interface by infiltrating lithium into a porous LLZO host structure has shown potential to reduce the required stack pressure further and eliminate the need for intermetallic interlayers, thereby simplifying cell architecture and improving mechanical compatibility. The three future research areas are displayed in **Figure 5-1**.

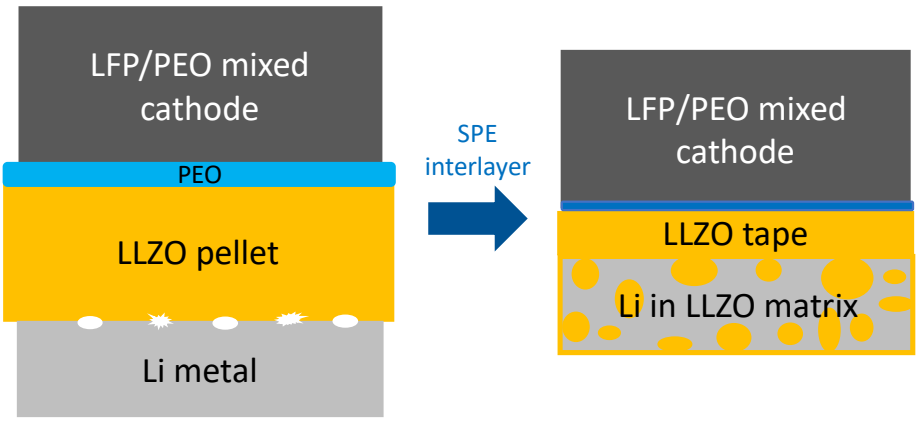

Figure 5-1: Next step in improving the hybrid LLZO-PEO battery setup by I) reducing the LLZO thickness via tape casing II) improving the LLZO-Li interface by infiltrating Li into a LLZO host matrix reducing the needed pressure and removing the need for intermetallic interlayers and III) adjusting the polymer interlayer to better wet the LLZO surface, making thinner films possible.

6 Experimental Section

6.1 Materials and Methods

General. All reactions with air- and moisture-sensitive substances were carried out under argon (99.996 vol.-%, Westfalen) atmosphere using standard *Schlenk* techniques or in a glove box (<1 ppm O_2 and H_2O, MBraun, Germany). Prior to use, all glassware was heat-dried under vacuum. Unless otherwise stated, all chemicals were purchased from Sigma-Aldrich, ABCR, or TCI Europe and used without further purification. Toluene, THF, and MeCN were dried using an MBraun SPS-800 solvent purification system and stored over 3 or 4 Å molecular sieves.

NMR spectra were recorded on a Bruker AV-400HD spectrometer. ^{1}H, ^{13}C and ^{31}P NMR spectroscopic chemical shifts δ are reported in ppm relative to the residual solvent signal of the deuterated solvent. The NMR spectra were analysed using the MestReNova software. Signal multiplicities are abbreviated as follows: s - singlet, d – duplet, t – triplet, m – multiplet. Unless otherwise stated, coupling constants (*J*) were the averaged values and refer to couplings between two protons. All deuterated solvents were obtained from Sigma-Aldrich and dried over activated 3 Å molecular sieve.

Molecular weight distribution. Absolute molecular weights and dispersities of P1-VP were determined via gel permeation chromatography with samples of 4 mg mL^{-1} on a combination of a Shimadzu LC-10ADVP with a DGU-3A as degasser (Shimadzu) and a column thermostat CTO-10A (Shimadzu) equipped with two PL Polargel-M columns (Agilent). The eluent used was a mixture of 50% THF and 50% water, treated with tetrabutylammonium bromide (TBAB) (9 g L^{-1}), and 340 mg L^{-1} 3,5-di-tert-butyl-4-hydroxytoluene (BHT) as a stabilizing agent at 40 °C. The samples were analysed via multiangle light scattering (MALS) using a Wyatt Dawn Heleos II in combination with a Wyatt Optilab rEX as RI detector unit. Absolute molecular weights and polydispersities of P2-VP and were measured on an Agilent PL-GPC 50 (Santa Clara, CA, USA) with two Agilent PolarGel M columns by triple detection using two-angle light scattering (15 and 90°), a refractive index detector, and a viscometer. As the eluent, *N,N*-dimethylformamide (DMF) with 2.096 g L^{-1} lithium bromide at 30 °C was used.

d*n*/d*c* was determined on a *WGE Dr. Bures* dn/dc-2010 from PSS equipped with a 620 nm light source via measurement of five samples with different concentrations (1-20 mg mL^{-1}) of polymers with various molar masses. It was determined as 0.1290 mL g^{-1} for P1-VP in THF/H_2O (50:50) and 0.0498 mL g^{-1} for P2-VP in DMF.

DSC analysis was performed on a DSC Q2000 from TA Instruments. It was measured in exo down mode with a heating rate of 10 K min^{-1} in a temperature range from −100 °C to 200 °C with samples of 6-9 mg. Three cycles were run per measurement (heating, cooling, heating) with the second heating cycle being used for the T_g determination. Analysis was performed using TA Analysis software.

TGA was measured on a TGA Q5000 from TA Instruments. The samples are heated with a heating rate of 10 K min^{-1} under argon. The following thermal program was applied using argon gas (20 mL min^{-1}) for purging: At 30 °C isothermal equilibration (30 min), ramp from 30 °C to 700 °C with 10 K min^{-1}. The thermal stability was defined at the onset point for the weight loss. Samples came in contact with ambient atmosphere for <1 min during transfer of the sample to the device before being the Ar flow turned on. Analysis was performed using TA Analysis software.

XRD Crystallographic characterization is performed on a *STOE STADI P* diffractometer in transmission geometry with Cu-$K_{\alpha 1}$ radiation (λ = 1.54051 Å), a Ge(111) monochromator and a Mythen1K detector (*DECTRIS*). Scans of at least 5 h in an area 2Θ = 5° to 80° are used for phase analysis. Samples are fixed airtight between two Scotch tapes in a flat sample holder.

SEM. The surface of the SPE films were characterized by the images taken by *JEOL JSM-7500F* field-emission scanning electron microscope coupled with EDX *INCA System* (software) with 50 mm^2 X-MAX detector from Oxford Instruments.

Cathode surfaces were analysed by a *JEOL JSM IT-800* field emission scanning electron microscope. The magnification and distance for each measurement are depicted on every SEM-image. EDX was conducted using an energy of 5 keV to depict K and L-radiation, for the elements Ni, Fe, O, C, H.

Cross-section polishing. For cathode bulk investigation, 8 mm sample disks were cut in half with a scalpel and a copper tape (G253A, from Plano, Germany) was stuck onto the Al-foil

(Cu-Al-Cat). The sample was polished at −120 °C with a cross-section polisher (IB-19520CCP, from JEOL, Japan). The surface was thinned using a dual beam focused ion beam (FIB) (Strata 400 STEM, FEI Company, USA) equipped with a Ga-ion source to cut the sample (6 kV/0.4 nA). The ion beam was turned on for 10 s followed by a cooling period for 10 s for a total polishing time of 2 h.

Thickness and porosity determination of cathodes.

$$\varepsilon_{coating} = 1 - \frac{V_{solid}}{V_{coating}} = 1 - \frac{\sum \frac{wt\%_i}{p_i}}{d_{coating} \cdot A_{coating}} \cdot m_{coating} \quad 15$$

The thickness of the cathodes before and after pressing was measured with a dial gauge (IP65, Mitutoyo, Japan). The cathode coating porosity ($\varepsilon_{coating}$) is 1 minus the ratio of the bulk volume of the electrode components (V_{solid}) over the volume of the coating ($V_{coating}$), with the letter determined by summing up the individual bulk volumes of the electrode components based on their bulk material density (p_i) and their relative weight fraction ($wt\%_i$) and dividing it by the coating area ($A_{coating}$) and the measured thickness of the coating ($d_{coating}$= $d_{cathode}$—$d_{Al-foil}$) and finally multiplying this term by the total mass of the coating on both sides ($m_{coating}$).

Table 6-1: Individual bulk material densities of cathode components

Component	Density [g cm^{-3}]	Source
$LiFePO_4$ (LFP)	1.0-1.4 (tape) 3.6 ($bulk_{theo}$)	IBUvolt LFP400 Yan et al.[289]
Conductive carbon (C65)	2.26	Timical[290]
PEO	1.21	ThermoFisher (300 kg mol^{-1})
PVDF	1.77	Solef® 5130[290]
LiTFSI	1.064	Sigma-Aldrich (99.95%)

General procedure for polymerization of vinylphosphonate monomers with Cp_2Y(*sym*-collidine)

To prepare the catalyst solution, $Cp_2YCH_2TMS(THF)$ (10 mg, 26 µmol, 1.0 eq.) is dissolved in 1 mL toluene and subsequently *sym*-collidine (3.4 mg, 28 µmol, 1.05 eq.) is added as a

1% solution in toluene. After stirring the solution for 3 h, the activated catalyst solution is diluted with toluene to reach a concentration of 100 mg mL^{-1} of monomer in toluene in the next step. Next, 500 eq. 1-VP or 2-VP monomer (13 mmol) is added to the yellow catalyst solution and the reaction mixture is stirred for 30 min. Instant initiation is indicated by discoloration upon monomer addition. Afterwards, the polymerization is terminated by the addition of 0.5 mL MeOH. The polymer is precipitated by pouring the solution into an excess of pentane and washed three times. The residual polymer is dissolved in dioxane, freeze-and vacuum dried at 60 °C for 24 h to yield the pure polymer as a colourless solid.

Preparation of the SPE/CPE membranes

PX-VP (solution casting)

150 mg polymer and a stochiometric amount of Li-salt was dissolved in 2 mL dry MeCN and stirred at RT for 3 h to form a uniform transparent solution. The amount of Li-conducting salt is calculated with respect to the ethylene oxide units in the respective monomers. **Table 8-3** shows exemplary the composition of SPE films of P1-VP and P2-VP with $LiBF_4$.Afterwards, the solution is poured into a Teflon dish (Ø 4.5 cm). The solvent is allowed to evaporate for 18 h before drying in vacuum for 24 h. The resulting membranes have a thickness of approximately 100 µm. Notably, the thickness in the center of the dish is up to 30 µm lower than at the edges, which is attributed to the increased wetting of the dish at the edges.

PEO (solution casting and doctor blading)

For the preparation of PEO-based solid (composite) polymer electrolytes, 100-200 mg of PEO and a stoichiometric amount of LiTFSI, corresponding to a molar ratio of $EO/Li^+ = 36/1$, were dissolved in 1-2 mL dry MeCN. Subsequently, a stochiometric amount of a SN stock solution in MeCN (80 mg mL^{-1}) was added. The final ratio was set to $EO/SN/Li^+ = 36/8/1$. The solution was stirred for at least 3 h at room temperature to ensure complete dissolution.

For the preparation of composite polymer electrolytes, inorganic fillers (SiO_2, Al_2O_3, or LLZO) were added after dissolution of the polymer and salt. The filler content was set to 15 wt% relative to the mass of PEO. The resulting suspensions were mixed in a planetary mixer (ARV-310, Thinky Corp., USA) in 20 mL screw lid vials at 1500 rpm for 5 min. The

polymer solutions were then cast into Teflon dishes (Ø 4.5 cm), covered with a paper towel to avoid contamination, and left to dry under inert atmosphere for 1 day. Final drying was carried out overnight in vacuo in a glove box antechamber. The resulting membranes exhibited a thickness of approximately 100 µm.

For thinner films the dispersion was doctor bladed onto PTFE foil (20 µm, Angst+Pfister, Switzerland) with a gap of 600 µm. The resulting films were left to dry under inert atmosphere for 1 day and consequently dried in a vacuum oven (G-300, Büchi, Germany) over night at 50 °C. The resulting membranes exhibited a thickness of 5-50 µm depending on the viscosity and coating speed (20-30 mm s^{-1}).

LLZO pellet fabrication

Cubic-phase $Li_{6.45}Al0.05La_3Zr_{1.6}Ta_{0.4}O_{12}$ (LLZO) powders were synthesized via a solid-state reaction as described by Rupp et al.[283] Sintered pellets were fabricated by uniaxially pressing the pre-synthesized powders at 5 MPa with a 10 mm die and isothermal sintering the green pellets at 1050 °C for 5 h under oxygen flow in magnesium oxide (MgO) crucibles (heating rate of 5 K min^{-1}). The resulting pellets had a diameter of 8-9 mm with a density of approximately 95%. After sintering, LLZO pellets were dry polished using silicon carbide paper with grid sizes of 400, 800, 1200, 2400, and 4000 to a thickness of 0.9-1 mm. The pellets were annealed in an argon filled glovebox at 600 °C for 2 h to remove Li_2CO_3 impurities on the surface.

To improve interfacial contact with lithium, a 50 nm layer of gold was sputtered onto LLZO pellets with a diameter of 6 mm. The formation of a Li_xAu intermetallic layer was achieved by placing an 8 mm lithium foil on top of the gold-coated pellet and heating it to 220 °C on a hot plate in an argon-filled glovebox.

Electrochemical measurements

Cells for electrochemical testing were assembled in an Ar-filled glove box (MBraun, O_2 and H_2O content <1 ppm) and equilibrated at 60 °C until a constant open-circuit potential (OCV) was reached (about 5 h) before measuring. For temperature dependent ionic conductivity measurements, SPE disks (Ø 10 mm) were placed between two stainless steel electrodes (Ø 8 mm) in a TSC battery cell (rhd instruments, Germany) with an applied pressure of 0.7 MPa. The cell was placed in a temperature-controlled cell stand (Microcell HC, rhd

instruments) and connected to a potentiostat (Metrohm Autolab B.V. Typ PGSTAT204). All EIS measurements were performed in a frequency range from 7 MHz to 100 mHz with an amplitude of 10 mV. The ionic conductivity (σ) of the samples is calculated by equation 16:

$$\sigma = \frac{\delta}{R_b A} \qquad 16$$

Where δ and R_b is the thickness and bulk resistance (measured by EIS) of the SPE membrane, respectively, and A corresponds to the contact area between the electrolyte and the stainless-steel electrodes. From the calculated ionic conductivity at different temperatures the activation energy for the ion hopping in the polymer is calculated using the Arrhenius equation 6:

$$\sigma = A \exp\left(\frac{-E_a}{RT}\right) \qquad 6$$

with E_a being the activation energy, T the absolute temperature, A the pre-exponential factor and R the Boltzmann constant.

Apart from the TSC battery cell, electrochemical measurements were also performed in 2032-type coin cells (MTI) and an ASC-T cell (described in the following section) using a potentiostat (SP-300/VMP3, BioLogic, France). If not stated otherwise the standard measuring temperature was 60 °C.

Sphere cell setup

For pressure and thickness monitoring during electrochemical measurements a heatable ASC-T cell was used (Sphere Energy, Germany) in the corresponding pressure frame with adjustable pressure, ranging from 0 to 400 MPa, and a sample holder of 8 mm diameter. Two cell tops were available, one directly connected to the measuring cell for a constant gap setup and one with exchangeable springs in between for a constant pressure setup. The samples were assembled in an argon filled GB with cathode, lithium and SPE films with a diameter of 6-8 mm. The closed cell was then transferred to the pressure frame outside of the GB under ambient atmosphere.

Linear sweep and cyclic voltammetry

Electrochemical stability measurements for LSV or CV were performed in Li|SPE|SS cell configurations. SPE samples (~100 µm, Ø 16 mm), Li metal (450 µm thickness, Ø 15 mm,

Rockwood Lithium, USA), and stainless-steel electrode (0.5 or 1 mm thickness, 15 mm diameter) were used in 2032-type coin cells. The amount and thickness of spacers were adjusted to reach a pressure between 0.7-1 MPa in the coin cell. If not stated otherwise LSV measurements were carried out from the OCV to 6 V vs. Li^+/Li, while CV measurements were conducted between −1 to 3 V vs. Li^+/Li. A scan rate of 0.5 mV s^{-1} at 60 °C was used.

DC polarization

The Bruce-Vincent-Evans method was employed to determine the Li^+ transference number (t_{Li^+}) of the electrolyte through DC polarization, by analyzing the change in interfacial impedance before and after polarization in symmetrical Li|SPE|Li cells at 60 °C. The values of t_{Li^+} were calculated using equation :[269,291,292]

$$t_{Li^+} = \frac{I_{SS}(\Delta V - I_0 R_{Int,0})}{I_0(\Delta V - I_{SS} R_{Int,SS})} \quad 17$$

where I_0 and I_{SS} are the current values at the initial and steady state, respectively, ΔV is the applied voltage (10 mV), $R_{Int,0}$ and $R_{Int,SS}$ are the interface resistance values before and after cell polarization, respectively, determined from the impedance spectra.

CCD and Li-shuttle

For the critical current density measurement, symmetric Li|SPE|Li cells were tested by gradually increasing the charge/discharge current density from 5 µA to 50 µA cm^{-2} at 60 °C with a standard time of 30 min for each platting/stripping step. The lithium plating and stripping behaviour of SPEs were measured using analogous Li|SPE|Li cells at the current density of 5 µA cm^{-2} for P1-VP and 10 µA cm^{-2} for P2-VP at 60 °C with a 30 min for each platting/stripping step.

Cathode preparation and half-cell testing

The optimized preparation procedure is described as follows:
$LiFePO_4$ cathodes were mixed at a mass ratio of 8:1:0.65:0.35:0.3 with carbon black (C65, carbon black SuperC65, 64 m^2 g^{-1}, TIMCAL, Switzerland), poly(ethylene oxide) (PEO, M_W = 300 kg mol^{-1}, thermo fischer scientific – Alfa Aesar, Germany), polyvinylidene difluoride (PVDF, Solef 5130, Solvay, Germany) and LiTFSI (99.95%, Sigma-Aldrich, Germany, EO/Li^+ = 13/1) with *N*-methyl-2-pyrrolidone (NMP, anhydrous, Sigma-Aldrich, Germany) as

dispersing agent in a planetary centrifugal mixer (ARV-310, Thinky Corp., USA), using a sequential mixing procedure. Mixing procedure: In a 25 mL Vial (Duran) 65 mg PEO, 35 mg PVDF and 33 mg of LiTFSI are dissolved in 2 mL NMP at 60 °C while stirring. 100 mg of C65 is added and mixed at 1500 rpm for 5 min. 800 mg LFP and 2 mL NMP is added and mixed again at 1500 rpm for 5 min. For the cycling experiments in coin cells with a lithium metal counter/reference electrode (Li-CE), the slurries (total solid content (TSC) of 25 wt%) were coated onto the rough side of an aluminum foil (δ = 18 µm, MTI, USA) with a box-type coating bar (300 µm gap, Erichsen, Germany) using an automated coater (33 mm s^{-1}, RK Print-Coat Instruments, United Kingdom). All cathode sheets were then dried in the GB for 5 days and consequently in a vacuum oven at 80 °C for 24 h before LFP working electrodes (LFP-WE, Ø 13 mm, $\delta_{coating,pressed}$ = 21 ± 3 mm) were punched out and compressed at 250 MPa for 2 min using a manual hydraulic press (Specac, United Kingdom). The LFP-WE for the cycling experiments had a loading of 3.5 ± 0.2 g_{CAM}/cm^2 which corresponds to a theoretical areal capacity of 521 ± 0.23 µAh/cm^2. Li-CEs (Ø 14 mm, δ = 450 µm, Rockwood Lithium, USA) with solid polymer electrolytes - PEO, P1-VP, and P2-VP - (Ø 16 mm, δ = 90 ± 30 mm) as separators. The half-cells were assembled with a pressure of ~0.7 MPa. All half-cell cycling tests were performed in a climate chamber (KB 115 or KB 720, Binder, Germany) at 60 °C with a CCCV protocol. Three charging-discharging cycles (with identical C-rates, C/10-C/5-C/3-1C) were performed before continuing with the next C-rate. The charging step with an upper cutoff potential of the LFP-WE of 4.0 V_{Li} included a CV hold for 1 h or until the current dropped below C/50. The discharge was performed with an identical C-rate to the previous charging step with a cutoff potential of 2.8 V_{Li}. An EIS measurement was performed after each discharging cycle at a potential of 2.8 V_{Li}.

Chronoamperometry

For temperature and pressure dependent electronic conductivity measurements of cathodes, pressed Cat disks (Ø 7 mm) were placed in an ASC-T cell in the constant pressure setup (k = 36.8 N mm^{-1}). After a 60 min OCV period for cell and temperature equilibration potentiostatic polarization was used applying voltages of 20, 40, 60, 80, and 100 mV for 3 min each. The electronic conductivity is calculated with the electronic resistance (R_{el}) determined from the difference of the average steady state current (ΔI_{SS}) of the plateaus between the voltage steps (ΔV) according to equation 18:

$$R_{el} = \frac{\Delta V}{\Delta I_{SS}} \qquad 18$$

Inserting this into equation 19 provides the electronic conductivity:

$$\sigma_{el} = \frac{\delta}{R_{el} A} \qquad 19$$

Where δ is the combined thickness of both cathode films (without the Al-foil), and A is the area of the cathode discs.

6.2 Synthesis

Vinylphosphonic dichloride

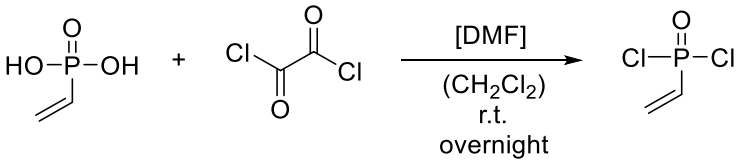

In an oven dried two-necked flask with magnetic stirrer, vinylphosphonic acid (45.0 g, 34.6 mL, 417 mmol, 1.0 eq.) is dispersed in 300 mL DCM. DMF (304 mg, 322 µL, 4.16 mmol, 0.01 eq.) is added and the dispersion is cooled to 0 °C. Next, oxalyl chloride (116 g, 78.6 mL, 916 mmol, 2.2 eq.) is added dropwise to the reaction mixture over a period of 4 h. After complete addition, the reaction is stirred at ambient temperature for 16 h. Solvent and excess oxalyl chloride is removed *in vacuo* resulting in a yellow liquid. The product is isolated via vacuum distillation (85 °C, 15 mbar) yielding vinylphosphonic dichloride as colourless liquid (46.5 g, 321 mmol, 77%).

^{1}H-NMR (400 MHz, C_6D_6, 300 K): δ (ppm) = 5.93 – 5.80 (dd, 1H, C*H*$_2$), 5.72 – 5.55 (m, 1H, C*H*), 5.27 – 5.07 (dd, 1H, C*H*$_2$).

^{31}P-NMR (162 MHz, C_6D_6, 300 K): δ (ppm) = 28.59.

^{1}H-NMR (400 MHz, $CDCl_3$, 300 K): δ (ppm) = 6.64 – 6.40 (m, 2H, C*H*$_2$, C*H*), 6.29 – 6.19 (m, 1H, C*H*$_2$).

^{31}P-NMR (162 MHz, $CDCl_3$, 300 K): δ (ppm) = 31.24.

The reduced integral of 0.75 for the proton in proximity to the phosphorous atom is attributed to the nuclear overhauser effect (NOE) which can change the relaxation time (T1) of the proton due to the coupling with ^{31}P and consequently lowers the signal intensity under the standard acquisition conditions.[293,294] The reduced intensity of this proton was observed for multiple spectra in C_6D_6 but is notably reduced in $CDCl_3$ (**Figure 6-3**).

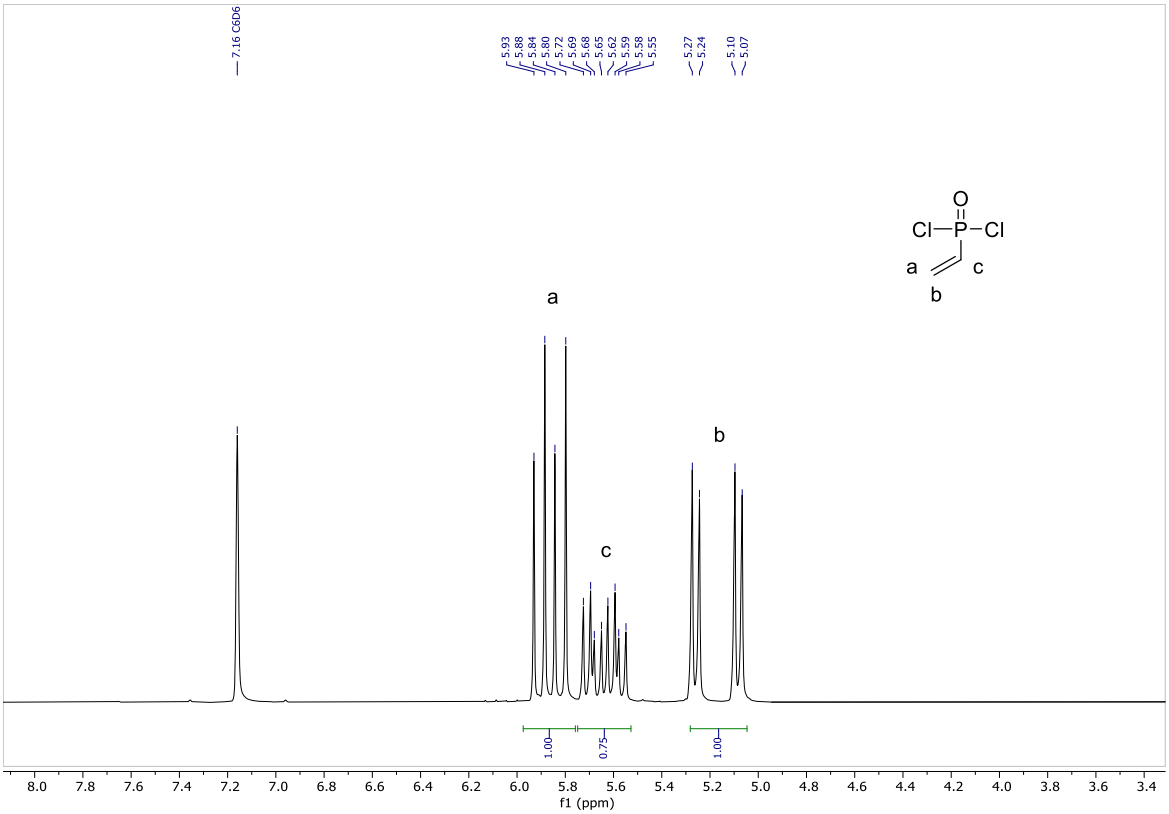

Figure 6-1: ^{1}H-NMR spectrum of vinylphosphonic dichloride in C_6D_6 (δ = 7.16 ppm) at 400 MHz.

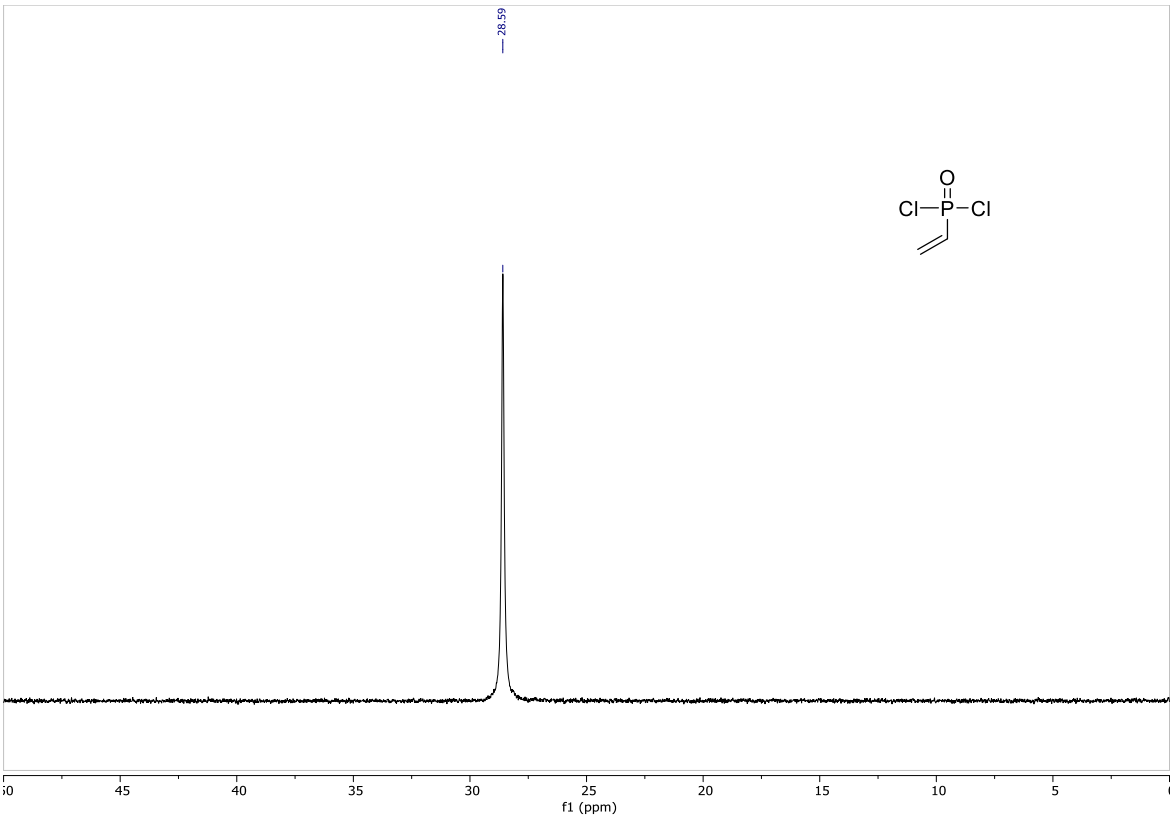

Figure 6-2: ^{31}P-NMR spectrum of vinylphosphonic dichloride in C_6D_6 at 162 MHz.

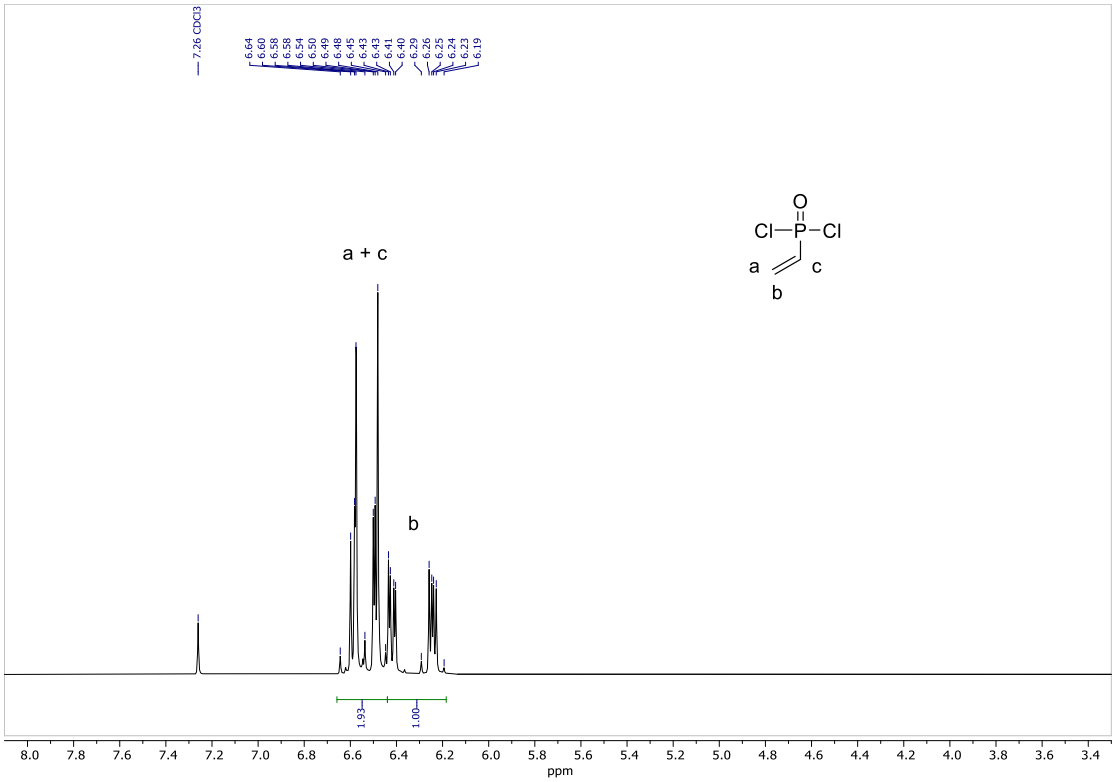

Figure 6-3: ^{1}H-NMR spectrum of vinylphosphonic dichloride in $CDCl_3$ (δ = 7.26 ppm) at 400 MHz.

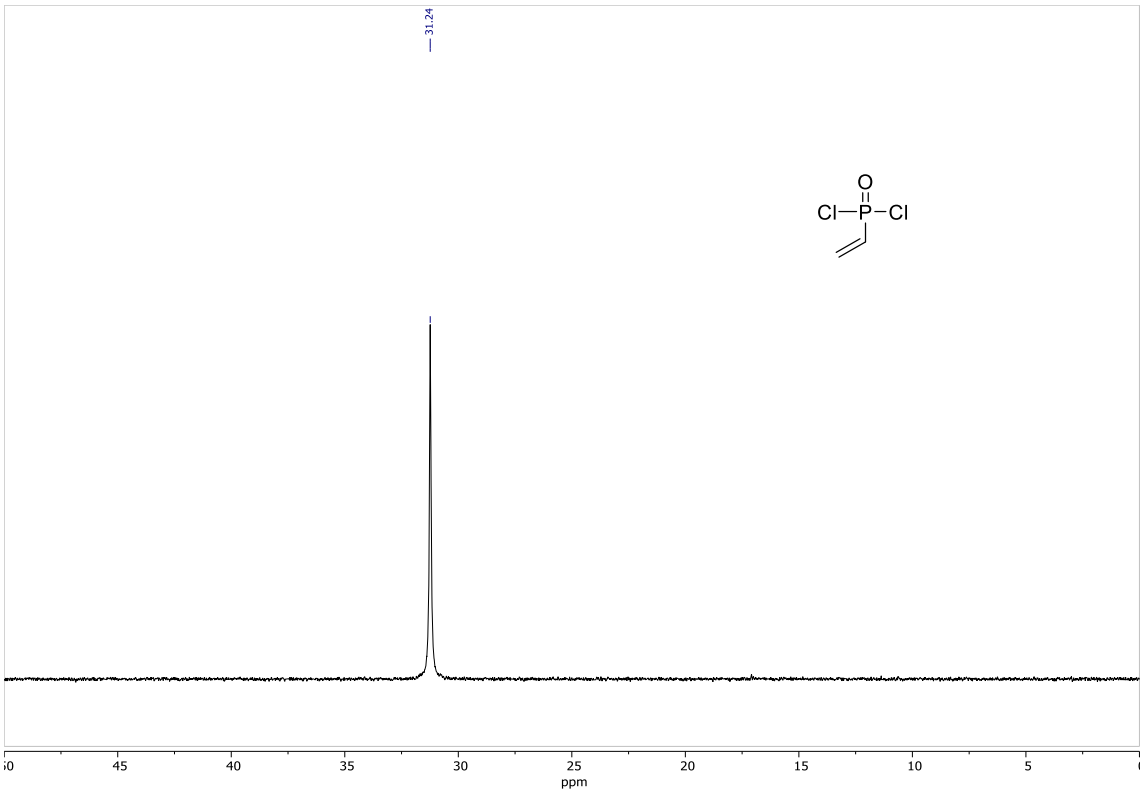

Figure 6-4: ^{31}P-NMR spectrum of vinylphosphonic dichloride in $CDCl_3$ at 162 MHz.

Bis(2-methoxyethyl) vinylphosphonate (1-VP)

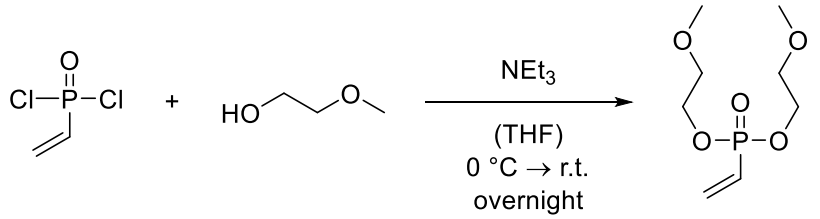

In an oven dried two-necked flask with magnetic stirrer, methoxyethanol (10.0 g, 10.5 mL, 132 mmol, 2.1 eq.) and vinylphosphonic dichloride (9.10 g, 6.50 mL, 62.8 mmol, 1.0 eq.) are dissolved in 100 mL THF. After cooling to 0 °C, NEt_3 (14.0 g, 19.3 mL, 138 mmol, 2.2 eq.) is added dropwise to the solution. After complete addition, the reaction is heated to ambient temperature and stirred for 16 h. Next, the precipitated NH_4Cl is removed via Whatman filtration and the THF and residual NEt_3 is removed *in vacuo*. The resulting crude yellowish product is then dried with an activated Al_2O_3 column (dry DCM used as eluent) and purified via vacuum distillation (110 °C, $2 \cdot 10^{-2}$ mbar), yielding 1-VP as colourless liquid (11.3 g, 50.2 mmol, 80%). The monomer is stored over activated 4 Å molecular sieves for two weeks prior to polymerization.

^{1}H-NMR (400 MHz, $CDCl_3$, 300 K): δ (ppm) = 6.38 – 6.25 (m, 1H, C*H*), 6.21 – 6.04 (m, 1H, C*H*), 4.18 – 4.14 (m, 4H, O-CH_2), 3.59 (t, *J* = 5.1 Hz, 4H, O-CH_2), 3.59 (s, 6H, O-CH_3).

^{31}P-NMR (162 MHz, $CDCl_3$, 300 K): δ (ppm) = 18.38.

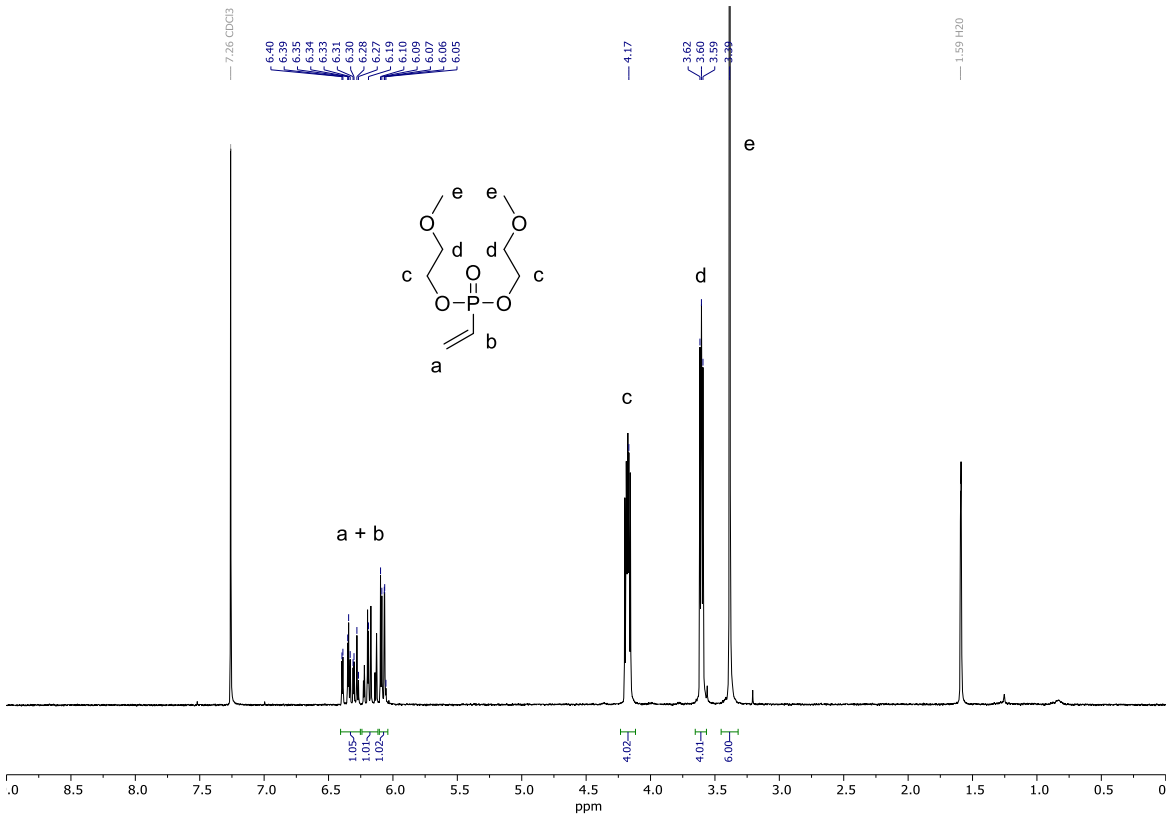

Figure 6-5: ^{1}H-NMR spectrum of 1-VP in $CDCl_3$ (δ = 7.26 ppm) at 400 MHz. H_2O peak origin from the solvent ($CDCl_3$).

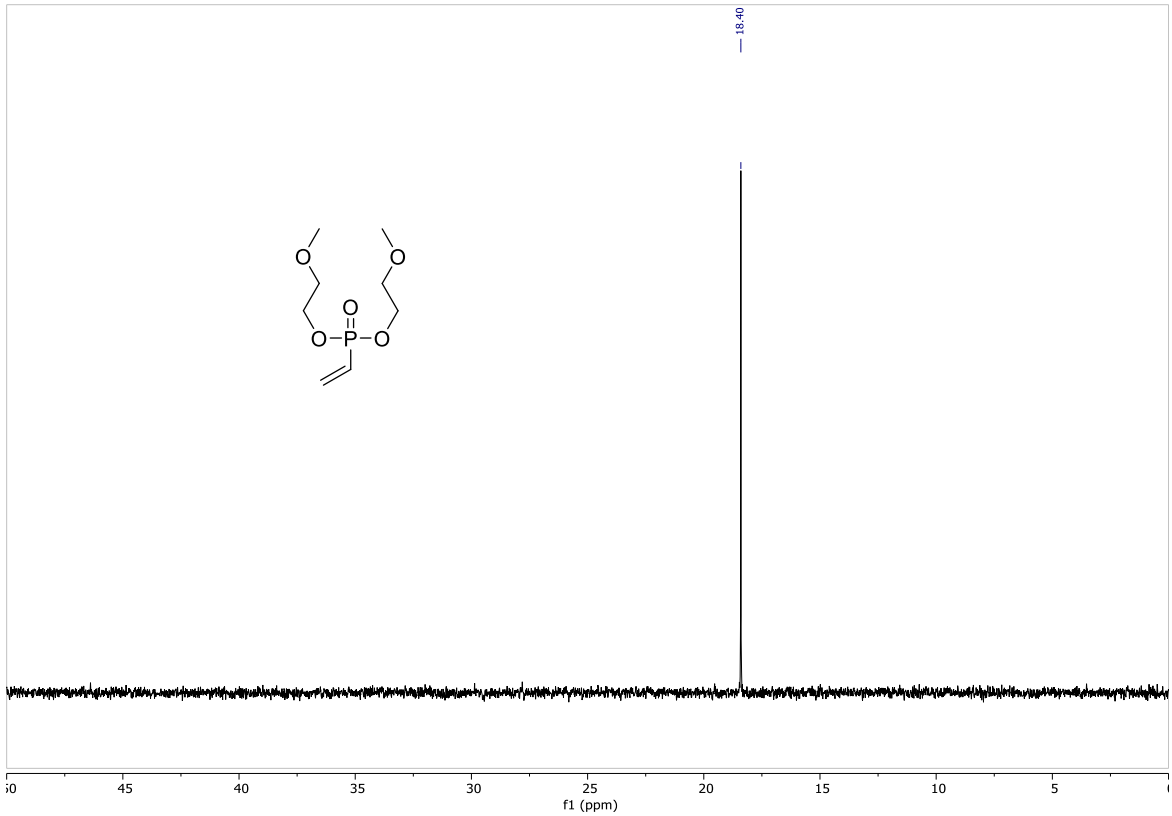

Figure 6-6: ^{31}P-NMR spectrum of 1-VP in $CDCl_3$ at 162 MHz.

Bis(2-(2-methoxyethoxy)ethyl) vinylphosphonate (2-VP)

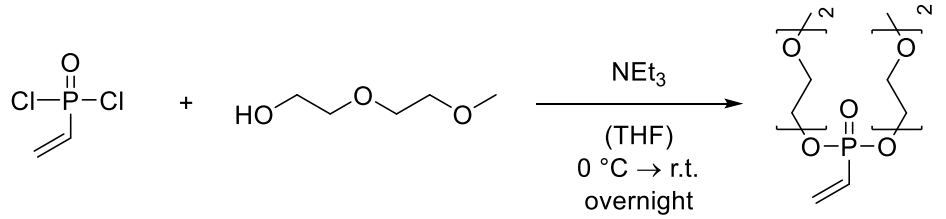

In an oven dried two-necked flask with magnetic stirrer, diethylene glycol monomethyl ether (15.8 g, 15.5 mL, 132 mmol, 2.1 eq.) and vinylphosphonic dichloride (9.10 g, 6.50 mL, 62.8 mmol, 1.0 eq.) are dissolved in 100 mL THF. After cooling to 0 °C NEt_3 (14.0 g, 15.5 mL, 132 mmol, 2.2 eq.) is added dropwise to the solution. After complete addition the reaction is heated to ambient temperature and stirred for 16 h. Next, the precipitated NH_4Cl is removed by Whatman filtration and the THF and residual NEt_3 is removed *in vacuo*. 20 mL of water is added to the crude product and the aqueous phase is extracted with DCM (4 × 30 mL). The organic phases are then combined, dried over $MgSO_4$, filtered, and the solvent removed in vacuo, yielding a yellowish liquid. The product is then dried with an activated Al_2O_3 column (dry DCM used as eluent) and purified by vacuum distillation (130 °C, $5 \cdot 10^{-3}$ mbar) yielding 3-VP as colourless liquid (14.3 g, 45.8 mmol, 73%). The monomer is stored over activated 4 Å molecular sieves for two weeks prior to polymerization.

^{1}H-NMR (400 MHz, $CDCl_3$, 300 K): δ (ppm) = 6.28 (dd, *J* = 18.7 Hz, 1H, C*H*), 5.95 (dd, *J* = 18.7 Hz, 1H, C*H*), 5.57 (dd, *J* = 12.7 Hz, 1H, C*H*), 4.10 – 4.06 (m, 4H, P-O-CH_2), 3.42 – 3.37 (m, 8H, O-CH_2), 3.29 – 3.27 (m, 4H, O-CH_2), 3.59 (s, 6H, O-CH_3).

^{31}P-NMR (162 MHz, $CDCl_3$, 300 K): δ (ppm) = 17.73.

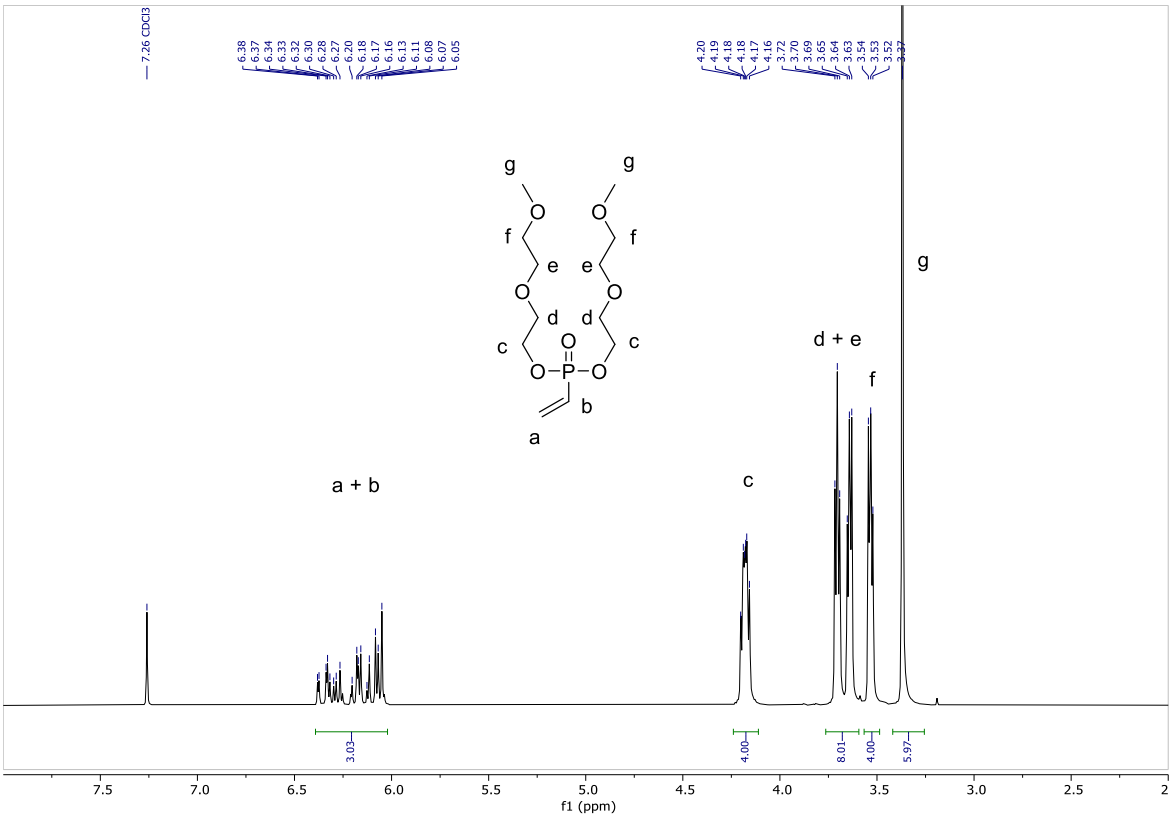

Figure 6-7: ^{1}H-NMR spectrum of 2-VP in $CDCl_3$ (δ = 7.26 ppm) at 400 MHz.

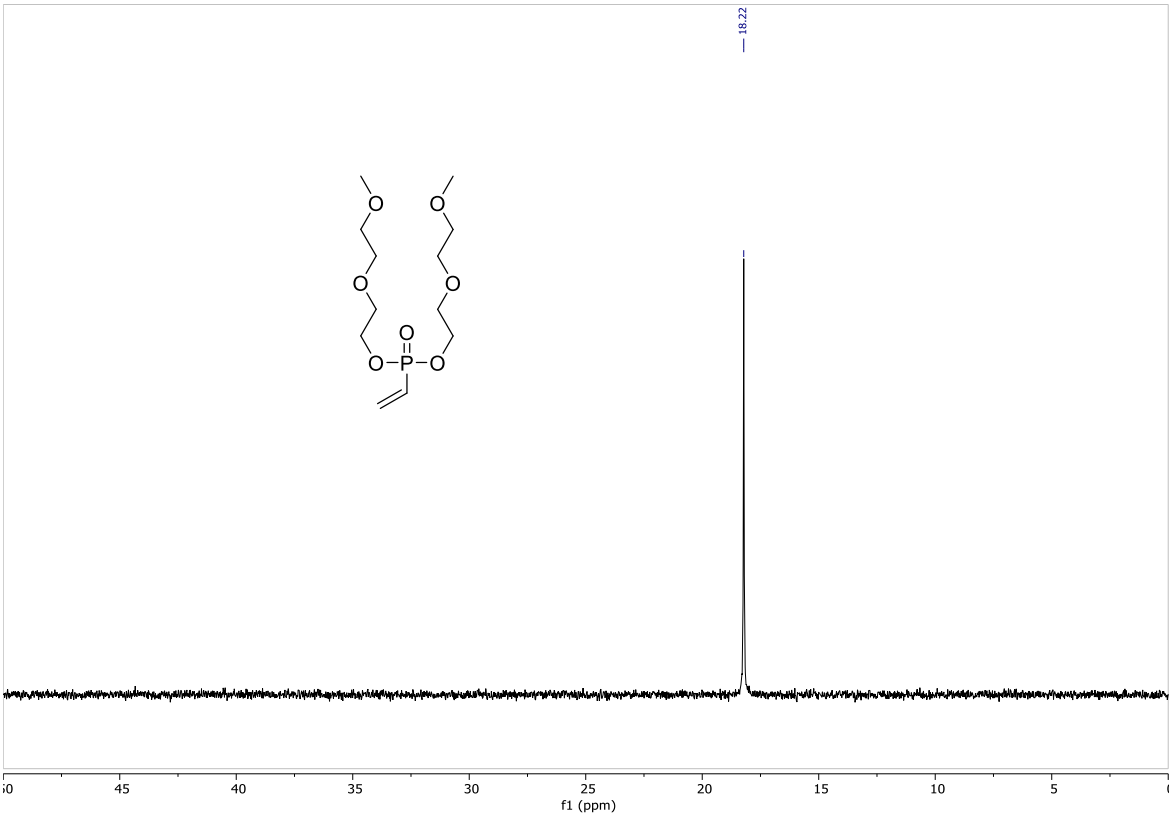

Figure 6-8: ^{31}P-NMR spectrum of 2-VP in $CDCl_3$ at 162 MHz.

Bis(2-(2-(2-methoxyethoxy)ethoxy)ethyl) vinylphosphonate (3-VP)

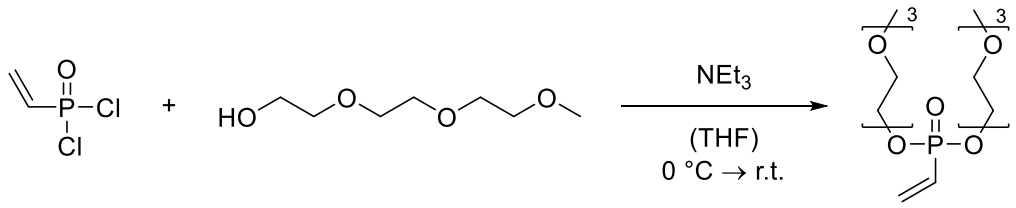

In an oven dried 1 L two-necked flask with magnetic stirrer, triethylene glycol monomethyl ether (30.0 g, 29.1 mL, 183 mmol, 2.1 eq.) and vinylphosphonic dichloride (12.6 g, 9.01 mL, 87.0 mmol, 1.0 eq.) are dissolved in 500 mL THF. After cooling to 0 °C NEt_3 (18.9 g, 25.9 mL, 187 mmol, 2.2 eq.) is added dropwise to the solution. After complete addition the ice bath is removed, and the reaction is stirred overnight. Next, the precipitated NH_4Cl is removed by Whatman filtration and the THF and residual NEt_3 is removed *in vacuo*. The crude product is purified by vacuum distillation (240 °C, $3 \cdot 10^{-5}$ mbar) yielding bis(2-(2-(2-methoxyethoxy)ethoxy)ethyl) vinylphosphonate as colourless liquid (20.9 g, 52.2 mmol, 60%).

^{1}H-NMR (400 MHz, $CDCl_3$, 300 K): δ (ppm) = 6.35 – 6.01 (m, 3H, P-C*H*-CH_2), 4.19 – 4.09 (m, 4H, P-O-CH_2), 3.68 – 3.59 (m, 16H, O-CH_2-O), 3.52 – 3.50 (m, 4H, P-O-CH_2-), 3.34 (s, 6H, -CH_3).

^{31}P-NMR (162 MHz, $CDCl_3$, 300 K): δ (ppm) = 17.73.

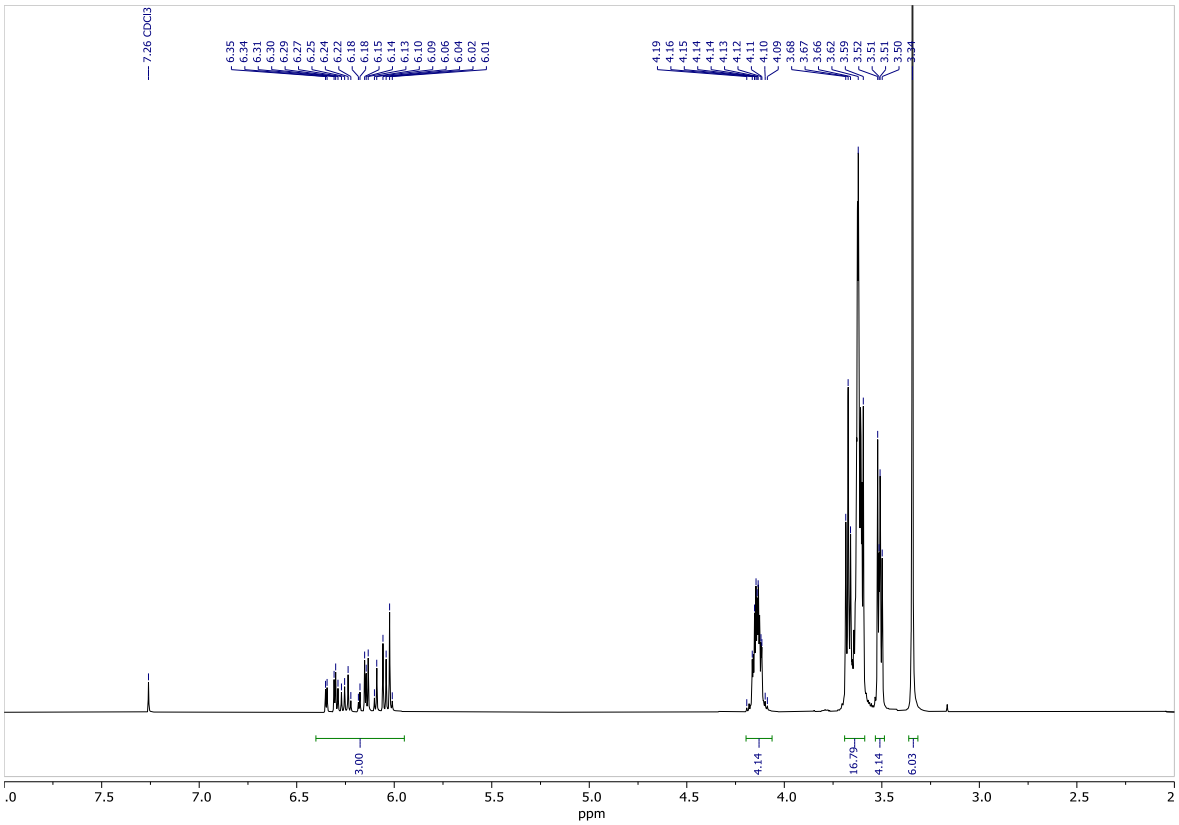

Figure 6-9: ^{1}H-NMR spectrum of 3-VP in $CDCl_3$ (δ = 7.26 ppm) at 400 MHz.

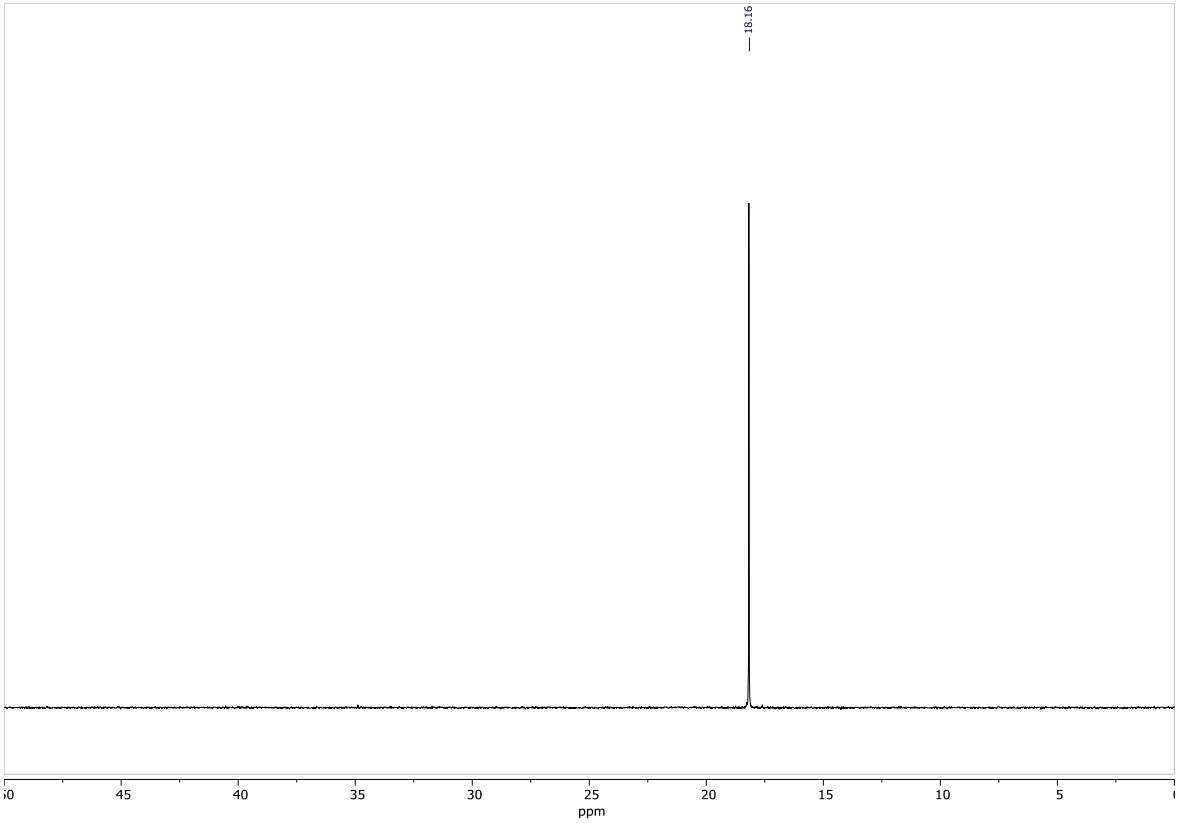

Figure 6-10: ^{31}P-NMR spectrum of 3-VP in $CDCl_3$ at 162 MHz.

7-VP Synthesis

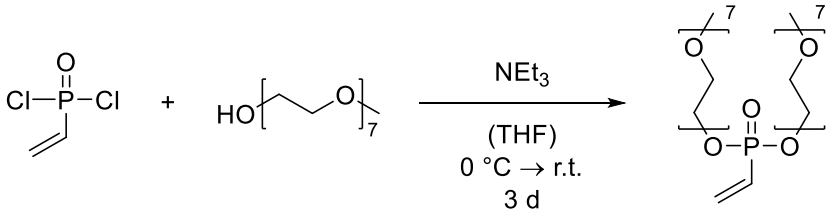

In an oven dried 250 mL two-necked flask with magnetic stirrer, polyethylenglykol monomethylether (14.6 g, 41.7 mmol, 2.1 eq.; average M = 350 g mol^{-1}, corresponds to 7-8 rep. units) and vinylphosphonic dichloride (3.03 g, 2.16 mL, 20.9 mmol, 1.0 eq.) are dissolved in 120 mL THF. After cooling to 0 °C NEt_3 (4.44 g, 6.12 mL, 43.9 mmol, 2.2 eq.) is added dropwise to the solution. After complete addition the ice bath is removed, and the reaction is stirred for 72 h. Next, the precipitated NH_4Cl is removed by Whatman filtration and the THF and residual NEt_3 is removed *in vacuo*. The crude product is purified by column chromatography (DCM/MeOH = 99/1 gradient to 96/4) yielding the vinylphosphonate monomer 7-VP as colorless liquid (1.50 g, 6.69 mmol, 32%). A $KMnO_4$ staining solution was used to check the chromatography process on silica thin layer chromatography plates. *p*-Anisaldehyde and CAM stain were also tested but gave worse results.

^{1}H-NMR (400 MHz, $CDCl_3$, 300 K): δ (ppm) = 6.38 – 6.04 (m, 3H, P-C*H*-CH_2), 4.21 – 4.10 (m, 4H, P-O-CH_2), 3.70 – 3.63 (m, 52H, O-CH_2-O), 3.55 – 3.53 (m, 4H, P-O-CH_2-), 3.37 (s, 6H, -CH_3).

^{31}P-NMR (162 MHz, $CDCl_3$, 300 K): δ (ppm) = 18.23.

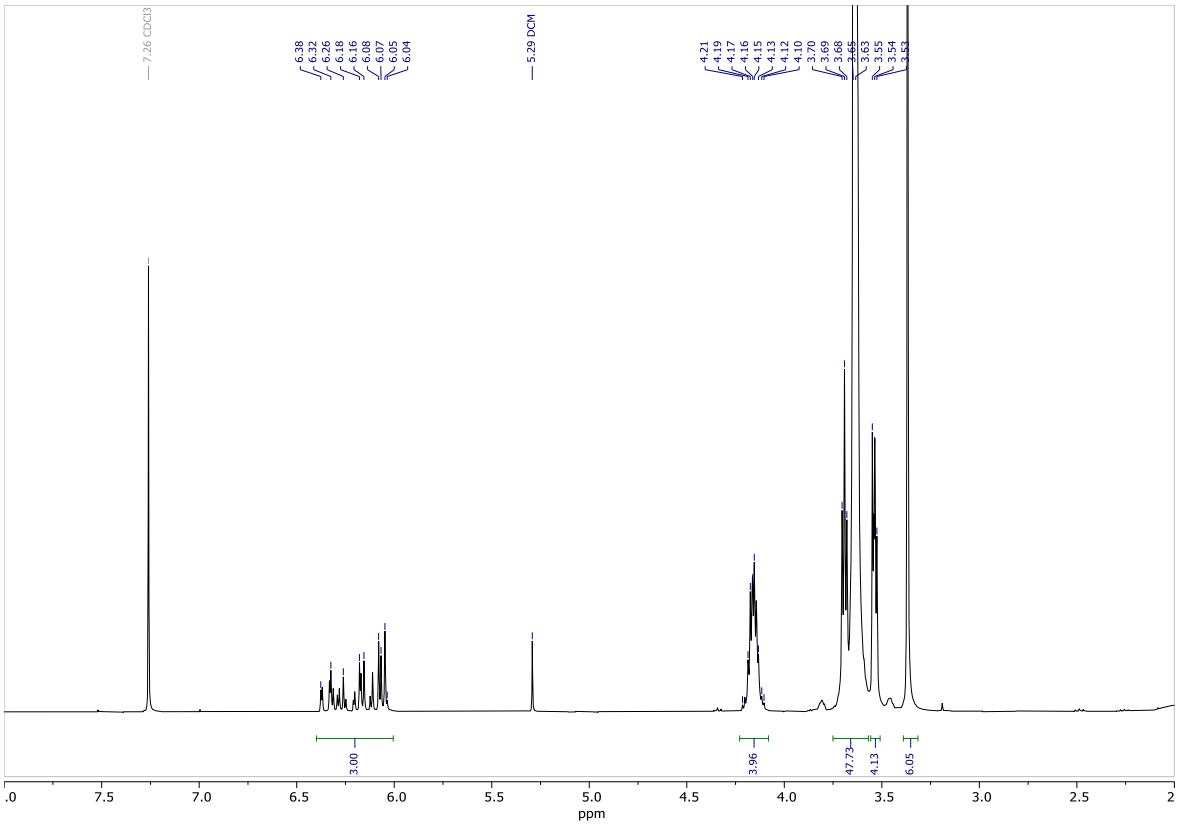

Figure 6-11: ^{1}H-NMR spectrum of 7-VP in $CDCl_3$ (δ = 7.26 ppm) at 400 MHz.

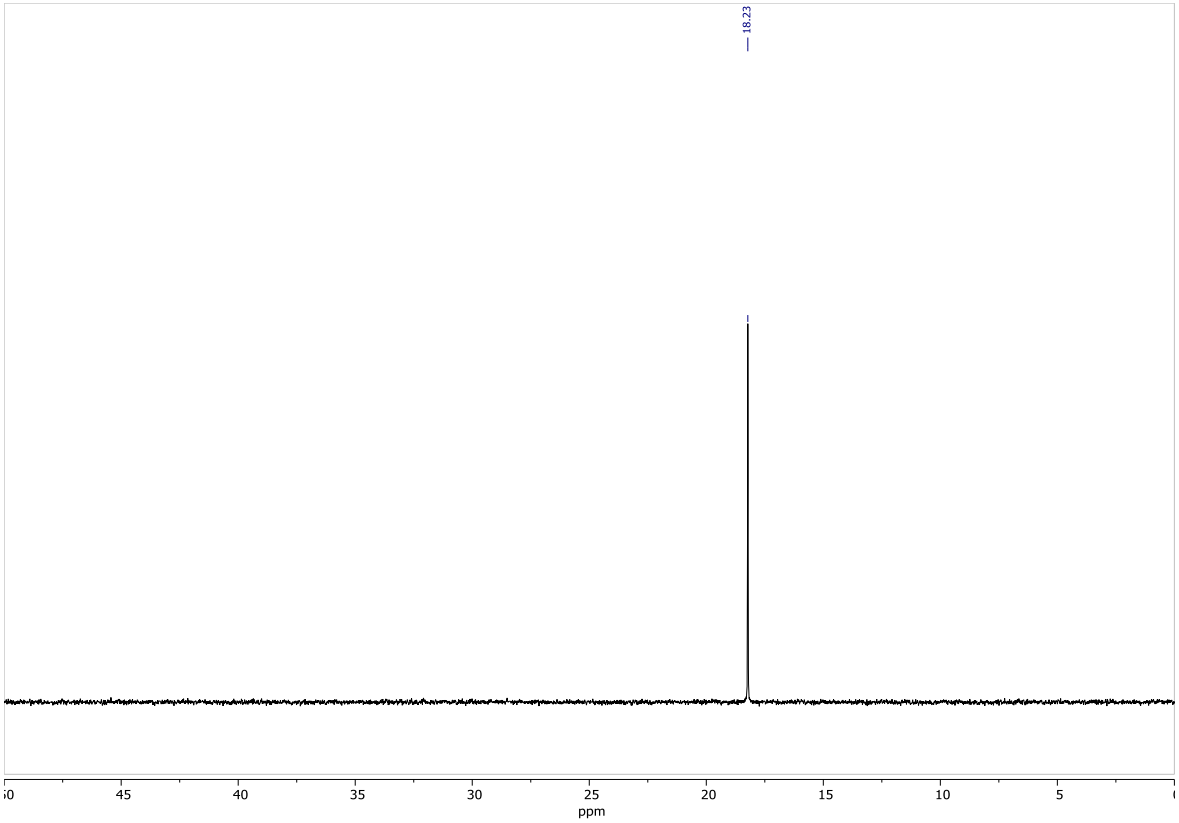

Figure 6-12: ^{31}P-NMR spectrum of 7-VP in $CDCl_3$ at 162 MHz.

2-(2-Hydroxyethoxy)ethyl methyl carbonate

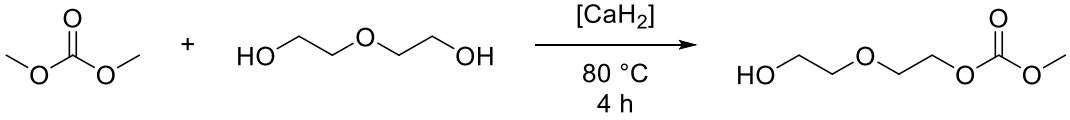

Potassium carbonate (3.1 g, 22.2 mmol, 0.3 eq.), dimethyl carbonate (8.0 g, 88.8 mmol, 1.0 eq.) and diethylene glycol (9.4 g, 88.8 mmol, 1.0 eq.) are dissolved in 100 mL of THF. Afterwards, the mixture is heated up to 65 °C for 4 h and filtrated. Subsequently, the solvent is removed and the residue is distilled at 130 °C and 5 mbar. The synthesis was adapted from literature but could not be purified to satisfaction.[295,296]

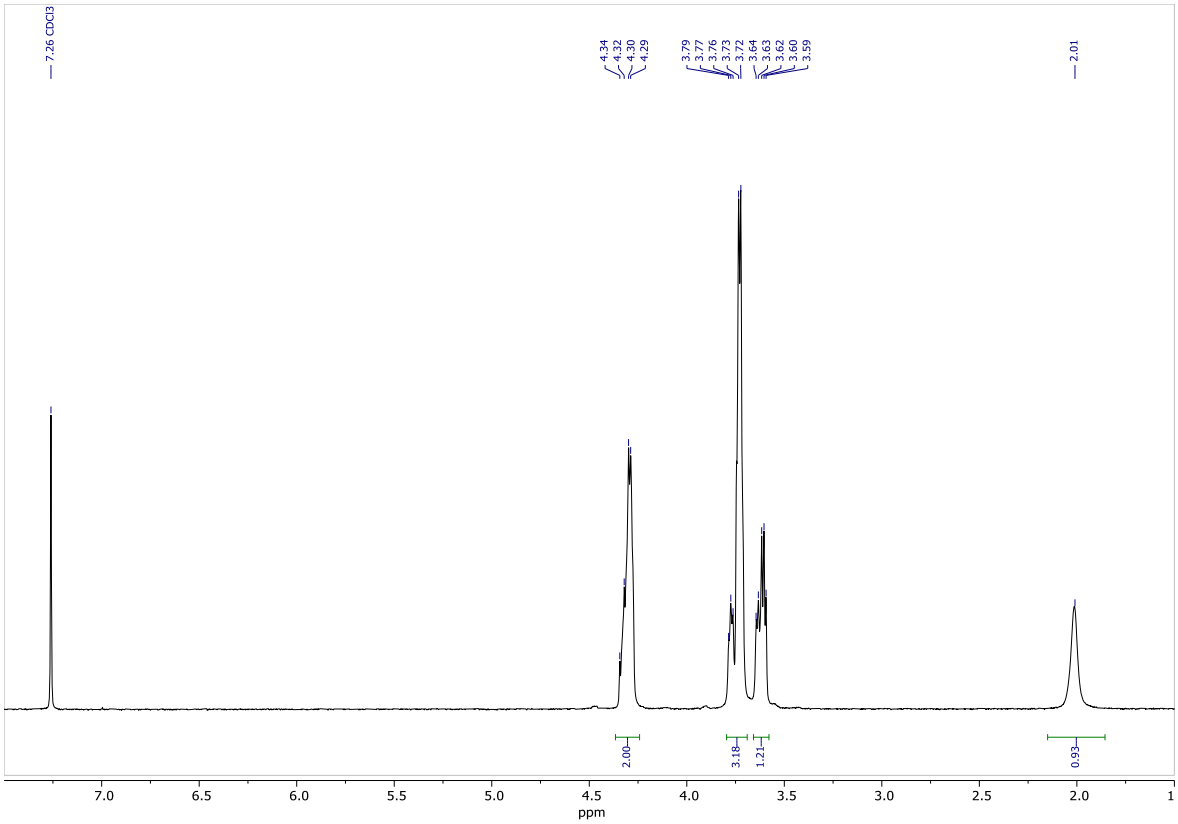

Figure 6-13: ^{1}H-NMR spectrum of 2-(2-Hydroxyethoxy)ethyl methyl carbonatein $CDCl_3$ (δ = 7.26 ppm) at 400 MHz.

Bis((2-oxo-1,3-dioxolan-4-yl)methyl) vinylphosphonate

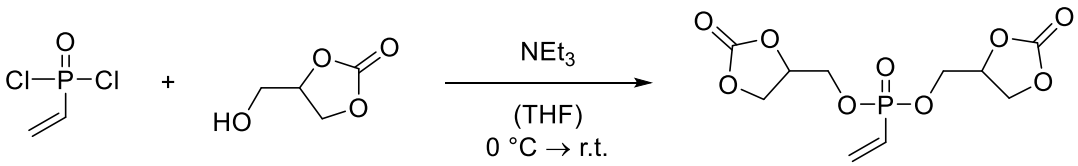

In an oven-dried 1 L two-necked flask with a magnetic stirrer, 4-(hydroxymethyl)-1,3-dioxolan-2-one (25. g, 17.9 mL, 191 mmol, 2.2 eq.) and vinylphosphonic dichloride (12.6 g, 8.97 mL, 86.6 mmol, 1.0 eq.) are dissolved in 500 mL THF and cooled to 0 °C. NEt_3 (20.2 g, 27.8 mL, 199 mmol, 2.3 eq.) is added dropwise to the solution. After complete addition, the reaction mixture is stirred for 2 h at 0 °C, then subsequently for an additional 4 days at room temperature. Afterward, 400 mL water is added, and the solvent is evaporated. The aqueous phase is extracted with dichloromethane (6 × 300 mL). The crude product is obtained as an orange solution.

Further attempts to purify the product via distillation and column chromatography were unsuccessful.

Tris(cyclopentadienyl)yttrium(III) (YCp3)

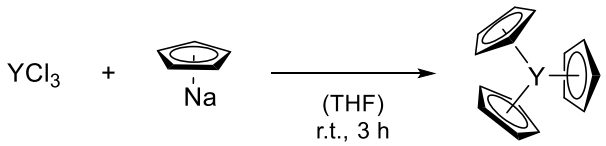

In an oven dried Schlenk tube with a magnetic stirring bar NaCp (505 mg, 5.74 mmol, 4.0 eq.) is dissolved in 2.5 mL THF giving an orange solution. YCl_3 (280 mg, 1.43 mmol, 1.0 eq.) is suspended in 3 mL THF and dropwise added to the NaCp solution. After complete addition the reaction mixture is stirred at r.t. for 3 h. The solvent is removed *in vacuo* and the product is purified by sublimation (100 °C, $2 \cdot 10^{-2}$ mbar) yielding YCp_3 as colorless crystals (252 mg, 0.88 mmol, 62%).

Tris(cyclopentadienyl)yttrium(III)-THF adduct (YCp_3·THF)

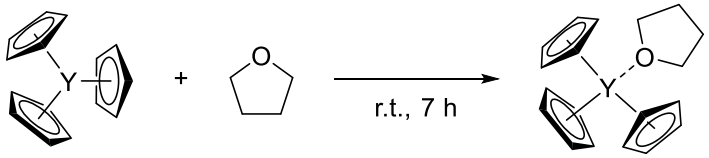

YCp_3 (252 mg, 0.88 mmol, 1.0 eq.) is suspended in 9 mL THF and stirred for 7 h. Subsequently, the solvent is removed *in vacuo* giving the THF adduct (**6**) as white power (316 mg, 0.88 mmol, 100%).

^{1}H-NMR (400 MHz, C_6C_6, 300 K): δ (ppm) = 5.94 (s, 15H, Cp-*H*), 3.32 – 3.28 (m, 4H, THF-*H*), 1.15 – 1.11 (m, 4H, THF-*H*).

Trimethylsilylmethyl lithium

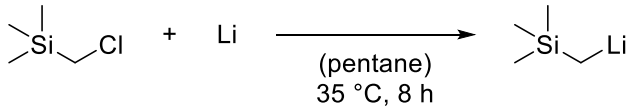

In a Schlenk tube Lithium granulate (1.49 g, 215 mmol, 3.3 eq.) is suspended in 100 mL hexane and while stirring chlorotrimethylsilane (8.00 g, 9.10 mL, 65.2 mmol, 1.0 eq) is added. The reaction mixture is stirred for 8 h at 35 °C while the Schlenk tube is placed hourly in an ultrasonic bath for 2 min. Subsequently, the violet reaction mixture is filtrated and the residue is extracted with pentane (3 × 4 mL). The solvents are removed in vacuo yielding trimethylsilylmethyl lithium a colourless powder (4.51 g, 47.9 mmol, 73%).

^{1}H-NMR (400 MHz, C_6C_6, 300 K): δ (ppm) = 0.16 (s, 9H, CH_3), -2.07 (s, 2H, CH_2).

$Y(CH_2TMS)_3(THF)_2$

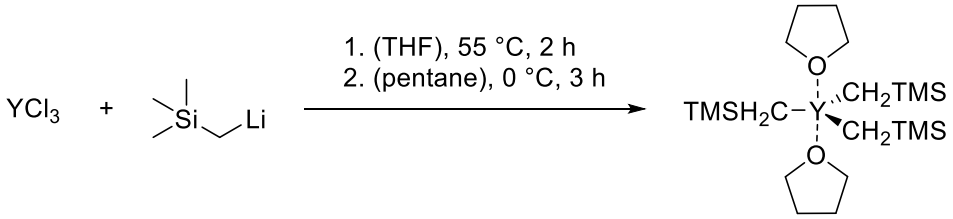

In a Schlenk flask YCl_3 (1.50 g, 7.68 mmol, 1.0 eq.) is suspended in 55 mL THF and stirred at 55 °C for 2 h. Followingly, the THF is removed *in vacuo* and the residue is suspended in

60 mL pentane. The reaction mixture is cooled to 0 °C and slowly a solution of $LiCH_2TMS$ (2.17 g, 23.1 mmol, 3.0 eq.) in 40 mL pentane is added. The resulting mixture is stirred at 0 °C for 3 h and then filtrated and the solvents removed *in vacuo* giving $Y(CH_2TMS)_3(THF)_2$ as a colourless solid (2.01 g, 4.06 mmol, 53%).

^{1}H-NMR (400 MHz, C_6C_6, 300 K): δ (ppm) = 3.96 – 3.93 (m, 8H, THF-*H*), 1.32 – 1.29 (m, 8H, THF-*H*), 0.30 (s, 27H, TMS-*H*), -0.68 (d, *J* = 2.65 Hz, 6H, C*H*$_2$).

^{13}C-NMR (100 MHz, C_6C_6, 300 K): δ (ppm) = 70.7, 33.9, 33.5, 25.1, 4.6.

^{29}Si-NMR (100 MHz, C_6C_6, 300 K): δ (ppm) = -4.6.

Synthesis of $Cp_2YCH_2TMS(THF)$

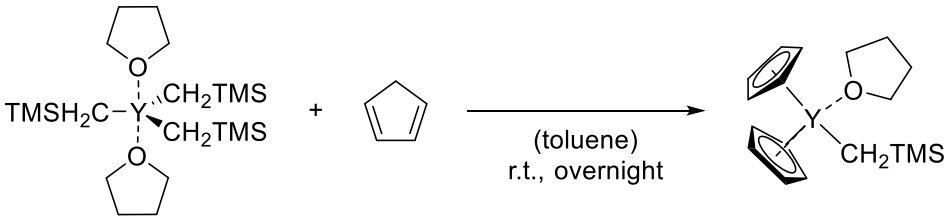

$Y(CH_2TMS)_3(THF)_2$ (1.90 g, 3.84 mmol, 1.0 eq.) is dissolved in 35 mL toluene and cooled to 0 °C. freshly cracked cyclopentadiene (507 mg, 7.69 mmol, 2.0 eq.) is added dropwise at room temperature. The mixture is stirred overnight. The volatile compounds are removed *in vacuo* and the product is recrystallized from benzene giving $Cp_2YCH_2TMS(THF)$ as white needles (912 mg, 2.42 mmol, 63%).

^{1}H-NMR (400 MHz, C_6C_6, 300 K): δ (ppm) = 6.12 (s, 10H, Cp-*H*), 2.98 – 2.93 (m, 4H, THF-*H*), 0.95 – 0.90 (m, 4, THF-*H*), 0.43 (s,*9*H, TMS-*H*), -0.67 (d, *J* = 3.54 Hz, 2H, C*H*$_2$).

^{13}C-NMR (100 MHz, C_6C_6, 300 K): δ (ppm) = 110.4, 71.2, 25.4, 24.9, 4.8.

^{29}Si-NMR (100 MHz, C_6C_6, 300 K): δ (ppm) = -3.0.

Activation of $Cp_2YCH_2TMS(THF)$ with *sym*-collidine

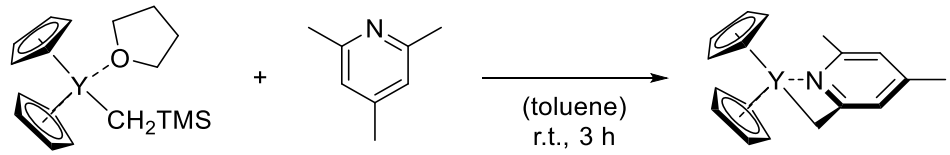

$Cp_2YCH_2TMS(THF)$ (365 mg, 0.96 mmol, 1.0 eq.) is dissolved in 7 mL toluene and *sym*-collidine (117 mg, 0.96 mmol, 1.0 eq.) is added giving a yellow solution. After stirring at r.t. for 3 h the complete activation of the catalyst could be certified *via* aliquot NMR and the solution is further used in polymerization reactions.

For isolation of the catalyst the volatile compounds are removed in *vacuo* and the residue is recrystallized from a toluene pentane mixture yielding YCp_2(*sym*-collidine) as yellow crystals (247 mg, 0.73 mmol, 76%).

^{1}H-NMR (400 MHz, C_6C_6, 300 K): δ (ppm) = 6.41 (s, 1H, Py-*H*), 6.05 (s, 10H, Cp-*H*), 5.80 (s, 1H, Py-*H*), 2.83 (s, 3H, C*H*$_3$), 2.44 (s, 2H, C*H*$_2$), 1.79 (s, 3H, C*H*$_3$).

7 References

[1] A. Ghafari, V. Bayat, S. Akbari, A. Yeklangi, *J NanoSci Tec* **2023**, *8*, 24–42, DOI 10.52319/j.nanoscitec.2023.21.

[2] A. Manthiram, *ACS central science* **2017**, *3*, 1063–1069, DOI 10.1021/acscentsci.7b00288.

[3] E. Sayed, A. Olabi, A. Alami, A. Radwan, A. Mdallal, A. Rezk, M. Abdelkareem, *Energies* **2023**, *16*, 1415, DOI 10.3390/en16031415.

[4] A. A. Kebede, T. Kalogiannis, J. van Mierlo, M. Berecibar, *Renewable and Sustainable Energy Reviews* **2022**, *159*, 112213, DOI 10.1016/j.rser.2022.112213.

[5] Z. Zhu, T. Jiang, M. Ali, Y. Meng, Y. Jin, Y. Cui, W. Chen, *Chemical reviews* **2022**, *122*, 16610–16751, DOI 10.1021/acs.chemrev.2c00289.

[6] Volta Foundation, Battery Report **2024**

[7] G. Bockey, H. Heimes, Atlas Maps: Asia, Battery Cell Production, https://battery-news.de/wp-content/uploads/2023/08/230804_Asia_BP-1.png, (accessed: 17.02.2025).

[8] G. Bockey, H. Heimes, Atlas Maps: North America, Battery Cell Production, https://battery-news.de/wp-content/uploads/2024/08/240716_Battery-Cell-Production_North-America_ACT.jpg, (accessed: 17.02.2025).

[9] G. Bockey, Atlas Maps: Europe, Battery Cell Production, https://battery-news.de/wp-content/uploads/2024/12/241212_EU_BP.png, (accessed: 17.02.2025).

[10] Northvolt, *Sustainability and Annual report* **2023**.

[11] C. Oemisch, S. Ernst, *Volkswagen media information No. 96/2021.* **2021**.

[12] European Investment Bank, Sweden: EIB finances Northvolt's battery factory with over $1 billion, https://www.eib.org/en/press/all/2024-011-eib-finances-northvolt-s-battery-factory-with-over-usd1-billion, (accessed: 17.02.2025).

[13] 36Kr, Northvolt's fall: How hubris and blunders shattered Europe's battery ambitions | KrASIA, https://kr-asia.com/northvolts-fall-how-hubris-and-blunders-shattered-europes-battery-ambitions, (accessed: 17.02.2025).

[14] Sebastian Schaal, Nach Produktionsstopp in Schweden: Arbeiten an Northvolt-Fabrik Heide laufen weiter - electrive.net, https://www.electrive.net/2025/05/23/nach-

angekuendigtem-produktionsstopp-in-schweden-arbeiten-an-northvolt-fabrik-heide-laufen-weiter/, (accessed: 26.05.2025).

[15] Urquhart, Tim - S&P Automotive Insights, CATL and BYD Battery Tech Could Disrupt the Global BEV market, https://www.spglobal.com/automotive-insights/en/blogs/2025/04/catl-byd-battery-tech-news?, (accessed: 11.05.2025).

[16] BYD, BYD Unveils Super e-Platform with Megawatt Flash Charging for Electric Vehicles, Matching Refueling Speeds, https://www.byd.com/mea/news-list/byd-unveils-super-e-platform-with-megawatt-flash-charging, (accessed: 11.05.2025).

[17] CATL, Naxtra Battery Breakthrough & Dual-Power Architecture: CATL Pioneers the Multi-Power Era, https://www.catl.com/en/news/6401.html, (accessed: 11.05.2025).

[18] F. Chimits, C. McMafferey, J. Mejino Lopez, Poitiers, Niclas, Frederic, V. Vicard, P. Wibaux, *European Economic Security: current practices and further development* **2024**.

[19] T. Gehrke, Recharge or regret: Why the EU must act decisively to secure Europe's struggling battery industry, https://ecfr.eu/article/recharge-or-regret-why-the-eu-must-act-decisively-to-secure-europes-struggling-battery-industry/, (accessed: 17.02.2025).

[20] J. Eddy, A. Pfeiffer, J. van de Staaij, The 2040 outlook for EV battery manufacturing | McKinsey, https://www.mckinsey.com/industries/oil-and-gas/our-insights/recharging-economies-the-ev-battery-manufacturing-outlook-for-europe#/, (accessed: 18.04.2025).

[21] H.-D. Lim, J.-H. Park, H.-J. Shin, J. Jeong, J. T. Kim, K.-W. Nam, H.-G. Jung, K. Y. Chung, *Energy Storage Mater.* **2020**, *25*, 224–250, DOI 10.1016/j.ensm.2019.10.011.

[22] R. Götz, R. Streng, J. Sterzinger, T. Steeger, M. M. Kaye, M. Vitort, A. S. Bandarenka, *InfoMat* **2024**, *6*, e12627, DOI 10.1002/inf2.12627.

[23] S. Link, C. Neef, T. Wicke, T. Hettesheimer, M. Diehl, O. Krätzig, F. Degen, F. Klein, P. Fanz, M. Burgard et al., *Development perspectives for lithium-ion battery cell formats 2022*, Fraunhofer-Gesellschaft. **2022,** DOI 10.24406/PUBLICA-1321.

[24] S. Schaal, BYD hat schon erste Feststoffzellen produziert - electrive.net, https://www.electrive.net/2025/02/17/byd-hat-schon-erste-feststoffzellen-produziert/, (accessed: 11.05.2025).

[25] P. Zhang, CATL ups bet on all-solid-state batteries, begins sample validation, report says, https://cnevpost.com/2024/11/06/catl-solid-state-batteries-begin-sample-validation-report/, (accessed: 11.05.2025).

[26] Maxell, All-Solid-State Batteries, https://www.maxell.eu/industry/all-solid-state-batteries/, (accessed: 11.05.2025).

[27] G. Bockey, Maxell beendet Produktion prismatischer Batterien - Battery-News, https://battery-news.de/2025/03/24/maxell-beendet-produktion-prismatischer-batterien/, (accessed: 11.05.2025).

[28] BloombergNEF, New Lithium Battery Technology Set to Disrupt Storage Market, https://about.bnef.com/blog/new-lithium-battery-technology-set-to-disrupt-storage-market/, (accessed: 11.05.2025).

[29] R. Korthauer, *Lithium-Ion Batteries: Basics and Applications*, Springer Berlin Heidelberg. **2018,** DOI 10.1007/978-3-662-53071-9.

[30] D. Pritzl, Electrochemical Impedance Spectroscopy (EIS) and Surface Analysis of High-Energy Cathodes for Lithium-Ion Batteries, Ph.D. Dissertation, Technical University of Munich, **2019**.

[31] K. Xu, *Chemical reviews* **2004**, *104*, 4303–4417, DOI 10.1021/cr030203g.

[32] G. J. May, A. Davidson, B. Monahov, *Journal of Energy Storage* **2018**, *15*, 145–157, DOI 10.1016/j.est.2017.11.008.

[33] Y. Kato, Z. Ogumi, J. M. Perlando Martín, *Lithium ion batteries*. *Overview, simulation, and diagnostics*, Pan Stanford Publishing Pte. Ltd. **2019,** DOI 10.1201/9780429259340.

[34] Y. Sato, S. Takeuchi, K. Kobayakawa, *Journal of Power Sources* **2001**, *93*, 20–24, DOI 10.1016/S0378-7753(00)00506-1.

[35] J.-F. Ding, Y.-T. Zhang, R. Xu, R. Zhang, Y. Xiao, S. Zhang, C.-X. Bi, C. Tang, R. Xiang, H. S. Park et al., *Green Energy & Environment* **2023**, *8*, 1509–1530, DOI 10.1016/j.gee.2022.08.002.

[36] C. Liu, Z. G. Neale, G. Cao, *Materials Today* **2016**, *19*, 109–123, DOI 10.1016/j.mattod.2015.10.009.

[37] M. Li, J. Lu, Z. Chen, K. Amine, *Adv. Mater.* **2018**, *30*, 1800561, DOI 10.1002/adma.201800561.

[38] Y. Song, L. Sheng, L. Wang, H. Xu, X. He, *Electrochemistry Communications* **2021**, *124*, 106948, DOI 10.1016/j.elecom.2021.106948.

[39] J. Janek, W. G. Zeier, *Nat Energy* **2016**, *1*, 16141, DOI 10.1038/nenergy.2016.141.

[40] T. A. Pham, K. E. Kweon, A. Samanta, M. T. Ong, V. Lordi, J. E. Pask, *J. Phys. Chem. C* **2020**, *124*, 21985–21992, DOI 10.1021/acs.jpcc.0c06842.

[41] Y. X., L. H., Z. J., *Lithium-ion batteries Advanced materials and technologies*, CRC Press. **2012**.

[42] M. Walter, M. V. Kovalenko, K. V. Kravchyk, *New J. Chem.* **2020**, *44*, 1677–1683, DOI 10.1039/C9NJ05682C.

[43] H. Xu, H. Jin, Z. Qi, Y. Guo, J. Wang, Y. Zhu, H. Ji, *Nanotechnology* **2020**, *31*, 205710, DOI 10.1088/1361-6528/ab72ba.

[44] M. Wakihara, *Materials Science and Engineering: R: Reports* **2001**, *33*, 109–134, DOI 10.1016/S0927-796X(01)00030-4.

[45] S. Zhong, B. Yuan, Z. Guang, D. Chen, Q. Li, L. Dong, Y. Ji, Y. Dong, J. Han, W. He, *Energy Storage Materials* **2021**, *41*, 805–841, DOI 10.1016/j.ensm.2021.07.028.

[46] W. A. Schalkwijk, B. Scrosati, *Advances in lithium-ion batteries*, Kluwer Academic/Plenum Publ. **2002,** DOI 10.1007/b113788.

[47] Y. Wu, *Lithium-Ion Batteries*, CRC Press. **2015**.

[48] K. Xu, *Chemical reviews* **2014**, *114*, 11503–11618, DOI 10.1021/cr500003w.

[49] K. Tasaki, *The journal of physical chemistry. B* **2005**, *109*, 2920–2933, DOI 10.1021/jp047240b.

[50] D. Aurbach, A. Zaban, Y. Ein-Eli, I. Weissman, O. Chusid, B. Markovsky, M. Levi, E. Levi, A. Schechter, E. Granot, *Journal of Power Sources* **1997**, *68*, 91–98, DOI 10.1016/S0378-7753(97)02575-5.

[51] D. Aurbach, *Journal of Power Sources* **2000**, *89*, 206–218, DOI 10.1016/S0378-7753(00)00431-6.

[52] J. C. Burns, R. Petibon, K. J. Nelson, N. N. Sinha, A. Kassam, B. M. Way, J. R. Dahn, *J. Electrochem. Soc.* **2013**, *160*, A1668-A1674, DOI 10.1149/2.031310jes.

[53] D. Y. Wang, J. Xia, L. Ma, K. J. Nelson, J. E. Harlow, D. Xiong, L. E. Downie, R. Petibon, J. C. Burns, A. Xiao et al., *J. Electrochem. Soc.* **2014**, *161*, A1818-A1827, DOI 10.1149/2.0511412jes.

[54] D. Zhou, D. Shanmukaraj, A. Tkacheva, M. Armand, G. Wang, *Chem* **2019**, *5*, 2326–2352, DOI 10.1016/j.chempr.2019.05.009.

[55] J. Dhom, R. Röß-Ohlenroth, B. Stumper, C. Berger, R. Daub, *Procedia CIRP* **2024**, *130*, 443–448, DOI 10.1016/j.procir.2024.10.112.

[56] Y. J. Nam, D. Y. Oh, S. H. Jung, Y. S. Jung, *Journal of Power Sources* **2018**, *375*, 93–101, DOI 10.1016/j.jpowsour.2017.11.031.

[57] W. Zaman, K. B. Hatzell, *Curr. Opin. Solid State Mater. Sci.* **2022**, *26*, 101003, DOI 10.1016/j.cossms.2022.101003.

[58] N. Boaretto, I. Garbayo, S. Valiyaveettil-SobhanRaj, A. Quintela, C. Li, M. Casas-Cabanas, F. Aguesse, *Journal of Power Sources* **2021**, *502*, 229919, DOI 10.1016/j.jpowsour.2021.229919.

[59] J. Li, C. Ma, M. Chi, C. Liang, N. J. Dudney, *Adv. Energy Mater.* **2015**, *5*, 1401408, DOI 10.1002/aenm.201401408.

[60] Y.-Y. Sun, Q. Zhang, L. Yan, T.-B. Wang, P.-Y. Hou, *Chemical Engineering Journal* **2022**, *437*, 135179, DOI 10.1016/j.cej.2022.135179.

[61] T. Famprikis, P. Canepa, J. A. Dawson, M. S. Islam, C. Masquelier, *Nature materials* **2019**, *18*, 1278–1291, DOI 10.1038/s41563-019-0431-3.

[62] K. J. Kim, M. Balaish, M. Wadaguchi, L. Kong, J. L. M. Rupp, *Advanced Energy Materials* **2021**, *11.* 2002689, DOI 10.1002/aenm.202002689.

[63] S. Kundu, Y. Ein-Eli, *J. Power Sources* **2023**, *553*, 232267, DOI 10.1016/j.jpowsour.2022.232267.

[64] S. Ohno, A. Banik, G. F. Dewald, M. A. Kraft, T. Krauskopf, N. Minafra, P. Till, M. Weiss, W. G. Zeier, *Prog. Energy* **2020**, *2*, 22001, DOI 10.1088/2516-1083/ab73dd.

[65] X. Ji, Y. Zhang, M. Cao, Q. Gu, H. Wang, J. Yu, Z.-H. Guo, X. Zhou, *J Adv Ceram* **2022**, *11*, 835–861, DOI 10.1007/s40145-022-0580-8.

[66] G. Liu, W. Weng, Z. Zhang, L. Wu, J. Yang, X. Yao, *Nano letters* **2020**, *20*, 6660–6665, DOI 10.1021/acs.nanolett.0c02489.

[67] S. P. Culver, A. G. Squires, N. Minafra, C. W. F. Armstrong, T. Krauskopf, F. Böcher, C. Li, B. J. Morgan, W. G. Zeier, *Journal of the American Chemical Society* **2020**, *142*, 21210–21219, DOI 10.1021/jacs.0c10735.

[68] J. Gu, H. Zhong, Z. Chen, J. Shi, Z. Gong, Y. Yang, *Chemical Engineering Journal* **2023**, *454*, 139923, DOI 10.1016/j.cej.2022.139923.

[69] J. Hartel, A. Banik, M. Y. Ali, B. Helm, K. Strotmann, V. Faka, O. Maus, C. Li, H. Wiggers, W. G. Zeier, *Chem. Mater.* **2024**, *36*, 10731–10745, DOI 10.1021/acs.chemmater.4c02281.

[70] D. H. S. Tan, Y.-T. Chen, H. Yang, W. Bao, B. Sreenarayanan, J.-M. Doux, W. Li, B. Lu, S.-Y. Ham, B. Sayahpour et al., *Science* **2021**, *373*, 1494–1499, DOI 10.1126/science.abg7217.

[71] I. Koresh, B. A. Klein, Z. Tang, V. K. Michaelis, T. Troczynski, *Solid State Ionics* **2022**, *380*, 115938, DOI 10.1016/j.ssi.2022.115938.

[72] M. Umair, S. Zhou, W. Li, H. T. H. Rana, J. Yang, L. Cheng, M. Li, S. Yu, J. Wei, *Batteries & Supercaps* **2024.** e202400667, DOI 10.1002/batt.202400667.

[73] Y. Han, Y. Chen, Y. Huang, M. Zhang, Z. Li, Y. Wang, *Ceramics International* **2023**, *49*, 29375–29390, DOI 10.1016/j.ceramint.2023.06.153.

[74] R. Wei, S. Chen, T. Gao, W. Liu, *Nano Select* **2021**, *2*, 2256–2274, DOI 10.1002/nano.202100110.

[75] H. Wu, H. Han, Z. Yan, Q. Zhao, J. Chen, *J. Solid State Electrochem.* **2022**, *26*, 1791–1808, DOI 10.1007/s10008-022-05230-x.

[76] R. Xu, Y. Wu, Z. Dong, R. Zheng, Z. Song, Z. Wang, H. Sun, Y. Liu, L. Zhang, *Nano Energy* **2024**, *132*, 110435, DOI 10.1016/j.nanoen.2024.110435.

[77] B. Tao, D. Zhong, H. Li, G. Wang, H. Chang, *Chemical science* **2023**, *14*, 8693–8722, DOI 10.1039/d3sc02093b.

[78] J. Ma, R. Quhe, Z. Zhang, C. Yang, X. Zhang, J. Li, L. Xu, J. Yang, B. Shi, S. Liu et al., *J. Mater. Chem. A* **2021**, *9*, 4810–4821, DOI 10.1039/D0TA07589B.

[79] M. Balaish, J. C. Gonzalez-Rosillo, K. J. Kim, Y. Zhu, Z. D. Hood, J. L. M. Rupp, *Nat Energy* **2021,** DOI 10.1038/s41560-020-00759-5.

[80] B. A. Maia, N. Magalhães, E. Cunha, M. H. Braga, R. M. Santos, N. Correia, *Polymers* **2022**, 403, DOI 10.3390/polym14030403.

[81] J. Kriegler, E. Jaimez-Farnham, M. Scheller, E. Dashjav, F. Konwitschny, L. Wach, L. Hille, F. Tietz, M. F. Zaeh, *Energy Storage Materials* **2023**, *57*, 607–617, DOI 10.1016/j.ensm.2023.03.008.

[82] P. Lennartz, B. A. Paren, A. Herzog-Arbeitman, X. C. Chen, J. A. Johnson, M. Winter, Y. Shao-Horn, G. Brunklaus, *Joule* **2023**, *7*, 1471–1495, DOI 10.1016/j.joule.2023.06.006.

[83] S. Ma, M. Jiang, P. Tao, C. Song, J. Wu, J. Wang, T. Deng, W. Shang, *Progress in Natural Science: Materials International* **2018**, *28*, 653–666, DOI 10.1016/j.pnsc.2018.11.002.

[84] J. G. Kim, B. Son, S. Mukherjee, N. Schuppert, A. Bates, O. Kwon, M. J. Choi, H. Y. Chung, S. Park, *Journal of Power Sources* **2015**, *282*, 299–322, DOI 10.1016/j.jpowsour.2015.02.054.

[85] R. Kan, Y. Xu, R. Chen, M. Jiang, B. Fu, C. Song, P. Tao, J. Wang, T. Deng, W. Shang, *Energy Storage Materials* **2024**, *68*, 103366, DOI 10.1016/j.ensm.2024.103366.

[86] Q. Zhao, S. Stalin, C.-Z. Zhao, L. A. Archer, *Nat Rev Mater* **2020**, *5*, 229–252, DOI 10.1038/s41578-019-0165-5.

[87] Y. Jiang, A. Lai, J. Ma, K. Yu, H. Zeng, G. Zhang, W. Huang, C. Wang, S.-S. Chi, J. Wang et al., *ChemSusChem* **2023**, *16*, e202202156, DOI 10.1002/cssc.202202156.

[88] L. Zhang, Y. Dai, C. Li, Y. Dang, R. Zheng, Z. Wang, Y. Wang, Y. Cui, H. Arandiyan, Z. Shao et al., *Energy Storage Materials* **2024**, *69*, 103378, DOI 10.1016/j.ensm.2024.103378.

[89] C.-H. Yim, M. S. Houache, E. A. Baranova, Y. Abu-Lebdeh, *Chemical Engineering Journal Advances* **2023**, *13*, 100436, DOI 10.1016/j.ceja.2022.100436.

[90] W. Zhao, J. Yi, P. He, H. Zhou, *Electrochem. Energ. Rev.* **2019**, *2*, 574–605, DOI 10.1007/s41918-019-00048-0.

[91] S. Sarkar, V. Thangadurai, *ACS Energy Lett.* **2022**, *7*, 1492–1527, DOI 10.1021/acsenergylett.2c00003.

[92] M. Clausnitzer, M. Ihrig, L. Cressa, S. Hein, M. Finsterbusch, S. Eswara, L.-Y. Kuo, T. Danner, P. Kaghazchi, D. Fattakhova-Rohlfing et al., *Energy Storage Materials* **2024**, *67*, 103262, DOI 10.1016/j.ensm.2024.103262.

[93] P. Dumaz, C. Rossignol, A. Mantoux, N. Sergent, R. Bouchet, *Journal of Power Sources* **2020**, *469*, 228337, DOI 10.1016/j.jpowsour.2020.228337.

[94] S. Sen, E. Trevisanello, E. Niemöller, B.-X. Shi, F. J. Simon, F. H. Richter, *J. Mater. Chem. A* **2021**, *9*, 18701–18732, DOI 10.1039/D1TA02796D.

[95] S. E. Holmes, F. Liu, W. Zhang, P. Sayavong, S. T. Oyakhire, Y. Cui, *ACS applied materials & interfaces* **2022**, *14*, 53736–53743, DOI 10.1021/acsami.2c14677.

[96] Y. Xiao, Y. Wang, S.-H. Bo, J. C. Kim, L. J. Miara, G. Ceder, *Nat Rev Mater* **2020**, *5*, 105–126, DOI 10.1038/s41578-019-0157-5.

[97] M. Jia, M. Khurram Tufail, X. Guo, *ChemSusChem* **2023**, *16*, e202201801, DOI 10.1002/cssc.202201801.

[98] L. Chen, W. Li, L.-Z. Fan, C.-W. Nan, Q. Zhang, *Adv Funct Materials* **2019**, *29.* 1901047, DOI 10.1002/adfm.201901047.

[99] S.-Y. Lee, J.-H. Han, H.-W. Gong, J. Ahn, K.-W. Yi, Y. W. Cho, *J. Mater. Chem. A* **2025**, *13*, 6342–6346, DOI 10.1039/D4TA08604J.

[100] M. Li, X. Chi, J. Yu, *PRX Energy* **2022**, *1*, 31001, DOI 10.1103/PRXEnergy.1.031001.

[101] A. Jonderian, E. McCalla, *Mater. Adv.* **2021**, *2*, 2846–2875, DOI 10.1039/D1MA00082A.

[102] T. Schmaltz, T. Wicke, L. Weymann, P. Voß, C. Neef, A. Thielmann, :unav, *Solid-State Battery Roadmap 2035+*, Fraunhofer-Gesellschaft. **2022,** DOI 10.24406/PUB-LICA-68.

[103] J. Lau, R. H. DeBlock, D. M. Butts, D. S. Ashby, C. S. Choi, B. S. Dunn, *Adv. Energy Mater.* **2018**, *8*, 1800933, DOI 10.1002/aenm.201800933.

[104] S. Wang, A. La Monaca, G. P. Demopoulos, *Energy Adv.* **2025**, *4*, 11–36, DOI 10.1039/D4YA00542B.

[105] H. Yang, N. Wu, *Energy Science & Engineering* **2022**, *10*, 1643–1671, DOI 10.1002/ese3.1163.

[106] J. C. Bachman, S. Muy, A. Grimaud, H.-H. Chang, N. Pour, S. F. Lux, O. Paschos, F. Maglia, S. Lupart, P. Lamp et al., *Chemical reviews* **2016**, *116*, 140–162, DOI 10.1021/acs.chemrev.5b00563.

[107] C. Wang, K. Fu, S. P. Kammampata, D. W. McOwen, A. J. Samson, L. Zhang, G. T. Hitz, A. M. Nolan, E. D. Wachsman, Y. Mo et al., *Chemical reviews* **2020**, *120*, 4257–4300, DOI 10.1021/acs.chemrev.9b00427.

[108] D. Karabelli, K. P. Birke, M. Weeber, *Batteries* **2021**, *7*, 18, DOI 10.3390/batte-ries7010018.

[109] H. Zhang, Y. Chen, C. Li, M. Armand, *SusMat* **2021**, *1*, 24–37, DOI 10.1002/sus2.6.

[110] J. Lopez, D. G. Mackanic, Y. Cui, Z. Bao, *Nat. Rev. Mater.* **2019**, *4*, 312–330, DOI 10.1038/s41578-019-0103-6.

[111] S. B. Aziz, T. J. Woo, M. Kadir, H. M. Ahmed, *J. Sci.: Adv. Mater. Devices* **2018**, *3*, 1–17, DOI 10.1016/j.jsamd.2018.01.002.

[112] X.-B. Cheng, C.-Z. Zhao, Y.-X. Yao, H. Liu, Q. Zhang, *Chem* **2019**, *5*, 74–96, DOI 10.1016/j.chempr.2018.12.002.

[113] L. Long, S. Wang, M. Xiao, Y. Meng, *J. Mater. Chem. A* **2016**, *4*, 10038–10069, DOI 10.1039/C6TA02621D.

[114] W.-S. Young, W.-F. Kuan, T. H. Epps, *J. Polym. Sci. Part B: Polym. Phys.* **2014**, *52*, 1–16, DOI 10.1002/polb.23404.

[115] Q. Yang, N. Deng, J. Chen, B. Cheng, W. Kang, *Chemical Engineering Journal* **2021**, *413*, 127427, DOI 10.1016/j.cej.2020.127427.

[116] X. Zhou, Y. Zhou, Le Yu, L. Qi, K.-S. Oh, P. Hu, S.-Y. Lee, C. Chen, *Chemical Society reviews* **2024**, *53*, 5291–5337, DOI 10.1039/d3cs00551h.

[117] P. Fan, H. Liu, V. Marosz, N. T. Samuels, S. L. Suib, L. Sun, L. Liao, *Adv. Funct. Mater.* **2021**, *31*, 2101380, DOI 10.1002/adfm.202101380.

[118] J. Feng, L. Wang, Y. Chen, P. Wang, H. Zhang, X. He, *Nano convergence* **2021**, *8*, 2, DOI 10.1186/s40580-020-00252-5.

[119] L. Li, Y. Deng, G. Chen, *Journal of Energy Chemistry* **2020**, *50*, 154–177, DOI 10.1016/j.jechem.2020.03.017.

[120] L. Wu, Y. Wang, X. Guo, P. Ding, Z. Lin, H. Yu, *SusMat* **2022**, *2*, 264–292, DOI 10.1002/sus2.67.

[121] B. R. Johnson, A. Sankara Raman, A. Narla, S. Jhulki, L. Chen, S. R. Marder, R. Ramprasad, K. Turcheniuk, G. Yushin, *ACS omega* **2024**, *9*, 15410–15420, DOI 10.1021/acsomega.3c10311.

[122] H. R. Allcock, C. Chen, *The Journal of organic chemistry* **2020**, *85*, 14286–14297, DOI 10.1021/acs.joc.0c01710.

[123] B. Notredame, F. Gauthy, V. Finsy, J.-F. Gohy, *Macromol. Chem. Phys.* **2022**, *223*, 2200152, DOI 10.1002/macp.202200152.

[124] S. Vauthier, M. Alvarez-Tirado, G. Guzmán-González, L. C. Tomé, S. Cotte, L. Castro, A. Guéguen, D. Mecerreyes, N. Casado, *Materials Today Chemistry* **2023**, *27*, 101293, DOI 10.1016/j.mtchem.2022.101293.

[125] E. Quartarone, P. Mustarelli, *Chemical Society reviews* **2011**, *40*, 2525–2540, DOI 10.1039/c0cs00081g.

[126] Z. Li, J. Fu, X. Zhou, S. Gui, L. Wei, H. Yang, H. Li, X. Guo, *Adv. Sci.* **2023**, *10*, e2201718, DOI 10.1002/advs.202201718.

[127] F. Gebert, J. Knott, R. Gorkin, S.-L. Chou, S.-X. Dou, *Energy Storage Materials* **2021**, *36*, 10–30, DOI 10.1016/j.ensm.2020.11.030.

[128] G. S. MacGlashan, Y. G. Andreev, P. G. Bruce, *nature* **1999**, *398*, 792–794.

[129] M. A. Webb, B. M. Savoie, Z.-G. Wang, T. F. Miller III, *Macromolecules* **2015**, *48*, 7346–7358, DOI 10.1021/acs.macromol.5b01437.

[130] Z. Xue, D. He, X. Xie, *J. Mater. Chem. A* **2015**, *3*, 19218–19253, DOI 10.1039/C5TA03471J.

[131] R. C. Agrawal, G. P. Pandey, *J. Phys. D: Appl. Phys.* **2008**, *41*, 1–18, DOI 10.1088/0022-3727/41/22/223001.

[132] D. Zhang, X. Xu, Y. Qin, S. Ji, Y. Huo, Z. Wang, Z. Liu, J. Shen, J. Liu, *Chemistry (Weinheim an der Bergstrasse, Germany)* **2020**, *26*, 1720–1736, DOI 10.1002/chem.201904461.

[133] X. Yang, M. Jiang, X. Gao, D. Bao, Q. Sun, N. Holmes, H. Duan, S. Mukherjee, K. Adair, C. Zhao et al., *Energy Environ. Sci.* **2020**, *13*, 1318–1325, DOI 10.1039/D0EE00342E.

[134] Z. Hei, S. Wu, H. Zheng, H. Liu, H. Duan, *Solid State Ionics* **2022**, *375*, 115837, DOI 10.1016/j.ssi.2021.115837.

[135] N. Wang, Y. Wei, S. Yu, W. Zhang, X. Huang, B. Fan, H. Yuan, Y. Tan, *Journal of Materials Science & Technology* **2024**, *183*, 206–214, DOI 10.1016/j.jmst.2023.10.005.

[136] X. Song, T. H. Zhang, R. Z. Fan, J. Biao, S. H. Huang, J. Travaš-Sejdić, W. Gao, P. Cao, *Solid State Ionics* **2023**, *403*, 116410, DOI 10.1016/j.ssi.2023.116410.

[137] W. Kou, R. Lv, S. Zuo, Z. Yang, J. Huang, W. Wu, J. Wang, *Journal of Membrane Science* **2021**, *618*, 118702, DOI 10.1016/j.memsci.2020.118702.

[138] P. Walke, A. Kirchberger, F. Reiter, D. Esken, T. Nilges, *Z. Naturfosch.* **2021**, *76*, 615–624, DOI 10.1515/znb-2021-0091.

[139] P. Walke, K. M. Freitag, H. Kirchhain, M. Kaiser, L. van Wüllen, T. Nilges, *Z. anorg. allg. Chem.* **2018**, *644*, 1863–1874, DOI 10.1002/zaac.201800370.

[140] J. Wang, Y. Yamada, K. Sodeyama, E. Watanabe, K. Takada, Y. Tateyama, A. Yamada, *Nat Energy* **2018**, *3*, 22–29, DOI 10.1038/s41560-017-0033-8.

[141] N. Varan, P. Merghes, N. Plesu, L. Macarie, G. Ilia, V. Simulescu, *Batteries* **2024**, *10*, 56, DOI 10.3390/batteries10020056.

[142] X. Liu, C. Zhang, S. Gao, S. Cai, Q. Wang, J. Liu, Z. Liu, *Materials Chemistry and Physics* **2020**, *239*, 122014, DOI 10.1016/j.matchemphys.2019.122014.

[143] J. Zheng, W. Li, J. Zhang, Y. Sun, W. Chen, *ACS Sustainable Chem. Eng.* **2022**, *10*, 7158–7168, DOI 10.1021/acssuschemeng.2c01531.

[144] H. Li, Y. Kuai, J. Yang, S. Hirano, Y. Nuli, J. Wang, *J. Energy Chem.* **2022**, *65*, 616–622, DOI 10.1016/j.jechem.2021.06.036.

[145] T. R. Totsch, I. Popov, V. L. Stanford, A. L. Lucius, S. H. Foulger, G. M. Gray, *Journal of Polymer Science* **2021**, *59*, 139–145, DOI 10.1002/pol.20200561.

[146] L. Bai, M. Webhi, G. Dolphijn, B. Améduri, J.-F. Gohy, *Macromol. Chem. Phys.* **2021**, *222*, 2000389, DOI 10.1002/macp.202000389.

[147] X. He, S. Schmohl, H.-D. Wiemhöfer, *ChemElectroChem* **2019**, *6*, 1166–1176, DOI 10.1002/celc.201801383.

[148] D.-P. Chen, J. Wang, *Macromolecules* **2006**, *39*, 473–475, DOI 10.1021/ma0517852.

[149] K. Halama, A. Schaffer, B. Rieger, *RSC Adv.* **2021**, *11*, 38555–38564, DOI 10.1039/d1ra06452e.

[150] D. Lanzinger, S. Salzinger, B. S. Soller, B. Rieger, *Ind. Eng. Chem. Res.* **2015**, *54*, 1703–1712, DOI 10.1021/ie504084q.

[151] B. S. Soller, S. Salzinger, B. Rieger, *Chem. Rev.* **2016**, *116*, 1993–2022, DOI 10.1021/acs.chemrev.5b00313.

[152] B. S. Soller, N. Zhang, B. Rieger, *Macromol. Chem. Phys.* **2014**, *215*, 1946–1962, DOI 10.1002/macp.201400271.

[153] S. Salzinger, B. Rieger, *Macromolecular rapid communications* **2012**, *33*, 1327–1345, DOI 10.1002/marc.201200278.

[154] T. M. Pehl, F. Adams, M. Kränzlein, B. Rieger, *Macromol.* **2021**, *54*, 4089–4100, DOI 10.1021/acs.macromol.1c00217.

[155] S. Liu, W. Liu, D. Ba, Y. Zhao, Y. Ye, Y. Li, J. Liu, *Advanced materials (Deerfield Beach, Fla.)* **2023**, *35*, e2110423, DOI 10.1002/adma.202110423.

[156] W.-Q. Ding, F. Lv, N. Xu, M.-T. Wu, J. Liu, X.-P. Gao, *ACS Appl. Energy Mater.* **2021**, *4*, 4581–4601, DOI 10.1021/acsaem.1c00216.

[157] D. Lin, P. Y. Yuen, Y. Liu, W. Liu, N. Liu, R. H. Dauskardt, Y. Cui, *Advanced materials (Deerfield Beach, Fla.)* **2018**, *30*, e1802661, DOI 10.1002/adma.201802661.

[158] K. K. Fu, Y. Gong, J. Dai, A. Gong, X. Han, Y. Yao, C. Wang, Y. Wang, Y. Chen, C. Yan et al., *Proceedings of the National Academy of Sciences of the United States of America* **2016**, *113*, 7094–7099, DOI 10.1073/pnas.1600422113.

[159] W. Liu, S. W. Lee, D. Lin, F. Shi, S. Wang, A. D. Sendek, Y. Cui, *Nat Energy* **2017**, *2,* DOI 10.1038/nenergy.2017.35.

[160] W. Liu, N. Liu, J. Sun, P.-C. Hsu, Y. Li, H.-W. Lee, Y. Cui, *Nano letters* **2015**, *15*, 2740–2745, DOI 10.1021/acs.nanolett.5b00600.

[161] P. Zhu, C. Yan, M. Dirican, J. Zhu, J. Zang, R. K. Selvan, C.-C. Chung, H. Jia, Y. Li, Y. Kiyak et al., *J. Mater. Chem. A* **2018**, *6*, 4279–4285, DOI 10.1039/C7TA10517G.

[162] S. Lee, A. Manthiram, *ACS Energy Lett.* **2022**, *7*, 3058–3063, DOI 10.1021/acsenergylett.2c01553.

[163] Y. Miao, P. Hynan, A. von Jouanne, A. Yokochi, *Energies* **2019**, *12*, 1074, DOI 10.3390/en12061074.

[164] J.-C. Zhang, Z.-D. Liu, C.-H. Zeng, J.-W. Luo, Y.-D. Deng, X.-Y. Cui, Y.-N. Chen, *Rare Met.* **2022**, *41*, 3946–3956, DOI 10.1007/s12598-022-02070-6.

[165] G. E. Blomgren, *J. Electrochem. Soc.* **2017**, *164*, A5019-A5025, DOI 10.1149/2.0251701jes.

[166] D. Schreiner, T. Zünd, F. J. Günter, L. Kraft, B. Stumper, F. Linsenmann, M. Schüßler, R. Wilhelm, A. Jossen, G. Reinhart et al., *J. Electrochem. Soc.* **2021**, *168*, 30507, DOI 10.1149/1945-7111/abe50c.

[167] A. Purwanto, C. S. Yudha, U. Ubaidillah, H. Widiyandari, T. Ogi, H. Haerudin, *Mater. Res. Express* **2018**, *5*, 122001, DOI 10.1088/2053-1591/aae167.

[168] M. S. Indu, G. V. Alexander, O. V. Sreejith, S. E. Abraham, R. Murugan, *Materials Today Energy* **2021**, *21*, 100804, DOI 10.1016/j.mtener.2021.100804.

[169] T. Li, X.-Z. Yuan, L. Zhang, D. Song, K. Shi, C. Bock, *Electrochem. Energ. Rev.* **2020**, *3*, 43–80, DOI 10.1007/s41918-019-00053-3.

[170] L. Ma, M. Nie, J. Xia, J. R. Dahn, *Journal of Power Sources* **2016**, *327*, 145–150, DOI 10.1016/j.jpowsour.2016.07.039.

[171] W. Pfleging, *Int. J. Extrem. Manuf.* **2021**, *3*, 12002, DOI 10.1088/2631-7990/abca84.

[172] T. Li, P. K. Panda, C.-T. Hsieh, Y. A. Gandomi, P.-C. Yang, *Journal of Energy Storage* **2024**, *81*, 110444, DOI 10.1016/j.est.2024.110444.

[173] K. Mizushima, P. C. Jones, P. J. Wiseman, J. B. Goodenough, *Materials Research Bulletin* **1980**, *15*, 783–789, DOI 10.1016/0025-5408(80)90012-4.

[174] M. Ank, A. Sommer, K. Abo Gamra, J. Schöberl, M. Leeb, J. Schachtl, N. Streidel, S. Stock, M. Schreiber, P. Bilfinger et al., *J. Electrochem. Soc.* **2023**, *170*, 120536, DOI 10.1149/1945-7111/ad14d0.

[175] Z. Sun, J. Zhao, M. Zhu, J. Liu, *Advanced Energy Materials* **2024**, *14.* 2303498, DOI 10.1002/aenm.202303498.

[176] M. M. Thackeray, W. David, P. G. Bruce, J. B. Goodenough, *Materials Research Bulletin* **1983**, *18*, 461–472, DOI 10.1016/0025-5408(83)90138-1.

[177] M. M. Thackeray, *Progress in Solid State Chemistry* **1997**, *25*, 1–71, DOI 10.1016/S0079-6786(97)81003-5.

[178] J. Zheng, S. Myeong, W. Cho, P. Yan, J. Xiao, C. Wang, J. Cho, J.-G. Zhang, *Adv. Energy Mater.* **2017**, *7.* 1601284, DOI 10.1002/aenm.201601284.

[179] D. H. Jang, Y. J. Shin, S. M. Oh, *J. Electrochem. Soc.* **1996**, *143*, 2204–2211, DOI 10.1149/1.1836981.

[180] K. Amine, H. Tukamoto, H. Yasuda, Y. Fujita, *Journal of Power Sources* **1997**, *68*, 604–608, DOI 10.1016/S0378-7753(96)02590-6.

[181] R. Qiao, L. A. Wray, J.-H. Kim, N. P. W. Pieczonka, S. J. Harris, W. Yang, *J. Phys. Chem. C* **2015**, *119*, 27228–27233, DOI 10.1021/acs.jpcc.5b07479.

[182] W. Li, E. M. Erickson, A. Manthiram, *Nat Energy* **2020**, *5*, 26–34, DOI 10.1038/s41560-019-0513-0.

[183] S. Ahmed, P. A. Nelson, K. G. Gallagher, N. Susarla, D. W. Dees, *Journal of Power Sources* **2017**, *342*, 733–740, DOI 10.1016/j.jpowsour.2016.12.069.

[184] S.-T. Myung, F. Maglia, K.-J. Park, C. S. Yoon, P. Lamp, S.-J. Kim, Y.-K. Sun, *ACS Energy Lett.* **2017**, *2*, 196–223, DOI 10.1021/acsenergylett.6b00594.

[185] D. Andre, S.-J. Kim, P. Lamp, S. F. Lux, F. Maglia, O. Paschos, B. Stiaszny, *J. Mater. Chem. A* **2015**, *3*, 6709–6732, DOI 10.1039/C5TA00361J.

[186] H.-J. Noh, S. Youn, C. S. Yoon, Y.-K. Sun, *Journal of Power Sources* **2013**, *233*, 121–130, DOI 10.1016/j.jpowsour.2013.01.063.

[187] K. R. Tallman, G. P. Wheeler, C. J. Kern, E. Stavitski, X. Tong, K. J. Takeuchi, A. C. Marschilok, D. C. Bock, E. S. Takeuchi, *J. Phys. Chem. C* **2021**, *125*, 58–73, DOI 10.1021/acs.jpcc.0c08095.

[188] S.-B. Son, D. Robertson, Y. Tsai, S. Trask, A. Dunlop, I. Bloom, *J. Electrochem. Soc.* **2020**, *167*, 160508, DOI 10.1149/1945-7111/abcb40.

[189] L. de Biasi, A. O. Kondrakov, H. Geßwein, T. Brezesinski, P. Hartmann, J. Janek, *J. Phys. Chem. C* **2017**, *121*, 26163–26171, DOI 10.1021/acs.jpcc.7b06363.

[190] V. Nagda, H. Ekström, A. Kulachenko, *J. Electrochem. Soc.* **2024**, *171*, 60526, DOI 10.1149/1945-7111/ad5622.

[191] G. Conforto, R. Ruess, D. Schröder, E. Trevisanello, R. Fantin, F. H. Richter, J. Janek, *J. Electrochem. Soc.* **2021**, *168*, 70546, DOI 10.1149/1945-7111/ac13d2.

[192] A. Jangde, M. Kumar, İ. Tuğrul Gülenç, L. Wheatcroft, B. J. Inkson, *Batteries & Supercaps* **2025.** e202400691, DOI 10.1002/batt.202400691.

[193] F. N. U. Khan, M. G. Rasul, A. Sayem, N. Mandal, *Energy Reports* **2023**, *9*, 11–21, DOI 10.1016/j.egyr.2023.08.069.

[194] A. K. Padhi, K. S. Nanjundaswamy, J. B. Goodenough, *J. Electrochem. Soc.* **1997**, *144*, 1188–1194, DOI 10.1149/1.1837571.

[195] H. Rostami, J. Valio, P. Tynjälä, U. Lassi, P. Suominen, *Chemphyschem : a European journal of chemical physics and physical chemistry* **2024**, *25*, e202400459, DOI 10.1002/cphc.202400459.

[196] T. Zhao, H. Mahandra, R. Marthi, X. Ji, W. Zhao, S. Chae, M. Traversy, W. Li, F. Yu, L. Li et al., *Chemical Engineering Journal* **2024**, *485*, 149923, DOI 10.1016/j.cej.2024.149923.

[197] S.-P. Chen, D. Lv, J. Chen, Y.-H. Zhang, F.-N. Shi, *Energy Fuels* **2022**, *36*, 1232–1251, DOI 10.1021/acs.energyfuels.1c03757.

[198] W. Yu, G. Ou, L. Qi, H. Wu, *J. Am. Ceram. Soc.* **2016**, *99*, 3214–3216, DOI 10.1111/jace.14426.

[199] X. Yang, J. Tu, M. Lei, Z. Zuo, B. Wu, H. Zhou, *Electrochimica Acta* **2016**, *193*, 206–215, DOI 10.1016/j.electacta.2016.02.068.

[200] X.-C. Tang, L.-X. Li, Q.-L. Lai, X.-W. Song, L.-H. Jiang, *Electrochimica Acta* **2009**, *54*, 2329–2334, DOI 10.1016/j.electacta.2008.10.065.

[201] F. Gao, Z. Tang, *Electrochimica Acta* **2008**, *53*, 5071–5075, DOI 10.1016/j.electacta.2007.10.069.

[202] P. Prosini, *Solid State Ionics* **2002**, *148*, 45–51, DOI 10.1016/S0167-2738(02)00134-0.

[203] Q. Wang, H. Li, X. Huang, L. Chen, *J. Electrochem. Soc.* **2001**, *148*, A737, DOI 10.1149/1.1377897.

[204] Z. Chen, H. Zhu, S. Ji, R. Fakir, V. Linkov, *Solid State Ionics* **2008**, *179*, 1810–1815, DOI 10.1016/j.ssi.2008.04.018.

[205] M. GABERSCEK, R. DOMINKO, J. JAMNIK, *Electrochemistry Communications* **2007**, *9*, 2778–2783, DOI 10.1016/j.elecom.2007.09.020.

[206] J. Zheng, S. Myeong, W. Cho, P. Yan, J. Xiao, C. Wang, J. Cho, J.-G. Zhang, *Advanced Energy Materials* **2017**, *7.* 1601284, DOI 10.1002/aenm.201601284.

[207] M. A. AL-SAMET, E. Burgaz, *Journal of Alloys and Compounds* **2023**, *947*, 169680, DOI 10.1016/j.jallcom.2023.169680.

[208] G. Donnely, A previously ignored battery chemistry is now surging in popularity. Here's why, https://www.emergingtechbrew.com/stories/2022/04/26/a-previously-ignored-battery-chemistry-is-now-surging-in-popularity-here-s-why?utm, (accessed: 09.04.2025).

[209] T. Nigel, BYD Blade - Battery Design, https://www.batterydesign.net/byd-blade/?utm, (accessed: 09.04.2025).

[210] S. Suttison, K. Pengpat, U. Intatha, J. Fan, W. Zhang, S. Eitssayeam, *Materials Today: Proceedings* **2022**, *65*, 2347–2350, DOI 10.1016/j.matpr.2022.05.302.

[211] T. Wicke, I. R. Inclán - Fraunhofer Institute for Systems and Innovation Research ISI, Analysis of global battery production: production locations and quantities of cells with LFP and NMC/NCA cathode material, https://www.isi.fraunhofer.de/en/blog/themen/batterie-update/globale-batterieproduktion-analyse-standorte-mengen-zellen-lfp-nmc-nca-kathoden.html, (accessed: 09.04.2025).

[212] L. Sun, Y. Liu, R. Shao, J. Wu, R. Jiang, Z. Jin, *Energy Storage Materials* **2022**, *46*, 482–502, DOI 10.1016/j.ensm.2022.01.042.

[213] Z. N. Ezhyeh, M. Khodaei, F. Torabi, *Ceramics International* **2023**, *49*, 7105–7141, DOI 10.1016/j.ceramint.2022.04.340.

[214] M. Ashuri, Q. He, L. L. Shaw, *Nanoscale* **2016**, *8*, 74–103, DOI 10.1039/c5nr05116a.

[215] C. Xu, B. Wang, H. Luo, P. Jing, X. Zhang, Q. Wang, Y. Zhang, H. Wu, *ChemElectroChem* **2020**, *7*, 2889–2895, DOI 10.1002/celc.202000827.

[216] S.-H. Yu, S. H. Lee, D. J. Lee, Y.-E. Sung, T. Hyeon, *Small (Weinheim an der Bergstrasse, Germany)* **2016**, *12*, 2146–2172, DOI 10.1002/smll.201502299.

[217] W.-Z. Huang, C.-Z. Zhao, P. Wu, H. Yuan, W.-E. Feng, Z.-Y. Liu, Y. Lu, S. Sun, Z.-H. Fu, J.-K. Hu et al., *Advanced Energy Materials* **2022**, *12*, 2201044, DOI 10.1002/a-enm.202201044.

[218] H. Zhang, Y. Yang, D. Ren, L. Wang, X. He, *Energy Storage Materials* **2021**, *36*, 147–170, DOI 10.1016/j.ensm.2020.12.027.

[219] C. Ma, Y. Zhao, J. Li, Y. Song, J. Shi, Q. Guo, L. Liu, *Carbon* **2013**, *64*, 553–556, DOI 10.1016/j.carbon.2013.07.089.

[220] S. Schweidler, L. de Biasi, A. Schiele, P. Hartmann, T. Brezesinski, J. Janek, *J. Phys. Chem. C* **2018**, *122*, 8829–8835, DOI 10.1021/acs.jpcc.8b01873.

[221] X. Yi, W.-J. Yu, M. A. Tsiamtsouri, F. Zhang, W. He, Q. Dai, S. Hu, H. Tong, J. Zheng, B. Zhang et al., *Electrochimica Acta* **2019**, *295*, 719–725, DOI 10.1016/j.electacta.2018.11.020.

[222] S. Friedrich, S. Stojecevic, P. Rapp, S. Helmer, M. Bock, A. Durdel, H. A. Gasteiger, A. Jossen, *J. Electrochem. Soc.* **2024**, *171*, 50540, DOI 10.1149/1945-7111/ad36e6.

[223] M. N. Obrovac, L. J. Krause, *J. Electrochem. Soc.* **2007**, *154*, A103, DOI 10.1149/1.2402112.

[224] H. Valencia, P. Rapp, M. Graf, J. Mayer, H. A. Gasteiger, *J. Electrochem. Soc.* **2024**, *171*, 120507, DOI 10.1149/1945-7111/ad9a06.

[225] A. Franco Gonzalez, N.-H. Yang, R.-S. Liu, *J. Phys. Chem. C* **2017**, *121*, 27775–27787, DOI 10.1021/acs.jpcc.7b07793.

[226] A. Varzi, K. Thanner, R. Scipioni, D. Di Lecce, J. Hassoun, S. Dörfler, H. Altheus, S. Kaskel, C. Prehal, S. A. Freunberger, *Journal of Power Sources* **2020**, *480*, 228803, DOI 10.1016/j.jpowsour.2020.228803.

[227] H. Yuan, X. Ding, T. Liu, J. Nai, Y. Wang, Y. Liu, C. Liu, X. Tao, *Materials Today* **2022**, *53*, 173–196, DOI 10.1016/j.mattod.2022.01.015.

[228] R. Zhang, X. Shen, Y.-T. Zhang, X.-L. Zhong, H.-T. Ju, T.-X. Huang, X. Chen, J.-D. Zhang, J.-Q. Huang, *Journal of Energy Chemistry* **2022**, *71*, 29–35, DOI 10.1016/j.jechem.2021.12.020.

[229] J. A. Lewis, C. Lee, Y. Liu, S. Y. Han, D. Prakash, E. J. Klein, H.-W. Lee, M. T. McDowell, *ACS Appl. Mater. Interfaces* **2022**, *14*, 4051–4060, DOI 10.1021/acsami.1c20139.

[230] S. Yang, Y. Zhang, Z. Li, N. Takenaka, Y. Liu, H. Zou, W. Chen, M. Du, X.-J. Hong, R. Shang et al., *ACS Energy Lett.* **2021**, *6*, 1811–1820, DOI 10.1021/acsenergylett.1c00514.

[231] W. Deng, X. Wang, *Green Energy & Environment* **2022**, *7*, 1129–1131, DOI 10.1016/j.gee.2021.12.005.

[232] L. Zhang, M. Al-Mamun, *Green Energy & Environment* **2022**, *7*, 173–175, DOI 10.1016/j.gee.2021.08.001.

[233] W. Hu, Y. Peng, Y. Wei, Y. Yang, *J. Phys. Chem. C* **2023**, *127*, 4465–4495, DOI 10.1021/acs.jpcc.3c00033.

[234] M. Gaberšček, *Nature communications* **2021**, *12*, 6513, DOI 10.1038/s41467-021-26894-5.

[235] A. Lasia, *Electrochemical Impedance Spectroscopy and its Applications*, Springer New York. **2014,** DOI 10.1007/978-1-4614-8933-7.

[236] S. Wang, J. Zhang, O. Gharbi, V. Vivier, M. Gao, M. E. Orazem, *Nat Rev Methods Primers* **2021**, *1,* DOI 10.1038/s43586-021-00039-w.

[237] X. Yang, A. L. Rogach, *Adv. Energy Mater.* **2019**, *9.* 1900747, DOI 10.1002/aenm.201900747.

[238] J. P. Schmidt, T. Chrobak, M. Ender, J. Illig, D. Klotz, E. Ivers-Tiffée, *Journal of Power Sources* **2011**, *196*, 5342–5348, DOI 10.1016/j.jpowsour.2010.09.121.

[239] Lvovich V. F., *Impedance Spectroscopy*. *Applications to Electrochemical and Dielectric Phenomena.* **2012**.

[240] M. E. Orazem, B. Tribollet, *Electrochemical impedance spectroscopy*, Wiley. **2008,** DOI 10.1002/9780470381588.

[241] N. Ogihara, Y. Itou, T. Sasaki, Y. Takeuchi, *J. Phys. Chem. C* **2015**, *119*, 4612–4619, DOI 10.1021/jp512564f.

[242] J. Moškon, M. Gaberšček, *Journal of Power Sources Advances* **2021**, *7*, 100047, DOI 10.1016/j.powera.2021.100047.

[243] H. Nara, D. Mukoyama, T. Yokoshima, T. Momma, T. Osaka, *J. Electrochem. Soc.* **2016**, *163*, A434-A441, DOI 10.1149/2.0341603jes.

[244] J. Landesfeind, D. Pritzl, H. A. Gasteiger, *J. Electrochem. Soc.* **2017**, *164*, A1773-A1783, DOI 10.1149/2.0131709jes.

[245] L. Wang, J. Qiu, X. Wang, L. Chen, G. Cao, J. Wang, H. Zhang, X. He, *eScience* **2022**, *2*, 125–137, DOI 10.1016/j.esci.2022.03.006.

[246] S. S. Shishvan, N. A. Fleck, R. M. McMeeking, V. S. Deshpande, *Journal of Power Sources* **2023**, *588*, 233745, DOI 10.1016/j.jpowsour.2023.233745.

[247] P. Pfändner, M. Wittig, T. Pehl, B. Rieger, *ACS Appl. Polym. Mater.* **2025**, *7*, 2102–2111, DOI 10.1021/acsapm.4c03951.

[248] R. H. Herpel, P. Vedantham, D. L. Flynn, P. R. Hanson, *Tetrahedron Letters* **2006**, *47*, 6429–6432, DOI 10.1016/j.tetlet.2006.06.130.

[249] B. S. Soller, S. Salzinger, C. Jandl, A. Pöthig, B. Rieger, *Organometallics* **2015**, *34*, 2703–2706, DOI 10.1021/om501173r.

[250] B. Bingöl, G. Hart-Smith, C. Barner-Kowollik, G. Wegner, *Macromolecules* **2008**, *41*, 1634–1639, DOI 10.1021/ma702225k.

[251] M. P. Rosenwinkel, R. Andersson, J. Mindemark, M. Schönhoff, *J. Phys. Chem. C* **2020**, *124*, 23588–23596, DOI 10.1021/acs.jpcc.0c08369.

[252] M. Philipp, R. Bhandary, F. J. Groche, M. Schönhoff, B. Rieger, *Electrochimica Acta* **2015**, *173*, 687–697, DOI 10.1016/j.electacta.2015.05.108.

[253] J. Denney, H. Huang, *J. Compos. Sci.* **2022**, *6*, 117, DOI 10.3390/jcs6040117.

[254] Y. Xia, T. Fujieda, K. Tatsumi, P. P. Prosini, T. Sakai, *J. Power Sources* **2001**, 234–243, DOI 10.1016/S0378-7753(00)00533-4.

[255] C.-W. Wu, X. Ren, W.-X. Zhou, G. Xie, G. Zhang, *APL Materials* **2022**, *10.* 040902, DOI 10.1063/5.0089891.

[256] S. S. Zhang, *Electrochem. Commun.* **2006**, *8*, 1423–1428, DOI 10.1016/j.elecom.2006.06.016.

[257] Z. Li, L. Wang, X. Huang, X. He, *Adv Funct Materials* **2024**, *34.* 2408319, DOI 10.1002/adfm.202408319.

[258] N. S. Murthy, H. Minor, C. Bednarczyk, S. Krimm, *Macromol.* **1993**, *26*, 1712–1721, DOI 10.1021/ma00059a034.

[259] H. Erabhoina, D. Rosenbach, J. Mohanraj, M. Thelakkat, *Electrochim. Acta* **2021**, *387*, 138455, DOI 10.1016/j.electacta.2021.138455.

[260] P. Törmala, *Eur. Polym. J.* **1973**, *10*, 519–521, DOI 10.1016/0014-3057(74)90201-8.

[261] D. Fragiadakis, S. Dou, R. H. Colby, J. Runt, *J. Chem. Phys.* **2009**, *130*, 64907, DOI 10.1063/1.3063659.

[262] D. Devaux, R. Bouchet, D. Glé, R. Denoyel, *Solid State Ion.* **2012**, *227*, 119–127, DOI 10.1016/j.ssi.2012.09.020.

[263] T. G. Fox, P. J. Flory, *Journal of Applied Physics* **1950**, *21*, 581–591, DOI 10.1063/1.1699711.

[264] S. I. Abdul Halim, C. H. Chan, H.-W. Kammer, *Polym. Test.* **2019**, *79*, 105994, DOI 10.1016/j.polymertesting.2019.105994.

[265] Y. Kumar, S. A. Hashmi, G. P. Pandey, *Solid State Ion.* **2011**, *201*, 73–80, DOI 10.1016/j.ssi.2011.08.010.

[266] J. I. Kim, Y. G. Choi, Y. Ahn, D. Kim, J. H. Park, *J. Membr. Sci.* **2021**, *619*, 118771, DOI 10.1016/j.memsci.2020.118771.

[267] X. Chen, L. Yi, C. Zou, J. Liu, L. Yang, Z. Zang, X. Tao, Z. Luo, B. Chang, Y. Shen et al., *Electrochim. Acta* **2023**, *446*, 142084, DOI 10.1016/j.electacta.2023.142084.

[268] G. Piana, F. Bella, F. Geobaldo, G. Meligrana, C. Gerbaldi, *J. Energy Storage* **2019**, *26*, 100947, DOI 10.1016/j.est.2019.100947.

[269] J. Evans, C. Vincent, P. Bruce, *Polymer* **1987**, *28*, 2324–2328, DOI 10.1016/0032-3861(87)90394-6.

[270] J. Song, K. Liao, J. Si, C. Zhao, J. Wang, M. Zhou, H. Liang, J. Gong, Y.-J. Cheng, J. Gao et al., *ACS Appl. Mater. Interfaces* **2023**, *15*, 2901–2910, DOI 10.1021/acsami.2c18298.

[271] C. F. N. Marchiori, R. P. Carvalho, M. Ebadi, D. Brandell, C. M. Araujo, *Chem. Mater.* **2020**, *32*, 7237–7246, DOI 10.1021/acs.chemmater.0c01489.

[272] S.-S. Chi, Y. Liu, N. Zhao, X. Guo, C.-W. Nan, L.-Z. Fan, *Energy Storage Mater.* **2019**, *17*, 309–316, DOI 10.1016/j.ensm.2018.07.004.

[273] S.-Y. Ham, H. Yang, O. Nunez-cuacuas, D. H. Tan, Y.-T. Chen, G. Deysher, A. Cronk, P. Ridley, J.-M. Doux, E. A. Wu et al., *Energy Storage Mater.* **2023**, *55*, 455–462, DOI 10.1016/j.ensm.2022.12.013.

[274] X. Lu, G. J. Lian, J. Parker, R. Ge, M. K. Sadan, R. M. Smith, D. Cumming, *Journal of Power Sources* **2024**, *592*, 233916, DOI 10.1016/j.jpowsour.2023.233916.

[275] A. M. Zyuzin, A. A. Karpeev, N. V. Yantsen, *Tech. Phys. Lett.* **2024**, *50*, 250–254, DOI 10.1134/S1063785023180219.

[276] J. Landesfeind, J. Hattendorff, A. Ehrl, W. A. Wall, H. A. Gasteiger, *J. Electrochem. Soc.* **2016**, *163*, A1373-A1387, DOI 10.1149/2.1141607jes.

[277] B. Xu, W. Diao, G. Wen, S.-Y. Choe, J. Kim, M. Pecht, *Journal of Power Sources* **2021**, *510*, 230390, DOI 10.1016/j.jpowsour.2021.230390.

[278] F. Dai, M. Cai, *Commun Mater* **2022**, *3,* DOI 10.1038/s43246-022-00286-8.

[279] C. D. Alt, S. Keuntje, I. L. Schneider, J. Westphal, P. Minnmann, J. K. Eckhardt, K. Peppler, J. Janek, *Advanced Energy Materials* **2025**, *15.* 2404055, DOI 10.1002/aenm.202404055.

[280] Materials Project, Materials Project, https://next-gen.materialsproject.org/materials/mp-22460?, (accessed: 07.05.2025).

[281] L.-Z. Fan, J. Maier, *Electrochemistry Communications* **2006**, *8*, 1753–1756, DOI 10.1016/j.elecom.2006.08.017.

[282] P. Walke, J. Venturini, R. J. Spranger, L. van Wüllen, T. Nilges, *Batteries & Supercaps* **2022**, *5,* DOI 10.1002/batt.202200285.

[283] J. Kriegler, H. Ballmes, S. Dib, A. G. Demir, L. Hille, Y. Liang, L. Wach, S. Weinmann, J. Keilhofer, K. J. Kim et al., *Adv Funct Materials* **2024**, *34.* 2313766, DOI 10.1002/adfm.202313766.

[284] Akila C. Thenuwara, Eric L. Thompson, Thomas F. Malkowski, Kenneth D. Parrotte, Kathryn E. Lostracco, Sooraj Narayan, Ryan T. Rooney, Lori A. Seeley, Melroy R. Borges, Brent D. Conway et al., *ACS Energy Lett.* **2023**, *8*, 4016–4023.

[285] H. Y. Jung, P. Mandal, G. Jo, O. Kim, M. Kim, K. Kwak, M. J. Park, *Macromolecules* **2017**, *50*, 3224–3233, DOI 10.1021/acs.macromol.7b00249.

[286] T. Pehl, Rare-earth metal-mediated synthesis of radical-containing polyvinylphosphonates: Novel materials for battery applications, Ph.D. Dissertation, Technical University of Munich, **2021**.

[287] M. J. Counihan, J. Lee, P. Mirmira, P. Barai, M. E. Burns, C. V. Amanchukwu, V. Srinivasan, Y. Zhang, S. Tepavcevic, *Energy Mater.* **2025**, *5,* DOI 10.20517/energymater.2024.195.

[288] A. Sharafi, E. Kazyak, A. L. Davis, S. Yu, T. Thompson, D. J. Siegel, N. P. Dasgupta, J. Sakamoto, *Chem. Mater.* **2017**, *29*, 7961–7968, DOI 10.1021/acs.chemmater.7b03002.

[289] X. Yan, Y. Li, C. Li, H. Wang, T. Wang, Y. Ma, S. Zhang, X. Zhang, W. He, *Solid State Ionics* **2024**, *410*, 116535, DOI 10.1016/j.ssi.2024.116535.

[290] J. Landesfeind, A. Eldiven, H. A. Gasteiger, *J. Electrochem. Soc.* **2018**, *165*, A1122-A1128, DOI 10.1149/2.0971805jes.

[291] M. Musil, J. Vondrák, *ECS Trans.* **2014**, *63*, 315–319, DOI 10.1149/06301.0315ecst.

[292] J. Popovic, D. Brandell, S. Ohno, K. B. Hatzell, J. Zheng, Y.-Y. Hu, *J. Mater. Chem. A* **2021**, *9*, 6050–6069, DOI 10.1039/D0TA11679C.

[293] P. Honegger, O. Steinhauser, *Phys. Chem. Chem. Phys.* **2019**, *22*, 212–222, DOI 10.1039/c9cp04752b.

[294] P. Lameiras, J.-M. Nuzillard, *Prog. Nucl. Magn. Reson. Spectrosc.* **2021**, *123*, 1–50, DOI 10.1016/j.pnmrs.2020.12.001.

[295] R. Chen, T. Chen, C. Zhu, Y. Fan, X. Hu, G. Wang, *J IRAN CHEM SOC* **2020**, *17*, 2507–2513, DOI 10.1007/s13738-020-01945-8.

[296] R. Chen, T. Chen, X. Hu, Y. Fan, G. Wang, *Journal of Chemical Research* **2019**, *43*, 211–216, DOI 10.1177/1747519819861318.

8 Appendix

Polymer NMR P1-VP

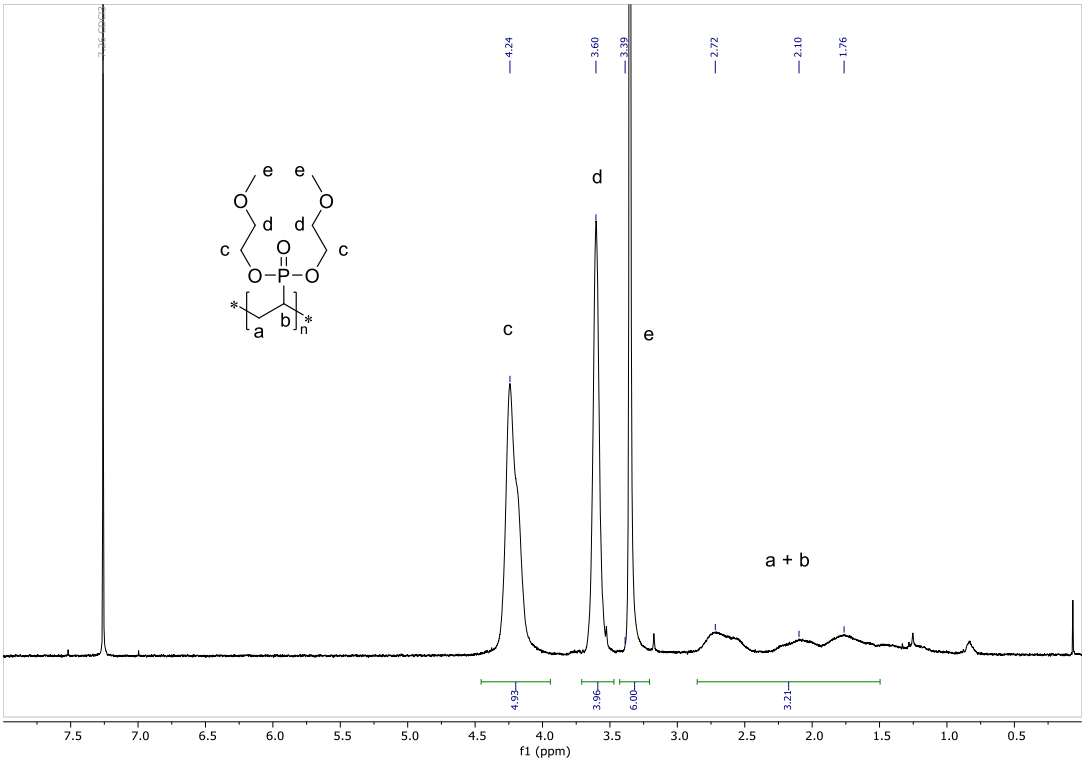

Figure 8-1: ^{1}H-NMR of P1-VP in $CDCl_3$ at 400 MHz.

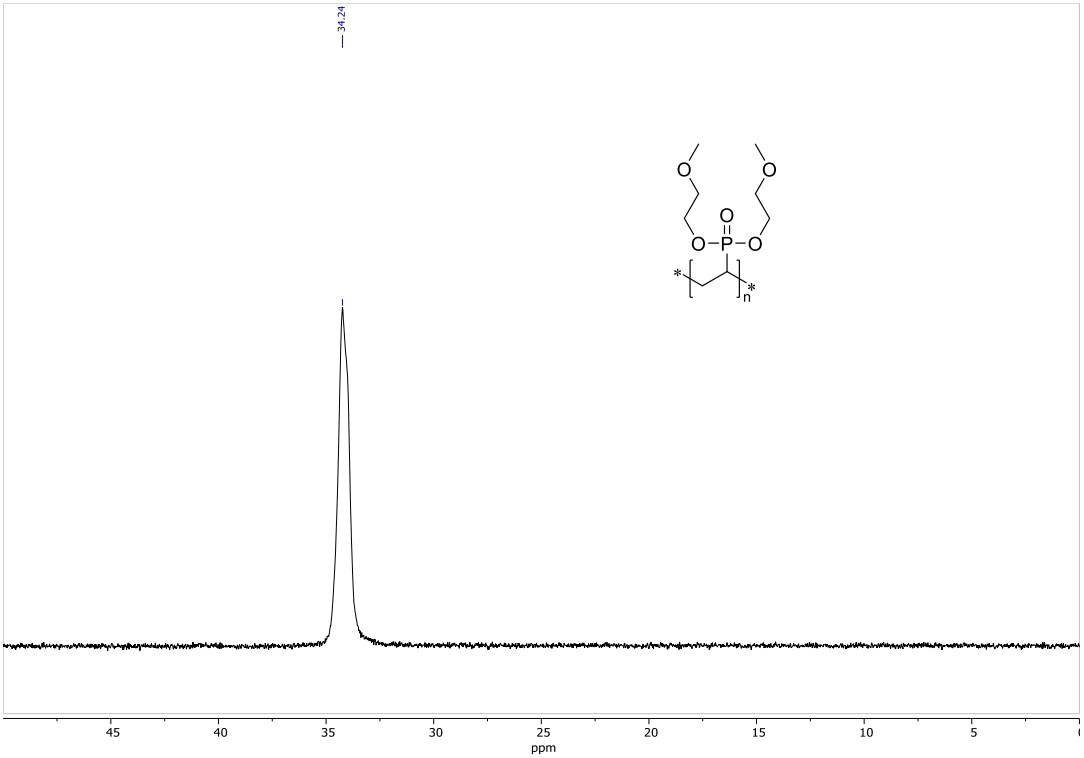

Figure 8-2: ^{31}P-NMR of P1-VP in $CDCl_3$ at 162 MHz.

GPC in THF/H_2O (for P1-VP)

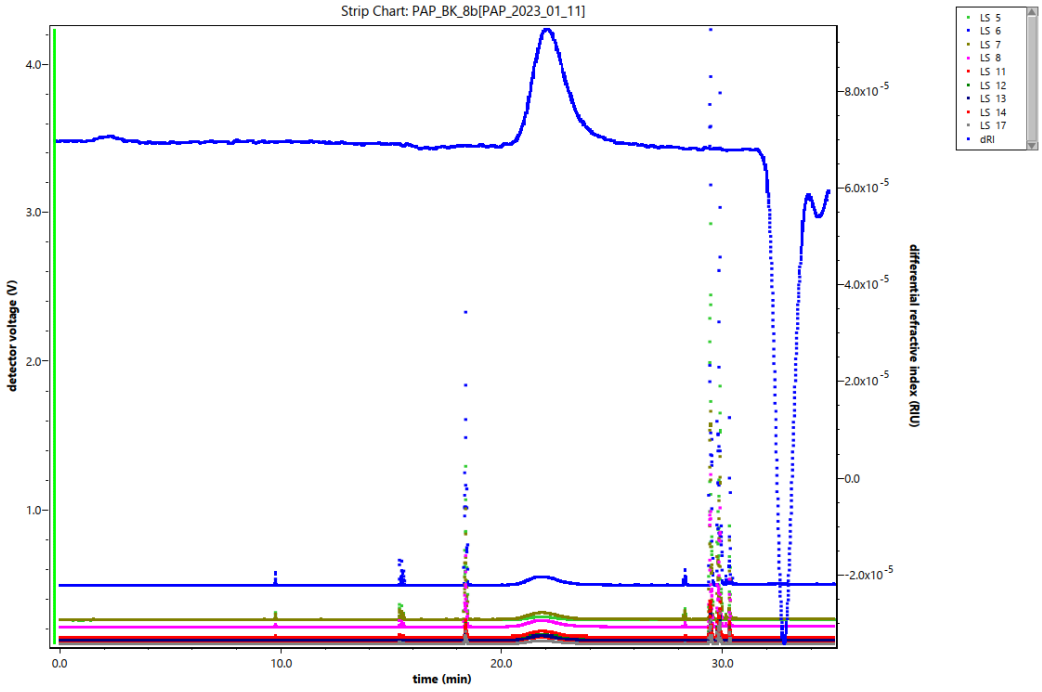

Figure 8-3: GPC trace of P1-VP; THF/H_2O (50:50) with 9 g L^{-1} TBAB and 0.34 g L^{-1} BHT as solvent, *dn/dc* = 0.129 mL g^{-1}, absolute determination of molecular weights and dispersity by multi angle light scattering at 40 °C. (Mon/Cat = 500/1) M_n(abs) = 185 kg mol^{-1}, **Đ** = 1.12.

P2-VP

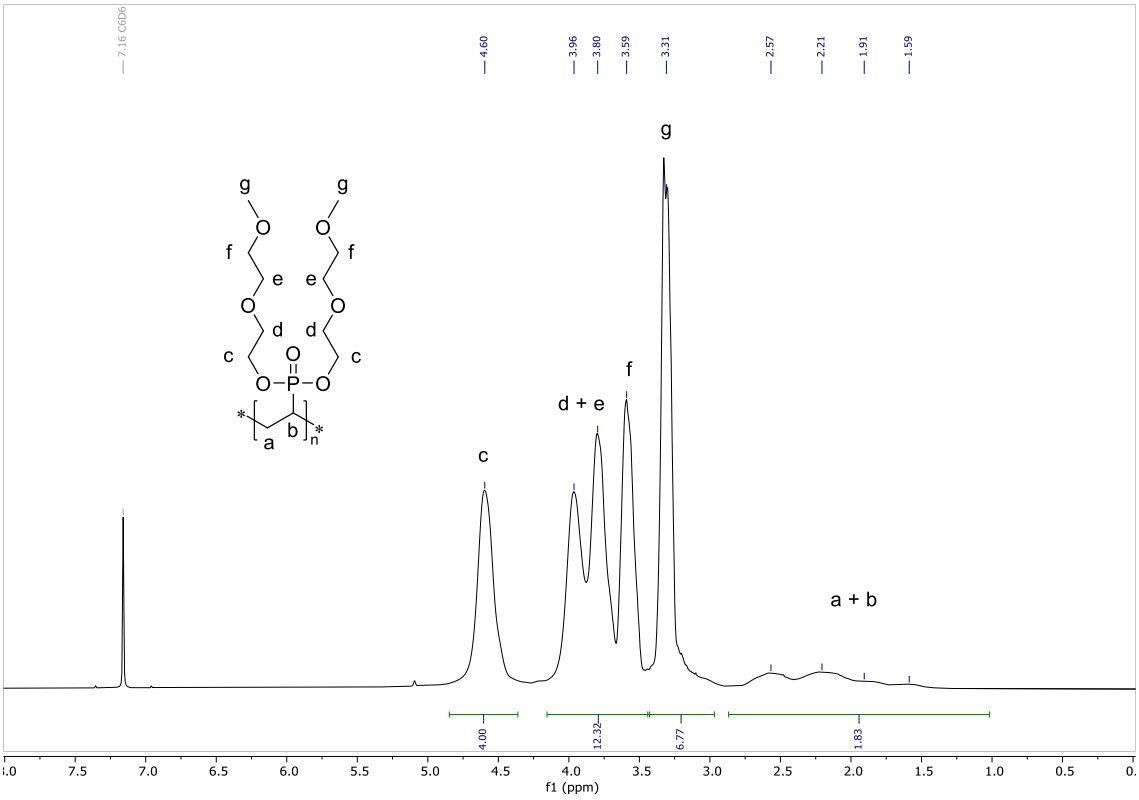

Figure 8-4: ^{1}H-NMR of P2-VP in C_6D_6 at 400 MHz.

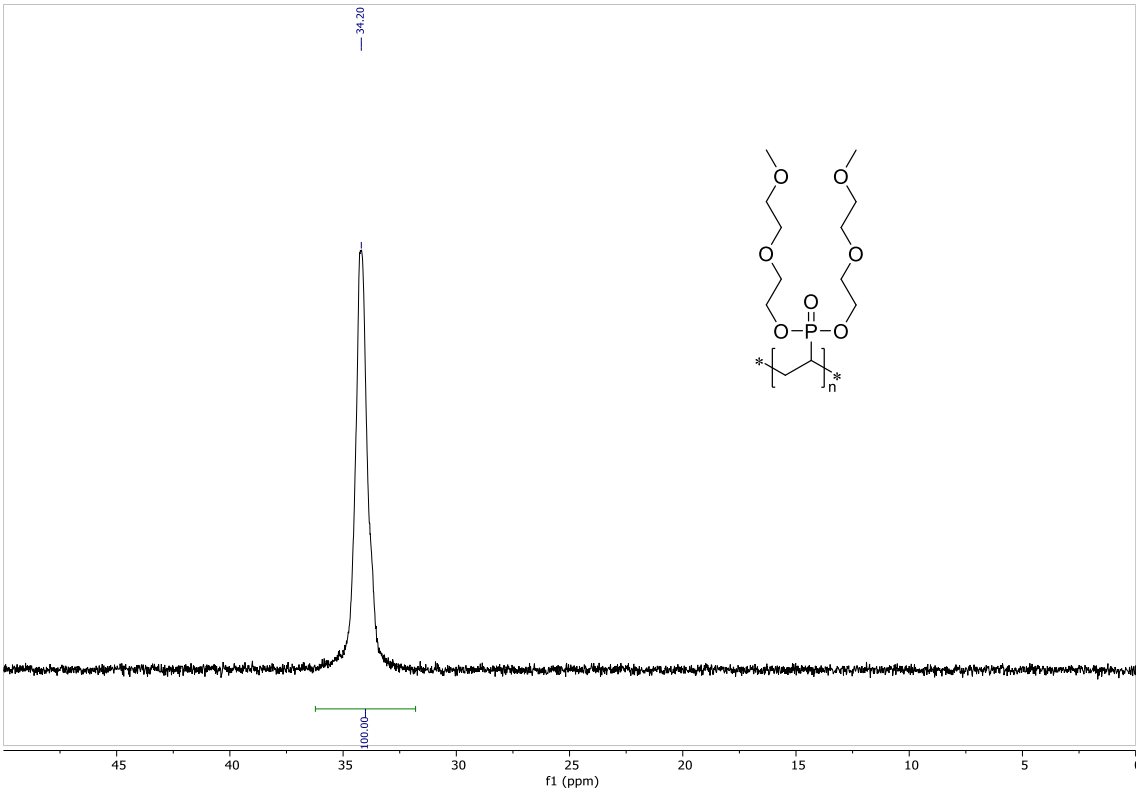

Figure 8-5: ^{31}P-NMR of P2-VP in C_6D_6 at 162 MHz.

GPC of P2-VP in DMF

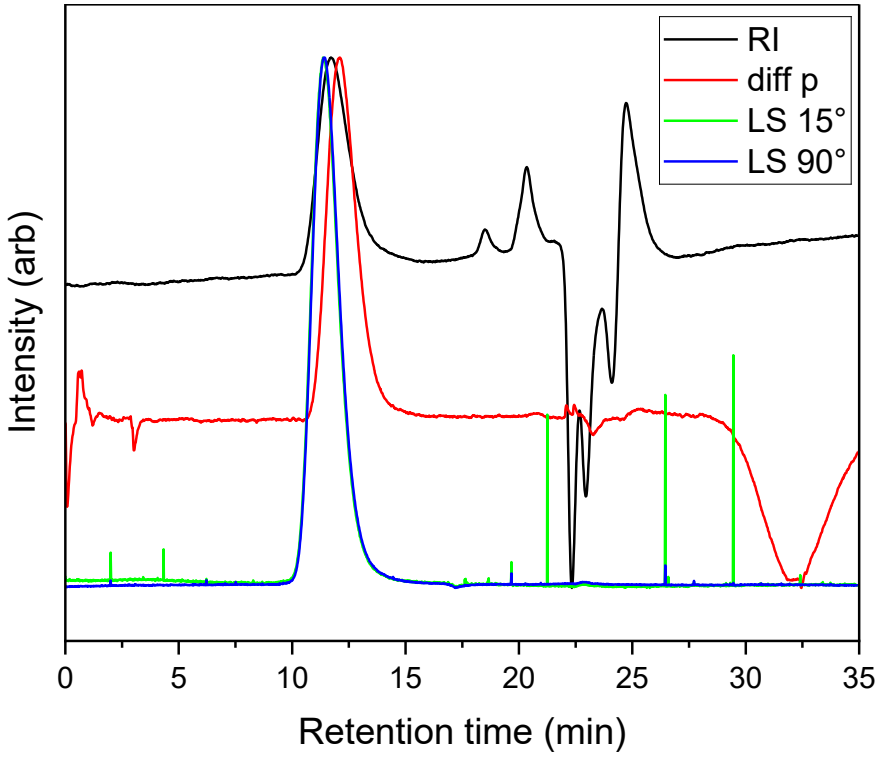

Figure 8-6: GPC trace of P2-VP; DMF + 2 g L^{-1} LiBr as solvent, *dn/dc* = 0.0498 mL g^{-1}, absolute determination of molecular weights and dispersity by triple detection (refraction index, differential pressure and light scattering) at 30 °C. ([Mon]/[Cat]= 2000/1) M_n(abs) = 670 kg mol^{-1}, Đ = 1.16.

GPC and polymer data

Table 8-1: Polymer parameters of P1-VP and P2-VP polymerized REM-GTP via using Cp_2Y(*sym*-collidine).[a]

Polymer	[Mon]/[Cat]	X_M [%][a]	$M_{n,abs}$ [kg/mol][b]	$Đ_{abs}$ [-][c]	I.E. [%][d]	T_g [°C][e]	$T_{d,\ onset}$ [°C][f]
P1-VP	500/1	100	185	1.12	60-95	-48	260
	1500/1	78	320	1.37			
P2-VP	500/1	100	205	1.04	60-80	-67	210
	2000/1	88	650	1.16			

[a]Reactions performed with [Mon] = 100 mg mL^{-1}, 10 mL of solvent, and a reaction time of 30 min at 25 °C. [b]Conversion of monomer (X_M) calculated from the ^{31}P NMR spectrum of aliquots at the end of the reaction via the ratio of signals of the polymer (δ = 32−35 ppm) and the monomer (δ = 16-18 ppm). [b,c]Determined via GPC dn/dc(P1-VP) = 0.129 mL g^{-1} (in THF/H_2O); dn/dc(P2-VP) = 0.0497 mL g^{-1} (in DMF). [d]Initiator efficience calculated by I.E. = $M_{n,calc}/M_{n,abs}$ at the end of the reaction with $M_{n,calc} = M \times (([Mon]/[Cat]) \times X_M$. [e]Determinded via DSC. [f]Determinded via TGA in argon.

Kinetic investigations of the PX-VP polymerization

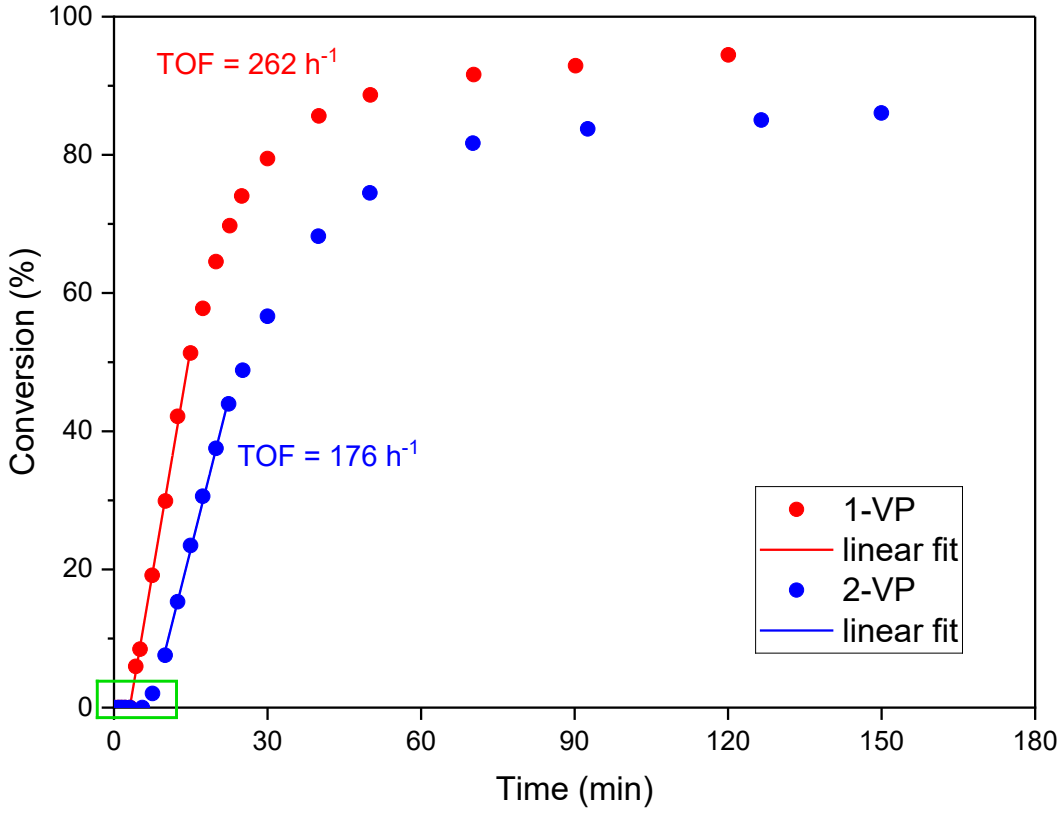

Figure 8-7: Determination of the catalytic activity of YCp_3·THF for the polymerization of 1-VP and 2-VP ([Mon]/[Cat] = 200/1). Both reactions show an initiation period (marked in green).

Table 8-2: Radical polymerization of 2-VP with various reaction conditions.

[Mon]/[Cat]	Initiator	V(toluene) [mL]	Temp. [°C]	Time [h]	Conversion [%]
200/1	AIBN	12	60	22	0
200/1	AIBN	0.75	90	2	18
200/1	AIBN	0.2	110	6	43
150/1	DBPO	0.2	90	4	0

Composition of SPE membranes

Table 8-3: Exemplary composition of the SPE films with $LiBF_4$ as a conducting salt.

Polymer	m(poly) [mg]	m($LiBF_4$) [mg]	EO/Li^+	Mon/Li^+	wt% ($LiBF_4$)
P1-VP	150	25.1	5/1	2.5/1	14.3
		12.5	10/1	5/1	7.7
		8.4	15/1	7.5/1	5.3
P2-VP	150	36.0	5/1	1.25/1	19.3
		18.0	10/1	2.5/1	10.7
		12.0	15/1	3.75/1	7.4

Table 8-4: Exemplary composition of the SPE films with LiTFSI as a conducting salt.

Polymer	m(poly) [mg]	m(LiTFSI) [mg]	EO/Li^+	Mon/Li^+	wt% (LiTFSI)
P1-VP	150	76.8	5/1	2.5/1	33.8
		38.4	10/1	5/1	20.6
		25.6	15/1	7.5/1	14.7
P2-VP	150	110	5/1	1.25/1	73.5
		55.2	10/1	2.5/1	36.7
		36.8	15/1	3.75/1	24.5
PEO[a]	150	27.2	36/1	36/1	18.1

[a] mostly used in an 36/8/1 ratio of EO/SN/Li^+ and therefore 60.6 mg of SN.

TGA data of PX-VP

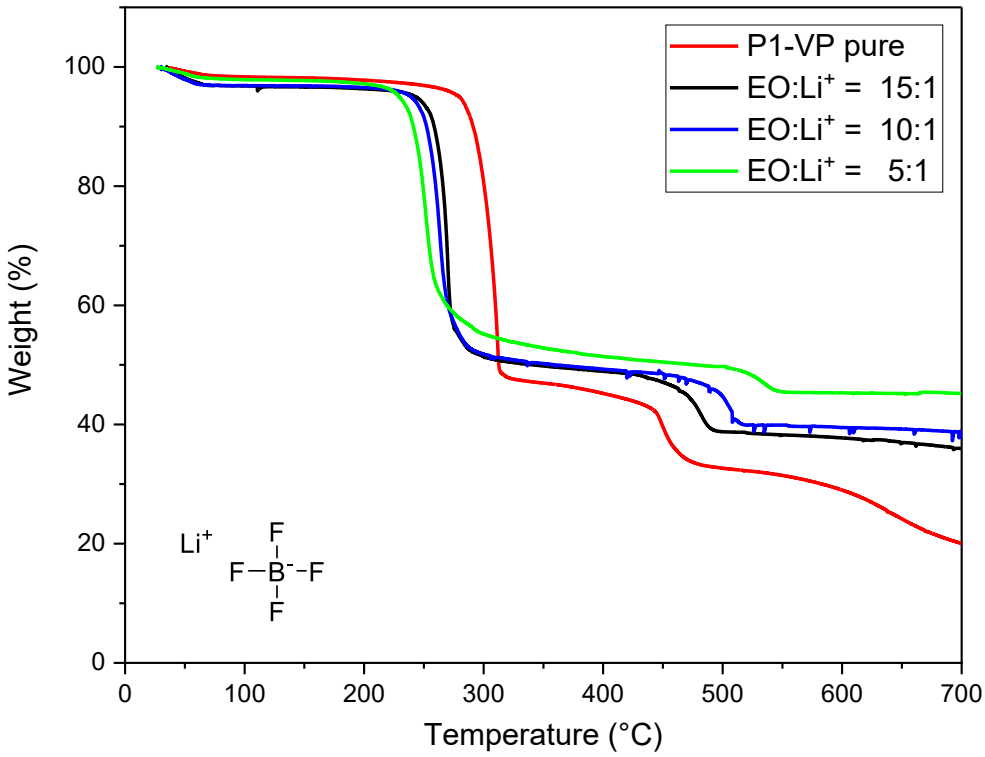

Figure 8-8: TGA curves of P1-VP pure polymers and SPEs with increasing amounts of $LiBF_4$, respectively. Amount of $LiBF_4$ is given as ratio of EO units in the monomer side chains to Li^+ ions.

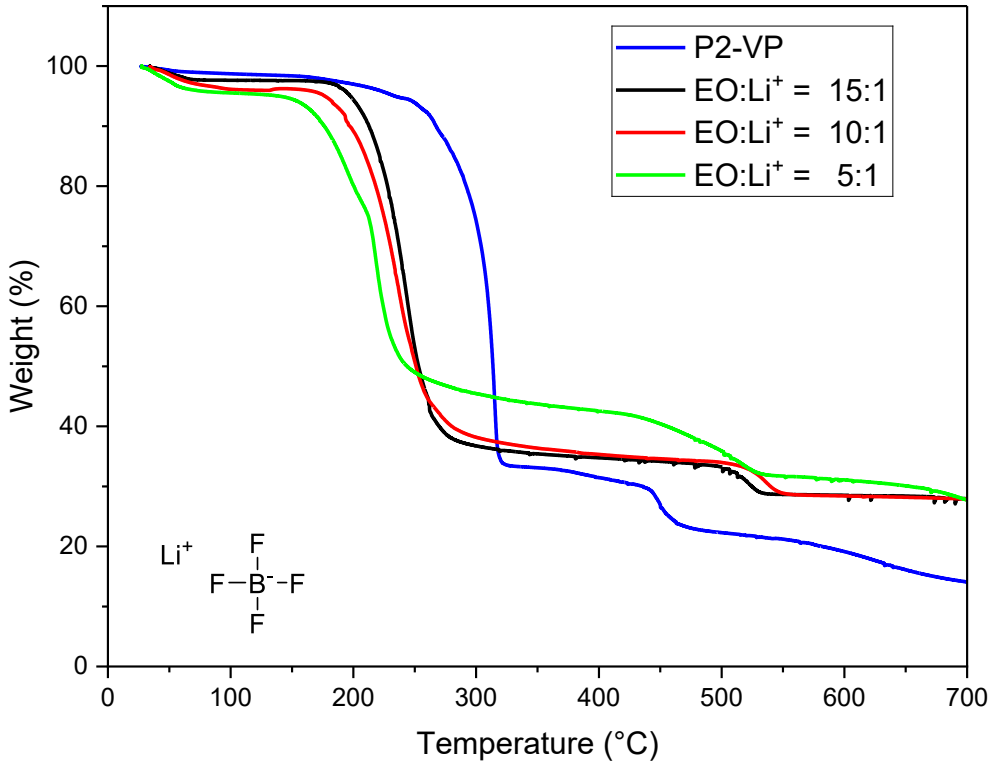

Figure 8-9: TGA curves of P2-VP pure polymers and SPEs with increasing amounts of $LiBF_4$, respectively. Amount of $LiBF_4$ is given as ratio of EO units in the monomer side chains to Li^+ ions.

DSC Measurements

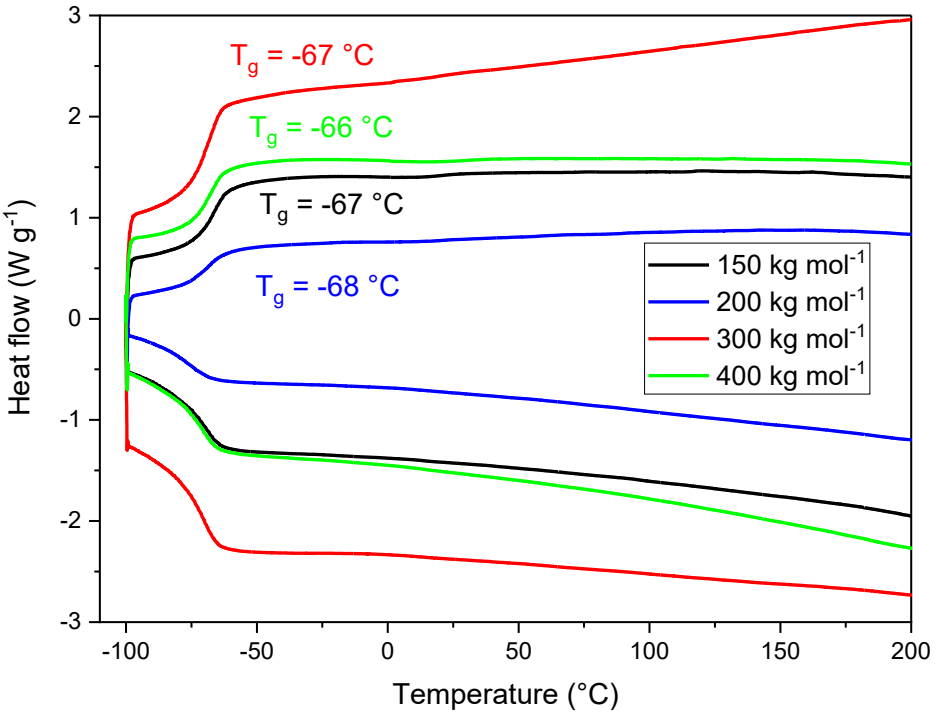

Figure 8-10: DSC curves of P2-VP of different molecular weights without Li-salt.

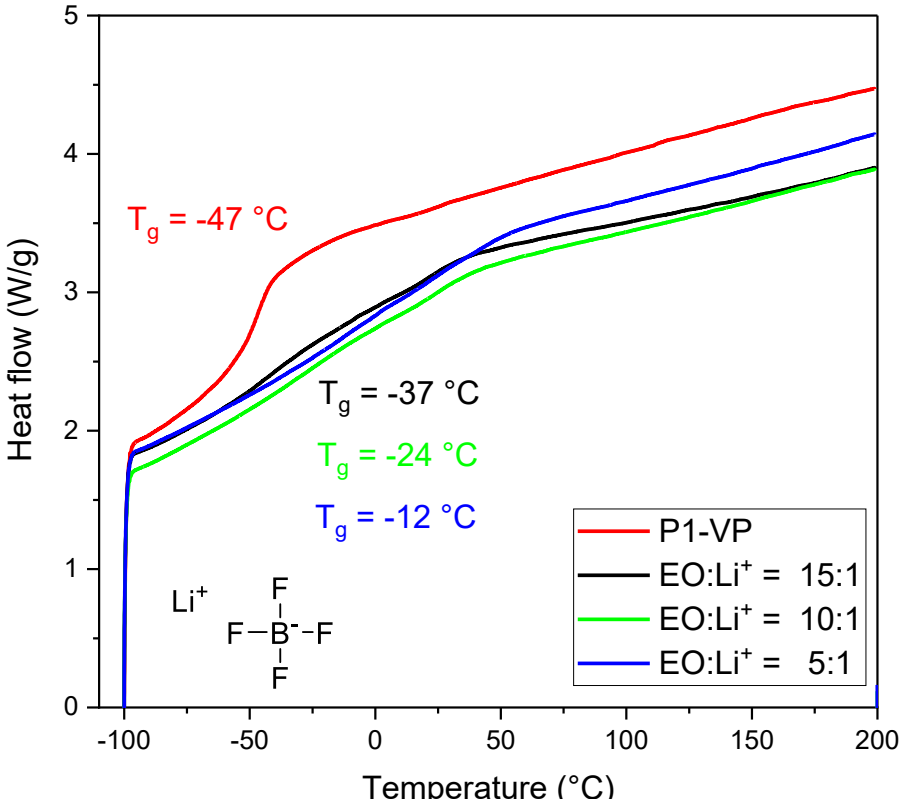

Figure 8-11: DSC curves of pure P1-VP and SPE films with various amounts of $LiBF_4$ (ratios are given as $EO:Li^+$).

Ionic conductivity of P2-VP with various conducting salts

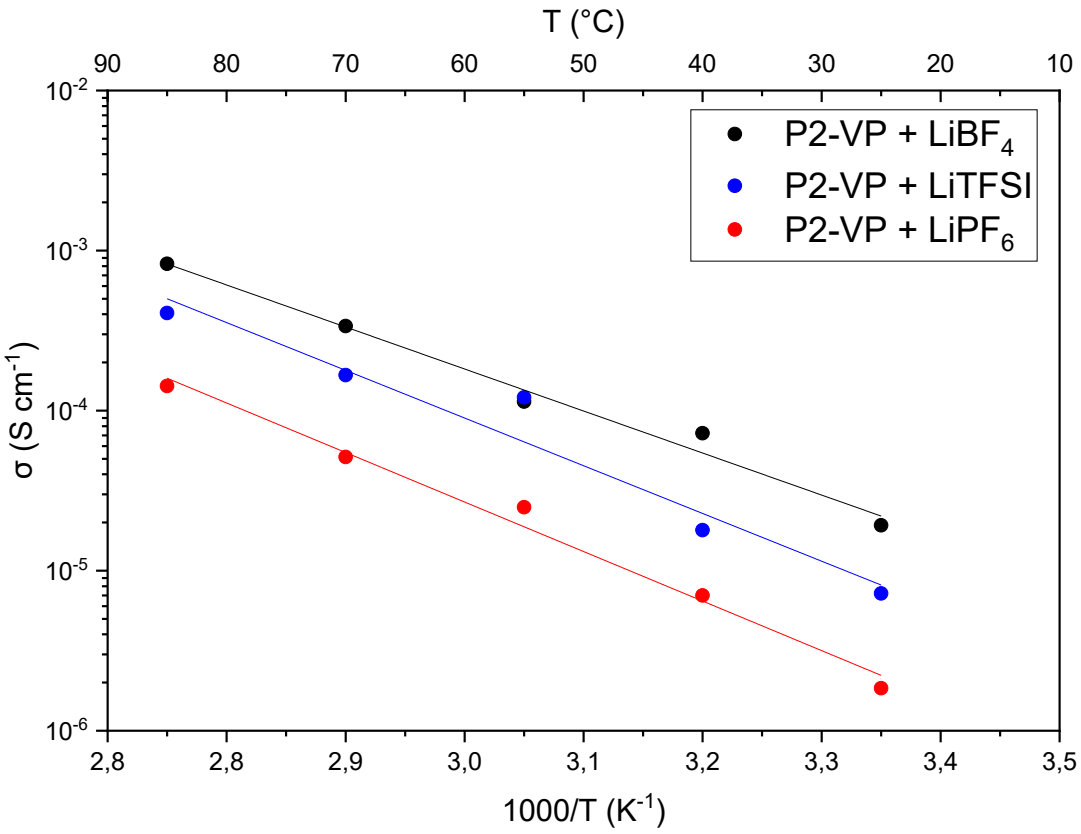

Figure 8-12: Temperature dependent ionic conductivity of P2-VP with various Li-salts (EO/Li^+ = 10/1).

Ionic conductivity P1-VP and P2-VP with different EO/Li^+ ratios

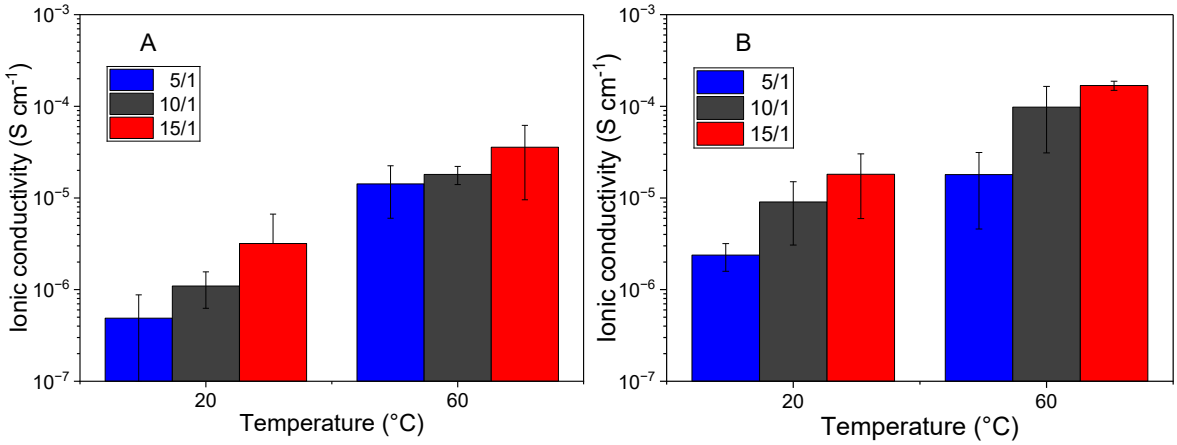

Figure 8-13: Ionic conductivity of **A** P1-VP and **B** P2-VP SPE films with various amounts of $LiBF_4$ (ratios are given as EO/Li^+).

Unsuccessful post mortem analysis of PX-VP after voltammetry measurements

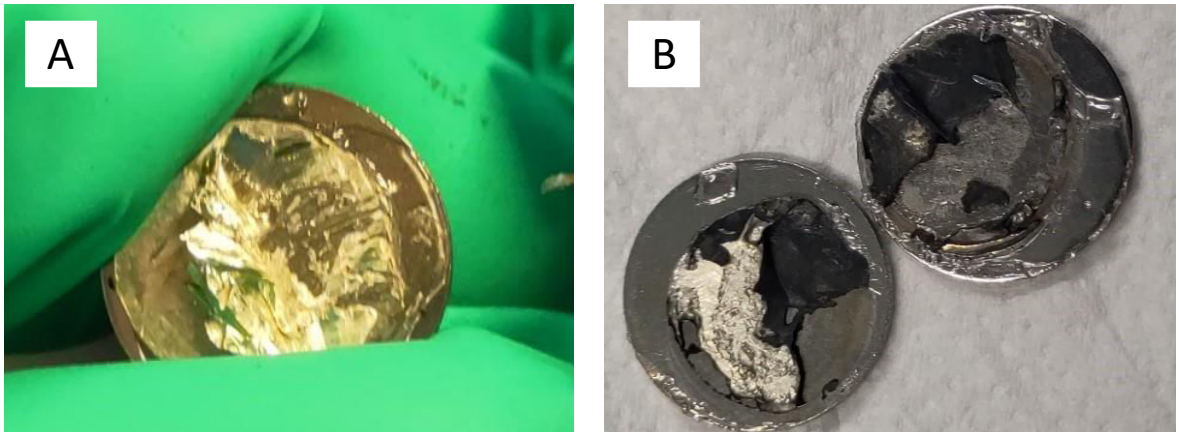

Figure 8-14: Post-mortem analysis attempts of Li|SPE|SS coin cells. **A** Lithium foil and polymer electrolyte remained inseparable after cooling the disassembled cell in a cold trap to −100 °C under inert conditions inside a GB. **B** Partially oxidized lithium observed after freezing the cell components in liquid nitrogen under ambient atmosphere. Separation of the lithium foil and PX-VP foils was not possible.

Cathodic stability of P1-VP and P2-VP SPEs

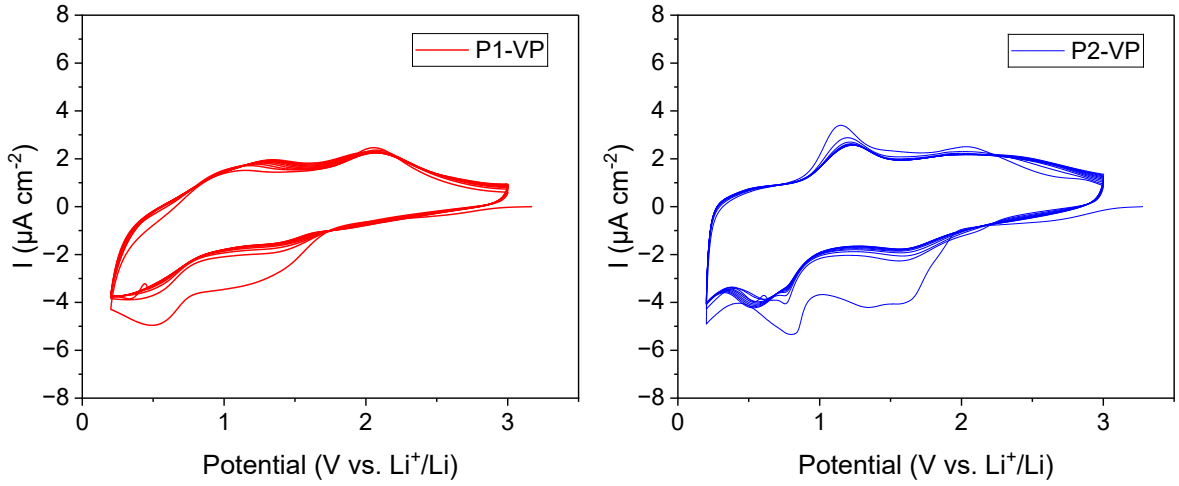

Figure 8-15: Cyclic voltammetry measurements of P1-VP and P2-VP SPEs with $LiBF_4$ ($EO/Li^+ = 10/1$) in Li|SPE|SS coin cells at 60 °C between 0.2 to 3 V vs. Li^+/Li with a scan rate of 0.5 mV s^{-1}.

Lithium transference number

Table 8-5: Parameters used to determine the Li^+ transference number (t_{Li^+}) of P1-VP and P2-VP SPE with $LiBF_4$ (EO/Li^+ = 10/1) in symmetrical Li|SPE|Li cells. Initial and steady state current are determined from chronoamperometry with a voltage of 10 mV over 90 min. Resistance values are obtained from the Nyquist plots by fitting in the Relaxis software to the respective equivalent circuits.

Polymer	Initial current (I_0) [µA]	Steady state current (I_0) [µA]	Initial resistance ($R_{Int,0}$)) [Ω]	Steady state resistance ($R_{Int, SS}$)) [Ω]	Li^+ transference number (t_{Li^+})
P1-VP	4.85	0.29	912	989	0.03
P2-VP	7.47	1.30	498	541	0.12

Cathode analysis – SEM imaging and EDX spectra

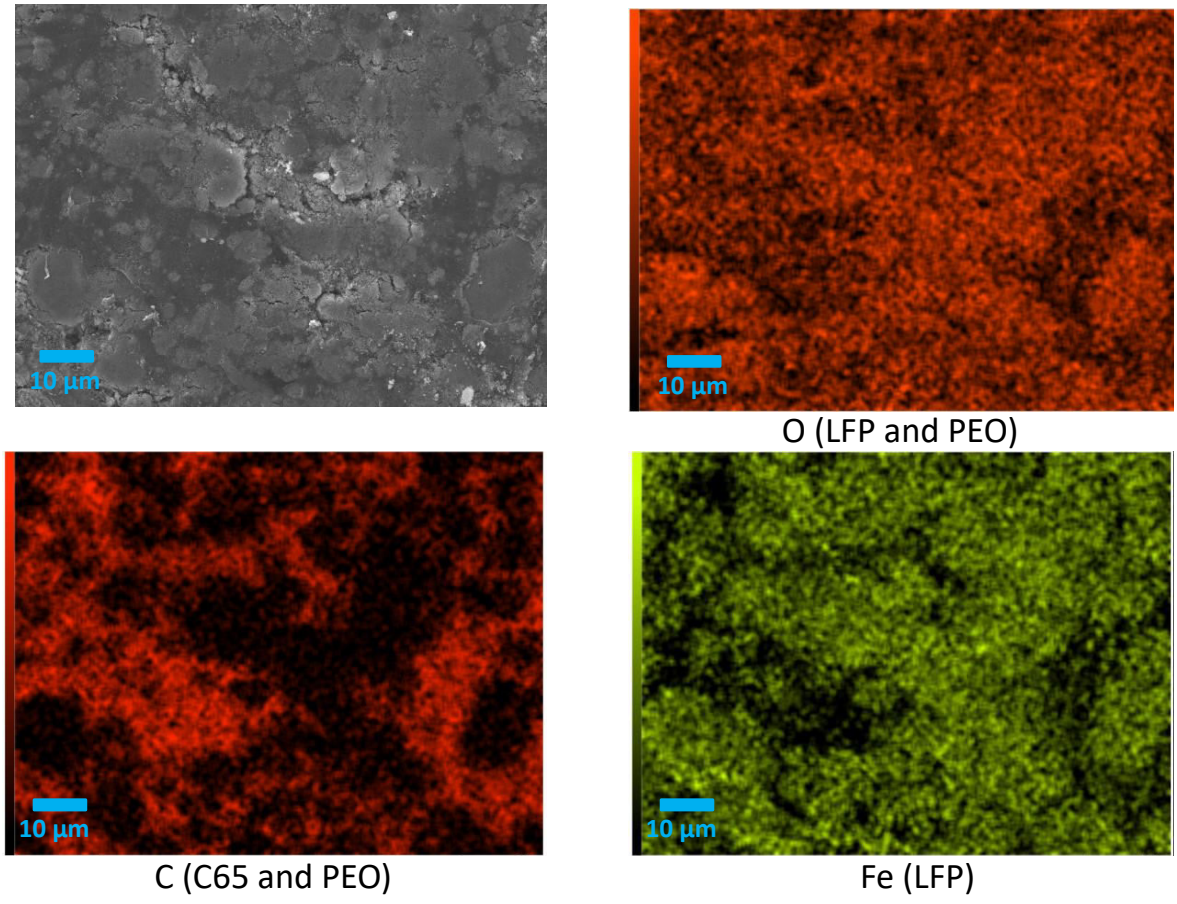

Figure 8-16: SEM and associated EDX spectra of a LFP cathode pressed in the ASC-T cell.

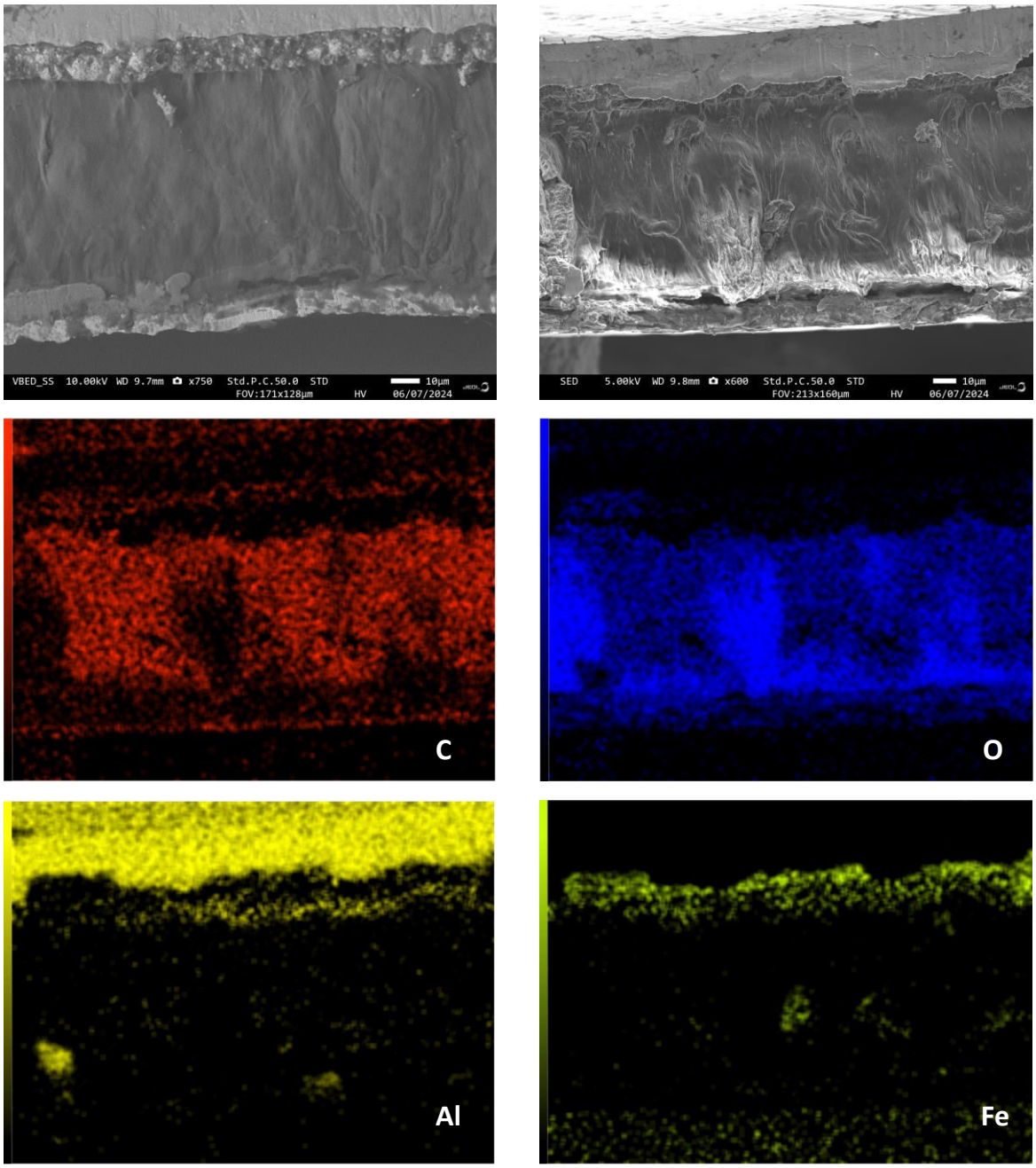

Figure 8-17: Top: SEM images of a half cell cut in half with a scalpel. VBED_SS detector for left image; SED detector for right image. Corresponding EDX spectra to top right SEM for C (C65), O (PEO, LiTFSI, LFP), Al (current collector), Fe (LFP). Lithium can hardly be detected by EDX and could therefore not be analysed.

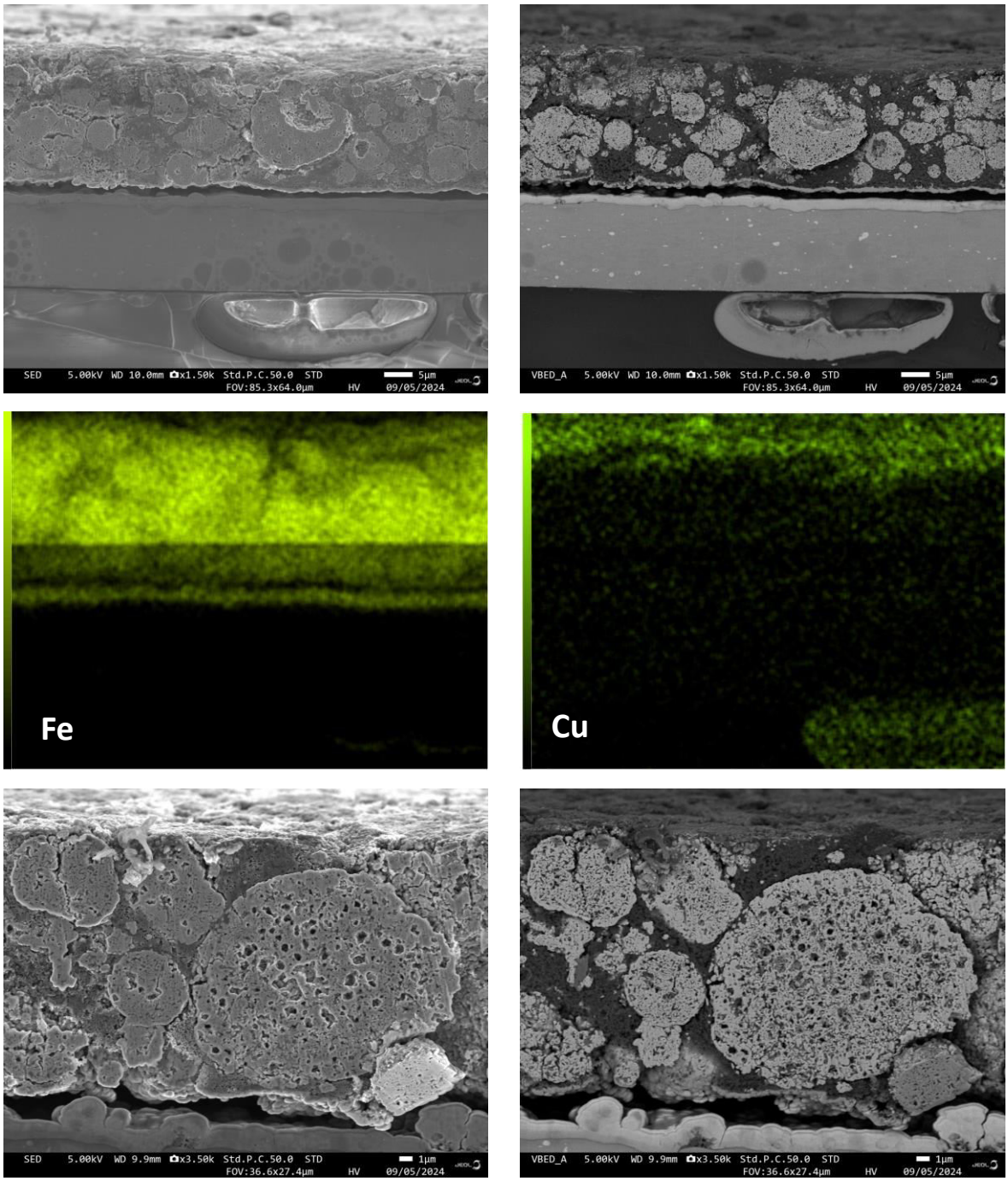

Figure 8-18: SEM images with two different magnifications and corresponding EDX spectra for Fe (LFP and suspected Al-Fe alloy band) and Cu (molten droplet in bottom right corner). SEM images on the left use SED detection while the ones on the right use a VBED_A detector.

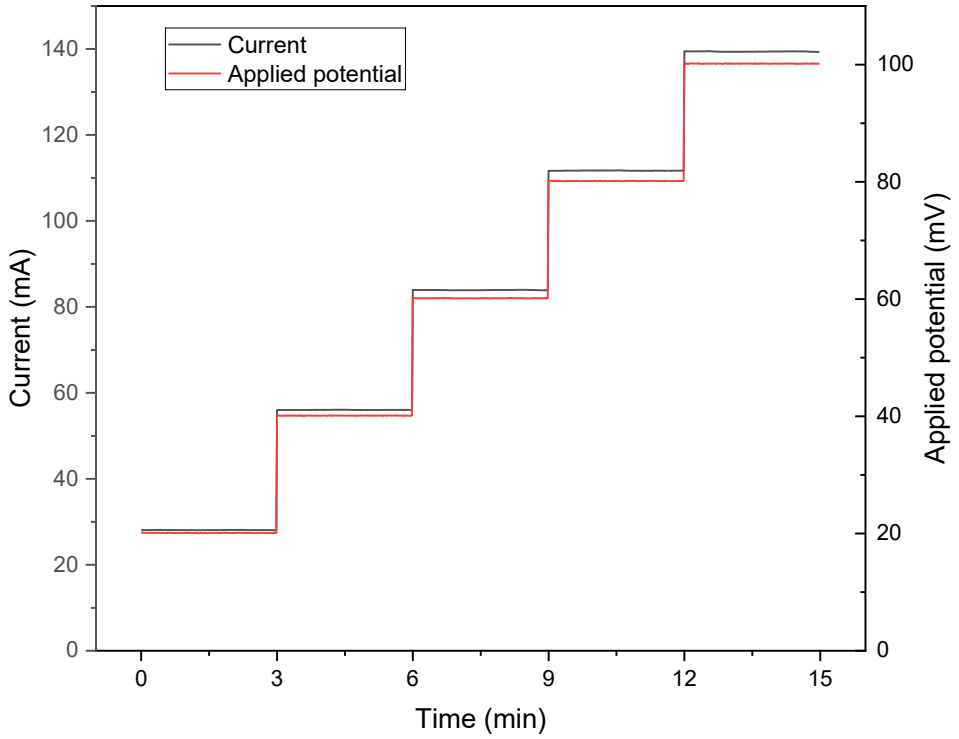

Figure 8-19: Exemplary chronoamperometry measurement of an LFP cathode in an Al-Cat|Cat-Al setup in the ASC-T cell at 5 MPa and 60 °C.

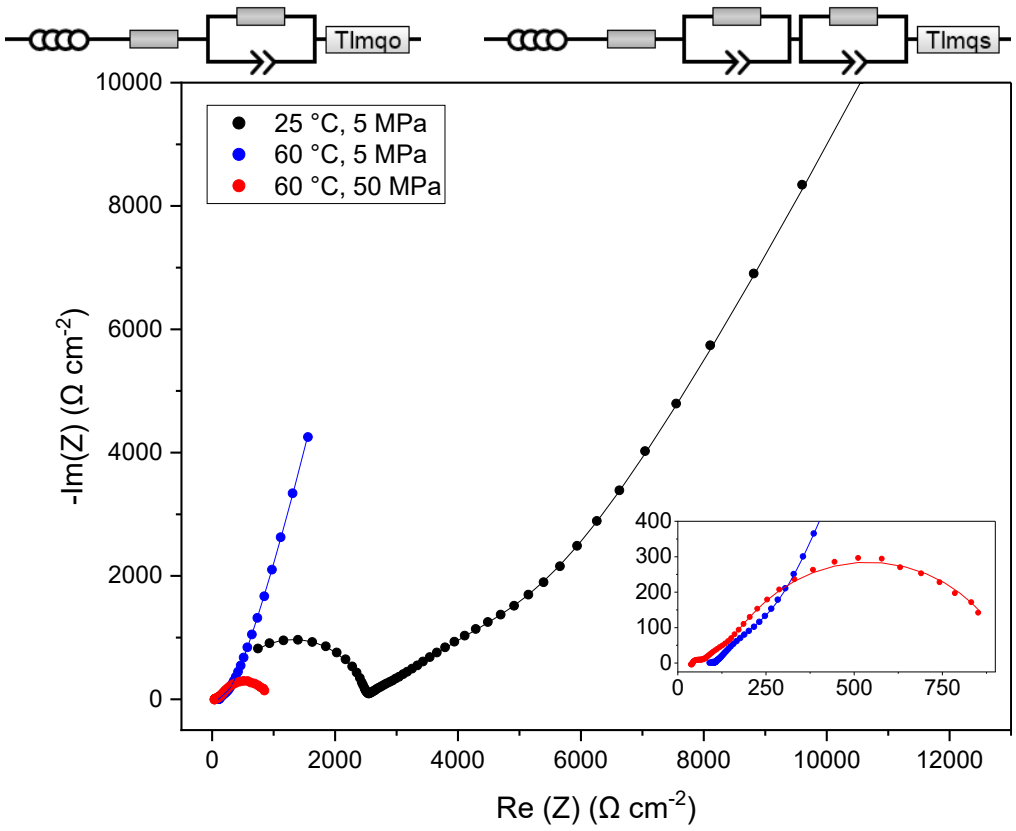

Figure 8-20: Impedance spectra of a LFP|PEO|LFP stack in the ASC-T cell at various temperatures and pressures with respective fits. Equivalent circuit for blocking features (5 MPa) shown top left. The non blocking feature in the red curve is fitted with a TLMqs (top right). δ(PEO) = 118 µm before assembly.

Half cell impedance measurements with PEO

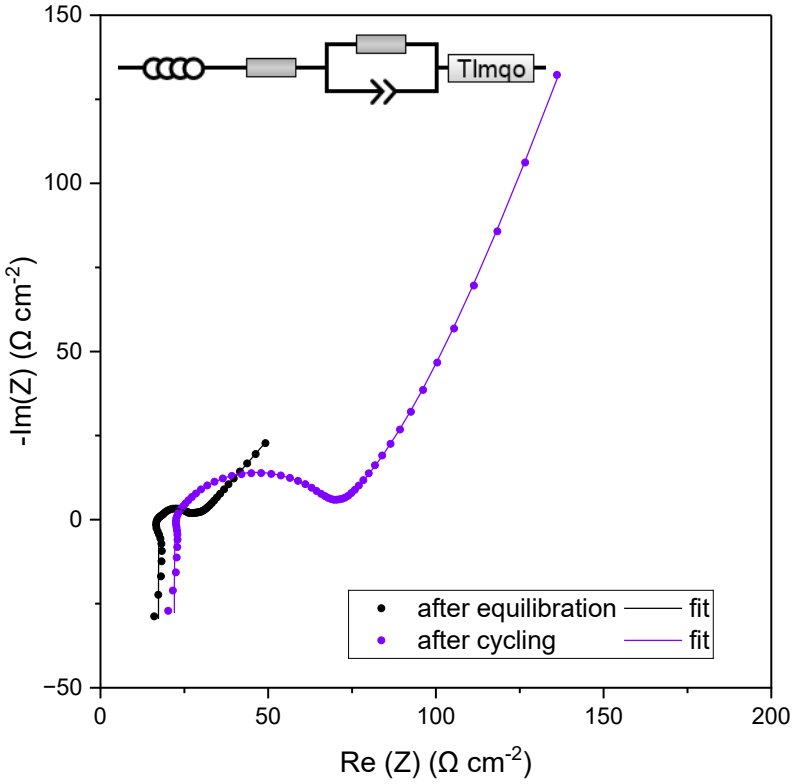

Figure 8-21: Impedance spectra of a LFP|PEO|Li half cell before and after cycling for 32 times with a CCCV protocol at 60 °C. Equivalent circuit used for fitting displayed at the top.

Half cell impedance measurements with P1-VP

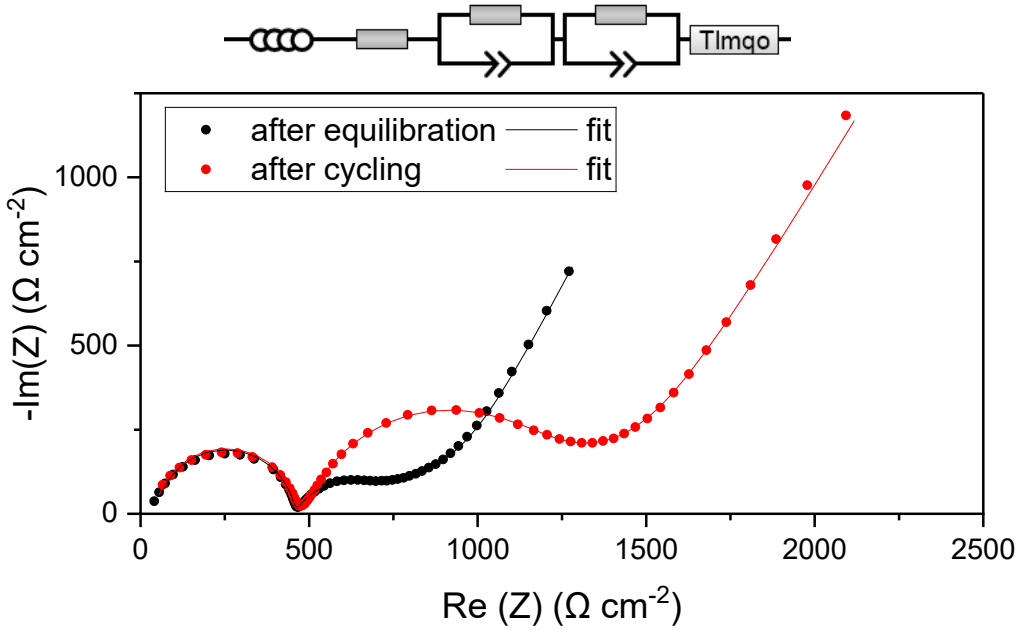

Figure 8-22: Impedance spectra of LFP|P1-VP|Li half cells at before and after cycling at 60 °C.

Half cell impedance measurements with P2-VP

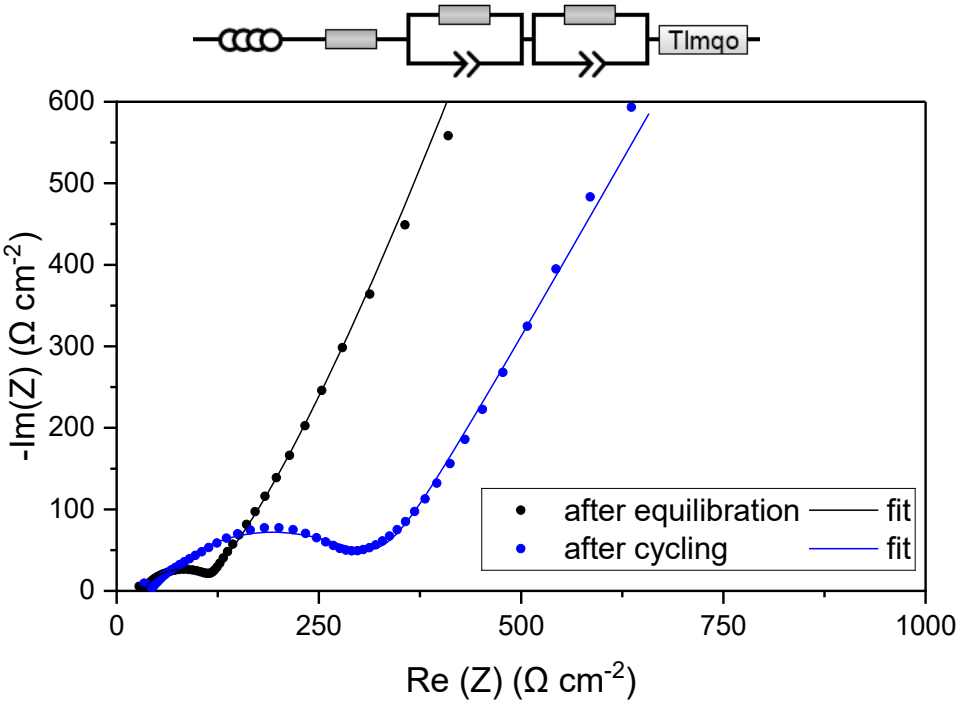

Figure 8-23: Impedance spectra of LFP|P2-VP|Li half cells at before and after cycling at 60 °C.

Validation of the ASC-T cell setup

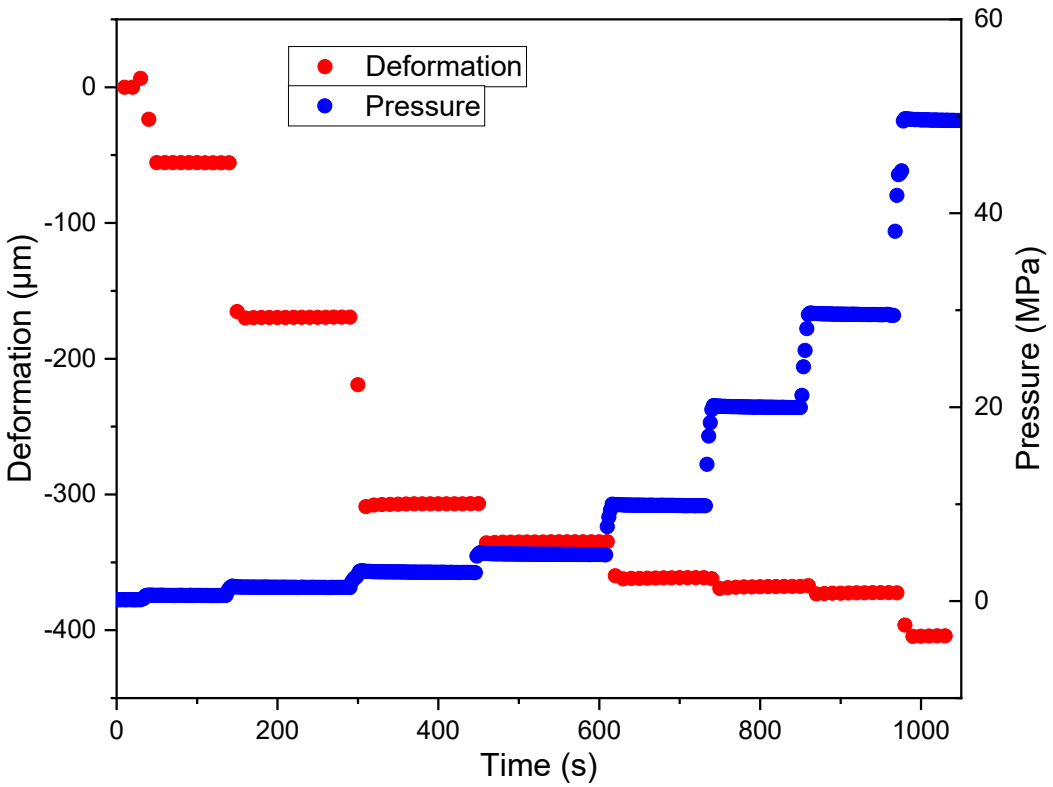

Figure 8-24: Relation of deformation and pressure with time in the ASC-T cell when stepwise increasing the applied pressure in an empty cell. Measurements are slightly shifted on the X-axis as the pressure and thickness measurement are independently started and recorded.

Figure 8-25: PEO-SPE film after a pressure test in the ASC-T cell. Clear indentation visible due to uneven pressure distribution in the cell setup.

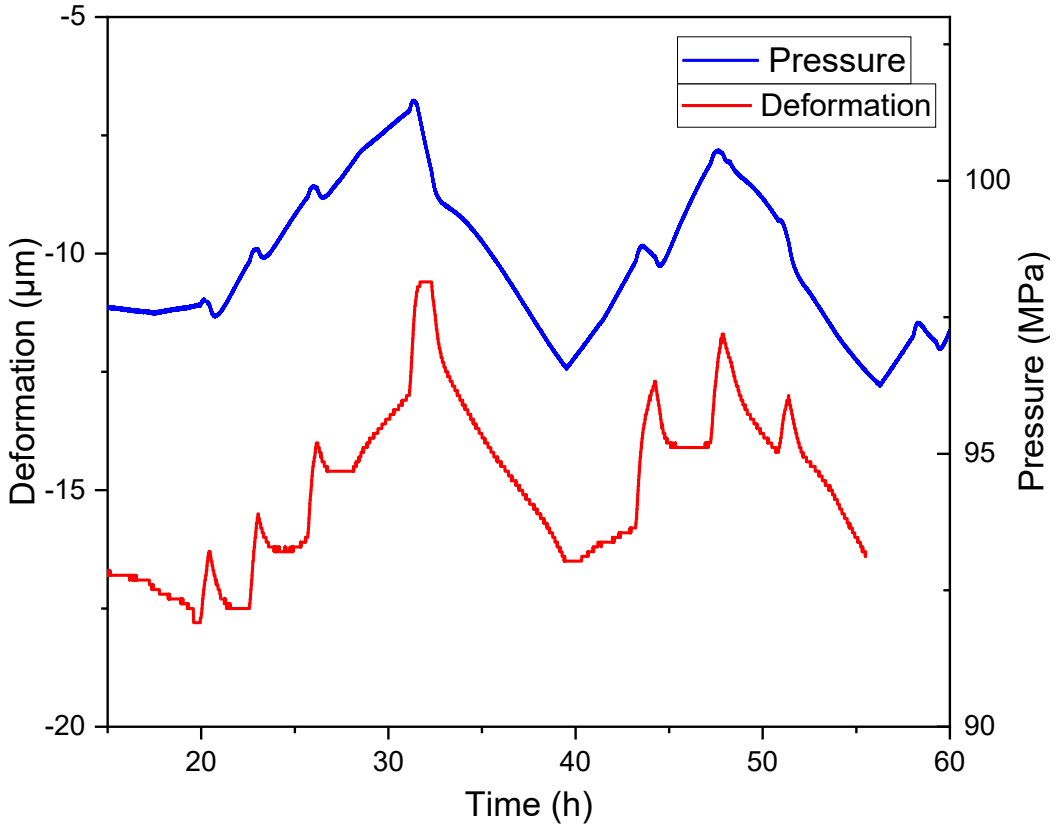

Figure 8-26: Measured pressure-deformation correlation of the NMC|LPSCl|InLi test cell in the ASC-T cell with the constant gap setup.

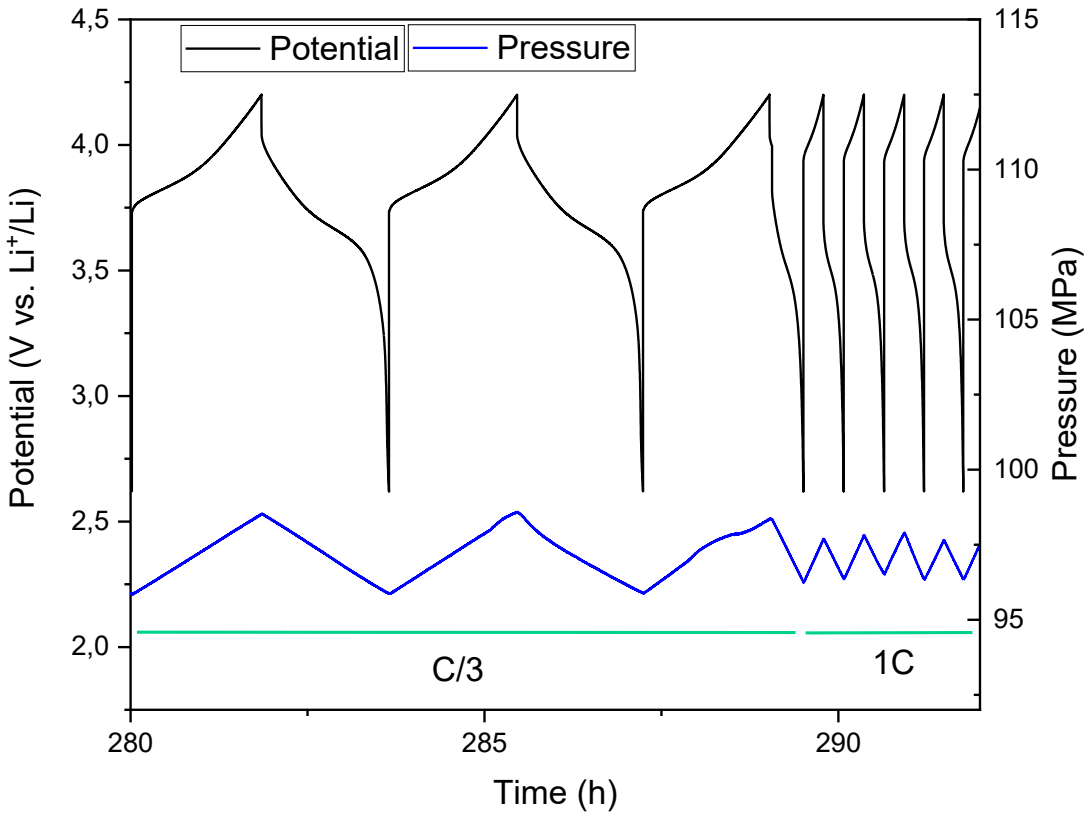

Figure 8-27: Cycling profile of an NMC|LPSCl|InLi test cell measured in the ASC-T cell setup with corresponding pressure at charging rates of C/3 and 1C. The cell was in the constant gap setup.

Half cell impedance measurements with a PEO separator in the ASC-T cell setup

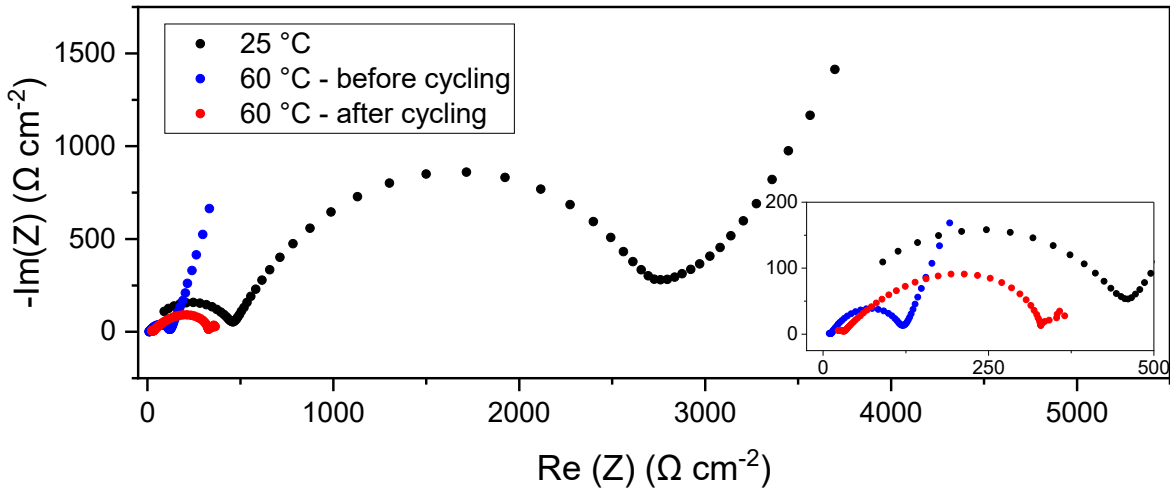

Figure 8-28: Impedance spectra of an LFP|PEO|Li half cell before and after cycling for 15 times with a CCCV protocol at 60 °C in the ASC-T cell setup at 2 MPa. Equivalent circuit used for fitting displayed at the top.

Impedance measurements of Li|LLZO|Li cells w/o Au for interface improvement

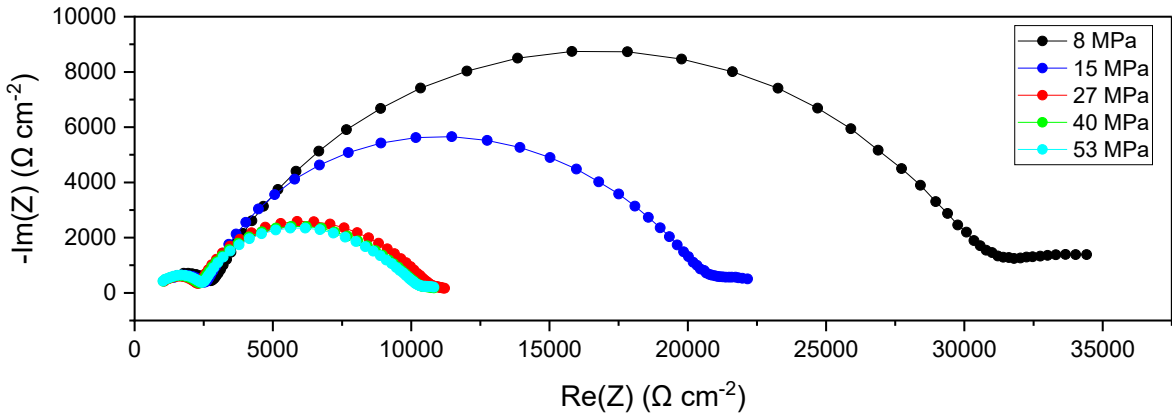

Figure 8-29: Impedance evolution with increasing applied pressure of an Li|LLZO|Li cell in the ASC-T cell in the constant pressure setup. Impedance measurements were taken when a constant pressure was reached, after about 3 min of equilibration time.

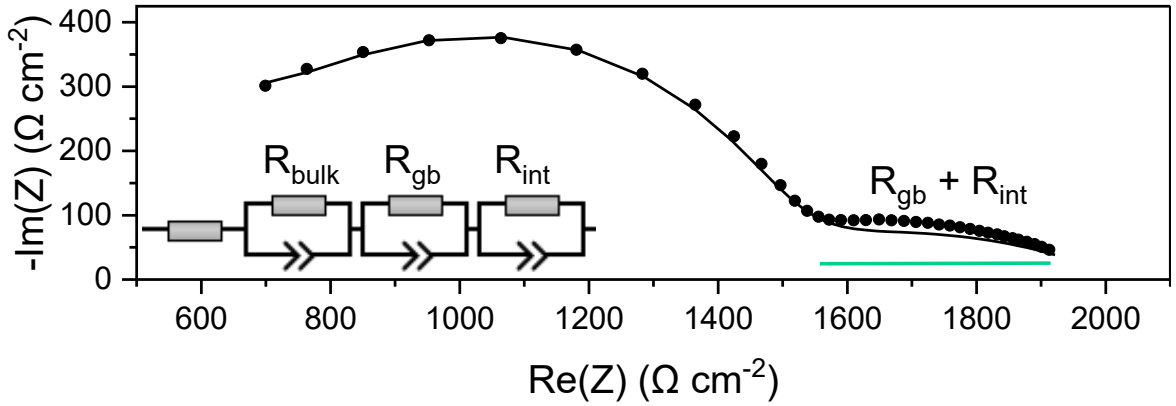

Figure 8-30: Impedance spectrum of a Li|LLZO|Li cell with Au sputtered ontop of the LLZO to improve the interface between LLZO and Li by creating a Li_xAu alloy.

Half cell measurements with only an LLZO pellet as the electrolyte in the ASC-T cell setup

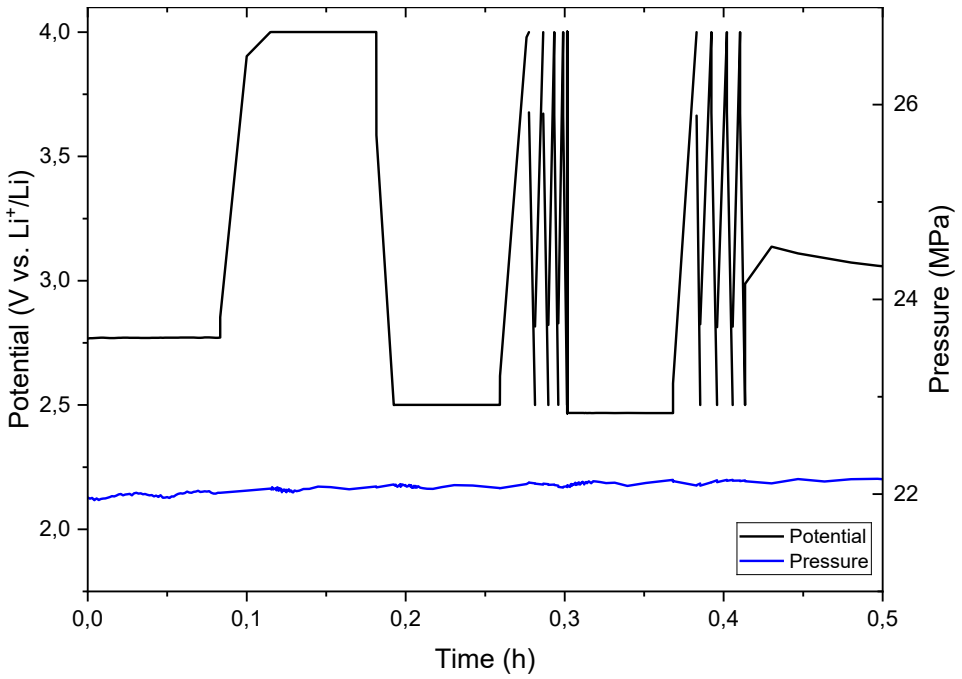

Figure 8-31: Cycling profile of an LFP|LLZO|Li cell with corresponding pressure. C-rates of C/10-C/5-1C were applied. Measured in the constant pressure setup of the ASC-T cell (spring constant k = 167 N mm^{-1}) at 60 °C. Thickness did not change over the measurement duration.

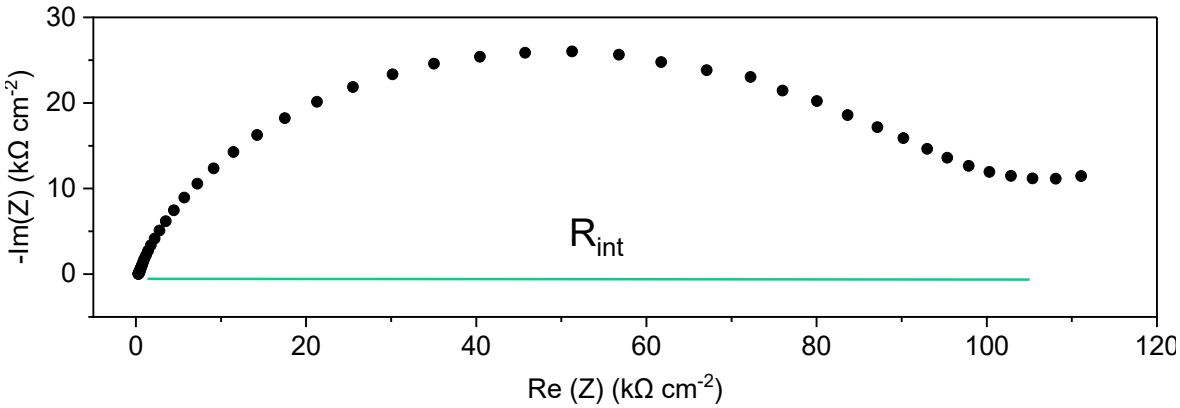

Figure 8-32: Impedance spectrum of an LFP|LLZO|Li cell in the ASC-T setup at 60 °C and 22 MPa. Interfacial resistance is far greater than bulk resistances.

Half cell measurements of an LFP|PEO|LLZO|Li cell with a thin PEO-CPE interlayer

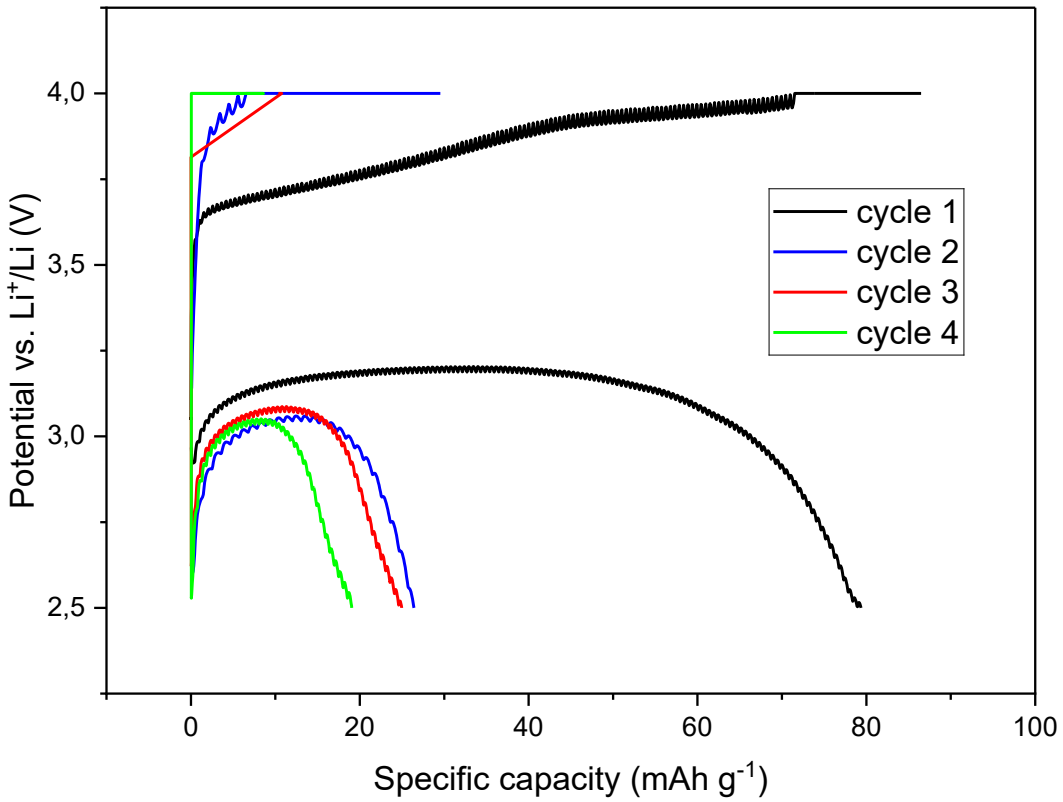

Figure 8-33: Charge-discharge profiles of LFP|PEO|LLZO|Li half cell cycled at C/10 in the ASC-T cell setup at 60 °C and 5 MPa. PEO-CPE composition EO/SN/LiTFSI = 36/8/1 with 20wt% SiO_2, δ = 5 µm.

8.1 List of Figures

8.2 List of Schemes

8.3 List of Tables

Publications

The following published publication is included in parts of this thesis:

P. Pfändner, M. Wittig, T. Pehl, B. Rieger, *ACS Applied Polymer Materials* **2025**, *7* (3), 2102-2111; title: Introducing a Catalytic Polymerization Approach for Bottlebrush Vinylphosphonate Solid Polymer Electrolytes with Ethylene Oxide Side Chains; DOI 10.1021/acsapm.4c03951.

The following published publication is beyond the scope of this thesis:

M. Wittig, **P. Pfändner**, B. Rieger *Polymer Chemistry* **2024**, *15*, 3071–3076; title: Synthesis of a sulfonamide functionalized poly(styrene oxide) and illustration of a potential post-polymerization strategy; DOI 10.1039/D4PY00460D.

J. N. Schwämmlein, G. S. Harzer, **P. Pfändner**, A. Blankenship, H. A. El-Sayed, H. A. Gasteiger, *Journal of The Electrochemical Society* **2018**, *165*, J3173-J3185; title: Activity and Stability of Carbon Supported PtxY Alloys for the ORR Determined by RDE and Single-Cell PEMFC Measurements; DOI 10.1149/2.0221815jes.

Conference contributions

Solid-state batteries V, Frankfurt am Main, Germany, 22-24 November 2022; poster title: Oligoethylene oxide functionalized vinylphosphonic esters as solid polymer electrolytes with adjustable flexibility, poster presentation

IBA 2022, Bled, Slovenia, 2-7 October 2022; poster title: Oligoethylene oxide functionalized vinylphosphonic esters as solid polymer electrolytes with adjustable flexibility, poster presentation

Batterieforum Deutschland 2022, 20/27 January 2022, Berlin, Germany, poster title: Novel solid polymer electrolytes based on PEO and vinylphosphonic esters for high safety ASSBs, poster presentation